



Faculteit Wetenschappen

Departement Fysica

Onderzoeksgroep Bimef

**Het Menselijke Middenoor - Een Multidisciplinaire  
Studie door middel van Tomografische Beeldvorming,  
Stroboscopische Holografie en Dynamische Eindige  
Elementen Modelling**

Proefschrift ingediend tot behalen van de graad van

**Doctor in de Wetenschappen: fysica**

aan de Universiteit Antwerpen,

verdedigd door

**Daniël De Greef**

**Promotor**

Prof. Joris J. J. Dirckx

Antwerp, 2017

## Contact information

*Postal address* Daniël De Greef  
Laboratory of Biophysics and Biomedical Physics – Department of  
Physics – University of Antwerp  
Groenenborgerlaan 171 – 2020 Antwerp – Belgium

*Phone* 0031/628.79.73.83

*Email* ddegreef2@gmail.com

## PhD defense

*Private defense* Held on Tuesday December 20, 2016, in meeting room De Rede, office U337 at campus Groenenborger, University of Antwerp

*Public defense* Held on Tuesday January 31, 2017, in auditorium G.010, at campus Middelheim, University of Antwerp

## Financial support

For this work, the author was financially supported by the Research Foundation Flanders (Fonds voor Wetenschappelijk Onderzoek – FWO) by means of a PhD Fellowship.



# **FRONT MATTER**



# Contents

---

<b>COVER.....</b>	<b>1</b>
<b>FRONT MATTER .....</b>	<b>3</b>
CONTENTS .....	5
DOCTORAL COMMITTEE.....	11
DANKWOORD/ACKNOWLEDGEMENTS .....	13
PREFACE.....	17
SUMMARY .....	19
<b>PART I - STROBOSCOPIC HOLOGRAPHY .....</b>	<b>23</b>
INTRODUCTION: HOLOGRAPHY AND DIGITAL HOLOGRAPHY .....	25
1. <i>Fresnel diffraction</i> .....	26
2. <i>Reconstruction of a digital hologram</i> .....	27
3. <i>Overview of part I of this dissertation</i> .....	29
CHAPTER 1.    DIGITAL STROBOSCOPIC HOLOGRAPHY SETUP FOR DEFORMATION MEASUREMENT AT BOTH QUASI-STATIC AND ACOUSTIC FREQUENCIES.....	31
<i>Abstract</i> .....	31
1. <i>Introduction</i> .....	32
2. <i>Method</i> .....	33
2.1 Concept.....	33
2.2 Setup.....	35
3. <i>Results</i> .....	38
3.1 Vibration of a circular membrane .....	38
3.2 Duration of the measurements.....	40
3.3 Evaluation of the technique: accuracy and repeatability.....	40
4. <i>Discussion</i> .....	44
4.1 Measurement range .....	44
4.2 Comparison to other techniques .....	45
4.3 Comparison to similar setups.....	45
4.4 Applications and future development .....	46
5. <i>Conclusion</i> .....	47
CHAPTER 2.    GRAPHICAL USER INTERFACE FOR A DIGITAL STROBOSCOPIC HOLOGRAPHY SETUP: EXPERIMENT CONTROL, DATA PROCESSING AND RESULTS ANALYSIS .....	49
1. <i>Introduction</i> .....	49
1.1 Minimizing measurement overhead time.....	49
1.2 Facilitating the training of other researchers to use the setup.....	50
2. <i>Elements of the GUI</i> .....	50
2.1 GUI Overview .....	50
2.2 Experiment control module and list of frequencies.....	51
2.3 Results module.....	55
<b>PART II - MIDDLE EAR MORPHOLOGY .....</b>	<b>59</b>
INTRODUCTION: THE MIDDLE EAR AND MICRO-COMPUTED TOMOGRAPHY ( $\mu$ CT) .....	61
1. <i>The hearing organ: an overview</i> .....	61

1.1	The external ear .....	62
1.2	The middle ear .....	63
1.3	The (cochlea of the) inner ear .....	64
2.	<i>The function of the ME in the auditory frequency regime</i> .....	64
2.1	The eardrum or tympanic membrane .....	65
2.2	The ossicles .....	67
2.3	Sound amplification mechanisms of the ME .....	68
2.4	The ligaments of the middle ear .....	70
2.5	The middle ear muscles .....	70
3.	<i>The function of the ME in the quasi-static frequency regime</i> .....	71
3.1	The Eustachian tube .....	72
3.2	Gas exchange with blood in the mucosa .....	73
3.3	Change of mucosa thickness though perfusion .....	73
3.4	The buffer capacity of the tympanic membrane .....	74
4.	<i>Micro-computed tomography (<math>\mu</math>CT)</i> .....	74
5.	<i>Overview of part II of this dissertation</i> .....	75
CHAPTER 3. DETAILS OF HUMAN MIDDLE EAR MORPHOLOGY BASED ON MICRO-CT IMAGING OF PHOSPHOTUNGSTIC ACID STAINED SAMPLES .....		
	<i>Abstract</i> .....	77
1.	<i>Introduction</i> .....	78
2.	<i>Method</i> .....	79
2.1	PTA-stained Micro-CT .....	79
2.2	Segmentation .....	80
2.3	Approach per Topic .....	81
3.	<i>Results</i> .....	88
3.1	Topic I: Effect of PTA on Ossicle Configuration .....	88
3.2	Topic II: Middle Ear Ligaments .....	89
3.3	Topic III: Ossicle Parameters and Dimensions .....	92
3.4	Topic IV: Morphology of the Distal Incus .....	94
3.5	Topic V: TM and stapes footplate Areas .....	97
3.6	Topic VI: Thicknesses of Different Structures .....	99
4.	<i>Discussion</i> .....	102
4.1	Method considerations .....	102
4.2	Interpretation of Results and Comparison to Literature .....	103
4.3	Relevance of Morphological Data for ME modeling .....	112
5.	<i>Conclusions</i> .....	112
CHAPTER 4. ON THE CONNECTION BETWEEN THE TYMPANIC MEMBRANE AND THE MALLEUS .....		
	<i>Abstract</i> .....	115
1.	<i>Introduction</i> .....	116
2.	<i>Materials and Methods</i> .....	117
2.1	Sample preparation .....	117
2.2	Micro-CT scans .....	117
2.3	Histologic preparation .....	119
2.4	Morphometrics .....	119
3.	<i>Results</i> .....	122
3.1	$\mu$ CT scans .....	122
3.2	Morphometric results .....	123
3.3	Interpretation of histologic sections .....	125
4.	<i>Discussion</i> .....	127

4.1	Morphometric results .....	127
4.2	Interpretation of the histologic sections.....	129
4.3	Implications in the clinical context and for middle ear modeling .....	129
4.4	Method considerations.....	130
5.	<i>Conclusions</i> .....	131
<b>PART III - MIDDLE EAR MECHANICS AND MODELING .....</b>		<b>133</b>
INTRODUCTION: SOLID MECHANICS, MIDDLE EAR MODELING AND THE FINITE ELEMENT METHOD.....		135
1.	<i>Solid mechanics</i> .....	135
1.1	Elasticity theory: static.....	136
1.2	Viscoelasticity: time dependency in the time domain .....	142
1.3	Vibration theory: time dependency in the frequency domain.....	145
2.	<i>Middle ear modeling</i> .....	149
2.1	Categories of model approaches .....	150
2.2	Electrical circuit models .....	152
3.	<i>The finite element method</i> .....	153
3.1	Basis functions .....	154
3.2	Example: Analysis of a single triangular element.....	154
3.3	Coupling the elements and applying boundary conditions.....	155
3.4	Solving the formulated problem .....	156
4.	<i>Overview of part III of this dissertation</i> .....	157
CHAPTER 5. VISCOELASTIC PROPERTIES OF THE HUMAN TYMPANIC MEMBRANE STUDIED WITH STROBOSCOPIC HOLOGRAPHY AND FINITE ELEMENT MODELING .....		159
<i>Abstract</i> .....		159
1.	<i>Introduction</i> .....	160
2.	<i>Methods</i> .....	161
2.1	Experiments .....	161
2.2	Finite element modeling.....	164
3.	<i>Results</i> .....	169
3.1	Experimental results .....	169
3.2	Finite element modeling.....	174
4.	<i>Discussion</i> .....	178
4.1	The combination of motion measurements and FE modeling .....	178
4.2	Internal damping smooths spatial and frequency-dependent variations in TM motion .....	178
4.3	Eardrum stiffness varies significantly between different specimens .....	179
4.4	The eardrum and manubrium motions are not well coupled by the more compliant manubrial fold ....	180
5.	<i>Conclusions</i> .....	180
<i>Appendix</i> .....		181
CHAPTER 6. EFFECTS OF MODEL DEFINITIONS AND PARAMETER VALUES IN FINITE ELEMENT MODELING OF HUMAN MIDDLE EAR MECHANICS.....		183
<i>Abstract</i> .....		183
1.	<i>Introduction</i> .....	184
2.	<i>Materials and methods</i> .....	184
2.1	Study strategy .....	184
2.2	Geometry .....	185
2.3	Finite element analysis .....	186
2.4	Model variations .....	189
3.	<i>Results</i> .....	191
3.1	Base models .....	191

3.2	Tympanic membrane variations .....	193
3.3	Cochlear impedance .....	195
3.4	Other quantitative variations.....	196
3.5	Qualitative changes to the ME model.....	198
4.	<i>Discussion</i> .....	199
4.1	Model validations .....	199
4.2	TM damping.....	199
4.3	Cochlear impedance .....	200
4.4	Other TM model variations.....	200
4.5	Qualitative changes to the ME model.....	201
4.6	Comparison to other studies and limitations of the current study.....	202
5.	<i>Conclusion</i> .....	203
CHAPTER 7. THE EFFECT OF MALLEUS HANDLE FRACTURE ON MIDDLE EAR TRANSMISSION, PREDICTED USING FINITE ELEMENT ANALYSIS 205		
	<i>Abstract</i> .....	205
1.	<i>Introduction</i> .....	206
2.	<i>Materials and methods</i> .....	207
2.1	Middle ear models .....	207
2.2	Malleus handle fracture models .....	208
3.	<i>Results</i> .....	209
3.1	Comparison to experiments .....	209
3.2	Model predictions for clinical scenarios .....	211
4.	<i>Discussion</i> .....	214
4.1	Comparison to experiments .....	214
4.2	Model predictions for clinical scenarios .....	216
4.3	Conclusions .....	216
CHAPTER 8. PRESSURE BUFFERING BY THE TYMPANIC MEMBRANE. IN VIVO MEASUREMENTS OF MIDDLE EAR PRESSURE FLUCTUATIONS DURING ELEVATOR MOTIONS .....		
	<i>Abstract</i> .....	219
1.	<i>Introduction</i> .....	220
2.	<i>Materials and Methods</i> .....	221
2.1	Participants .....	221
2.2	Instrumentation .....	222
2.3	Experiments .....	222
2.4	Data acquisition and analysis.....	224
2.5	Assumptions .....	224
2.6	Calculations.....	224
3.	<i>Results</i> .....	226
3.1	Elevator measurements.....	226
3.2	TM buffer capacity.....	227
3.3	ME volume estimations .....	228
3.4	TM compliance .....	229
3.5	Buffer capacity vs. ME volume correlation .....	230
4.	<i>Discussion</i> .....	231
4.1	Study design and outcomes.....	231
4.2	Limitations of the study .....	232
4.3	Clinical relevance of the study .....	234
5.	<i>Conclusions</i> .....	235
	<i>Appendices</i> .....	235

---

Appendix I: calculation of the TM buffer capacity .....	235
Appendix II: calculation of the ME volume .....	237
Appendix III: Expression for TM compliance .....	239
Appendix IV: correction for the catheter tube volume .....	240
Appendix V: Theoretical relation between TM buffer capacity, TM compliance and ME volume .....	243
<b>GENERAL CONCLUSIONS .....</b>	<b>247</b>
SUMMARY OF CONCLUSIONS .....	247
LINKS BETWEEN THE CHAPTERS OF THIS THESIS .....	249
<b>BACK MATTER .....</b>	<b>251</b>
SAMENVATTING (NEDERLANDS) .....	253
LIST OF ABBREVIATIONS .....	257
BIBLIOGRAPHY .....	261
LIST OF PUBLICATIONS .....	273
<i>Journal publications with peer review</i> .....	273
<i>Conference contributions</i> .....	274



## Doctoral committee

---

### **Chair**

Prof. Dr. Sara Bals: *Department of Physics, University of Antwerp*

### **Supervisor**

Prof. Dr. Joris J. J. Dirckx: *Department of Physics, University of Antwerp*

### **Internal members**

Em. Prof. Dr. Dirk Van Dyck: *Department of Physics, University of Antwerp*

Prof. Dr. Steve J. A. Vanlanduit: *Department of Electromechanical Engineering, University of Antwerp*

### **External members**

Prof. Dr. Michael Gaihede: *Department of Clinical Medicine, Aalborg University*

Dr. Ivo Dobrev: *Department of Otorhinolaryngology, University of Zurich*



## Dankwoord/acknowledgements

---

Het werken aan een doctoraat is grotendeels een eenzame opdracht. Niemand begrijpt waar je mee bezig bent en op sommige dagen begrijp je dat zelf ook niet. Dat de eindstreep uiteindelijk gehaald wordt is daarom niet in het minst te danken aan de personen die rondom de doctorandus staan en hem of haar, elk op hun eigen manier, de broodnodige en hartverwarmende steun geven die de doctorandus er keer op keer toe aanmoedigt om door te zetten.

Het is traditie om de promotor van het onderzoek als eerste aan bod te laten komen in het dankwoord. Terecht. Joris Dirckx begeleidt me nu al acht en half jaar (ruim een kwart van mijn leven tot nu toe dus!), vanaf het begin van mijn Bachelor-thesis, overheen mijn Master-thesis, tot het einde van mijn doctoraat. Het spreekt dan ook voor zich dat ik enorm veel van mijn huidige kennis en vaardigheden te danken heb aan zijn onwaarschijnlijke expertise in het vak en zijn toewijding om steeds een aanspreekbare promotor te zijn voor elk van zijn doctoraatstudenten. Voor dit en nog zoveel meer: bedankt Joris!

Met warmte denk ik terug aan de jaren met mijn (ex-)collega's in de koffiekamer van Bimef. De vriendschappelijke sfeer tussen de collega's zorgde steeds voor frisse afleiding van de lange onderzoeksprojecten, maar ook voor interessante uitwisselingen van ideeën. De kaartsessies op het scherpst van de snee tijdens de middagpauzes zal ik zeker missen, al zullen mijn hart en zelfbeeld er wel weer op vooruitgaan nu ik ze achterlaat. In de beginjaren heb ik vele interessante gesprekken gehad met intussen ex-collega's Jan, Jef, Joris, Johan, Jana, John (als ik een 'J' vergeten zou zijn, laat het mij weten!), Wasil, Adriaan, Daniel en Uriel. In het bijzonder met Jan en Jana heb ik intensief maar erg aangenaam samengewerkt en het feit dat we ook op persoonlijk vlak veel gemeen hadden maakte deze tijd alleen maar mooier.

De huidige generatie doctorandi, Pieter, Raf, William, Kilian en Felipe, is een gezellige, lekker absurde en vooral veelbelovende groep onderzoekers aan wie ik het allerbeste toewens in hun verdere onderzoeksaanloop, met veel struisvogeloren, hemelse koffies en Comsol-frustraties. Sam, 'den ancien' onder de Bimef-jeugd, verdient dan weer een vermelding als uitmuntend kaartter, kwisser en onderzoeker. De (ex-)collega's van de practicum-afdeling, Ilse, Arne, Tine en Balder zijn stuk voor stuk prachtmensen waarmee ik in verschillende mate heb samen mogen werken tijdens practica Fysica. De (ex-)CMT'ers Ortwin ('Pico' voor de vrienden) en Bob waren niet alleen erg welgekomen om het aantal kaartters steeds op minstens vier te krijgen, maar vooral om hun warme en humoristische persoonlijkheden tijdens de middagpauzes.

Er zijn nog een aantal externe onderzoeksinstanties waarmee ik tijdens mijn doctoraat heel prettig heb samengewerkt. Van het UZA bedank ik Vincent Van Rompaey, Paul Van den Heyning, Evert Hamans en Jeroen Caremans; van de UA onderzoeksgroep Celbiologie en Histologie bedank ik Isabel Pintelon, John-Paul Bogers, Inge Brouns, Sofie Thys en Carine Moers; from the University of Aalborg, Denmark, I thank Michael Gaihede and Simona Padurariu for the wonderful and fruitful collaboration! Ik dank ook Jean-Marc Gerard van de Cliniques Universitaires Saint-Luc (UCL) en Cochlear Technology Centre Belgium voor het ter beschikking stellen van onderzoeksmateriaal voor deze thesis. Tenslotte bedank ik ook de mensen van het Laboratory of Plant Biology and Nature Management aan de Vrije Universiteit Brussel en de mensen van het Center for X-Ray Tomography (UGCT) van de Universiteit Gent voor het ter beschikking stellen van hun micro-CT toestellen en het bieden van technische hulp hierbij.

I would also like to honor the members of my doctoral jury: internal jury members Prof. Sara Bals, Prof. Steve Vanlanduit, and Prof. Dirk Van Dyck and external members Prof. Michael Gaihede and Dr. Ivo Dobrev. I thank you very kindly for taking the time to read my lengthy thesis and discussing it with me in a constructive and friendly manner during my pre-defense on December 20<sup>th</sup> 2016.

Een doctoraat schrijven zonder financiële steun is voor een jonge onderzoeker ondenkbaar. Daarom dank ik ook van harte het FWO (Fonds voor Wetenschappelijk Onderzoek) voor het toekennen van een vierjarige onderzoeksbeurs voor mijn project.

Twee mensen van onze technische afdeling verdienen een zeer speciale vermelding in dit dankwoord: mechanicus Fred Wiese en elektronicus William Deblauwe. In bijna elke fase van mijn doctoraat waren zij betrokken bij het realiseren van zaken in verband met meetopstellingen, elektronica of software. Zonder hun hulp zat ik hier nu ongetwijfeld met een vinger of drie en een doctoraat minder.

Graag bedank ik ook de hardwerkende mensen van het secretariaat Fysica, bij wie ik altijd terecht kon voor hulp en advies over administratieve aangelegenheden: Hilde Evans, Gert Beyers en Nathalie Ruys. Ik bedank ook Greet Eyckmans voor de heerlijke Cornetto's op de momenten waarop deze het meest nodig waren.

Gelukkig was er de afgelopen jaren nog ruim de tijd om te genieten van het leven in de vorm van reizen, sporten en gezellige café-avonden. Hiervoor spreek ik een grote dank uit voor mijn geweldige vrienden Timo, Toon, Ivo, Thomas, Met, Livio en Wim. Ook andere vrienden, sportmaten en kennissen hebben ertoe bijgedragen dat mijn geestelijke gezondheid (meestal) ver boven het alarm-niveau bleef hangen.

Natuurlijk kon ik op elk moment ook rekenen op de mentale, emotionele, maar ook praktische steun van mijn familie. Mijn ouders Jan en Nicole hebben mij altijd gestimuleerd om het beste uit mezelf te halen en hebben ervoor gezorgd dat ik kan staan waar ik nu sta. Bedankt mama en papa! Mijn broer Stefan was altijd te vinden voor een toffe babbel na werktijd en mijn zus Jessica, schoonbroer Luc en hun wondertjes Amelie en Leon zorgden voor heerlijk zorgeloze familiemomenten. Ook mijn schoonfamilie Gerrit, Willy, Lianne, Matthijs, Gerwout, Marieke en Anne maakten mijn leven een stuk aangenamer met de vele gezellige ~~vreetpartijen~~ familiebijeenkomsten.

Tenslotte wordt het hoog tijd om de meest bijzondere persoon van allemaal te bedanken. Sinds 3 september 2016 zijn Ellen en ik voor de buitenwereld getrouwd, maar onze harten waren al veel langer onlosmakelijk in elkaar gevlochten. Tijdens mijn doctoraat rondde ook jij een erg veeleisende specialisatiestudie af, terwijl je daarnaast ook nog full-time werkte als fysiotherapeut. Toch heb ik op elk moment een immense steun van jou voor mij gevoeld. Ik bedank je ook voor de ontelbare kleine momentjes van geluk en voor de onvergetelijke reizen die we samen gemaakt hebben. Wat mij betreft staan we nog maar aan het begin van een levenslang verhaal, want ik hou van jou met heel m'n hart. Bedankt lieve pop!

Aan iedereen hierboven, maar ook aan de mensen die ik vergeten ben te vernoemen, zeg ik ...



*Daniël*



## Preface

---

Our ability to hear is a fundamental part of engaging with other people and with society in general. It enables us to be informed, warned, and entertained. Hearing connects us to our surroundings in a way that none of our other sense is able to. This is why a loss of hearing has such a dramatic and profound effect on the experience of everyday life.

According to the World Health Organization, 360 million people worldwide have disabling hearing loss<sup>1</sup>, which is defined by a hearing loss greater than 40 dB in the better hearing ear for adults and a hearing loss greater than 30 dB in the better hearing ear for children. This is roughly one in twenty of Earth's inhabitants. Even people with milder degrees of hearing loss experience considerable difficulties in everyday life, such as participating in conversations in noisy or crowded situations.

Finding adequate treatment for hearing loss is therefore one of the most relevant medical challenges of our time. One of the many difficulties is that the possible causes of hearing loss are so numerous: it may result from genetic causes, complications at birth, certain infectious diseases, chronic ear infections, the use of particular drugs, exposure to excessive noise, ageing, and traumas. Each of these broad categories of causes has in turn many different subcategories and pathologies that need specific treatments. Therefore, fundamental knowledge of the

---

<sup>1</sup> Source: [www.who.int](http://www.who.int); consulted on October 18, 2016; page updated in March 2015.

functioning of the complete hearing organ is essential in the prevention and treatment of all these types of hearing loss.

This PhD dissertation (or thesis) focusses on the human middle ear, the subsystem of the hearing organ that is situated between the ear canal of the external ear and the cochlea of the inner ear. The middle ear contains the eardrum (or tympanic membrane), the three smallest bones in the human body (called the ossicles), and supporting structures such as tiny muscles, tendons, and ligaments. Its main function is to transmit the energy and information of incoming sound waves from the ear canal to the inner ear. There, waves are generated in the inner ear fluid by the vibration of the last of the three ossicles, the stirrup. These waves stimulate the actual receptors of the hearing organ, the cochlear hair cells, which generate neuronal signals for the brain.

## Summary

---

Our ability to hear is a fundamental part of engaging with other people and with society in general. According to the World Health Organization, 360 million people worldwide have disabling hearing loss<sup>2</sup> and even people with milder degrees of hearing loss experience considerable difficulties in everyday life, such as participating in conversations in noisy or crowded situations. Finding adequate treatment for hearing loss is therefore one of the most relevant medical challenges of our time. This PhD dissertation focusses on the human middle ear, the subsystem of the hearing organ that is situated between the ear canal of the external ear and the cochlea of the inner ear. The middle ear contains the eardrum (or tympanic membrane), the three smallest bones in the human body (called the ossicles), and supporting structures such as small muscles, tendons, and ligaments. Its main function is to transmit the energy and information of incoming sound waves from the ear canal to the inner ear.

This dissertation comprises eight Chapters about either stroboscopic holography or middle ear research, five of which were published and two are under review for publication. The Chapters are grouped into three Parts, each of which begins with an introductory Chapter providing basic knowledge and background information that is relevant for the Chapters that follow in that Part.

**Part I** presents two chapters about our hardware setup, control software and graphical user interface for stroboscopic digital holography. This optical measurement technique enables the

---

<sup>2</sup> Source: [www.who.int](http://www.who.int); consulted on October 18, 2016; page updated in March 2015.

measurement of full-field vibration maps of oscillating surfaces with vibration amplitudes ranging from several nanometers to several micrometers. In middle ear research, it can be (and has been) used to measure the vibration response of the eardrum and the stapes footplate<sup>3</sup> to sound stimulation. **Chapter 1** covers the specifics of the optical setup and the electronics involved in controlling and monitoring the setup. The technique was demonstrated by measurements on a rubber membrane and evaluated by means of an accuracy and a repeatability test. **Chapter 2** describes the graphical user interface that was developed to control the stroboscopic holography setup and process the measurement data.

In **Part II**, the focus is shifted to the human middle ear. The two Chapters in this Part zoom in on multiple detailed features of the morphology<sup>4</sup> of the middle ear. Their results were interpreted in the light of their possible importance for middle ear mechanics and modeling. **Chapter 3** presents a study of six different aspects of human middle ear morphology, that were studied qualitatively and/or quantitatively. The studied topics include (among others) the middle ear ligaments, the morphology of the distal incus, and the thickness of the tympanic membrane. This was done through the post-processing and interpretation of micro-CT (micro X-ray computed tomography) data on six human temporal bones. **Chapter 4** reports a focused study on the connection between the eardrum and the malleus, or tympanomalleolar connection. Again, the main imaging tool was micro-CT (on thirteen specimens), this time complemented by histologic microscopy (on three of those thirteen specimens). The dimensions of the tympanomalleolar connection were measured in two directions perpendicular to the malleus handle. Both dimensions were found to exhibit a remarkable degree of variation between individuals.

**Part III** covers four research papers about the mechanics and modelling of the human middle ear. In Chapters 5, 6 and 7, the main tool of research was finite element modeling, a numerical simulation technique that enables the researcher to model the physical behavior of complex systems such as the middle ear.

In **Chapter 5**, a first finite element model is presented, consisting of the eardrum and the first ossicle bone, the malleus. The geometry of the model was based on micro-CT images of a temporal bone. The study focused on the material properties of the tympanic membrane, more specifically its stiffness and internal damping. The model results were complemented by

---

<sup>3</sup> The eardrum could be considered as the 'input' surface for vibration energy of the middle ear. In a similar way, the stapes footplate could be considered as the 'output surface' of the middle ear. The stapes is the ossicle that sits the farthest away from the eardrum

<sup>4</sup> Morphology is a branch of biology dealing with the study of the form and structure of organisms.

experimental vibration data obtained through stroboscopic holography and laser Doppler vibrometry<sup>5</sup>.

In **Chapter 6**, the model from Chapter 5 is extended to include the entire human middle ear, from eardrum to stapes footplate. Two other models were created, so that three middle ear models in total could be used for this study. The main purpose of this project was to evaluate the effects of changes in the definition of the model on the mechanical behavior of the model. This information is relevant, since many choices that need to be made during the definition of the model are necessarily based on incomplete information, and it is valuable to know which of these choices have larger effects on the final model compared to others.

**Chapter 7** comprises a study about the effect of an isolated fracture in the malleus on middle ear sound transmission. This rare but interesting condition has not been studied very often in the literature, and using our three finite element models from Chapter 6, it could now be investigated in detail without the need for randomized clinical studies. Fractures were introduced in the models by removing small (virtual) slices of bone of the malleus. The model results were first compared to experimental data on temporal bones and the match was good for mid and high frequencies. The models were also used to predict the effect of removing the fractured part of the malleus.

Finally, **Chapter 8** presents a study of middle ear pressure regulation on seven live patients. The studied phenomenon is called the buffer effect of the tympanic membrane. If the pressure inside the middle ear is equal to the outside (or ambient) pressure, the eardrum is in its neutral position. A change in ambient pressure then causes the eardrum to deform, thereby changing the enclosed volume of the middle ear cavity and thus reducing the pressure difference between the ambient and the middle ear. In this study, the middle ear pressure of the patients was monitored during elevator trips. By measuring the actual ambient pressure change corresponding to the elevator trips as well, the capacity of the buffer effect of the eardrum could be quantified for the first time in live patients. In addition, measurements also provided new values for the volume of the middle ear cavity and the compliance of the tympanic membrane. The latter quantity is relevant for the mechanics of the middle ear in the regime of quasi-static pressure fluctuations.

---

<sup>5</sup> Laser Doppler vibrometry is an optical technique that measures the vibration of surfaces on a single point with a high temporal resolution. It detects the velocity of the vibrating object by exploiting the Doppler shift, a physical phenomenon in which the frequency of a wave is altered if the wave is radiated or reflected by a moving surface.



# **PART I - STROBOSCOPIC HOLOGRAPHY**



## Introduction: Holography and Digital Holography

---

Holography is a lensless imaging technique, originally developed by Gabor in 1948 (Gabor, 1948), for which he received the Nobel prize in Physics in 1978 (Lundqvist, 1992). A hologram is a recording of an entire light field while a classic photograph only records the intensity of the light <sup>6</sup>. This difference has two important consequences: (i) a hologram needs to be *reconstructed* in a specific way in order to be interpreted by human eyes and (ii) a hologram contains much more information than a traditional photograph. The latter property enables observers for example to observe depth in the image and to view the recorded object from different angles.

In terms of optics, a hologram stores the interference pattern of two coherent beams, usually labeled the object beam and the reference beam. By illuminating the recorded hologram with either of the two beams, the other one gets *reconstructed* by diffraction of the illumination beam on the hologram. This creates the illusion that both beams are still present in front of the hologram, while in reality only one of the two beams is present. An important characteristic of holography is that not only the intensity of the object beam is recorded, but also the optical phase.

This introductory chapter will cover the background of digital holography by first introducing the Fresnel diffraction theory and then applying it in order to arrive at the central

---

<sup>6</sup> This is related to the etymology of holography; *holos* (Greek) means ‘whole’ and *graphein* (Greek) means ‘to write’: holography therefore means ‘writing the whole’ or ‘recording everything’

reconstruction formula of digital holography. For a more detailed introduction on this and holography in general, the reader can consult the following sources: Kreis (2005), Poon (2007), De Greef (2011) (my Master's thesis, Dutch).

## 1. Fresnel diffraction

By applying vector identities to Maxwell's equations of electromagnetism and assuming no external source of electromagnetism, three scalar wave equations can be constructed:

$$\Delta\psi - \frac{1}{v^2} \frac{\partial^2 \vec{\psi}}{\partial t^2} = 0, \quad \text{Eq. I - 1}$$

with  $\psi = E_x, E_y, E_z$  the components of the electrical field and  $v$  the speed of light of the propagation medium.

The simplest non-trivial solution for this equation is the plane wave:

$$\psi(x, y, z, t) = \exp[i(\omega t - \vec{k} \cdot \vec{R})], \quad \text{Eq. I - 2}$$

with  $\omega$  the angular frequency and  $\vec{k}$  the wave vector. This is a valid solution if  $\frac{\omega^2}{|\vec{k}|^2} = v^2$  holds true.

Scalar diffraction theory deals with the solution of the wave equation Eq. I - 1 in the presence of a given initial condition of the wave. If we assume (without loss of generality) that the plane wave propagates along the  $z$ -direction of an orthogonal system, the initial condition can be represented by  $\psi_{p0} = \psi_p(x, y; z = 0)$ . The model solution of the problem has the following shape:

$$\psi(x, y, z, t) = \psi_p(x, y; z) \exp[i\omega t]. \quad \text{Eq. I - 3}$$

$\psi_p(x, y; z)$  is the unknown, called complex amplitude. The exact solution of this problem is a convolution of the initial condition and the spatial impulse response function of the propagation of light,  $G$  (Poon, 2007):

$$\psi_p(x, y; z) = \psi_{p0} * G(x, y; z). \quad \text{Eq. I - 4}$$

$$G(x, y; z) = \frac{ik \cdot \exp[-ik\sqrt{x^2 + y^2 + z^2}]}{2\pi\sqrt{x^2 + y^2 + z^2}} \quad \text{Eq. I - 5}$$

$$\times \frac{z}{\sqrt{x^2 + y^2 + z^2}} \left( 1 + \frac{1}{ik\sqrt{x^2 + y^2 + z^2}} \right).$$

Fresnel diffraction theory is an approximation of the general diffraction theory that is a good approximation close to the optical axes ( $z^2 \gg x^2 + y^2$ ) and at distances from the aperture that are large relative to the wavelength ( $z \gg \lambda$ ). In this approximation, the spatial impulse response function becomes the *spatial impulse response function of Fourier optics*:

$$G_F(x, y; z) = \frac{ik \cdot \exp[-ikz]}{2\pi z} \exp\left[\frac{-ik(x^2 + y^2)}{2z}\right]. \quad \text{Eq. I - 6}$$

## 2. Reconstruction of a digital hologram

The Fresnel diffraction theory is very useful for digital holography if the used imaging target is small compared to the object's dimensions and distance to the target. Figure I - 1 illustrates the different planes involved in the reconstruction of a digital hologram.

As stated in the introduction, recording a hologram involves recording the interference pattern of an object beam  $OB(\xi, \eta)$  and a reference beam  $RB(\xi, \eta)$ . This interference takes place in the hologram plane. The intensity distribution of the interference pattern in the hologram plane  $(\xi, \eta)$  can be expressed mathematically by:

$$h(\xi, \eta) = (OB(\xi, \eta) + RB(\xi, \eta)) \cdot (OB(\xi, \eta) + RB(\xi, \eta))^*, \quad \text{Eq. I - 7}$$

where \* denotes the complex conjugate (Kreis, 2005).

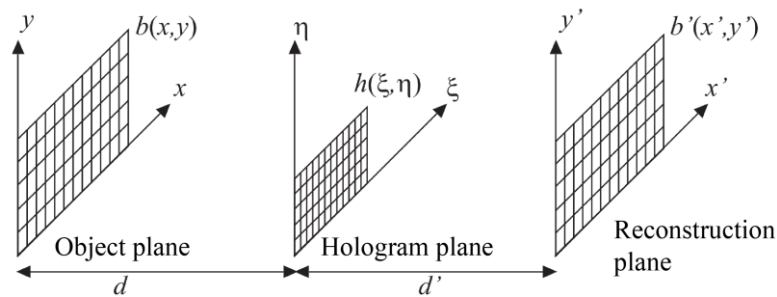


Figure I - 1: Illustration of the different planes involved in recording and reconstructing a digital hologram.

The expression of the OB in the hologram plane is found by convoluting the complex wave  $b(x, y)$ , describing the light with the spatial impulse response function of Fourier optics:

$$\text{OB}(\xi, \eta) = b(x, y) * G_F(\xi, \eta; d) \quad \text{Eq. I - 8}$$

Reconstruction of the hologram involves the diffraction of the reference beam on the recorded hologram. Mathematically, this is equivalent to the multiplication of the recorded hologram,  $h(\xi, \eta)$ , with the reference wave  $RB(\xi, \eta)$  or its complex conjugate and propagating this product over a distance  $d'$ :

$$\begin{aligned} b'(x', y') &= \overbrace{(h(\xi, \eta) \cdot \text{RB}^*(\xi, \eta))}^{\text{Illumination}} * \overbrace{G_F(x', y'; d')}^{\text{Propagation}} \\ &= \frac{ik \cdot \exp[-ikd']}{2\pi d'} \exp\left[-\frac{ik}{2d}(x'^2 + y'^2)\right] \iint h(\xi, \eta) \cdot \text{RB}^*(\xi, \eta) \cdot \\ &\quad \exp\left[-\frac{ik}{2d'}(\xi^2 + \eta^2)\right] \exp\left[\frac{ik}{d'}(\xi x' + \eta y')\right] d\xi d\eta. \end{aligned} \quad \text{Eq. I - 9}$$

The first factor,  $\frac{ik \cdot \exp[-ikd']}{2\pi d'}$  is independent of the spatial coordinates and can therefore be set to 1 if we are not interested in the absolute values of the light intensities. If the RB is a plane wave, its intensity and phase are homogeneous across the entire cross-section of the optical field at any place along the optical axis. Therefore, we can represent it by a constant and without further loss also set it to 1 if absolute intensity and phase are not of interest to the end user (as in most applications is the case). In order to obtain a simpler expression for digital holography, the variables are discretized:  $\xi = n\Delta\xi$ ;  $\eta = m\Delta\eta$ ;  $x' = n\Delta x'$ ;  $y' = m\Delta y'$ . These new coordinates are related by:

$$\Delta x' = \frac{d\lambda}{N\Delta\xi}, \quad \text{Eq. I - 10}$$

$$\Delta y' = \frac{d\lambda}{M\Delta\eta}, \quad \text{Eq. I - 11}$$

where  $M$  and  $N$  are the number of pixels in the CCD camera. Using these relations and  $k = \frac{2\pi}{\lambda}$ , we arrive at the *central reconstruction formula of digital holography*:

$$\begin{aligned} b'(n\Delta x', m\Delta y') &= \exp\left[-i\pi d' \lambda \left( \left(\frac{n}{N\Delta\xi}\right)^2 + \left(\frac{m}{M\Delta\eta}\right)^2 \right)\right] \sum_{k=0}^{N-1} \sum_{l=0}^{M-1} h(k\Delta\xi, l\Delta\eta) \\ &\quad \exp\left[-\frac{i\pi}{\lambda d'} ((k\Delta\xi)^2 + (l\Delta\eta)^2)\right] \exp\left[i2\pi \left(\frac{kn}{N} + \frac{lm}{M}\right)\right]. \end{aligned} \quad \text{Eq. I - 12}$$

The summation term in this formula can be calculated by executing a fast-fourier transform (FFT) operation on the recorded hologram  $h(k\Delta\xi, l\Delta\eta)$ , multiplied with the *chirp function*

$\exp\left[-\frac{i\pi}{\lambda d'}((k\Delta\xi)^2 + (l\Delta\eta)^2)\right]$ . The prefactor  $\exp\left[-i\pi d'\lambda\left(\left(\frac{n}{N\Delta\xi}\right)^2 + \left(\frac{m}{M\Delta\eta}\right)^2\right)\right]$  influences only the intensity of the result, not the phase. For interferometric purposes, in which only the phase information of the reconstructed holograms is relevant, this factor can be omitted. The researcher still needs to choose a value for the reconstruction distance  $d'$ . It can be shown, by considering the recording and reconstruction of a hologram of a point source, that the optimal reconstruction distance is equal to the recording distance  $d$ , the distance between the object and the recording target (De Greef, 2011). On this distance, one of the two first order diffraction beams will be focused. When choosing  $d' = -d$ , the other first order beam will be focused and since both beams contain identical information, these choices are equivalent.

### 3. Overview of part I of this dissertation

Chapter 1 is a published article describing the concepts of digital holographic interferometry and stroboscopic digital holography, along with our specific setup for stroboscopic digital holography. Results of a vibrating membrane are provided, along with the results of various performance test. Note: after the publication of this article, several improvements were made to the setup, mostly in order to simplify the electronics of the setup. For example, the two function generators and oscilloscope were replaced by a single Digital I/O PCI card from National Instruments (National Instruments Corporation, Austin, Texas, USA).

Chapter 2 is devoted to describing the graphical user interface for controlling the setup and processing and displaying its results, that was developed during the course of this thesis (after the publication of Chapter 1).



# Chapter 1. Digital Stroboscopic Holography Setup for Deformation Measurement at Both Quasi-Static and Acoustic Frequencies

---

## Abstract

A setup for digital stroboscopic holography that combines the advantages of full-field digital holographic interferometry with a high temporal resolution is presented. The setup can be used to identify and visualize complicated vibrational patterns with nanometer amplitudes, ranging from quasi-static to high frequency vibrations. By using a high-energy pulsed laser, single-shot holograms can be recorded and stability issues are avoided. Results are presented for an acoustically stimulated rubber membrane and the technique is evaluated by means of an accuracy and a repeatability test. The presented technique offers wide application possibilities in areas such as biomechanics and industrial testing.

*Major contributions to the development of the optical setup, trigger hardware and control software, the execution of the experiments, the data analysis and the writing of the paper.*

*This chapter was published in: De Greef, D., Soons, J., Dirckx, J.J.J., 2014. Digital Stroboscopic Holography Setup for Deformation Measurement at Both Quasi-Static and Acoustic Frequencies. Int. J. Optomechatronics 8, 275–291. doi:10.1080/15599612.2014.942928*

## 1. Introduction

In the past, numerous holographic techniques have been developed and applied to measure full-field vibrational motion of a surface in various frequency ranges. Time-average holography has been widely used, in analogue as well as digital version (Powell and Stetson, 1965; Rosowski et al., 2009). It requires a technically simpler setup than the technique presented in this work in terms of controlling electronics, yet still provides very valuable data for a lot of applications, as it supplies quantitative information regarding harmonic deformations, changing refractive indices etc. Various setups for digital double-exposure stroboscopic holography have been published as well (Hariharan and Oreb, 1986; Hernandez-Montes et al., 2009; Furlong et al., 2009). In recent years, a new concept of stroboscopic holography has been implemented, based on multiple very short phase-locked pulses cycling through the vibration period so that the entire time-dependent motion of the studied surface can be visualized (Pedrini, et al., 2006; Trillo et al., 2009; Cheng et al., 2010; De Greef and Dirckx, 2012; De Greef and Dirckx, 2014b, i.e. Chapter 5 of this thesis).

The setup for stroboscopic holography that is presented in this paper allows imaging of dynamic out-of-plane displacements over the entire surface of an object as a function of time over a very wide frequency range. The current setup has advantages over earlier published methods (Pedrini et al., 2006; Trillo et al., 2009). A wider frequency range (measured and presented: 5 Hz – 16.7 kHz; theoretically: 0 Hz – 250 kHz), a shorter acquisition time and a better spatial resolution than in similar setups can be achieved, as will be covered in detail in the discussion of this paper. Since both amplitude and phase of the excitation signal are precisely measured relative to the ultra-short high-energy laser pulses, the complex transfer function (i.e. magnitude and phase) of the studied surface relative to the input is available after the experiment. The setup is controlled and monitored using two function generators, an oscilloscope, a PC and custom made electronics containing a programmed microprocessor.

Results from measurements on a test subject will be presented and discussed, as well as results from two independent quality tests for the setup. The current setup is optimized and being used for the study of eardrum vibrations of humans, other mammals and avian species.

## 2. Method

### 2.1 Concept

#### 2.1.1 Digital holography

In digital holography, the interference pattern of a mutually coherent object beam and reference beam is recorded on a digital imaging matrix, such as a CCD or a CMOS. The main advantage over analogue holography, aside from flexibility and off-line reconstruction, is the direct access to the optical phase of the object wave after digital reconstruction. Therefore, quantitative information about the object's displacement between two recorded states is acquired by simply subtracting the reconstructed object wave phase maps of the two holograms. The result is a wrapped phase difference map. The same result can be obtained by a complex division of the reconstructed holograms, but this did not yield different results from the subtraction method described before.

By applying a two-dimensional phase-unwrapping algorithm (Herráez et al., 2002), the actual phase difference  $\Delta\phi$  between the two object waves is obtained. The change in optical path length  $\Delta\delta$  of the object beam between the two recorded states is related to the change in object wave phase  $\Delta\phi$  through  $\Delta\delta = \lambda \frac{\Delta\phi}{2\pi}$ , with  $\lambda$  the optical wavelength. In our setup, the illumination direction is parallel to the observation direction, so that the object's deformation  $d$  is related to the change in optical path length through  $d = \frac{\Delta\delta}{2}$ , so that:

$$d = \lambda \frac{\Delta\phi}{4\pi}. \quad \text{Eq. 1-1}$$

Using this equation for all object points, the full field displacement map of the deformation can be calculated.

All calculations in this paper, as well as experiment control, are performed in Matlab (MATLAB Release 2012b, The MathWorks, Inc., Natick, Massachusetts, United States). In order to minimize the needed calculation time, a region of interest (ROI) is determined by the user along the border of the object and the unwrapping algorithm is only applied to this ROI, which drastically reduces the computational load. In order to have a spatial displacement reference, the inclusion of several decades of object points (pixels) with a known displacement equal or close enough to zero in the ROI is essential.

Reconstruction of a digital hologram starts by multiplication of the recorded interference pattern with the numerical equivalent of the reference wave. The resulting wave is then propagated numerically over the distance  $d$  between the CCD and the object that was used during the recording. For this purpose we use the Fresnel diffraction formula. The Fresnel approximation, required for this approach, is allowed as the condition for it reads (derived from Kreis, 2005):

$$F := \left( \frac{D_{\text{CCD}} - D_{\text{obj}}}{d} \right)^2 \ll 1, \quad \text{Eq. 1-2}$$

with  $D_{\text{CCD}}$  and  $D_{\text{obj}}$  the lateral dimensions of the CCD-targeted and the object, respectively, and  $d$  the distance between CCD and object. In our setup, these values are  $D_{\text{CCD}} = 8.5$  mm,  $D_{\text{obj}} = 8$  mm,  $d = 160$  mm, resulting in  $F = 0.011$ .

The total reconstruction formula for calculating the reconstructed hologram  $b$  is as follows (Kreis, 2005):

$$b(n\Delta x, m\Delta y) = e^{i\pi d\lambda \left( \frac{n^2}{N^2\Delta\xi^2} + \frac{m^2}{M^2\Delta\eta^2} \right)} \sum_{k=0}^{N-1} \sum_{l=0}^{M-1} h(k, l) r^*(k, l) e^{\frac{i\pi}{d\lambda} (k^2\Delta\xi^2 + l^2\Delta\eta^2)} e^{-2i\pi \left( \frac{kn}{N} + \frac{lm}{M} \right)}, \quad \text{Eq. 1-3}$$

with  $n, m$  the image indices;  $\Delta x, \Delta y$  the image pixel center-to-center distances;  $\Delta\xi, \Delta\eta$  the CCD pixel distances;  $\lambda$  the optical wavelength of the laser;  $N, M$  the number of pixels in  $x$ - and  $y$ -direction;  $k, l$  the CCD indices;  $h$  the recorded hologram and  $r^*$  the conjugated reference wave. The advantage of this technique over phase-shifting methods (Yamaguchi and Zhang, 1997) is that a single hologram is sufficient to extract both wave intensity and phase. The drawback is that there will be other orders of diffraction visible on the image (the DC term and the conjugated twin image), so that not all pixels can be used to display the real image.

### 2.1.2 Stroboscopic digital holography

In stroboscopic digital holography, a periodically moving object is illuminated by either one or multiple very short pulses, synchronized to a single phase within the motion period. After combining this vibration hologram with a hologram of the object at rest state, a full field displacement map of the objects displacement at the chosen vibration phase is obtained. By cycling the phase-locked illumination pulse stepwise through the vibration period (Figure 1-1) one can collect displacement maps for evenly distributed time instants within the period. Therefore, we are able to measure the object's full-field deformation as a function of time with a temporal resolution that is only limited by the pulse length of the laser and the precision of the triggering. Obviously, the imaged object has to fulfill generic requirements for digital holography such as short-term nanometer stability, sufficient reflectivity and dimensions that do not cause the interference pattern to violate the Nyquist-Shannon sampling theorem for the chosen viewing distance.

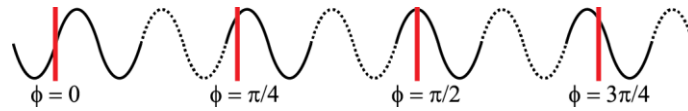


Figure 1-1: The concept of stroboscopically illuminated holography. Very short illumination pulses are phase-locked and cycle stepwise through the vibration period.

## 2.2 Setup

### 2.2.1 Optical arrangement

An overview of the setup, including optical, electronic and acoustic components, is depicted in Figure 1-2. The used laser is a frequency doubled pulsed Nd:YAG laser (JK Lasers,  $\lambda = 532 \text{ nm}$ ), producing pulses of up to 5 mJ with a duration of 8 ns. Its beam is broadened by a Galilean beam expander (GBE) and polarization is controlled using a  $\lambda/2$  plate, before it is divided into an object and reference beam (OB and RB) by a polarizing beam splitter (PBS). The OB is partially reflected by a non-polarizing beam splitter (NPBS 1), directing it towards the object. This NPBS allows a perpendicular illumination of the object and therefore maximizes the resolution of out-of-plane displacement. The OB is reflected and diffracted by the object and travels back through the NPBS 1 towards NPBS 2, where it is combined with the RB.

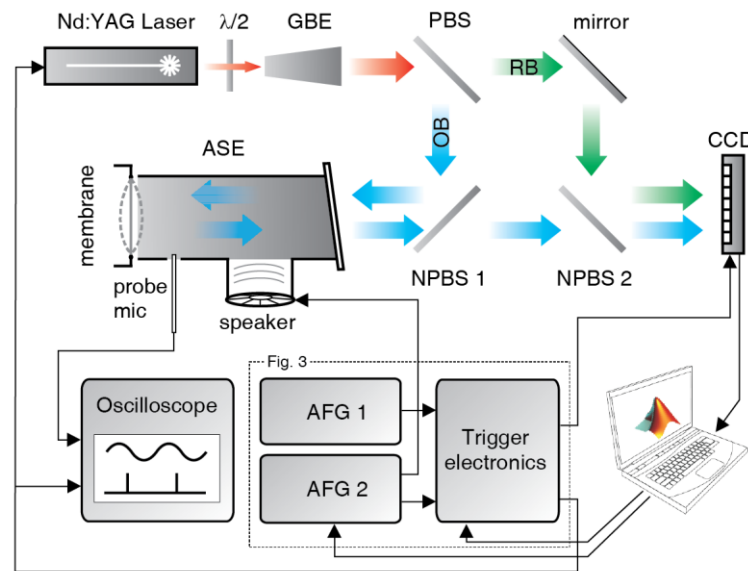


Figure 1-2: Schematic overview of the setup. Components are discussed in section 2.2.1. GBE: Galilean beam expander. (N)PBS: (Non-) polarizing beam splitter. OB: object beam. RB: Reference beam. ASE: Acoustic stimulation element. CCD: Charge-coupled device. AFG: Arbitrary function generator.

Both waves pass a polarizer in front of the CCD that is aligned with the polarization of the RB, so that only the OB light of the same polarization hits the target, thus maximizing interference fringe contrast. Indeed, when the used object surface is diffuse, the scattered light will be randomly polarized so that only the relevant half of the object light passes the polarizer and

interferes with the RB. In our applications, specular reflecting surfaces are avoided, but if it is unavoidable, an additional  $\lambda/2$  plate should be placed in the OB to realign the polarization of both waves. The OB and RB interference pattern is recorded by a CCD camera (AVT Pike 505-B, 2452 x 2054, 14bit). The frame rate of the camera at the highest resolution is 6.5 fps. Often, lower resolution is sufficient and frame rate can be increased to 10 fps, but not higher as the pulsed laser cannot produce high-energy pulses at frequencies  $> 10$  Hz.

### 2.2.2 Electronic aspects: trigger sequence

All electronic components are controlled and/or monitored by one or more of the following: a personal computer, two function generators (Tektronix AFG 3102), an oscilloscope (Tektronix TDS 210) and a piece of custom made trigger electronics, containing a microprocessor (Microchip PIC18F2410). A close-up view of the trigger timing sequence is shown in Figure 1-3. The first generator provides pulses to the microchip with the same frequency as the camera frame rate. The second generator produces the excitation stimulus signal and a series of pulses synchronized to the stimulus that serves as the second input for the microprocessor.

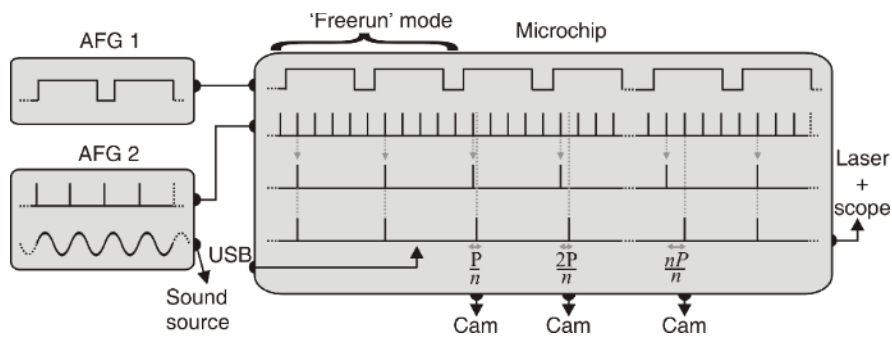


Figure 1-3: Close-up of the trigger sequence inside the microchip. The details are discussed in section 2.2.2.

The program on the chip selects the first pulse of the AFG 2 in every active interval of AFG 1. In 'freerun mode', this series of pulses is passed to the laser without further alteration. In this way, the laser is flashing at a fixed rate, allowing the laser cavity temperature to stabilize. To record the rest frame, the stimulus is disabled, the 'freerun mode' is applied and the camera is triggered manually. After this, the stimulus signal is enabled and a USB-signal from the PC initiates a series of delays upon the laser trigger pulses that is programmed in the microchip. This program delays every outgoing pulse with an ascending multiple integer of  $\delta = P/n$ , where  $P$  is the vibration period and  $n$  is the number of desired frames within a period. At the same time, the program ensures that one hardware trigger pulse is sent to the camera for every delayed pulse. For every pulse, the delay time is increased by  $\delta$ , so that holograms are recorded stepwise through the entire vibration period. This will be repeated until  $n$  frames are delayed, the last frame being delayed by exactly  $P$ , after which the program ends, the camera trigger pulses will be stopped and the microchip will re-enter the 'freerun' mode.

Although the frequency of laser pulses is not strictly fixed due to the delays imposed upon these pulses, these fluctuations are insignificant with regard to the overall rate so that the average firing frequency remains unchanged. This keeps the laser cavity temperature stable so that a constant laser pulse energy and beam profile is maintained.

The smallest possible time step  $\delta$  for the used microprocessor is 1  $\mu$ s, which, as a result, is the temporal resolution of the setup. Nyquist's criterion demands a sampling frequency of twice the frequency of the signal; hence the theoretical upper frequency limit is 500 kHz. However, in order to compute the amplitude and phase of a sine-shaped vibration with an acceptable reliability, experience teaches that the minimal number of phase steps is at least 4, hence the actual upper frequency limit for the setup is 250 kHz. This is merely limited by the trigger electronics and could be extended if needed.

### 2.2.3 Acoustic aspects: the acoustic stimulation element and sound phase measurement

For measurements using acoustic excitation, an acoustic stimulation element (ASE) was constructed and placed in front of the object (Figure 1-2). The ASE is a fixed rigid tube with at one end an opening for the studied object and at the other end an oblique window. This window prevents the acoustic signal from escaping from this side, while allowing the laser beam to enter the element without producing disturbing reflections into the optical path thanks to its obliqueness.

The wall of the ASE contains two openings, one to provide an entrance for the acoustic stimulation and one for a probe tube microphone (Bruel & Kjaer 4182), of which the tip is placed at a distance of 5 mm away from the object. This probe microphone monitors the magnitude and phase of the acoustic stimulus so that the magnitude and phase of the object motion relative to the sound can be obtained. If we know the sound phase at the probe tip  $\phi_{s,t}$ , the sound phase at the object  $\phi_{s,o}$  is equal to:

$$\phi_{s,o} = \phi_{s,t} + 2\pi \frac{5 \text{ mm}}{\lambda_s}, \quad \text{Eq. 1-4}$$

with  $\lambda_s$  the sound wavelength, i.e.  $\lambda_s = \frac{c}{f}$ , with  $c = 343$  m/s the speed of sound at room temperature and  $f$  the sound frequency. Eq. 1-4 accounts for the phase delay of  $2\pi \frac{d}{\lambda_s}$  for a sound wave with wavelength  $\lambda_s$  that travels a distance of  $d = 5$  mm. The phase of the outgoing signal from the microphone controller  $\phi_{s,OUT}$  is given by:

$$\phi_{s,OUT} = \phi_{s,t} + 2\pi \frac{l_t}{\lambda_s} + \phi_{el}, \quad \text{Eq. 1-5}$$

with  $l_t$  the length of the tube, i.e. the distance of the probe tip to the microphone diaphragm and  $\phi_{el}$  a phase difference due to electronic delays. The second term of the right hand expression in Eq. 1-5 is similar to the last term in Eq. 1-4. The last term accounts for additional

phase delays imposed by the microphone preamplifier and controller (originating from frequency cut-off filters). Data for this phase delay are provided by the manufacturer's manual (Bruel & Kjaer, Probe Microphone Type 4182, User manual, 1990). Combining Eq. 1-4 and Eq. 1-5, the sound phase at the object can be determined from the knowledge of the phase of the microphone signal and the technical parameters of the microphone, provided by the manufacturer (Bruel & Kjaer). This signal is compared to the pulses that trigger the laser flash tube (the second output of the microprocessor in Eq. 1-3) on an oscilloscope. The actual light pulse is fired 4 to 5 ns after the pulse that is sent to the laser flash tube, which is a negligible time delay at all frequencies. In this way, we know the exact acoustic stimulus phase for every laser pulse and thus for every recorded hologram. Combined with the displacement results from stroboscopic holography, we are able to extract the object's full-field transfer function, defined as the complex vibration wave at every object point divided by the complex stimulus wave.

### 3. Results

#### 3.1 Vibration of a circular membrane

We present results on a stretched circular rubber membrane (diameter 8 mm, diffuse), excited acoustically at a broad frequency range (5 - 16752 Hz, covering more than 11 octaves), demonstrating the wide applicability of the technique. For this recording, the distance between the CCD target and the object was equal to 160 mm. The measurements were made using the acoustical stimulation element (ASE), as described in section 2.2.3, which provided controllable acoustic stimulation and monitoring.

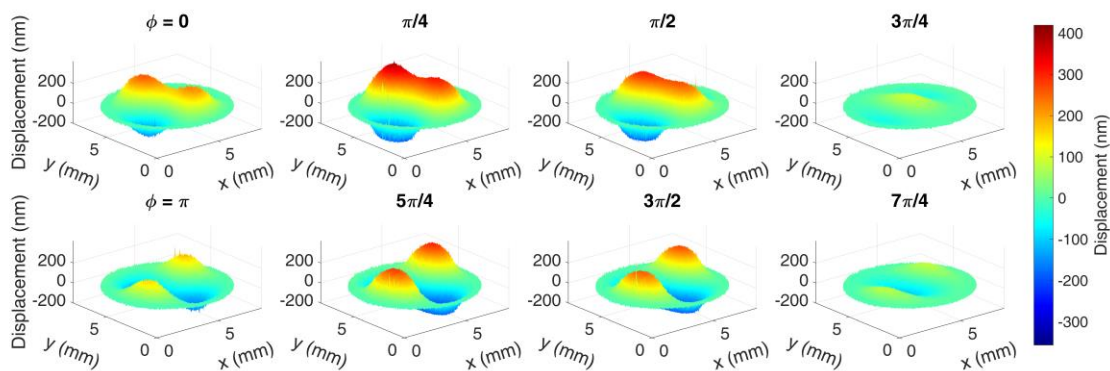


Figure 1-4: Displacement maps of a stretched rubber membrane acoustically stimulated at a frequency of 3805.5 Hz and a sound pressure of 100 dB SPL. The applied stroboscopic illumination is equivalent to Figure 1-1.

Figure 1-4 shows eight displacement maps of the membrane, excited at 3805.5 Hz with a SPL of 100 dB. The phase steps between each two consecutive maps are equal to  $\pi/4$ , i.e.  $1/8^{\text{th}}$  of a period in terms of time, so that the pulses are distributed evenly inside the vibration period and this recording is consistent with the illumination in Figure 1-1.

In order to extract full field magnitude and phase information of the membrane's transfer function, we calculated the complex *FFT*-spectrum of the temporal displacement for every object point and extract the magnitude and phase of the principal component, i.e. the component that oscillates with the acoustic stimulus frequency. This component is generally much larger than other harmonics, which means that the motion is undistorted. The result of this full field *FFT* analysis is presented in Figure 1-5 (left: magnitude map; right: phase map). The phase map in Figure 1-5 (right) presents the phase of the object relative to the acoustic stimulus phase: a value of -0.25 cycles means that the object's vibration is delayed by a time of 0.25 times the period in relation to the stimulus. One clearly sees four local maxima in Figure 1-5 (left), while continuous phase transitions are noticed over the entire membrane in Figure 1-5 (right), indicating a non-modal pattern that is not predicted by a theoretical circular clamped elastic membrane (Fletcher, 1992).

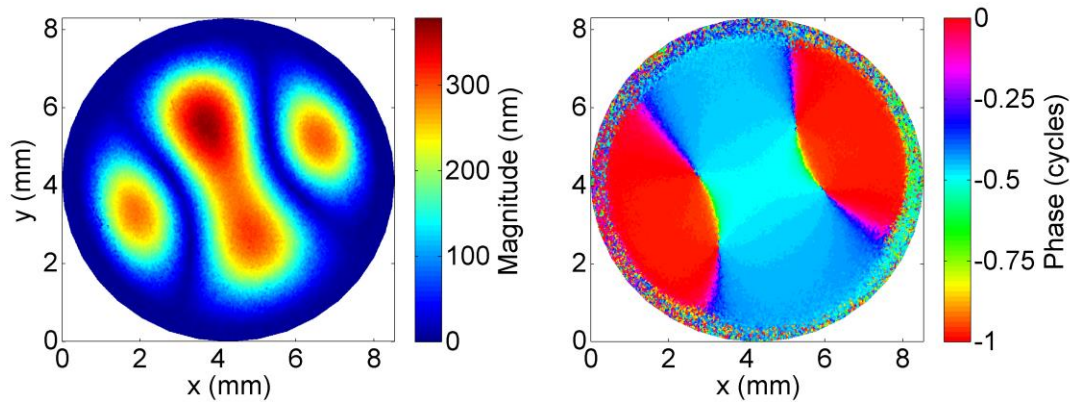


Figure 1-5: Full-field transfer function magnitude (left) and phase (right) maps of a stretched rubber membrane acoustically stimulated at a frequency of 3805.5 Hz and a sound pressure of 100 dB SPL. These figures originate from the same measurement data as Figure 1-4.

In Figure 1-6, the magnitude (6A) and phase maps (6B) of four more vibrational patterns are presented with stimulation frequencies ranging from 5 Hz to 16.7 kHz. This shows that the developed setup produces acceptable to very good results for a frequency range of more than 11 octaves for this particular sample. At 5 Hz, the membrane is not exactly in phase with its stimulus, which could be due to viscoelastic effects of the material. At frequencies close to but below its resonance frequency (cfr. 1903 Hz in Figure 1-6), the membrane moves exactly in phase with the sound stimulus.

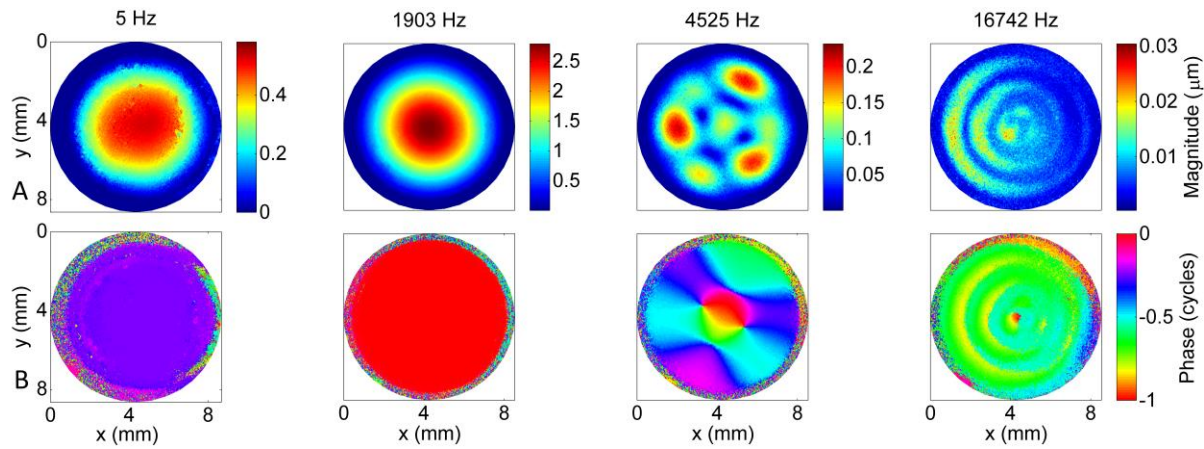


Figure 1-6: A. Magnitude maps and B. phase map of a vibrating membrane at different frequencies, covering the entire measurement range for our setup and this sample. The applied sound pressure values are 90 dB SPL for 5 Hz, 95 dB SPL for 1.9 kHz, 100 dB SPL for 4.5 kHz and 95 dB SPL for 16.7 kHz.

### 3.2 Duration of the measurements

The optimal working frequency of the pulsed laser is 10 Hz, so the time needed to record  $n$  vibration holograms is  $n$  times 100ms. A measurement of vibration holograms at 8 phase steps thus takes 0.8 s plus the additional time needed to record a reference rest hologram which is around 1 s. The recording of 100 vibration holograms plus reference frame takes 11 s.

A full spectrum measurement from 25 Hz to 25600 Hz at 4 frequency steps per octave, i.e. 41 frequencies, at 8 vibration holograms plus 1 reference frame per frequency takes less than three minutes.

### 3.3 Evaluation of the technique: accuracy and repeatability

#### 3.3.1 Accuracy

In order to evaluate the reliability of the technique, two test measurements were carried out. The first test evaluated the accuracy of the technique for measuring static deformations by imposing several known static displacements on the object. Holograms of a surface are recorded before and after the deformation, and the full-field displacement is calculated from these two holograms. The deformation is realized by indenting it from the reverse side using a metal pin that is connected to a calibrated Piezo actuator. The used surface was a stretched rubber membrane. Figure 1-7 shows the result of this test measurement for applied indentations of 10nm, 500nm and 3  $\mu\text{m}$ , covering the entire measurement range of the setup with this object. The smallest and largest deformations are at the limits of the technique's measurement range, so some challenges are to be expected.

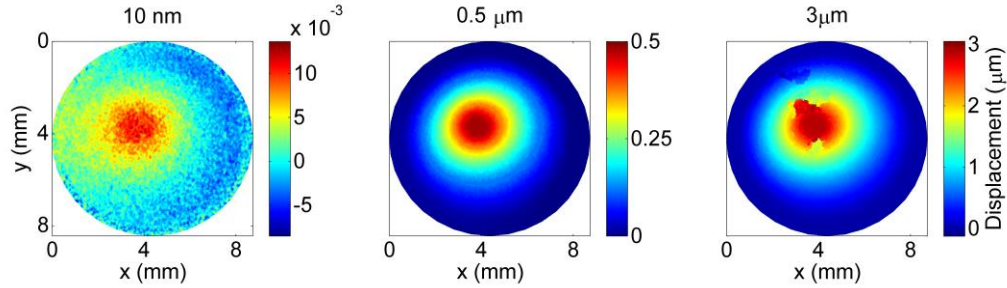


Figure 1-7: Accuracy test measurements of static deformations at the edges and in the middle of the measurement range for our setup and the chosen demonstration sample. The displacements were applied by a metal pin connected to a piezo transducer. Chosen indentation values are 10 nm, 0.5  $\mu\text{m}$  and 3  $\mu\text{m}$ .

A statistical analysis of the data is presented in Table 1-1. To obtain this numbers, data was taken from pixels that cover the indented surface of the object. The tip of the pin has a diameter of 1,3 mm and the pixel dimension is 10  $\mu\text{m}$  and 12  $\mu\text{m}$  in  $x$ - and  $y$ - directions, so data within a circle with radius 50 pixels around the center of the indented area was extracted. The statistical average and standard deviation (SD) are shown in Table 1-1, as well as the relative SD (i.e. the SD divided by the average). The standard deviation was calculated by:

$$\sigma_z = \sqrt{\frac{\sum_i (z_i - \langle z \rangle)^2}{N}}, \quad \text{Eq. 1-6}$$

with  $N$  the number of selected pixels. The motivation for this form is the assumption that the chosen dataset to be the entire population (opposed to a partial population, in which case the denominator should be  $\sqrt{N-1}$ ). The correspondence between the applied and measured deformation is a measure for accuracy, whereas the SD and relative SD can be interpreted as measures for the precision of the technique. While the SD increases with increasing deformation, the relative SD decreases.

In the case of smallest indentation, the maximal displacement at a single data point is 13.6 nm, which is larger than the applied 10 nm. However, when averaging a circle with a radius of 50 pixels at the location where the indentation was applied, this value dropped to 10.1 nm, indicating that the error of 3.5 nm in one of the pixels is due to measurement noise. Nevertheless, thanks to the excellent spatial resolution, the indentation peak is unmistakably detectable. Displacement values lower than 0 near the edge of the membrane are probably caused by very small static motions between the recording of the reference frame and the deformation frame.

As can be seen in Figure 1-7, the displacement map for the largest indentation (3  $\mu\text{m}$ ) shows some issues that are the result of phase unwrapping errors. In these areas, the high density of  $\pi/2$  phase jumps in combination with a possible slightly lower reflectivity in these areas of the surface, cause wrongly detected  $\pi/2$ -jumps and thus erroneous unwrapping results.

At the largest indentation values, the measured deformation is significantly lower than the applied indentation (see Table 1-1). This is probably caused by compression of the rubber membrane due to the pressure applied by the indentation pin, rather than a systematic error in the technique.

Table 1-1: Overview of accuracy measurement results. The first column presents the applied indentation using a Piezo actuator; the second column lists the average measured deformation in a circle with a diameter equal to the used indentation pin; the third and fourth column provide the standard deviation and relative standard deviation on this data.

Indentation (nm)	$\langle z \rangle$ (nm)	$\sigma_z$ (nm)	$\sigma_{rel}$
10	10,1	1,0	9,9%
500	474,8	6,9	1,5%
3000	2848	37	1,3%

### 3.3.2 Repeatability

The second test evaluated the repeatability of the setup through a repeated full-spectrum analysis of a membrane using the same input stimuli at the same frequencies without changing anything of the setup in between measurements and with an interval of 3 minutes between measurements. The results of the repeatability measurements are presented in Figure 1-8 (magnitude) and Figure 1-9 (phase), where the frequency-dependent transfer function of the center point of the membrane is shown. These data were extracted from a single data point and neither smoothing nor averaging has been applied to reduce noise effects.

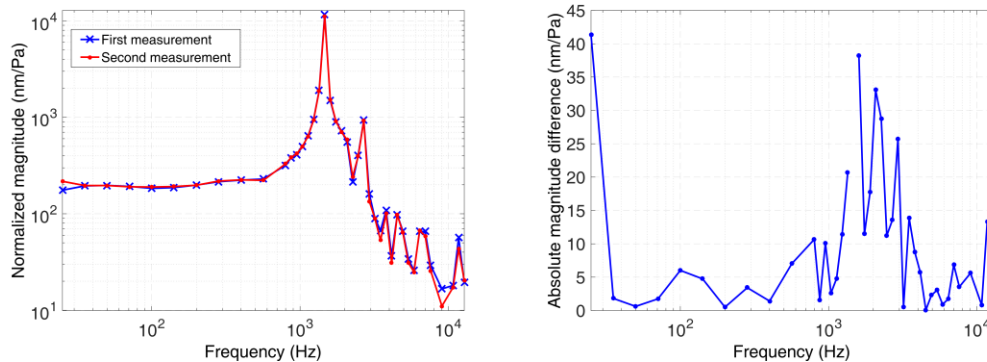


Figure 1-8: Left: Transfer function magnitude results from two full-spectrum repeatability tests. Results are extracted from the center point a vibrating rubber membrane. In between measurements, an interval of 3 minutes was left. Right: Absolute magnitude difference between the repeated measurements. Only close to the resonance peak (1.2 – 2 kHz) and at quasi-static frequencies, this difference is significant. In both these regions, the differences are due to the sample and the stimulating device rather than the technique itself, as discussed in section 3.3.

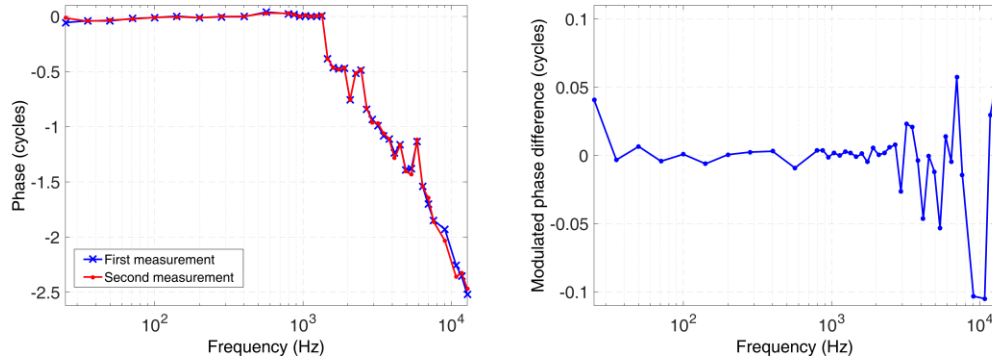


Figure 1-9: Left: Transfer function phase results from the two full-spectrum repeatability tests. These figures originate from the same data as Figure 1-8. Right: Modulated phase difference between the repeated measurements. The most distinct differences are found at the highest frequencies, where small errors in time measurements can lead to significant phase differences.

For the sake of consistent evaluation, the data of both the magnitude and phase are normalized to the incident sound pressure. 43 frequencies are measured: 2 logarithmically spaced points per octave in the range 25 – 800 Hz and 8 per octave in the range 0.8 – 12.8 kHz. The reason for this uneven distribution is the more complex and quickly changing behavior on the higher frequencies. Unreliable measurements at 8.30 kHz and 9.87 kHz were removed from the dataset, since the used speaker was not able to produce acceptable sound signals at these frequencies.

The calculated intra-class correlation (ICC) coefficients of these repeated datasets were 99,86% for the magnitude and the 99,92%, indicating a very good repeatability (McGraw and Wong, 1996).

The absolute magnitude difference in Figure 1-8 (right) is defined as:

$$m_{diff} = |m_2 - m_1|, \quad \text{Eq. 1-7}$$

with  $m_1$  and  $m_2$  being the frequency dependent magnitude from the first and second measurement, respectively. Overall, the average absolute magnitude difference is 8,7 nm/Pa. At most frequencies lower than 1200 Hz and higher than 2000 Hz, this value is well below 10nm. As can be expected, difference values are higher in areas where the transfer function has large values and steep tangents, i.e. close to the sample's resonance frequency. One data point very close the resonance frequency (at 1467 Hz) was considered as unrepresentative and was removed from the figure as in this very narrow but sensitive area the repeatability of the measurement is far more dependent on the sample than on the technique itself. Indeed, the sample, an undamped vibrating membrane, features a very sharp and high resonance peak, so that a tiny shift in resonance frequency causes the measured magnitude at a frequency close to this peak to change strongly compared to other frequencies. At quasi-static frequencies, the larger difference is explained by difficulties from the speaker to produce a harmonic acoustic signal with a sufficient pressure level at this frequency. Therefore, a lower sound pressure level

is applied (90 dB instead of 100 dB or more like at most other frequencies), resulting in a smaller motion range and a lower signal-to-noise ratio. This induces a larger random relative error and thus a larger difference between subsequent measurements. Furthermore, the measurement result at this frequency is possibly influenced by viscoelastic effects of the sample as well.

The modulated phase difference in Figure 1-9 (right) is defined as:

$$p_{diff} = \begin{cases} \text{mod}(p_2 - p_1, 1) & \text{if } < 0.5 \\ \text{mod}(p_2 - p_1, 1) - 1 & \text{if } > 0.5 \end{cases} \quad \text{Eq. 1-8}$$

with  $p_1$  and  $p_2$  being the frequency dependent phase from the first and second measurement, respectively. By applying this modulation, all values lie between -0.5 and 0.5 cycles. Overall, the average of the absolute value of the phase difference is 0,017 cycles. The absolute value of the modulated phase difference is well below 0.05 cycles for most frequencies below 7 kHz and is more variable for values above 7 kHz. At these high frequencies, however, very small errors in time measurement can lead to considerable differences in phase. A preferred sign for the phase difference is observed in none of the frequency ranges, so the errors appear to be random rather than systematic.

## 4. Discussion

### 4.1 Measurement range

The measurement range is difficult to determine since it is dependent on a large number of factors. On our demonstration sample, motion amplitude needed to have a magnitude of at least 5 nm in order to be distinguishable from the measurement noise. Since magnitude is a function of frequency and this response function can differ between different samples, the frequency range of the technique can be different for other samples. Furthermore, the level of noise is also variable, depending on the sample's reflectivity. The maximal measurable displacement is dependent on the density of  $2\pi$ -jumps on the object surface. If these jumps are too close to each other, unwrapping algorithms are incapable of extracting the unwrapped phase map such as demonstrated in Figure 1-7 (right). Thus, the upper measurement limit is dependent on the maximal displacement, the number of pixels covering the studied surface and the complexity of the vibration pattern, which determines the steepness of the shape of the displacement maps. The maximal magnitude that was measurable on our demonstration sample was around 5  $\mu\text{m}$  (sample covered 670 x 822 pixels). Furthermore, in order to study single harmonically isolated motions, the setup range is limited by the range of the chosen excitation device in which one can be certain of undistorted sine-wave stimulus signals.

The spatial resolution of the setup is also dependent on different parameters and is given by (Kreis, 2005):

$$\Delta x = \frac{d\lambda}{N\Delta\xi}, \quad \text{Eq. 1-9}$$

with  $d$  being the chosen reconstruction distance,  $\lambda$  the laser wavelength,  $N$  the number of CCD pixels and  $\Delta\xi$  the CCD center-to-center pixel distance (i.e. the pixel pitch). In our setup, this resulted in a lateral spatial resolution of 10  $\mu\text{m}$  in  $x$ -direction and 12  $\mu\text{m}$  in  $y$ -direction. As a consequence of Eq. 1-9, the field of view does not depend on the actual size of the sensor array, as it is equal to  $N\Delta x = \frac{d\lambda}{\Delta\xi}$ .

## 4.2 Comparison to other techniques

The advantage of the presented time-resolved full field imaging technique over time-average holography (Powell and Stetson, 1965) and its digital variant is obvious, since time-averaging does not provide any time-resolved information at all. Therefore, vibrations studied with time-average holography can be mistakenly identified as purely modal with strict in- and out-of-phase regions and nodal lines, while in reality there could be significant continuous phase gradients over the surface, such as seen in Figure 1-5 (right) and 6B (at frequencies above 3000 Hz). Stroboscopic holography however requires a longer and more complicated recording procedure.

Another important advantage of the presented technique is the capability of single-shot full-field measurement with an excellent spatial resolution without the need for scanning, as opposed to laser Doppler vibrometry (LDV) based approaches (Lewin et al., 1990).

A disadvantage is its sensitivity to (quasi-)static motions in between recordings. On the other hand, methods that measure velocity instead of displacements, such as scanning LDV, are by design insensitive to uncontrolled (quasi-)static motions.

## 4.3 Comparison to similar setups

Stroboscopic digital holography is not a new technique in itself. In 1986, Hariharan and Oreb published a hybrid setup that utilized a holocamera to record double-exposure pulsed analogue holograms on a television camera, thereby not being true digital holography (Hariharan and Oreb, 1986). More recently, stroboscopic holography was truly digitized when phase-shifted double-exposure holograms were recorded on a digital CCD camera for subsequent reconstruction (Furlong et al., 2009; Hernandez-Montes et al., 2009). In other approaches, the laser pulses were not only timed at two opposite phases within the vibration period, but spread out to different vibration phases (Pedrini et al., 2006; Trillo et al., 2009; Cheng et al., 2010), such as in Figure 1-1 from this paper. The approaches chosen in (Pedrini et al., 2006) and (Trillo et al., 2009) are based on a high-power continuous laser ( $\sim 10$  W) and high frame rate recordings (within-period acquisition) and are both aimed for industrial applications at  $< 1$  kHz frequencies. Although very promising setups, no follow-up studies have been published. The setups feature

camera frame rates of 4.000 – 10.000 fps, posing an intrinsic limitation of around 1-2 kHz on the highest frequency that can be measured by the setups. Provided that a very expensive ultra-high frame rate camera of ~500.000 fps is used, this limit could be increased to ~100 kHz. However, provided that the motion is periodic, the setup presented in the current paper is able to measure up to 250 kHz using a low frame rate camera. As discussed in section 4.1 even higher frequencies are achievable when using further optimized electronics, which is not expensive at all in comparison to ultra-high frame rate cameras. Furthermore, as the camera frame rate is no limiting factor in our setup, the CCD target resolution can be allowed to be much higher (2452x2054), compared to 256x256 (Pedrini et al., 2006) and 856x848 (Trillo et al., 2009) in the mentioned papers. The advantages of more available pixels include a better spatial resolution and a lower limit on the allowed distance between the camera and the object.

The approach chosen by (Cheng et al., 2010) is the one closest to the currently presented setup. In that setup, however, a continuous laser was strobed using an acousto-optic modulator, resulting in lower energy pulses compared to our setup, in which a high-energy pulsed laser has been introduced. In order to collect a sufficient amount of light on the CCD using the lower power pulses, longer pulse lengths are needed (10 % of the vibration period) and a number of these pulses need to be integrated, causing three disadvantages compared to our setup. Firstly, since the illumination covers 10% of the vibration period, different positions in time of the objects will contribute to the recorded hologram, resulting in a loss of resolution. Secondly, since the pulse length increases for decreasing frequency, stability problems arise in the low-frequency range, resulting in a low-frequency limit of 200 Hz in the published results. Thirdly, the capability of recording single-shot holograms with an ultra-short single laser pulse enables us to extend the technique to measurement of extremely fast transient phenomena with a sub-microsecond temporal resolution, as discussed in the next section. These resolutions are not achievable when using a strobed continuous wave laser. Furthermore, the mentioned setup does not record a reference hologram in rest state, but rather computes deformations between every subsequent vibration hologram (at stimulus phases  $\pi/4$ ,  $\pi/2$ ,  $3\pi/4$  ...) and the vibration hologram at stimulus phase zero. This does not allow the determination of absolute displacement maps, since the surface's shape at stimulus phase zero is not always equal to its shape in rest, certainly at higher frequencies.

#### 4.4 Applications and future development

Our lab uses the presented technique to study the motion of the eardrum of humans, other mammals and avian species. Acquiring full-field vibration response information of these membranes across both quasi-static and acoustic frequencies is of major interest in a better understanding of the characteristics and the role of the eardrum. The results are used as validation data for finite element models with highly realistic geometries, so that we can construct a true-to-nature computer model of the entire human middle ear. Steps in this direction have been made already (De Greef et al., 2014b, i.e. Chapter 5 of this thesis; Aernouts et al., 2012b) and further developments in this research line will be published in the future.

The technique can however be used in many other fields than biomechanics, basically in any field where full-field vibration information in a frequency range from 1 Hz to 250 kHz could be valuable.

In the future, the setup will be adapted to measure very rapid transient motions. Such measurements are important to characterize viscoelastic behavior of materials, or to study propagation of traveling waves. Since the laser pulses have a length of 8 ns and one pulse is sufficient to record a hologram, very rapid transient motions can be visualized with a temporal resolution of 1  $\mu$ s, which currently is the smallest time step on our microchip's program. With further optimized trigger electronics, the setup could be able to measure transient motions with a sub-microsecond temporal resolution. Note that the transient phenomenon needs to be reproducible, as the different holograms cannot be recorded during a single event.

## 5. Conclusion

In this paper, a new setup for stroboscopic digital holography, incorporating a high-energy pulsed laser and advanced trigger electronics, was described and presented. The basic concepts of digital and stroboscopic digital holography, as well as the technical details, including optical, electric and acoustic aspects, were covered. Results of measurements on a vibrating rubber membrane are shown in section 3.1, for frequencies ranging from 5 Hz to 16.7 kHz. This range is limited by the demonstration object and the stimulation device (i.e. in our case an acoustic speaker) rather than the technique itself. It needs to be noted that the possible range of the technique with the current components extends to 250 kHz. Furthermore, measurements are very quick, as shown in section 3.2.

Two tests were performed to make an assessment of the accuracy and repeatability of the technique: known static displacements were measured (for accuracy and precision) and a full-spectrum series of vibration measurement was tested for its repeatability. The accuracy tests revealed that the measured displacements are in good accordance with the applied indentations, provided that material compression was taken into account. The standard deviation of the technique increases from 1,0 nm at 10 nm indentation to 37 nm at 3  $\mu$ m indentation, with the relative standard deviation decreasing from 9,9 % to 1,3% in the same range. The repeatability tests showed intra-class correlation coefficients of 99,86% and 99,92% for the magnitude and phase, respectively. The average absolute magnitude and phase difference at a single data point between subsequent measurement of the same phenomenon was 8,7 nm/Pa and 0,017 cycles, respectively, averaged over all frequencies.

The measurement range of the technique was discussed in depth and shown to be dependent on several factors such as camera resolution, object dimensions, light reflectivity and limits of the stimulation device. The technique was qualitatively compared to other techniques and setups that are similar to ours. Finally, possible applications, such as providing validation data

for finite element models, and future ambitions, such as adapting the setup for measuring extremely fast transient phenomena, were addressed.

# Chapter 2. Graphical User Interface for a Digital Stroboscopic Holography Setup: Experiment Control, Data Processing and Results Analysis

---

## 1. Introduction

This chapter presents a short description of the graphical user interface for the control and analysis of stroboscopic digital holography measurements that was developed during the course of this PhD thesis. There were two main reasons for developing this GUI: minimizing measurement overhead time and facilitating the training of other researchers to use the setup.

### 1.1 Minimizing measurement overhead time

When measuring biological material *ex-vivo*, it is important that the total duration of the experiment is minimized in order to minimize dehydration effects.

The optimal measurement range of displacement amplitudes for digital stroboscopic holography is roughly  $50\ \mu\text{m} - 3000\ \mu\text{m}$  for the laser wavelength of our setup (in which a laser wavelength of  $532.8\ \mu\text{m}$  was used). Lower amplitudes result in a poor signal to noise ratio, while higher amplitudes result in phase jumps that are too dense, causing phase unwrapping difficulties. The vibration response of human tympanic membranes can vary up to an order of magnitude between individuals (Aibara et al., 2001). Therefore, in order to obtain amplitudes within the optimal range, it is often necessary to adjust stimulation levels at multiple frequencies between samples. The GUI was designed in order to optimize this procedure by maximizing the flexibility of the measurement protocol. For example, the user is allowed to

change the stimulation level of a single or multiple frequencies at once, then measure user-selected frequencies at a low resolution (to maximize speed), readjust the stimulation level again if necessary, check the amplitude again at low resolution, and finally measure all frequencies at the desired, higher resolution. This can be done in any order, without unnecessary loss of previous measurements or settings.

Furthermore, a number of other causes can induce sub-optimal measurement results at one or more frequencies. Therefore, it is desirable to be able to fully analyze and explore the results as soon as possible after the measurement. This enables the researcher to decide quickly whether a repetition of the measurement is needed and to perform this repetition at user-selected frequencies.

## 1.2 Facilitating the training of other researchers to use the setup

The availability of an easy-to-use and intuitive user interface facilitates the training of other people to use the setup. Furthermore, it increases the portability of the code needed to control the setup. This means that the code can be easily transferred to another PC and another measurement setup (which has been demonstrated already).

# 2. Elements of the GUI

## 2.1 GUI Overview

The GUI was built in Matlab (MATLAB Release 2014b, The MathWorks, Inc., Natick, Massachusetts, United States). The layout was designed using the GUIDE (Graphical User Interface Development Environment) environment in Matlab. The code behind the GUI contains approx. 3700 lines, including comments and whitespaces, is logically structured, and well documented. The layout consists of three main parts: the experiment control module, the list of frequencies, and the results module. Figure 2-1 displays the overall layout of the GUI. At any time, the dataset in memory can be saved to the hard disk. Saved datasets can be reloaded and viewed in the same GUI. When the GUI is closed, a temporary file is made in which the experimental setting are saved. This file will be loaded when the GUI is restarted, so that all settings from the previous session will be filled in again. Multiple instances of the GUI can be opened at once so that different datasets can be compared.

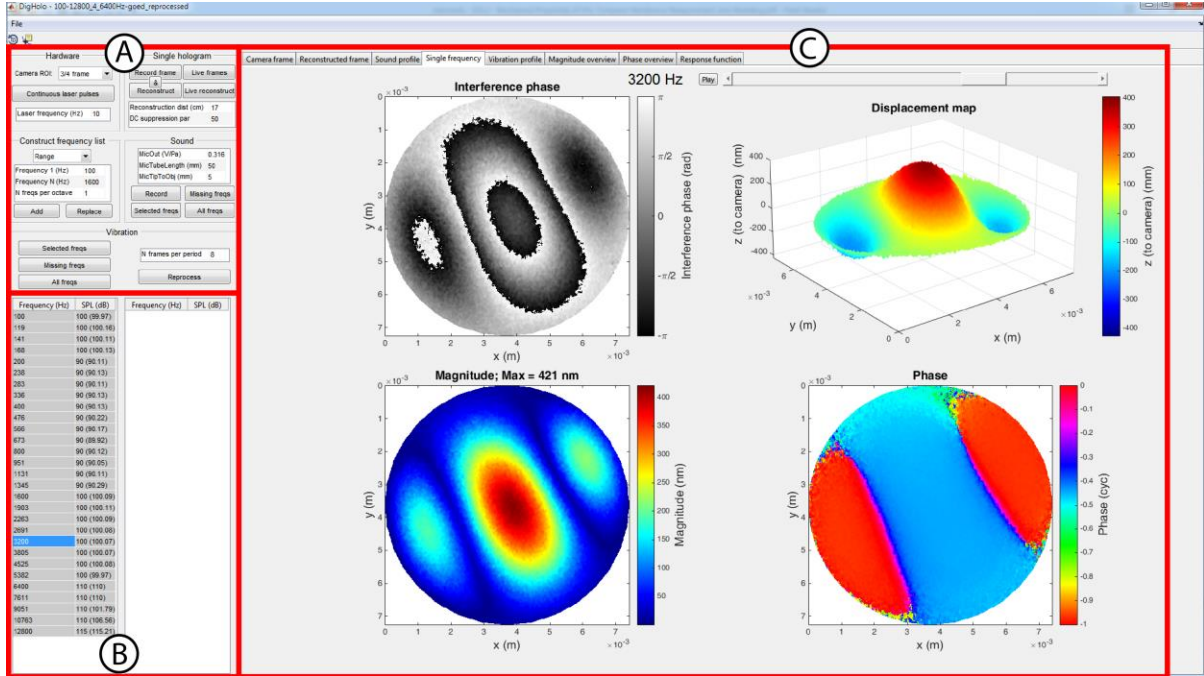


Figure 2-1: Overview of the developed Matlab graphical user interface for the control and analysis of stroboscopic digital holography measurements.

## 2.2 Experiment control module and list of frequencies

Figure 2-2 A displays the top-left section of the GUI, containing all experimental control tools.

### 2.2.1 Hardware panel

This panel gives the user the choice to use a region of interest (ROI) for the CCD camera (AVT Pike 505-B, 2452 x 2054, 14bit). The user can choose in drop-down menu between full frame (2452 x 2054),  $\frac{3}{4}$  frame (1840 x 1540),  $\frac{1}{2}$  frame (1228 x 1028) or  $\frac{1}{4}$  frame (612 x 512). The ROI position on the physical CCD target is always chosen to be central in both horizontal and vertical direction. This way, the reconstructed image will always cover the exact same field in space, only with a different spatial sampling frequency (since the field of view is given by  $N\Delta x = \frac{d\lambda}{\Delta\xi}$ , see section 444.1 in Chapter 1). This way, the user can switch between ROIs without having to reposition the object on the hologram.

For optimal measurements results, the full frame option is obviously desirable. However, there are multiple scenarios when opting for a smaller ROI could be preferred. In general, the smaller the camera ROI, the faster the data processing. So for initial measurements with new specimens, this is a good choice. Stroboscopic holography measurements recorded using the  $\frac{1}{4}$  frame ROI setting are sufficient to adjust the position of the sample on the hologram and to adjust stimulation levels in order to obtain a vibration amplitude in the optimal amplitude range. After

determining the optimal experimental settings, higher resolution recordings can be made by choosing another camera ROI.

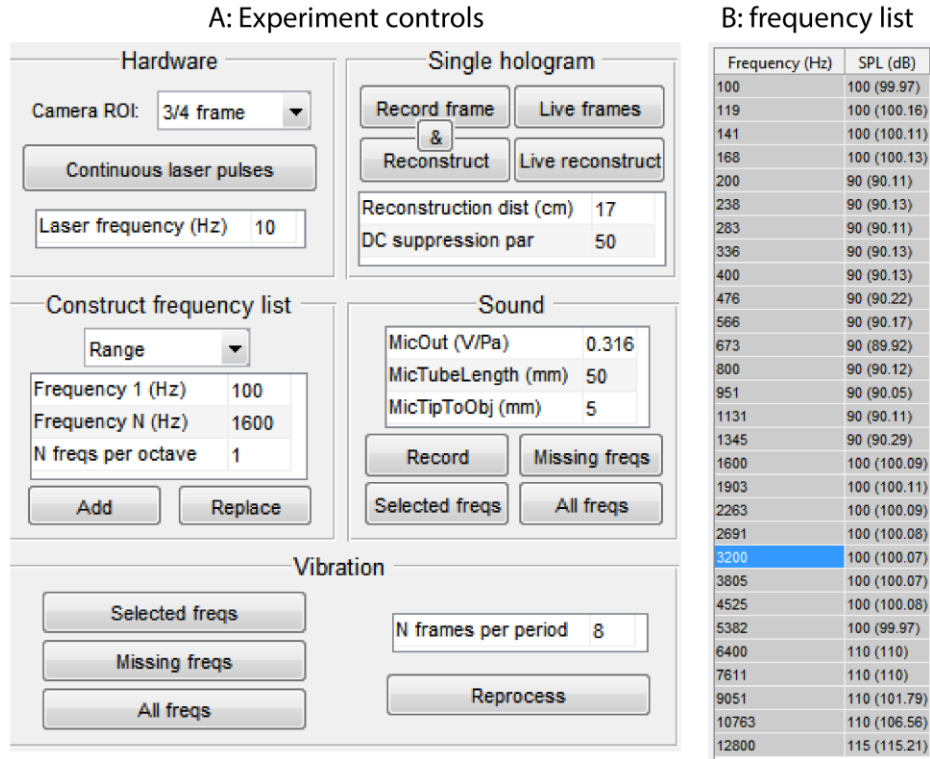


Figure 2-2: Close-up views of (A) the experiment control module containing different tools and settings and (B) the list of frequencies, including sound pressure levels for all frequencies.

Besides the camera ROI selection, this panel contains a toggle button that initiates the hardware to fire continuous trigger pulses to the laser. Finally, the user can also choose the frequency of these laser pulses in an edit box. This frequency is 10 Hz by default, but when the camera is chosen to operate at full resolution, the maximal camera frame rate is only 6.5 Hz. Therefore, the laser pulse frequency should be reduced as well when choosing this option. This is changed automatically when the ROI setting is changed, but there are scenarios in which the user still prefers to change the laser pulse frequency manually, which is why the value can be changed at any time. One example of such a scenario is when low-resolution holograms (where the camera can handle 10 Hz) are used to optimize setup and object positioning as preparation for a resolution at the highest resolution (where the camera cannot handle 10 Hz). In this case, it is undesirable that the laser pulse frequency is different for the optimization stage and for the final recording stage.

### *2.2.2 Single hologram panel*

In this panel, pushbuttons enable the user to record single camera frames and to reconstruct them holographically. There are also toggle buttons for starting an infinite stream of live camera frames and live reconstructed frames. Live camera frames and live holographic reconstructions are useful and time-saving tools for adjusting the optical setup and the positioning of the specimen.

In this panel it is also possible to change reconstruction parameters that often need to be adapted: the reconstruction distance and the parameter that controls the degree of DC term suppression. Mathematically, this parameter is the standard deviation of a 2D inverted Gauss filter that is multiplied with the camera frame in the Fourier space. This filter action, followed by an inverse Fourier transformation, eliminates most of the power contained in the DC term of the hologram, so that the first order diffraction beams (i.e. the focused reconstructed object and its unfocused twin image) are better visible on the reconstructed hologram.

### *2.2.3 Construct frequency list panel*

Here, the user can construct the list of frequencies that will become available in the list of frequencies table of the GUI (described in section 2.2.6). This can be done either by entering parameters for a logarithmically spaced array of frequencies, or explicitly. When done by entering parameters, the user specifies a start and end frequency and the number of frequencies per octave. When done explicitly, the user can insert any Matlab command that generates a 1D array. In both cases, the user can choose to either add the new frequencies to the existing frequencies in the table (button 'Add') or to replace the existing list in the table entirely by the new list (button 'Replace').

### *2.2.4 Sound panel*

Three edit boxes in this panel enable the user to change setup-specific properties that are related to the microphone measurement: the output conversion factor of the microphone (in Volts per Pascal), the length of the probe tube that is used and the distance from the tip of the tube to the object. These last two are needed to correctly calculate the phase of the sound at the object's surface.

The button 'Record' will play and record a short sound with the frequency that is currently selected in the list of frequencies at the bottom-left of the GUI. The other buttons in this panel will initiate an algorithm that finds the input voltage for the speaker amplifier that is required to generate the requested sound pressure level (SPL). These SPL's can be inserted in the 'list of frequencies' table (described in section 2.2.6). The user can choose to find the voltages for either the frequencies that are selected manually in the frequency and SPL table (button 'Selected freqs'), or the frequencies for which the voltage has not yet been determined (button 'Missing freqs'), or all frequencies (button 'All freqs').

### 2.2.5 Vibration panel

In this panel, the user can initiate the measurement of stroboscopic holography data by clicking one of the three pushbutton on the left of the panel. Similar to the 'Find voltages' panel, the user can choose to perform the measurements for either the frequencies that are selected manually in the frequency and SPL table (button 'Selected freqs'), or the frequencies for which the measurement was not performed yet (button 'Missing freqs'), or all frequencies (button 'All freqs'). After pressing one of these buttons, an algorithm starts that records and processes stroboscopic holography measurements for the requested frequencies. This includes:

- Finding the correct voltage for the frequencies for which this has not yet been done (cfr. Section 2.2.4);
- Recording a reference hologram of the object in rest (without stimulation);
- Starting the stimulation for vibration at the first frequency and voltage;
- Recording stroboscopic holograms;
- Repeating the above two steps for all selected frequencies;
- Reconstructing all holograms;
- If this is the first measurement with the current settings, the GUI will ask the user to draw an ROI around the object on the reconstructed hologram. If this ROI selection was already done with these settings, this will not be asked again;
- Calculating the optical phase difference between the vibration holograms and the reference hologram;
- Unwrapping these phase maps and calculating all displacement maps;
- Calculating the magnitude and phase maps for all frequencies through point-wise Fourier analysis in the time domain;
- Displaying all results in the correct result tabs.

This panel also contains an edit box to change the number of frames per period that should be recorded and a push button that enables the user to reprocess the recorded vibration data.

### 2.2.6 List of frequencies

The list of frequencies is depicted in Figure 2-2 B. This table contains two columns: 'Frequency Hz)' and 'SPL (dB)' (sound pressure level). In the frequency column, the frequency list that was constructed through the 'Frequency list' panel is displayed. Next to each frequency, the currently chosen SPL for that frequency is displayed. The SPL column is editable at any time. Multiple SPL's can be set simultaneously by selecting multiple rows and typing the desired SPL. The actual, measured SPL (which is seldom exactly equal to the requested value) is displayed in brackets, if for this frequency and SPL the correct output voltage for the speaker has been determined already (see '2.2.4: Sound panel'). The frequencies for which a stroboscopic holography measurement is done already are marked with a gray background.

Sometimes the sound signal is distorted because the requested SPL is too high, which means, in mathematical terms, that other frequencies than the stimulation frequency are present in the signal. This is undesired, as the setup aims to measure the response at isolated frequencies. We quantify the harmonic distortion by the ratio of the second highest peak in the Fourier spectrum of the sound to the highest (which is at the stimulation frequency). If the recorded sound profile exhibits a harmonic distortion larger than 10%, the table row will be marked with a red background, so that the user can decide whether or not to decrease the stimulation level.

## 2.3 Results module

### 2.3.1 Camera frame tab

In this tab, a single camera frame will be displayed using a grayscale color map. Live camera frames are also displayed here. The color map is tweaked so that underexposed and overexposed pixels are displayed in blue and red, respectively. If a stroboscopic dataset was recorded, this tab shows the camera frame corresponding to the ‘rest hologram’.

### 2.3.2 Reconstructed frame tab

In this tab, a single reconstructed hologram will be displayed using a grayscale color map. Live reconstructions are also displayed here. If a stroboscopic dataset was recorded, this tab shows the hologram corresponding to the ‘rest hologram’.

### 2.3.3 Sound profile tab

This tab displays a line plot of ten periods of the recorded sound pressure as a function of time. When multiple frequencies are recorded, the user can view other frequencies by selecting the desired frequency in the frequency table. This view is useful for identifying harmonic distortions in the stimulus, which is undesirable.

### 2.3.4 Single frequency tab

This tab contains four sub-plots and is ideal for exploring a processed stroboscopic holography dataset at a specific frequency. A screenshot of this tab is displayed in Figure 2-1. The top-left plot displays the interference phase map before phase unwrapping, which is useful to evaluate the density of the  $2\pi$  phase jumps. The top-right display a 3D-surface plot of the displacement map that corresponds to the interference phase map in the top-left. Above it, a slider allows cycling through the calculated displacement maps for the currently selected frequency. When scrolling, the interference phase maps will cycle through the vibration period as well. A ‘Play’ button starts automatic cycling of both these plot, so that the user can see an animated reconstruction of the recorded object’s vibration.

The bottom two figures summarize the vibration at the current frequency by displaying the magnitude and phase maps of the vibration, obtained through point-by-point Fourier analysis

in the time dimension. If another frequency is selected in the frequency list table, the corresponding dataset for that frequency will be displayed in this tab.

### 2.3.5 Vibration profile tab

This tab allows a detailed exploration of the vibration data at the selected frequency. A screenshot of this tab is displayed in Figure 2-3. The top plot displays the vibration of a single point on the object as a function of time. Although only one vibration period is actually measured, two periods (i.e. two copies of the same data) are displayed to facilitate the interpretation. The bottom plot displays the stimulating sound pressure as a function of time and the data is processed in such a way that the time axis is actually shared, i.e. the phase relation between the plots is correct. This can be seen in Figure 2-3: the displacement and sound pressure are in phase, as is expected at a frequency far below the natural frequency of the measured system (around 1350 Hz). This phase relation is also visible in the bottom-right vibration phase plot, where the red color indicates zero phase difference. The object point of which the vibration profile is displayed can be changed by clicking on the magnitude and phase maps on the right-hand-side of the window.

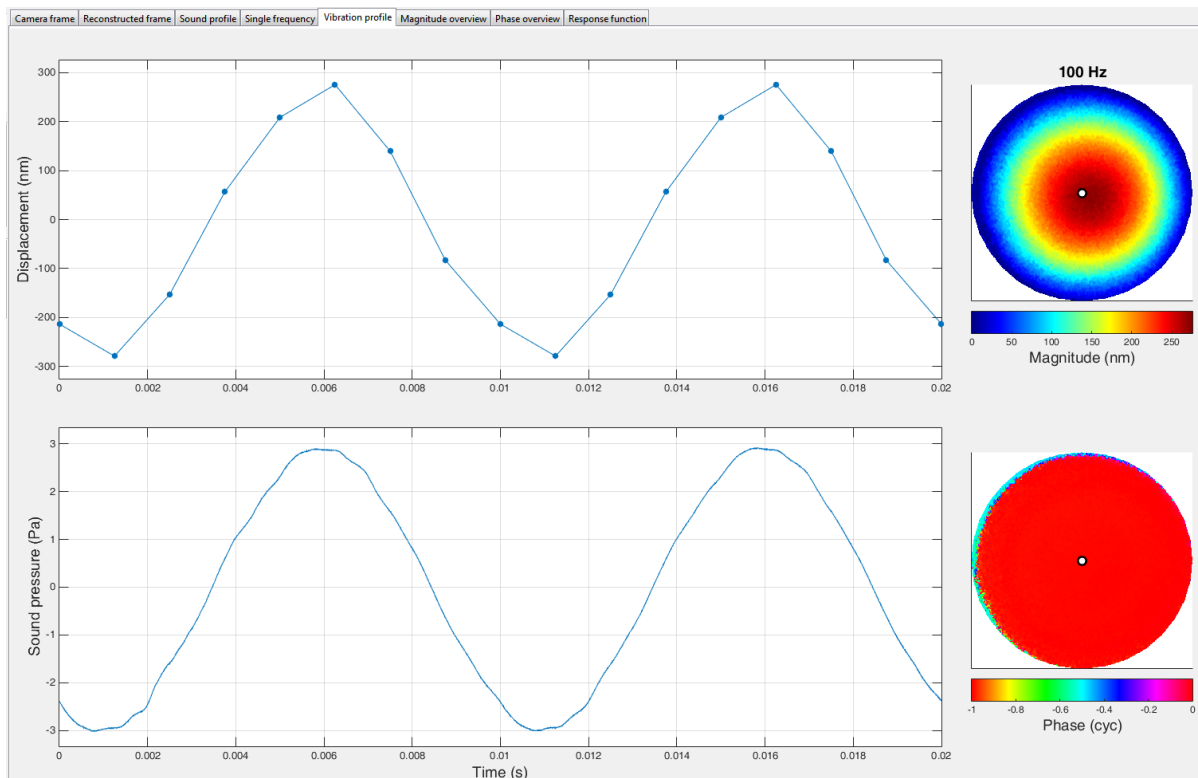


Figure 2-3: Vibration profile tab. The top graph displays (two copies of) the measured displacement of the object point that is selected on the vibration maps on the right-hand-side. The bottom graph displays measured sound pressure profile.

### 2.3.6 Magnitude overview tab

In this tab, the magnitude maps of all measured frequencies are displayed in a grid. This provides a good overview of the frequency-dependent characteristics of the object's vibration response. A screenshot of this tab is displayed in Figure 2-4 A.

### 2.3.7 Phase overview tab

In this tab, the phase maps of all measured frequencies are displayed in a grid. A screenshot of this tab is displayed in Figure 2-4 B.

### 2.3.8 Response function tab

This final tab displays the response function of a single object point as a function of frequency, separated in the magnitude and phase. The object point can be changed by clicking on the small plots of the magnitude and phase maps on the right-hand-side of the window. A screenshot of this tab is displayed in Figure 2-5.

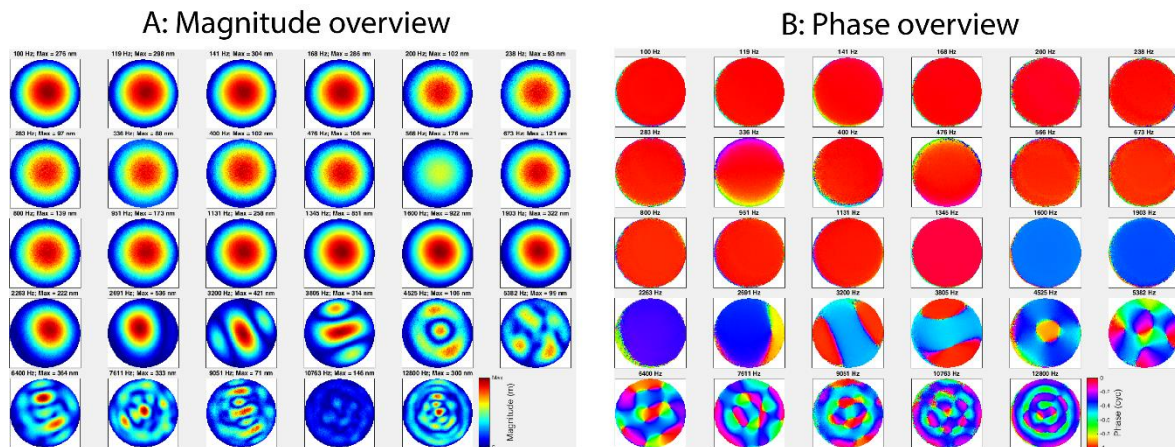


Figure 2-4: A: The magnitude overview tab displays the vibration magnitude patterns for all measured frequencies. B: The phase overview tab displays the vibration phase maps for all measured frequencies.

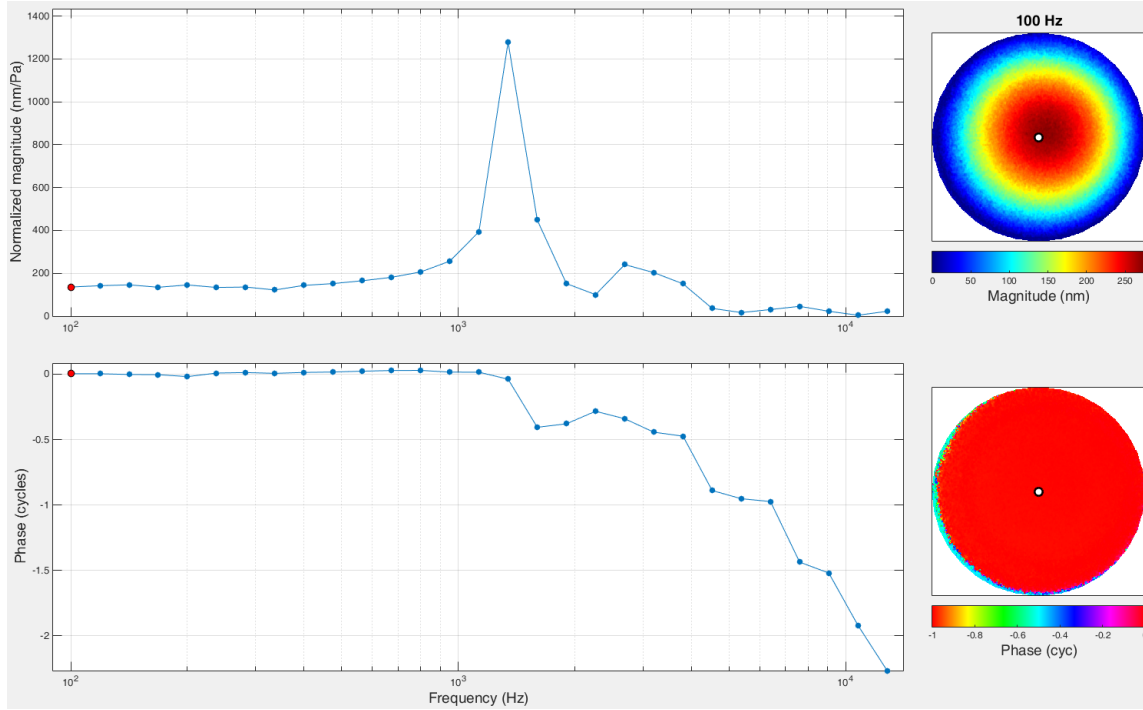


Figure 2-5: The response tab displays the complex transfer function of a single object point. The top graph presents the (normalized) magnitude, the bottom graph the phase (relative to the sound pressure). Similar to the vibration profile tab, the point of interest can be selected on either of the two vibration maps on the right-hand-side.

## **PART II - MIDDLE EAR MORPHOLOGY**



# Introduction: The Middle Ear and Micro-computed Tomography ( $\mu$ CT)

---

This second part of the thesis presents research in the field of middle ear morphology in the form of two journal publications. The third and last part includes four research papers in the field of middle ear mechanics and modeling. Therefore, the general introduction of the middle ear in this introduction is relevant for both parts. First, a description of the complete human hearing organ is provided. Then the focus will be directed to the middle ear (ME), whose main role is to conduct sound energy from the outer to the inner ear, but also needs to cope with large (quasi-)static ambient pressure variations. Both of these subjects will be introduced and discussed. Finally, a very brief introduction on micro-computed tomography is provided, as this imaging technique is used extensively as a tool in the research of this thesis.

## 1. The hearing organ: an overview

In this section, a general overview of the anatomy and physiology of the human ear is given. Although shapes and sizes do differ between species, most of this description also applies to other mammals. In fact, the possession of three separated ossicle bones in the ME is one of the defining characteristics of the mammalian class (next to having a neocortex, hair, and mammary glands).

The primary purpose of the hearing organ is to gather sound and convert it into neural signals that can be interpreted by the brain. The organ can be broken into three functionally and anatomically distinct components: the external, middle, and inner ear, as illustrated in Figure II - 1.

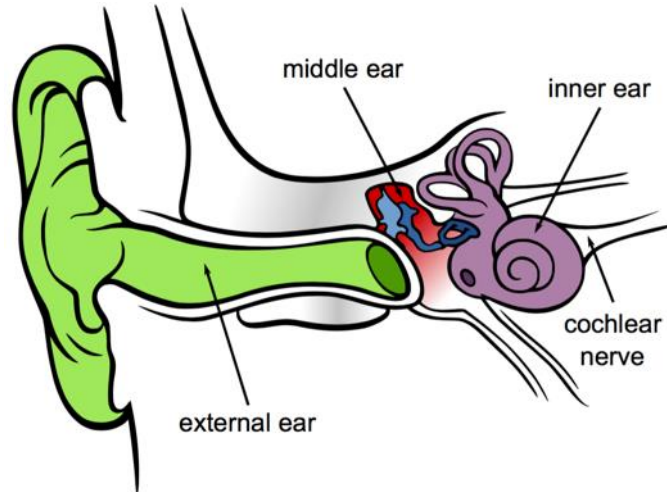


Figure II - 1: Basic overview of the human ear. Original figure from (L. Chittka, A. Brockmann, Creative Commons Attribution 2.5 License)

## 1.1 The external ear

The external ear is the most peripheral and lateral part of the hearing organ. It consists of the pinna or auricle and the cylindrical external ear canal (EC). A typical human pinna is on average 6.7 cm in height and 3.5 cm in width, while a typical human EC is about 0.75 cm in diameter and 2.3 – 2.7 cm long (Shaw, 1974). However, there is much variation in size and details of the external ear structure within humans. The EC connects the pinna with the ME. The first third of the EC is a continuation of the cartilage that forms the pinna. The last two thirds are embedded in the skull bone.

When externally generated sound (i.e. pressure waves travelling through a medium such as air or water at acoustic frequencies, i.e. 20-20,000 Hz) reaches the head, a fraction of it is collected by the pinna or auricle and travels through the ear canal towards the tympanic membrane or eardrum. The pinna and EC together create a broad resonance which enhances sound levels at the TM over the frequency range from about 1.5 to 5 kHz. The maximum boost is typically about 12-15 dB in the region around 2.5 kHz (Shaw, 1974). At medium and high frequencies, the sound reaching the TM is significantly modified by the pinna (and also by the head and upper torso). Specifically, when the sound contains a broad range of frequencies, the pinna introduces a complex pattern of peaks and notches in the spectrum. This pattern varies systematically with the direction of the sound source relative to the head, and the spectral patterns thus provide important information about the location of sound sources (Kulkarni and Colburn, 1998). At low frequencies (< 2.5 kHz), time differences of sound information between the two ears are the dominant cues for the location of the sound source (Wightman and Kistler, 1992).

## 1.2 The middle ear

This section is rather brief since the ME will be described in detail in section 2 of this introduction chapter. Figure II - 2 A-C provides three-dimensional representations of the ME and its elements. Figure II - 2 D illustrates the size of the ossicle bones, the three smallest bones in the human body.

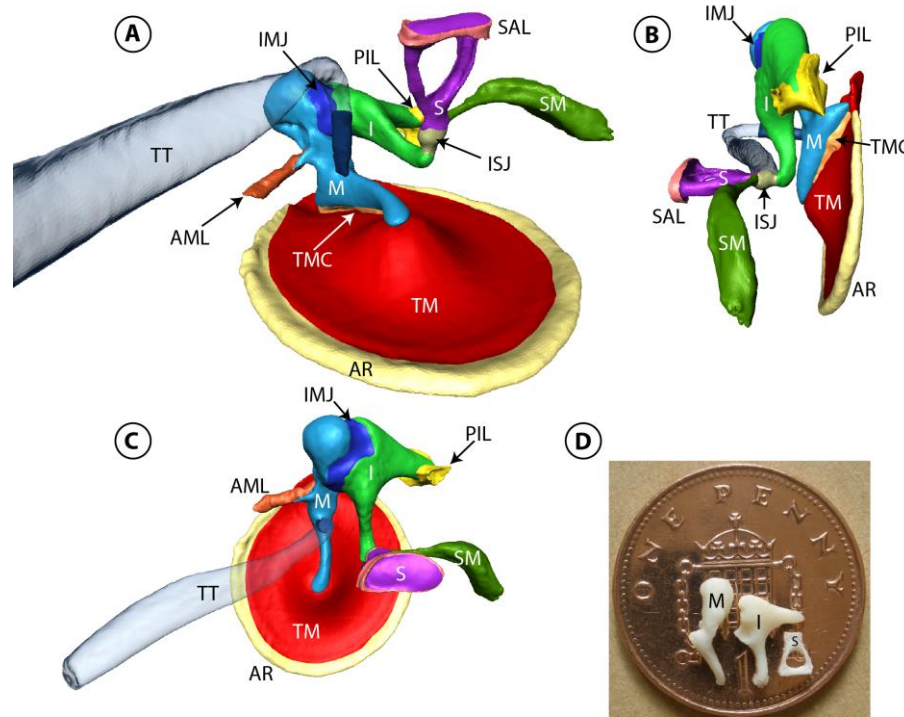


Figure II - 2: A-C: Different views of the human middle ear. This image is based on segmented images obtained with micro-computed tomography. Abbreviations: TM: Tympanic membrane - M: Malleus - I: Incus - S: Stapes - IMJ: Incudomalleal joint - ISJ: Incudostapedial joint - TT: Tensor tympani - SM: Stapedius muscle - AR: Annular ring of the TM - TMC: Tympanomalleal connection - AML: Anterior malleal ligament - PIL: Posterior incudal ligament - SAL: Stapedial annular ligament. D: Size comparison of the human ossicles to one British penny (comparable to a two Euro cent coin).

The eardrum or tympanic membrane (TM) is a natural boundary between the environment and the tympanic cavity, in which the elements of the ME are situated. Sound waves that enter the external ear canal eventually reach the TM. Their energy is converted into a vibration of the TM, which in turn sets the system of three small ossicle bones, or the ossicular chain, into vibration. The ossicles are, from lateral to medial, the hammer (or in Latin: *malleus*), the anvil (or *incus*), and the stirrup (or *stapes*)<sup>7</sup>. The footplate of the stapes is inserted into the oval

<sup>7</sup> From now on, the Latin names will be used as they are far more frequent in the research literature.

window of the inner ear. The ossicles are connected to each other through synovial joints and to the wall of the tympanic cavity by two muscles (one connected to the malleus and one to the stapes) and multiple ligaments.

The tympanic cavity in humans is extended by surrounding mastoid bone, which is porous and consists of many air cells. The aeration of the ME air space is maintained by intermittent opening of the Eustachian tube, a tube connecting the ME cavity with the nasopharynx (the uppermost part of the part of the throat situated immediately behind the mouth).

### 1.3 The (cochlea of the) inner ear

The footplate of the final ossicle, the stapes, is attached to the oval window of the cochlea in the inner ear. This inner ear is comprised of two parts: the vestibular organ and the cochlea. The vestibular organ, that contributes to balance and motion awareness, does not contribute to the perception of sound and is therefore not further described here. The spirally coiled cochlea, a fluid filled structure, is the part of the inner ear that contributes to hearing. The footplate of the stapes generates a pressure wave in the cochlear fluid which in turn excites tiny hair-shaped cells on the inner boundary of the cochlea. These hair cells are the actual sensory receptors of our hearing organ and, when set into motion, generate an electrical potential which eventually triggers an action potential in the auditory nerve. These action potential contain encoded information about the pitch and loudness of the acoustic signal that was collected by the hearing organ.

## 2. The function of the ME in the auditory frequency regime

The ME is the portion of the hearing organ that is situated between the eardrum or tympanic membrane (TM) and the oval window of the inner ear. It is contained within the tympanic cavity which is surrounded by the temporal bone. Its main function is to convert the sound waves in the air of the external ear canal to sound waves in the fluid of the cochlea in the inner ear in an efficient manner. There is a considerable gap in acoustic impedance between the low impedance air in the external ear canal and the high impedance cochlear fluid in the inner ear. The ME's role is to bridge this gap. Without this bridging, 99.9% of the sound energy would be reflected back into the surroundings<sup>8</sup> and thereby not be absorbed by our hearing organ. The ME has multiple mechanisms in place to amplify the sound pressure so that part of this impedance gap is bridged. Furthermore, it needs to overcome the natural sharp resonance

---

<sup>8</sup> The acoustic impedances at room temperature of water and air are  $Z_{\text{water}} = 1.48 \cdot 10^6 \frac{\text{Pa}\cdot\text{s}}{\text{m}}$  and  $Z_{\text{air}} = 415 \frac{\text{Pa}\cdot\text{s}}{\text{m}}$  (Kinsler, 2000). The reflection coefficient is therefore  $R = \left(\frac{Z_{\text{water}} - Z_{\text{air}}}{Z_{\text{water}} + Z_{\text{air}}}\right)^2 = 0.9989$ .

peaks in the response of mechanical systems to harmonic loads. Without appropriate properties, we would be able to hear very well at some frequencies and much worse in between these resonances.

In this section, the different parts of the ME and their role in sound transmission will be described.

## 2.1 The eardrum or tympanic membrane

The tympanic membrane (TM) is a multi-layered membrane that is on the external (lateral) side continuous with the epithelial skin of the ear canal, and on the internal (medial) side continuous with the thin mucosa layer that covers the of the tympanic cavity wall and every element within the cavity. On the medial side, the manubrium of the malleus (i.e. the long process of the malleus) is connected to the TM along a radius of the membrane. The most inferior point of the attachment between the TM and the manubrium is called the umbo. The attachment itself is labeled the tympano-malleolar connection (TMC), which was researched in Chapter 4 of this thesis (in Chapter 5, the TMC is called the manubrial fold (MF)). On the lateral side, nothing is attached to the TM. The shape of the TM is often elliptical rather than round with an average diameter of  $7.5 \pm 0.5$  mm in the inferior-superior direction and  $7.8 \pm 0.5$  mm in the anterior-posterior direction (Kirikae 1960). The membrane is not flat but has a tent-like shape with its apex towards the tympanic cavity. The height of the apex is typically 1.5 to 2.0 mm (Van der Jeught et al., 2013). Along the edge, a thick, almost bony (fibrocartilaginous) ring called the annular ring attaches the TM to the ear canal.

The tympanic membrane can be subdivided into two distinct parts: the pars tensa and the pars flaccida. The pars tensa is in most mammals much larger than the pars flaccida (although the relative sizes differ greatly among species, as shown in Figure II - 3) and is thinner and stiffer. The pars flaccida is positioned superior to the attachment of the malleus to the TM and is not surrounded by the annular ring. Rather, the ring is continuous with the notch of Rivinus, which separates the pars flaccida from the pars tensa.

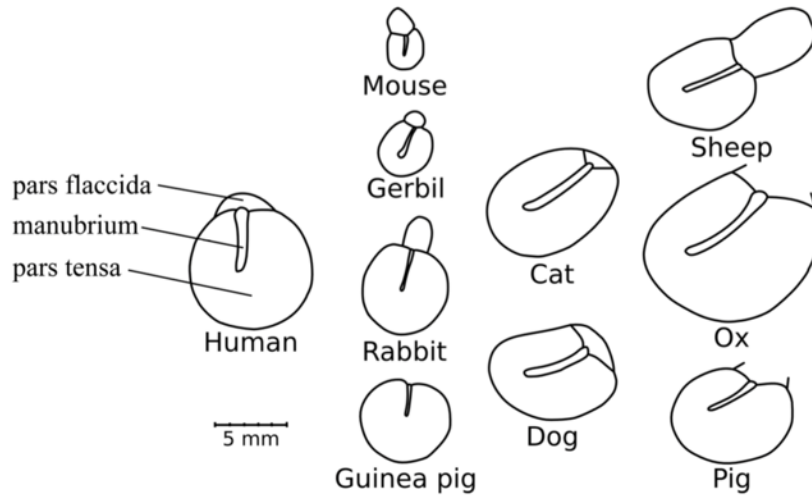


Figure II - 3: Illustration of the pars tensa and pars flaccida in different mammal species. Figure with annotations from Aernouts (2012a), original from Decraemer and Funnell, 2008. All figures depict the pars tensa, the pars flaccida and the attachment of the manubrium, i.e. the long process of the malleus.

The thickness of the human TM is not uniform and exhibits large differences between individuals, as demonstrated by Kuypers et al. (2005) and Van der Jeught et al. (2013). Averaged over individuals and position, the TM thickness is approximately 80  $\mu\text{m}$ . Towards the annular ring and towards the connection to the malleus, the TM becomes significantly thicker. In between, an open-ring-shaped minimum is observed in most TM's. Figure II - 4 depicts an average thickness map of the human tympanic membrane.

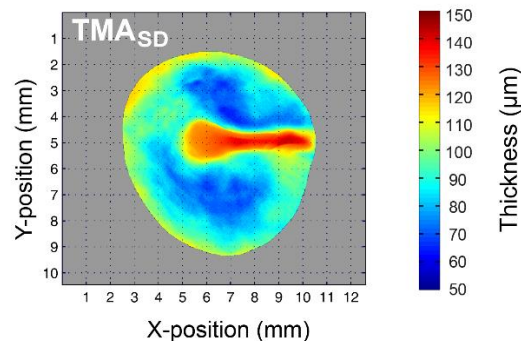


Figure II - 4: Average thickness map of the human tympanic membrane, based on five different individuals. The attachment position of the manubrium coincides with the horizontal region of higher thickness on the right-hand-side of the figure. Data obtained using OCT, figure from Van der Jeught et al. (2013).

Both the pars tensa and pars flaccida are composed of three layers. The most lateral layer consists of stratified (i.e. multi-layered) squamous epithelium and is continuous with the skin of the ear canal. The most medial layer is simple (i.e. single-layered) squamous epithelium that is continuous with the mucosal layer that covers all ME structures and the tympanic cavity wall. The main function of both outer layers of the TM is to protect the middle layer from pathogens

and dirt and to prevent dehydration of the middle layer. This middle layer consists of connective tissue. Two types of connective tissue can be identified within the TM: dense, regular connective tissue (DRCT) and loose connective tissue (LCT). The DRCT is responsible for most of the mechanical strength of the TM, while the LCT adds mass and thickness without influencing the stiffness significantly. The LCT is most prominent around the attachment of the TM to the malleus (De Greef et al., 2015, i.e. Chapter 4 of this thesis).

The DRCT consists of highly organized collagen fibers. Within this layer, a further clear subdivision can be made between circumferentially and radially organized fibers. The layer of radial fibers lies laterally relative to the circumferential fiber layer and has a larger thickness.

## 2.2 The ossicles

The ossicles are the three smallest bones in the human body and are visible from different angles in Figure II - 2.

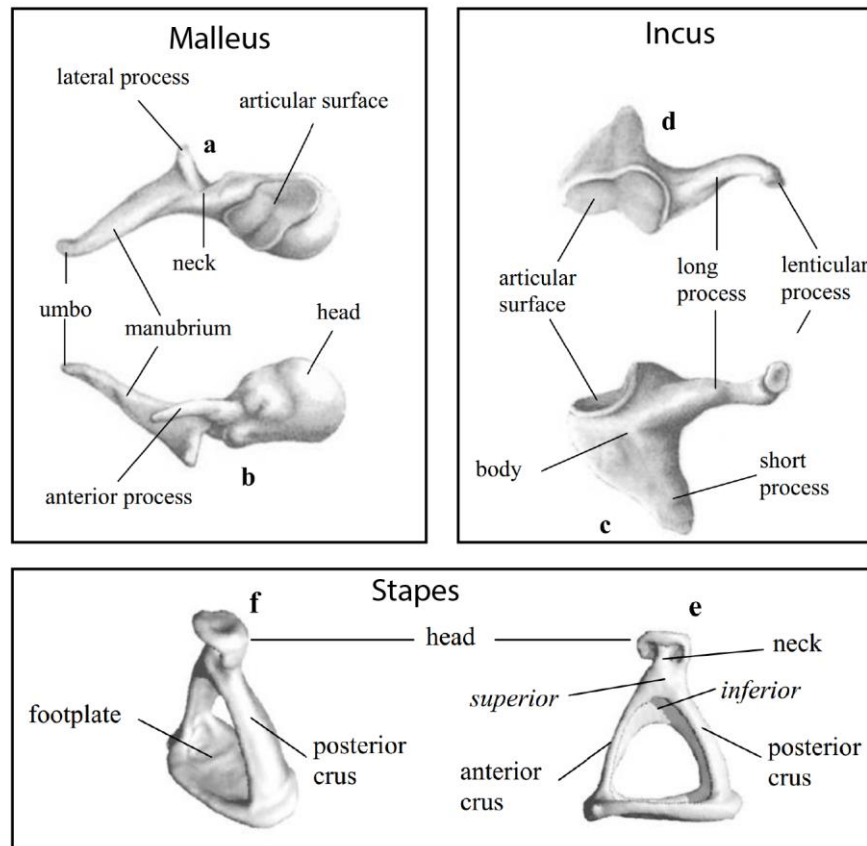


Figure II - 5: Views of the separate ossicles with anatomical annotations. a & b: malleus – c & d: incus – e & f: stapes. Figure modified from Ferrazzini (2003).

The malleus resembles a hammer and can be virtually subdivided into its arm (or *manubrium*), its neck, and its head. The manubrium is the part of the malleus that is attached to the TM. The

inferior tip of the manubrium is called the umbo, the superior tip the lateral process of the malleus (LPM) or the *processus brevis*. The head of the malleus exhibits the first joint surface of the saddle-shaped incudo-malleal (IM) joint between the malleus and the next ossicle, the incus.

The incus resembles an anvil and it contains the short process, the long process, and the lenticular process (attached to the long process). The body of the incus exhibits the second joint surface of the IM joint that tightly connects the stapes to the malleus. The malleus and the incus are often considered to be one functional unit, labeled as the IM complex. However, the flexibility of the joint may be important in some scenarios, such as during vibration in particular eigenmodes of the system or in case of large quasi-static pressures (Puria 2013). The lenticular process of the incus is a delicate outgrowth of bone at the distal end of its long process. It contains a thin bony stem and an ellipse-shaped lenticular plate that forms the first joint surface of the incudo-stapedial (IS) joint. It was studied in detail in Chapter 3 of this thesis.

Finally, the stapes resembles the shape of a stirrup and is often subdivided into the head, the neck, the two *crura*, and the oval footplate. The footplate is surrounded by the stapedial annular ligament (SAL), that secures the footplate into the oval window of the cochlea of the inner ear. Medially, it is in contact with the cochlear fluid.

### 2.3 Sound amplification mechanisms of the ME

As briefly discussed above, the main function of the ME is to bridge the gap in acoustical impedance between the low-impedance air in the ear canal and the high-impedance fluid in the cochlea, by amplifying the sound pressure. Traditionally, three mechanisms are assumed to contribute to this amplification, although it needs to be noted that their contributions changes across the acoustic frequency range. All three mechanisms are schematically given in Figure II - 6.

#### 2.3.1 The hydraulic principle of the ME

The TM and the stapes footplate (SFP) can be considered as the pressure input and output surfaces of the middle ear, respectively. The pressure applied to the TM is associated with a certain force. If none of the other amplification mechanisms would be in place (and if energy loss effects are disregarded), the same force that is exerted by the air molecules in the EC to the TM is also applied by the stapes footplate on the liquid molecules in the cochlea. Since the surface areas of these surfaces differ, the resulting pressure will differ as well, obeying the following relation:

$$\frac{P_{\text{SFP}}}{P_{\text{TM}}} = \frac{A_{\text{TM}}}{A_{\text{SFP}}}. \quad \text{Eq. II - 1}$$

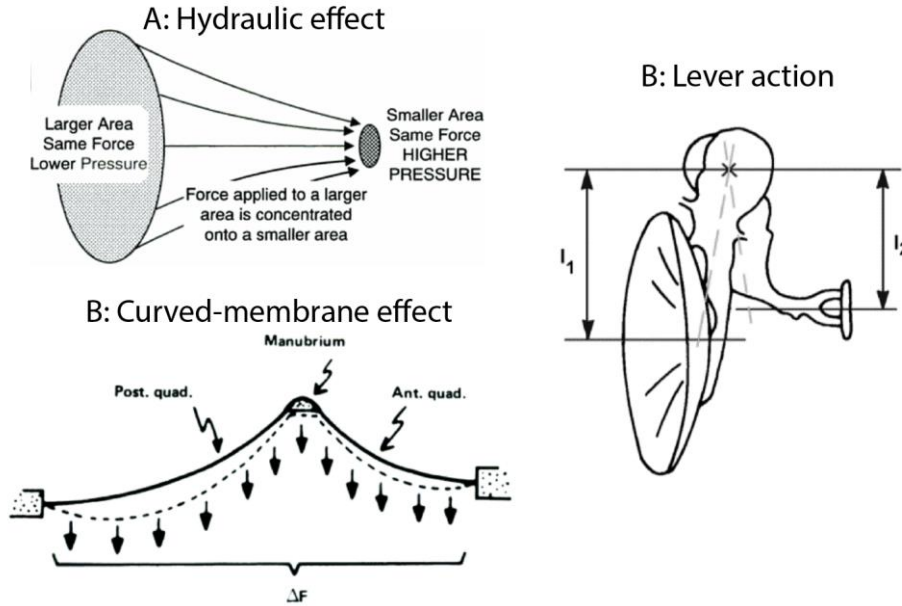


Figure II - 6: Overview of the sound amplification mechanisms in the middle ear. A: Hydraulic principle stemming from the ratio of the eardrum to stapes footplate surface areas Figure from Gelfand (2009) – B: Lever action of the incudomalleal complex. Figure from Zwislocki (1965) – C: The catenary lever action or ‘curved-membrane’ effect of the eardrum. Figure from Tonndorf and Khanna (1970).

On average, the hydraulic ratio in humans is  $19.6 \pm 2.3$  (De Greef et al 2015, i.e. Chapter 3 of this thesis). However, this factor assumes that both the TM and the stapes execute perfect piston-like motions. At frequencies below 1 kHz, this is a good approximation, but for higher frequencies it becomes increasingly inaccurate. This will be further discussed in Chapter 3.

### 2.3.2 The lever action of the IM complex

As will be explained in the next section, two of the stiffest ligaments in the ME are the anterior malleal ligament and the posterior incudal ligament. Due to their perceived stiffness, it is generally assumed that the main mode of vibration of the IM complex is rotation around the axis that connects these two ligaments. Both the malleus and the incus possess a long process that is roughly perpendicular to the rotational axis and parallel to the other’s long process (see Figure 3-3 in Chapter 3 of this thesis). This geometry creates a mechanical lever when the manubrium of the malleus is displaced by the TM. Since the lever arm of the malleus is different from the incus lever arm, the force  $F_{\text{inc}}$  that is transmitted by the incus to the stapes head is related to the force  $F_{\text{mall}}$  exerted at the umbo of the malleus through:

$$\frac{F_{\text{inc}}}{F_{\text{mall}}} = \frac{l_{\text{mall}}}{l_{\text{inc}}}. \quad \text{Eq. II - 2}$$

In human ME’s, the lever ratio is on average  $1.30 \pm 0.11$  (De Greef 2015, i.e. Chapter 3 of this thesis).

### 2.3.3 *The catenary lever action of the TM*

The catenary lever action of the TM or ‘curved-membrane effect’ was first proposed by Helmholtz (1873). Having large displacements in the middle of the anterior and posterior curved sections compared to small displacements of the manubrium, Helmholtz proposed that the tympanic membrane provides a catenary lever that aids the transformation function of the middle ear. In the 1970s, Tonndorf and Khanna measured full-field displacement magnitude maps of the tympanic membrane with time-averaged holography (e.g. Tonndorf and Khanna (1972)). They observed smaller motions at connections with the umbo and the manubrium as compared to the area between the manubrium and the annulus, consistent with Helmholtz’ theory.

## 2.4 The ligaments of the middle ear

The ossicles of the middle ear are held into position by a number of ligaments attached to the wall of the tympanic cavity. The existence and naming of many ligaments is inconsistent throughout literature and the research in this thesis (De Greef et al., 2015, i.e. Chapter 3 of this thesis) demonstrated why there is so much confusion about them: no less than 12 different ligaments could be identified in six ME samples, but only four of them were present in all six samples.

Three ligaments are generally assumed to be the most important for ME functioning: the anterior malleal ligament (AML), the posterior incudal ligament (PIL) and the stapedia annular ligament (SAL). The AML and PIL define the rotational axis of the IM complex at low frequency vibration modes (< 1 kHz). The morphology of the AML is thoroughly discussed in Chapter 3 of this thesis, but in summary it is in reality the combination of two ligaments that connect the middle ear to the temporomandibular joint region. The SAL secures the footplate of the stapes into the oval window of the cochlea while still allowing sufficient motion of the footplate.

## 2.5 The middle ear muscles

Besides the ligaments, two skeletal muscles connect the ossicles to the temporal bone: the tensor tympani (TT) muscle and the stapedius muscle (SM). Like other skeletal muscles, they are not directly attached to the bone but by means of tendons.

The tendon of the TT muscle is attached to the medial side of the manubrium of the malleus. From there it travels medially towards the tympanic cavity wall, where it bends towards the anterior direction. After the bend, the tendon transitions into the muscle and its cross-section starts to increase. The stapedius muscle is the smallest skeletal muscle in the human body. Its tendon is attached to the posterior side of the stapes head and disappears into a hole in the tympanic cavity wall.

Contractions of the SM are associated with the ‘acoustic reflex’, a phenomenon in which moderate to loud sounds (60-100 dB SPL) in conscious humans and animals produce reflex contractions that lead to a decrease in middle ear sound transmission (Moller, 1974; Pang and Peake, 1986). The TT is closely associated with the muscles that control tension in the walls of the Eustachian tube and it has been suggested that tensor tympani contraction is an important part of the reflex that opens the tube (Ingelstedt and Jonson, 1966).

### 3. The function of the ME in the quasi-static frequency regime

The ME’s main function of sound transmission is, on a frequency spectrum, situated in the auditory range of frequencies, i.e. from 20 Hz to 20 kHz. Sound waves with a frequency outside of this range are imperceptible to humans. Sounds with higher frequencies (ultrasound) have generally not a sufficient amplitude to interact meaningfully with the hearing organ. On the other end of the frequency spectrum, quasi-static ambient pressure changes can cause large deformations of the TM because the ME is an air-filled cavity and the TM is a non-rigid boundary to the surroundings. Multiple mechanisms exist to cope with these slow pressure variations, that typically have a much larger pressure amplitude than acoustic waves.

The tympanic cavity is connected to a porous part of the temporal bone, called the mastoid, that consists of many air-filled cells (an illustration of the mastoid air cell system is provided in Figure II - 7 B). The combined volume of the ME cavity and the mastoid is referred to as the ME cleft. Both the interior wall of the ME and the air cells are covered with mucosa that is perfused by blood vessels. The Eustachian tube (ET) forms a connection between the ME cavity and the nasopharynx, and for the great majority of time it is closed. The TM forms a non-rigid boundary between the ME cleft and the environment.

Keeping the ideal gas law in mind<sup>9</sup>, it is apparent that the air pressure inside the ME can change in multiple ways. Temperature changes are generally too small to have a significant influence, but changes in the amount of gas and changes in volume do have important roles. The amount of gas in the ME cleft can be altered either through ET openings or by gas exchange with the blood through the mucosa. The volume of the ME cleft can change due to deformations of the TM as well as to changes of the mucosa thickness.

---

<sup>9</sup> The ideal gas law relates the pressure  $p$ , temperature  $T$ , volume  $V$  and amount of gas  $n$ :  $pV = nRT$ , where  $R$  is the universal gas constant,  $R = 8.3144598 \text{ J} \cdot \text{mol}^{-1} \cdot \text{K}^{-1}$ .

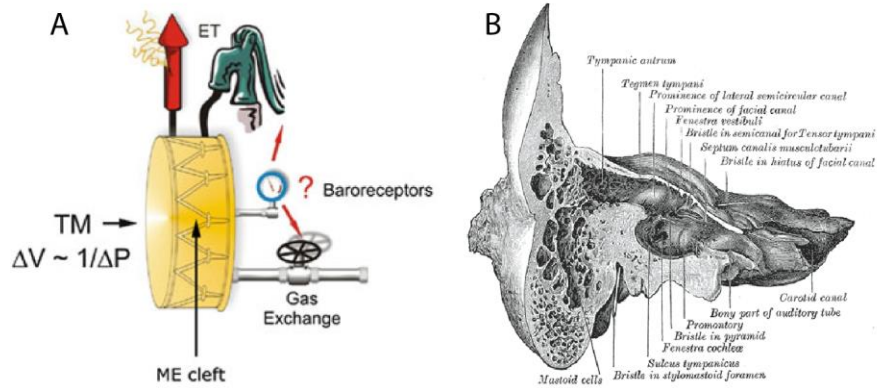


Figure II - 7: A: An artist's impression of the pressure regulating mechanisms in the middle ear. Figure from Puria (2013) – B: Illustration of a coronal section of the temporal bone, including the mastoid air cell system. Figure by Henry Vandyke Carter - Henry Gray (1918) *Anatomy of the Human Body* (See “Book” section below) Bartleby.com: Gray's Anatomy, Plate 139, Public Domain, <https://commons.wikimedia.org/w/index.php?curid=566509>

This section briefly introduces the different coping mechanisms for quasi-static pressure change variations. Figure II - 7 A presents an artist's impression of these different mechanisms. This introduction is related to the research presented in the next part, in Chapter 8 of this thesis, but is provided here to keep all introductory information on the middle ear gathered in one chapter. For an elaborate review of this subject, the reader is referred to Chapter 5 by Dirckx et al. in the book ‘The Middle Ear’ by Puria et al. (2013).

### 3.1 The Eustachian tube

One could wonder why the tympanic cavity would not be opened all of the time, avoiding any build-up of static pressure gradient over the TM at all. The answer to this is twofold. The first reason is to prevent dehydration of the tissues in the middle ear. The second reason is to prevent acoustic shortcut, an event in which the TM receives the same pressure stimulation from both sides. This would considerably decrease the efficiency of sound transmission through the ME, especially at low frequencies.

There is however a mechanism that enables the middle ear to be opened to the surroundings. This mechanism is the opening of the Eustachian tube (ET), which connects the ME to the nasopharynx. The length of the ET is about 31–38 mm (Bluestone and Doyle, 1988). It consists of a bony part, of about one third of its total length, as well as a cartilaginous part, of around two thirds of its length (Prades et al., 1998). Two muscles control the opening and closing of the ET: the tensor veli palatini and the levator veli palatini.

The ET has three main functions, according to Bylander (1986): equilibration of pressure, drainage or clearance of the ME, and protection of the ME. Only the first of these three will be discussed here. The aeration function of the ET was recently investigated clinically using live recordings of the TM pressure gradient using a pressure transducer (Gaihede et al., 2013). The

authors concluded that the duration of ET openings (average: 0.34 s) was not correlated to the pressure gradient, but the pressure change in response to ET openings was correlated to the pressure gradient ( $p < 0.001$ ). Thus, larger pressure gradients are not equilibrated to ambient pressure by longer ET opening times, but rather a series of ET openings, as illustrated by a direct measurement, presented in Figure II - 8.

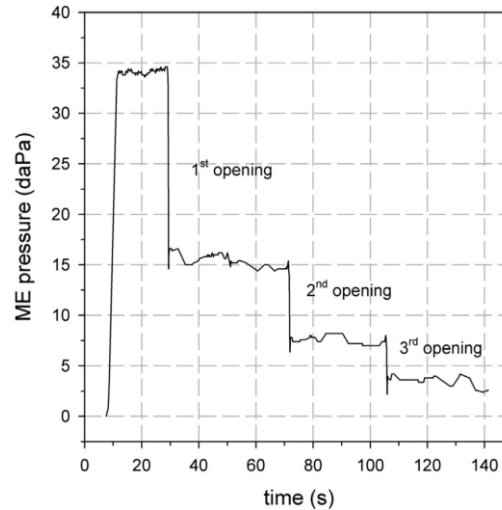


Figure II - 8: A series of three of Eustachian tube ET openings with step-wise counter-regulation in response to an experimental overpressure. Figure from Gaihede et al. (2013).

### 3.2 Gas exchange with blood in the mucosa

The mucosa layer that covers the entire surface of the tympanic cavity, the ME structures and all air cells of the mastoid, is perfused by venous blood vessels. Dissolved gases in this blood have a different composition and therefore different partial pressures than ambient air. In steady-state, the air within the ME cleft has the same composition as the air in the blood. Whenever this equilibrium is disturbed, e.g. by introducing new air to the ME cleft by an ET opening, a continuous net absorption of gases by the blood is triggered before a new equilibrium is reached. This eventually leads to the formation of underpressures in the ME cleft.

Whether this gas exchange is limited by the rate of diffusion across the vessel walls, or the rate of perfusion, is a question that is still under debate. If perfusion is the limiting factor, then, in principle, an active control mechanism could exist that may change the perfusion rate of the mucosa by contraction or dilatation of blood vessels.

### 3.3 Change of mucosa thickness through perfusion

Apart from gas exchange, swelling and de-swelling of the mucosa may also influence ME pressure by changing the effective ME gas volume (Magnuson 2003). This process is clearly

perfusion bound. It may act quickly and therefore also has the potential to be part of a regulatory mechanism.

### 3.4 The buffer capacity of the tympanic membrane

This mechanism was examined as a part of this thesis in a collaboration with the Aalborg University and the Aalborg University Hospital (see Chapter 8Chapter 8). In short, the TM forms a boundary with a finite stiffness that deforms under everyday ambient pressure changes. Because of this deformation, the enclosed volume and therefore the pressure inside the ME cleft changes. The sign of this pressure change is so that the overall pressure gradient over the TM is smaller than it would be in case of a perfectly rigid TM. The ratio of ME to ambient pressure changes as a result of this passive mechanism is called the buffer capacity of the TM and is on average 23% (Padurariu et al., 2016).

## 4. Micro-computed tomography ( $\mu$ CT)

Both chapters in this part focus on investigating the morphology of the human middle ear. The main technique used for this was micro-computed tomography (also micro-CT or  $\mu$ CT) and is introduced briefly in this section. It was used as a tool to directly observe morphological aspects of the middle ear, and as an intermediate step towards the construction of finite element models of the middle ear in later chapters of this thesis. Another technique that was used to investigate anatomy is histologic microscopy (only used in Chapter 4 and not carried out by the author of this thesis), but it is not introduced here.

Micro-CT is conceptually similar to CT but is optimized for measuring small objects (from the order of a few centimeters) with very high resolution (voxel sizes in the range from 1 to 100  $\mu$ m). The technique can be summarized as follows: a sample is placed in the path of a wide X-ray beam so that it casts an 'X-ray shadow image' on an X-ray sensitive detector array. This is repeated for different angles, either by rotating the sample itself or rotating the source and detector around the sample. The sequence of shadow images is then virtually 'back-projected' onto the imaged volume, resulting in a stack of virtual tomographical slices through the sample. Mathematically, this stack of images is represented by a 3D matrix where the value of each element is a measure for the amount of X-ray energy that was absorbed in the voxel that corresponds to the element.

In five of the six remaining chapters of this thesis,  $\mu$ CT was used as a tool to obtain geometrical information of middle ear samples. For chapters 3, 5, 6, and 7, the data is all originating from the same set of samples that was measured in the  $\mu$ CT setup of the UGCT facility at Ghent University (Masschaele, 2007). For Chapter 4, a commercial desktop system was used: model Skyscan 1172 micro CT scanner (Bruker, Kontich, Belgium), located at the Vrije Universiteit Brussel (VUB).

## 5. Overview of part II of this dissertation

Chapter 3 covers an elaborate study of multiple aspects of ME morphology. Six human ME samples were scanned using micro-CT and these scans were converted into three-dimensional geometrical models of the various components of the middle ear. Both the original  $\mu$ CT images and the 3D models were used to investigate morphological aspects such as the presence of ME ligaments, the dimensions and inertia parameters of the ossicles, and the thickness of various ME components.

Chapter 4 describes a study about the connection between the TM and the malleus, or the tympano-malleolar connection. This connection was poorly documented in literature, and the current study casts new light on the actual shape and inter-individual variation of this peculiar middle ear feature. The main tool of this study was  $\mu$ CT, but it was complemented with histology in order to investigate the presence and configuration of different tissue types in and around the tympano-malleolar connection.



## Chapter 3. Details of Human Middle Ear Morphology based on Micro-CT Imaging of Phosphotungstic Acid Stained Samples

---

### Abstract

A multitude of morphological aspects of the human middle ear (ME) were studied qualitatively and/or quantitatively through the post-processing and interpretation of micro-CT (micro X-ray computed tomography) data of six human temporal bones. The samples were scanned after phosphotungstic acid (PTA) staining to enhance soft-tissue contrast. The influence of this staining on ME ossicle configuration was shown to be insignificant. Through post-processing, the image data were converted into surface models, after which the approaches diverged depending on the topics of interest. The studied topics were: the ME ligaments; morphometric and mechanical parameters of the ossicles relating to inertia and the ossicular lever arm ratio; the morphology of the distal incus; the contact surface areas of the tympanic membrane and of the stapes footplate; and the thickness of the tympanic membrane, round window of the cochlea, ossicle joint spaces and stapedia annular ligament. Some of the resulting insights are relevant in ongoing discussions concerning ME morphology and mechanical functions, while other results provide quantitative data to add to existing data. All findings are discussed in the light of other published data and many are relevant for the construction of mechanical finite element simulations of the ME.

*Major contributions to the finalizing of the segmentation, post processing and analysis of the data, performing literature studies, and the writing of the paper.*

*This chapter was published in: De Greef, D., Buytaert, J.A.N., Aerts, J.R.M., Van Hoorebeke, L., Dierick, M., Dirckx, J., 2015. Details of human middle ear morphology based on micro-CT imaging of phosphotungstic acid stained samples. J. Morphol. 276, 1025–46. doi:10.1002/jmor.20392*

## 1. Introduction

The mammalian middle ear (ME) conducts acoustic signals entering the external ear to the cochlea in the inner ear. Through various mechanisms, the ME collects and amplifies the pressure of the incident sound waves before transmitting them to the cochlea, in order to match the acoustic impedances of outside air and cochlea fluid. Human ME morphology has been a focal point in otologic research in the past and the present (e.g. (Kirikae, 1960; Fleischer, 1978; Gulya and Schuknecht, 1995; Hemila et al., 1995)). However, there still remain a number of topics where no consensus has been reached, either in terms of shape, volume, point of attachment, spatial coordinates, material properties, inter-individual variability or even tissue type. The challenge of fully understanding ME functionality is made considerably more difficult by the presence of many different tissue types, both generic and specialized, in the ME, and their delicate interfaces and interactions.

Knowledge on ME morphology is especially relevant for two otologic fields of study. First, it is important for the construction of highly realistic finite element models (FE models) of ME mechanics, a research branch that is very popular in the field (Funnell and Laszlo, 1978; Funnell and Medical, 1983; Williams and Lesser, 1990; Wada et al., 1992; Kelly et al., 2003; Fay et al., 2006; Gan et al., 2006, 2009; Wang et al., 2007; Hoffstetter et al., 2010; Gentil et al., 2014a; Volandri et al., 2011, 2012; Gentil et al., 2011; Aernouts et al., 2012b; Böhnke et al., 2013; Muyschondt et al., 2014; De Greef et al., 2014, i.e. Chapter 5 of this thesis; Gan and Wang, 2014). Secondly, new data and statistical knowledge about these structures are of direct relevance to the field of otologic surgery, for example for surgical interventions or for the implantation of hearing aids.

The present work covers a range of topics in ME morphology, studied through micro-CT measurements of six stained human samples. The study of each topic serves one of the two

following purposes: either it brings clarification to a topic which has been a subject of confusion, inconsistency and debate in the past; or it confirms or at least adds to quantitative data and properties on a topic about which a consensus already exists but can benefit from additional numerical data. Each of the topics has a subsection in 'Materials and methods', 'Results', and 'Discussion'. The research questions of the topics are:

- What is the influence of the PTA (phosphotungstic acid) staining on the angles of the incudomalleolar joint and the incudostapedial joint?
- ME ligaments: how many do exist; what is their prevalence, location of attachment, thickness and apparent/presumed importance?
- Ossicle parameters and dimensions: what are the total volume and mass of each ossicle; what are the (relative) volume, mass and mechanical influence of the intertrabecular spaces of the ossicles; what are the coordinates of the center of mass, the values of the principal moments of inertia and the directions of the principal axis of rotation of the ossicles; what is the efficiency of rotation of the incudomalleolar complex around the classic anatomical axis, defined by the tip of the anterior process of the malleus and the posterior tip of the short process of the incus; what are the values of the ossicular lever arm lengths and other important morphometric dimensions?
- Morphology of the distal incus: what is the nature and what are the dimensions of the pedicle (also sometimes called strut or stem) of the lenticular process at the distal end of the incus; is there a 4th ossicle?
- Surface area of the tympanic membrane (TM) and the stapes footplate: what are the values for TM and footplate surface areas as well as their ratio, i.e. the hydraulic ratio of the ME?
- What are the thicknesses of the TM, ossicle joints, stapedial annular ligament and the round window of the cochlea?

## 2. Method

### 2.1 PTA-stained Micro-CT

Six fresh human temporal bone samples were obtained from Cochlear Technology Centre Belgium. The temporal bones were separated from the cadaver within 48h post mortem and frozen immediately afterwards. After transportation, the temporal bones were defrosted and further reduced using a saw, surgical scissors and a dental drill in size to allow for an optimal scanning resolution. The resulting samples were approximately 25 x 25 x 25 mm<sup>3</sup>. While middle and inner ear structures were kept intact during these manipulations, mastoid cell damage was unavoidable to sufficiently reduce the sample size. The samples were then preserved in a 4 wt. % solution of formaldehyde in water (formol) until further transportation.

A first micro-CT scan - without contrast-enhancement through staining - of all samples was made at the Centre for X-ray Tomography of the Ghent University (UGCT) facility (Masschaele et al., 2007). Before the scans, the samples were rinsed by submerging them for a short time in a 100 % saline solution. During scanning, the samples were not submerged in a liquid but were kept in a closed plastic container with a layer of water at the bottom to provide atmospheric saturation, as a measure to minimize tissue dehydration effects during the scan. For each sample, scanning parameters were iteratively optimized to maximize image quality for segmentation purposes. For this, UGCT relies on an in-house developed evaluation tool that calculates X-ray transmissions based on Monte-Carlo simulations of the X-ray source and detector, for different inputs like sample size and composition, kV setting, filtration etc. (Masschaele et al., 2007). The resulting dataset of the scans had an isotropic voxel pitch of 22.8  $\mu\text{m}$  (samples 1, 3-6) and 18.5  $\mu\text{m}$  (sample 2).

For the second scan, contrast-enhancing staining was applied using phosphotungstic acid (PTA) to enhance the visibility of soft tissue structures in the samples. One opening of approximately 4x4 mm<sup>2</sup> was drilled in the tympanic cavity wall of each sample and the samples were submerged in a 3 wt. % solution of PTA in water. For a short period of time, the PTA-solution with the submerged sample was kept in a decreased pressure environment, to allow air to escape from the middle ear cavity through the opening and thereby enable an optimal penetration of the PTA-solution in the middle ear cavity. Then, the sample was kept for 48 hours in the solution to obtain sufficient absorption of the staining agent by the soft tissue middle ear structures. Afterwards, the samples were rinsed in saline once more, with the purpose of extracting any excessively absorbed staining agent. Finally, the samples were scanned again at the UGCT facility.

## 2.2 Segmentation

After 2D-reconstruction of the micro-CT scans, every dataset was segmented using Amira® 5.3 (FEI Visualization Sciences Group, Hillsboro, Oregon, USA). This was performed using a combination of automatic and manual segmentation tools. A first distinction between separate structures was made by threshold-based region growing starting from a user-defined point. However, despite the sample staining, this semi-automatic segmentation technique proved insufficient to detect all boundaries between components, especially between adjacent soft-tissue structures. Significant manual input and sometimes a-priori knowledge of the ME anatomy was required in order to distinguish all structures. Therefore, in a second stage, all cross-sections were visually inspected and improved with manual and semi-automatic segmentation tools and algorithms such as paint brush, hole-filling, interpolation etc. The segmentation process resulted for each dataset in a 'label' dataset with the same dimensions as the 3D CT image-stack, containing for each voxel the anatomical structure that was assigned to it by the operator. For most post-processing purposes, the label data needed to be converted into geometrical surface models, described by a number of contiguous triangles, through a triangulating, surface generating algorithm in Amira®.

## 2.3 Approach per Topic

After acquiring the micro-CT data and performing the image segmentation, the next analytical steps were determined by the different studied topics, depending on the respective goal and research question. This section describes the strategic approach per topic.

### 2.3.1 Topic I: Influence of PTA on Ossicle Configuration

If the used PTA staining alters the spatial configuration of the ossicles significantly and systematically, the relevance of most other results in this study could be questioned. Therefore, all samples were scanned by means of micro-CT before and after PTA staining. In the datasets without staining, soft tissue structures were difficult to distinguish, as for example can be seen in Figure 3-1. Therefore, only the bony ossicles (malleus, incus and stapes) of the ME could be segmented confidently in the unstained datasets. After conversion into surface models, the two incudes of the datasets before and after staining were aligned based on a minimal surface distance algorithm (see Amira<sup>®</sup> documentation), so that the difference in spatial position of the incus is almost zero between the datasets. Then, using Amira<sup>®</sup> software tools, two 3D angles were determined, to quantify the angle change in the incudomalleolar joint (IMJ) and the incudostapedial joint (ISJ) respectively. First, the angle  $\alpha = \widehat{ABC}$  was measured, in which A and C are the most inferior points of the malleus in the 'before' and 'after' dataset, respectively, and B the central point of articulation in the IMJ. The determination of point B is somewhat subjective, but careful attention was paid to choosing it consistently. Second, the angle  $\beta = \widehat{DEF}$  was measured, in which D and F are points on the stapes footplate in the 'before' and 'after' dataset, respectively, and E the central point of articulation in the ISJ, which is easier to determine compared to point B due to the simpler shape of the ISJ. Points D and F are defined as the outer point of the medial surface of the stapes footplate in the direction of maximal rotation between the 'before' and 'after' datasets. Figure 3-2 presents an example of the measurements of these angles in one sample. Furthermore, we observed the dominant axes and direction of rotation and categorized them into anatomical axes and directions, to ascertain whether these properties are consistent, regardless of the magnitude of the angles.

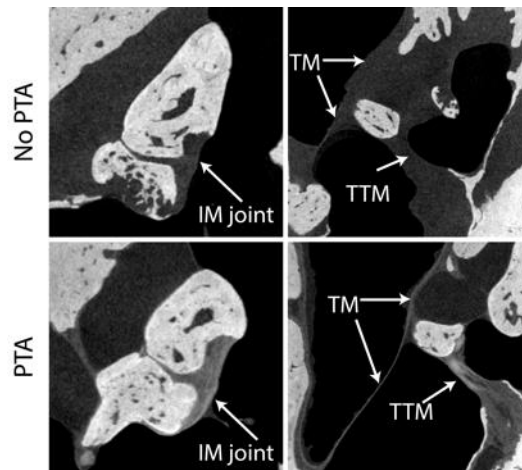


Figure 3-1: Comparison of soft-tissue contrast on  $\mu$ CT images of the same temporal bone sample (sample 1) before and after PTA staining. Slices are in slightly different orientations because the sample was removed from the scanning stage between the scans. Also note the improved contrast between tissue and fluid that is in contact with the tissue in the PTA-stained images. IM joint: Incudomalleal joint; TM: Tympanic membrane; TTM: Tensor tympani muscle.

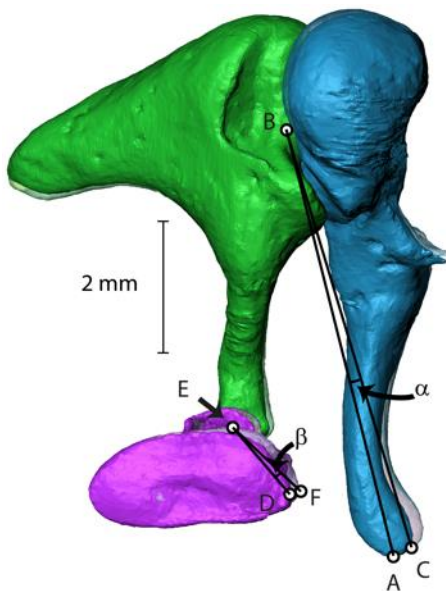


Figure 3-2: Influence of PTA-staining on the ossicle configuration of sample 1. This figure is in isometric perspective for a better appreciation of distances. This sample showed overall the largest deformation of all samples. The opaque ossicles represent the dataset before staining and the transparent ossicles represent the dataset after staining. Points A, B and C define angle  $\alpha$  and points D, E and F define angle  $\beta$ , as described in section 2.3.1, which represent the ossicular joint angle change between the datasets.

### 2.3.2 Topic II: Middle Ear Ligaments

We aimed to identify the different ligaments in each ME sample and determine their prevalence, starting and attachment points and runway direction. Specific remarks on the individual ligaments were noted. The assessment of the presence of different ligaments was performed by interpreting the virtual 2D slices and by visualizing the data using a 3D rendering

method in Amira®. This mode visualizes the CT image stack by assigning transparency to each voxel depending on its gray value. The thresholds for maximal and minimal transparency can be adjusted. This way, the often difficult-to-distinguish ligaments could be detected, identified and evaluated at the aforementioned criteria.

### 2.3.3 Topic III: Ossicle Parameters and Dimensions

The obtained data are perfectly suitable to evaluate multiple earlier studied parameters of the ME ossicles. For this purpose, a rigidly defined coordinate system *needed* to be chosen and applied consistently. The coordinate system chosen for this work is visualized in Figure 3-4. The origin is located at the most inferior point of the malleus (= the umbo). The y-axis runs superiorly, the z-axis medially and the x-axis posteriorly. Therefore, the coordinate system is either right-handed (for a right ear) or left-handed (for a left ear). The orientation of the xy-plane is determined to be parallel to the plane of the annular ligament.

Starting from the 3D surface models, created as explained in section 2.2, we determined the volumes of the ossicles and their intertrabecular spaces (defined below), as well as the ratio of intertrabecular space volumes to ossicle volumes; mechanical parameters such as the mass, the center of mass (COM), the principal moments of inertia (PMI) and the principal axes of rotation (PAR); and spatial dimensions such as those defining the ossicle lever arm ratio, but also other dimensions that are often mentioned in literature.

The ossicles are no solid bodies, but contain internal blood vessels (Kirikae, 1960) and cavities containing connective tissue, for example at the distal end of the long process of the incus (Karmody et al., 2009). From here on, we will refer to both these inhomogeneities as the “intertrabecular spaces” of the ossicles. The influence of these lower-density spaces on mechanical parameters such as COM, PMIs and PARs has not been quantitatively assessed yet. Therefore, we have separated the bony parts from the non-bony intertrabecular spaces during segmentation, and have calculated all mechanical parameters for two different cases:

1. Homogeneous ossicles: the mass density for intertrabecular spaces was equal to bone and the homogeneous ossicle densities were based on literature values of total ossicle densities.
2. Inhomogeneous ossicles: the intertrabecular spaces were assigned a lower mass density, based on literature values for soft tissue and blood, while the mass density of the bone was increased to make the total mass of the ossicles equal to case 1.

To test for significant differences in results between density cases 1 and 2, a non-parametric repeated measures test, the Wilcoxon signed rank test, was applied. Statistical significance is assumed when  $p < 0.05$ .

For our calculations, average mass density values of 2.31 g/ml and 2.14 g/ml for the malleus and the incus bone, including intertrabecular spaces, respectively were taken from Sim and Puria (2008). For the stapes, the average mass density of 2.20 g/ml was taken from Zhao et al. (2009).

The intertrabecular spaces were assigned a density value of 1.06 g/ml (Harley et al., 1977; Cutnell and Johnson, 1999; Joseph et al., 1999; Alexander, 2003). For a discussion and motivation of these values, we refer to the ‘Discussion’ section.

**Calculation of the mechanical parameters** – In order to calculate different mechanical parameters, the surface models of the ossicles were converted to volume models, constructed of tetrahedral volume elements using a native Amira® algorithm. This allowed the assignment of different mass density values to the different structures. The coordinates of the tetrahedral meshes were imported in Matlab (MATLAB Release 2012b, The MathWorks, Inc., Natick, Massachusetts, United States), where subsequent calculations resulted in values for the following parameters:

- volume and mass of the bony ossicle and the intertrabecular spaces,
- COMs of the entire ossicles, comprising bone and intertrabecular spaces,
- PMIs of the entire ossicles, absolute and relative to individual mass density, and
- PARs of the entire ossicles.

The inertia parameters of each structure were determined through the following steps

- Translation of the origin to the COM of the studied structure.
- Calculation of the individual moments of inertia  $I_{x_i x_i, k}$  and products of inertia  $I_{x_i x_j, k}$  of all elements through the following equations:

$$I_{x_i x_i, k} = m_k \cdot d_{x_i, k}^2, \quad \text{Eq. 3-1}$$

$$I_{x_i x_j, k} = m_k \cdot d_{x_i, k} \cdot d_{x_j, k}, \quad \text{Eq. 3-2}$$

where  $m_k$  denotes the mass of element  $k$  and  $d_{x_i, k}$  the perpendicular distance of element  $k$  to axis  $x_i = x, y$  or  $z$ .

- Construction of the inertia matrix  $[I_{x_i x_j}] = [\sum_k I_{x_i x_j, k}]$ .
- Calculation of the eigenvalues and eigenvectors of the inertia matrix by diagonalization of the matrix. The PMIs are the eigenvalues, the PARs are the eigenvectors.

In addition to the separate ossicles, the algorithms were performed on the incudomalleal complex (IMC), including the malleus and the incus, their intertrabecular spaces and the IMJ tissue. The IMJ tissue was assigned the same density value as the intertrabecular spaces, as it mainly consists of collagen, cartilage and synovial fluids. Besides the calculation of the PMIs, the following parameters were calculated as well:

- $I_{\text{tot}}$ : the total moment of inertia of the IMC for rotation around its anatomical rotation axis (which is classically defined as the axis connecting the tips of the anterior process of the malleus and the short process of the incus); calculated numerically;

- $I_{AnAx-COM}$ : the moment of inertia of a point particle with mass  $m_{IMC}$  and located at the COM of the IMC, for rotation around the anatomical axis; calculated using  $I_{AnAx-COM} = m_{IMC} \cdot d_{AnAx-COM}^2$ , with  $d_{AnAx-COM}$  the perpendicular distance from the COM to the anatomical axis.

Finally, the ratio  $r_{eff} = I_{AnAx-COM}/I_{tot}$  and the relative frequency shift  $\Delta f_n = \sqrt{\frac{I_{tot} - I_{AnAx-COM}}{I_{tot}}} - 1$  were calculated. The interpretations of these values are elaborated in the Discussion of the paper. The intention of these calculations was to determine the degree of efficiency loss and natural frequency alteration due to misalignment of the COM of the IMC away from the anatomical axis (Fleischer, 1978).

**Ossicle dimensions** – Three groups of ossicle dimension measurements were performed. For a visual indication of all measurement locations, see Figure 3-3.

- First, the classic lever arm ratio of the IMC was assessed. To this end, the coordinates of four anatomical points were measured: the inferior tip of the malleus (A), the middle point of the distal plate of the lenticular process of the incus (B), the tip of the anterior malleal process (C) and the tip of the short process of the incus (D). Points C and D define the classic anatomical axis of rotation of the IMC, while points A and B represent the end points of the ossicles when they are considered as lever arms. These points are indicated by squares and the anatomical axis by a dashed line in Figure 3-3. Then the perpendicular distances from points A ( $d_{1,ax}$ ) and B ( $d_{2,ax}$ ) to the anatomical axis were calculated using the following formula (for point A):

$$d = \frac{|(\mathbf{A} - \mathbf{C}) \times (\mathbf{A} - \mathbf{D})|}{|\mathbf{D} - \mathbf{C}|}, \quad \text{Eq. 3-3}$$

where the bold symbols represent the vector notation of the coordinates of the points. The formula for the distance from point B to the axis was analogous.

In order to compare this method to the suggested method in (Hemila et al., 1995), the following measurements were performed as well:

- $d_{1,IMJ}$ : the distance from the inferior tip of the malleus (A') to the center point of the IMJ (C');
- $d_{2,IMJ}$ : the distance from the inferior tip of the incus (B') to the same IMJ point (C').

These points are represented by circles in Figure 3-3.

- Secondly, multiple relevant ossicle dimension measurements as defined by Kirikae (1960) have been repeated on the new data:
  - Malleus: the length of the neck and the head (K<sub>1</sub>) and the length of the manubrium (K<sub>2</sub>);
  - Incus: the short process length (K<sub>3</sub>) and the length from the tip of the short process to the tip of the long process (K<sub>4</sub>);

- Stapes: its height (K5) and the long (K6) and short diameter (K7) of the stapes footplate.

These distances are indicated by solid lines ending in asterisks (\*) in Figure 3-3.

- Thirdly, three ossicle lengths that are relevant according to Ars (1977) were reproduced: The distance from the manubrium tip (point X) to the inferior point of the IMJ (point Y); from the middle of the lenticular process of the incus (point Z) to point Y; and from point X to point Z. These points are denoted by triangles in Figure 3-3.

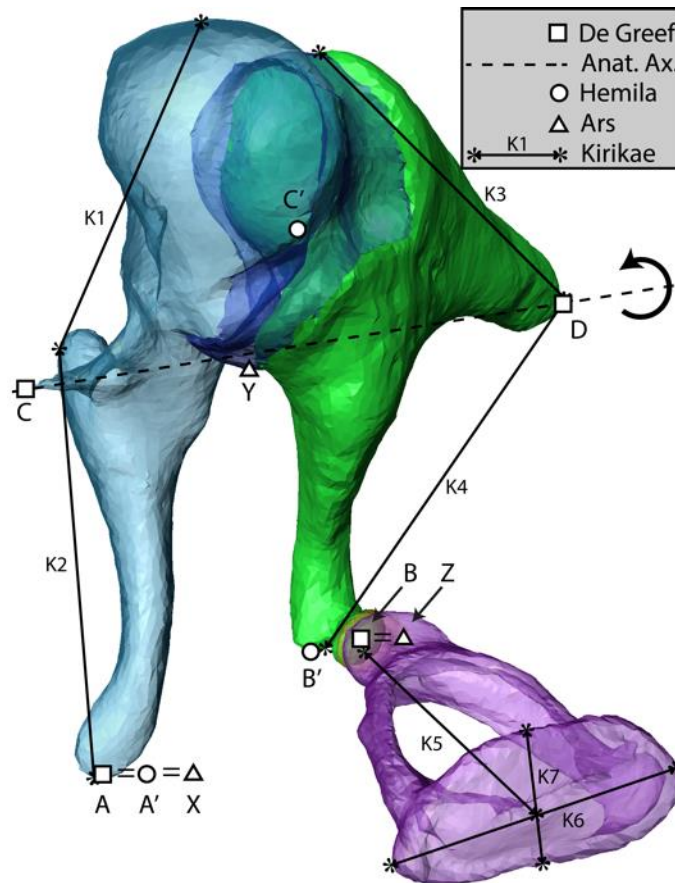


Figure 3-3: Illustration of all measured ossicle dimensions. For detailed descriptions, see text section 2.3.3. Data from sample 2.

#### 2.3.4 Topic IV: Morphology of the Distal Incus

The distal part of the incus includes three distinct bony components that are surrounded by soft tissue: 1. the long process of the incus that runs inferiorly from the body of the incus; 2. a thin lateral-medial bony connection (referred to as pedicle); and 3. an oval shaped disk perpendicular to the lateral-medial direction. The long lasting confusion regarding these features, as well as their relevance, will be discussed in section 4.2.4. During the segmentation we have distinguished between the bony core of the incus and the surrounding soft tissue, including collagen, joint tissue and blood vessels. As consistent as possible, the anterior-posterior width of the bony pedicle at its narrowest and widest point, and the superior-inferior

thickness of the pedicle have been measured in each sample. These measurements were performed on the 3D surface models.

### 2.3.5 Topic V: TM and stapes footplate Areas

Using the high-resolution 3D surface models that were constructed in this work, it was possible to determine both the area of the lateral surface of the TM's pars tensa and the of the medial surface of the stapes footplate (SFP) with a good accuracy. To assess the influence of different possible approaches, the areas were calculated in three different ways:

1. The ellipse approximation: The short and long diameters ( $a$  and  $b$ ) of both TM and SFP were measured in Amira® and the subsequent ellipse surface was calculated through  $S_{\text{ell}} = \pi ab/4$ .
2. 2D projection: The surface area of the conical TM is approximated by the surface area of the 2D projection of the lateral TM surface onto the plane that is defined by the tympanic annulus. The slightly irregular medial surface of the SFP was projected onto the plane defined by the annular ligament. The areas were calculated through a pixel counting technique in Matlab.
3. 3D surface: The real surface area was calculated, taking into account the curvature and irregularities of the surfaces. This was performed using a native algorithm of Amira®, based on the triangulated surface models.

All measurements of the TM surface area were performed on the pars tensa only, as the pars flaccida is believed to have little to no contribution to sound collection (Rosowski, 1994).

### 2.3.6 Topic VI: Thickness of Different Structures

The segmented voxel data of the TM was subjected to the 'Shortest distance' thickness algorithm as described in Van der Jeught et al. (2013), and a possible correlation between the resulting mean thickness of the TM and the inferior-superior length of the TM was calculated, as suggested in Van der Jeught et al. (2013) as well.

For three other structures we could determine relevant thickness values as well: the ossicle joint gaps, the stapedia annular ligament and the round window of the cochlea. The thickness of the joints corresponds to the gap between the ossicles, while the SAL thickness corresponds to the gap between the SFP and the cochlea bone. These three structures, however, feature more irregular shapes than the TM and are therefore unsuited for application of any of the automated algorithms of Van der Jeught et al. (2013). A native thickness calculation of Amira® was applied and the minimal thickness, maximal thickness and the locations of both were manually measured on the surface models.

### 3. Results

Figure 3-1 illustrates the difference in soft-tissue contrast on  $\mu$ CT images of the same temporal bone sample between pre- and post-stained samples for different ME structures. Figure 3-4 provides an overview of the entire ME surface model for one of our samples. For clarity reasons, not all ligaments are included in the figure and some structures are depicted transparently. In general, to summarize results for all six samples, we provide the average and corrected standard deviation as statistical parameters. The uncertainty for length measurements on the data is equal to the voxel size of  $20\ \mu\text{m}$ . If the standard deviation of a set of measurements is smaller than this individual measurement error, we mention the individual error as uncertainty intervals in the text.

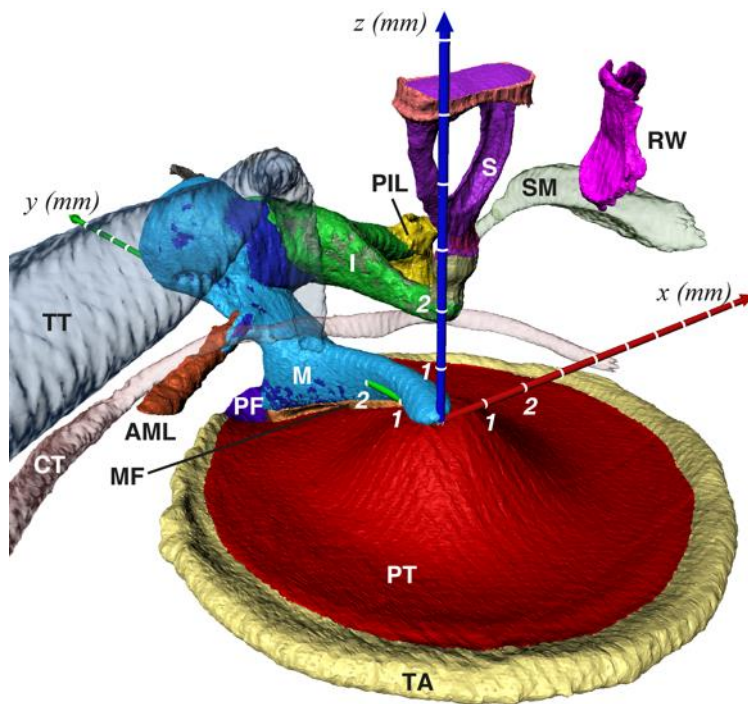


Figure 3-4: Overview of the entire ME surface model of sample 2. Not all ligaments and mucosal folds are shown, for reasons of clarity. The abbreviations represent: PT: Pars tensa of the TM; PF: Pars flaccida of the TM; TA: Tympanic annulus; M: Malleus; I: Incus; S: Stapes; TT: Tensor tympani & tendon; SM: Stapedius muscle & tendon; MF: Manubrial fold; AML: anterior malleolar ligament; PIL: posterior incudal ligament; CT: Chorda tympani; RW: Round window of the cochlea;

#### 3.1 Topic I: Effect of PTA on Ossicle Configuration

Table 3-1 presents the results of the manual measurement of the incudomalleolar joint (IMJ) angle change ( $\alpha = \widehat{ABC}$ ) and incudostapedial joint (ISJ) angle change ( $\beta = \widehat{DEF}$ ), as explained in section 2.3.1, as well as their categorized axis of rotation and the direction of positive rotation. For both angles  $\alpha$  and  $\beta$ , only the magnitude of the angles are reported, while their sign is

communicated through the direction of rotation. The measurement error for every angle measurement was estimated to be  $0.2^\circ$ , being the largest difference between multiple independent repetitions of the same measurement. It is apparent that for both joints, neither a consistent axis nor direction of rotation is found, with only a slight favor for rotation towards inferior around the anterior-posterior axis for the ISJ. The mean rotation magnitude (independent from the axis or direction) for the IMJ is  $(1.10 \pm 0.67)^\circ$  and for the ISJ is  $(1.3 \pm 1.0)^\circ$ . Furthermore, observed angle changes are never larger than  $3.0^\circ$ . Figure 3-2 gives a visual impression of the magnitude of the ossicle rotation. The presented model is sample 1, for which the angle changes in the IMJ and the ISJ are respectively  $2.1^\circ$  and  $1.9^\circ$ , two of the three largest angle changes in our dataset. For this figure, like for the angle measurements, the incudes of both datasets are aligned as well as possible.

Table 3-1: Influence of PTA staining on ossicle configuration.  $\alpha$  and  $\beta$  represent the angle changes in the IMJ and ISJ, respectively, between micro-CT measurements before and after staining and have measurement errors of  $0.2^\circ$ . For easy interpretation, the axes and direction of rotation are categorized into anatomical axes and directions.

	Incudomalleal joint			Incudostapedial joint		
	$\alpha$ ( $^\circ$ ) *	axis	direction	$\beta$ ( $^\circ$ ) *	axis	direction
<b>Sample1</b>	2,1	lat-med	ant	1,9	sup-inf	ant
<b>Sample2</b>	0,8	lat-med	post	0,0	-	-
<b>Sample3</b>	1,8	lat-med	ant	1,3	ant-post	inf
<b>Sample4</b>	0,5	ant-post	lat	0,6	ant-post	inf
<b>Sample5</b>	0,7	ant-post	lat	1,1	ant-post	inf
<b>Sample6</b>	0,7	ant-post	lat	3,0	ant-post	inf
<b>Mean (<math>^\circ</math>)</b>	1,10			1,3		
<b>St. dev. (<math>^\circ</math>)</b>	0,67			1,0		

\*  $\pm 0,2^\circ$

## 3.2 Topic II: Middle Ear Ligaments

### 3.2.1 General observations

One general observation is the difficulty to identify some of the ligaments, because all ligaments are embedded in and bordered by larger mucosal folds and strands that envelope all structures in the ME (Gulya and Schuknecht, 1995). Hence, multiple spaces in the ME are formed, such as Prussak's space, the interior incudal space, and the anterior and posterior pouches of von Troeltsch (Sanjay et al., 2012). Figure 3-5 provides an impression of the mucosal folds around the ossicles and their ligaments. We have identified structures as being ligaments only if they were clearly distinguishable and had a higher gray value on the CT slices than other soft tissue structures surrounding the ossicles. All other ambiguous strands and folds of tissue were identified as mucosa strands.

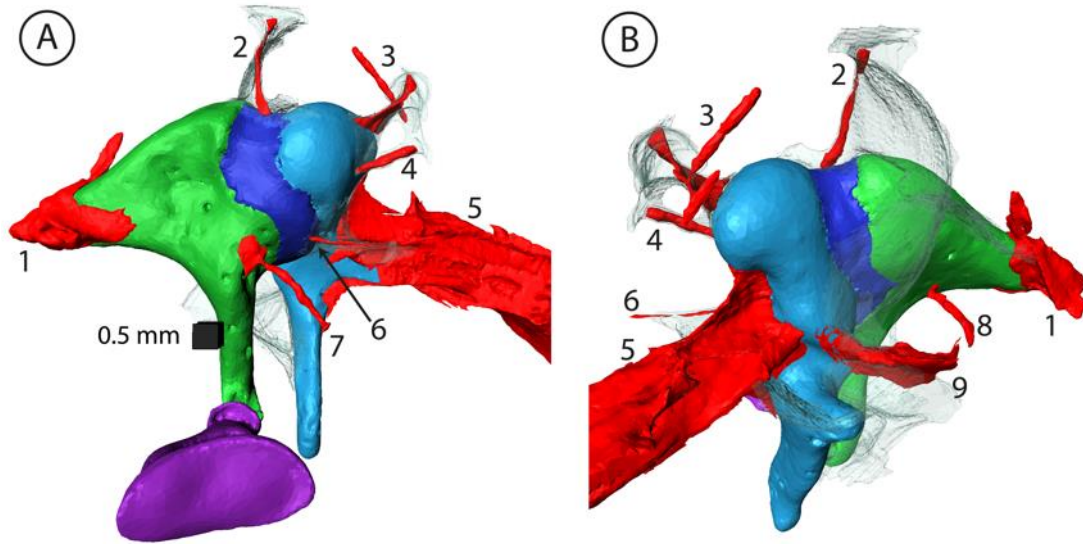


Figure 3-5: Mucosal folds and strands surrounding the ME ossicles and ligaments in sample 4. A. Medial view. B. Latero-superior view. Structures identified as ligaments are red and opaque, mucosa is transparent. The AML is not shown to its full extent to limit the size of the figure. The numbered ligaments are (for abbreviations see table 1 or 3): 1. PIL; 2. P-SML; 3. A-SML; 4. S-AML; 5. AML; 6. M-AML; 7. MIL; 8. LIL; 9. LML. Notice that, in this sample, both the P-SML (2) and the M-AML (6) attach to the IMJ, rather than to the malleus.

Table 3-2 summarizes our findings for all observed ME ligaments, including their starting and attachment points, runway direction and ligament-specific remarks in the footnotes.

Sample 5 had remarkably many deviations from the other samples in terms of ligaments. Some floating bone shards were observed in the ME cavity, suggesting a fractural trauma in the temporal bone, which could explain the absence of some ligaments that were found in the other samples.

### 3.2.2 Observed irregularities for specific ligaments

The structure that has been named posterior malleal ligament (PML) was never confidently interpreted as a ligament, but rather as mucosal strands and folds. There was however consistency in its appearance (observed in all 6 samples) and we acknowledge probable confusion when observing this structure in surgical circumstances. The same remark of possible confusion is valid for the superior anterior malleal ligament (S-AML) (prevalence of 1/6).

Two ligaments had remarkable variation in attachment point to the ossicular chain: the posterior superior malleal ligament (P-SML) and the medial anterior malleal ligament (M-AML). Both ligaments attach to the malleus surface in some samples, blend with the capsule of the IMJ in others, and exhibit a combination in yet other samples. This could very well be another source of confusion in nomenclature between different authors. The P-SML could also be named the superior incudomalleal ligament, similar for the M-AML, which could be identified as an anterior incudomalleal ligament.

Table 3-2: Properties of all observed ligaments or mucosa structures that could be confused with ligaments

	Ligament	Abbrev.	Prevalence	Origin	Attachment	Direction	Remarks
Malleus	Anterior	AML	6/6 (100 %)	Ant. proc. and neck of the mall.	PTF wall	Ant	Very thick and long; Only partially attaches to the PTF wall and then runs through beyond our dataset limits.
	Medial anterior	M-AML	5/6 (83 %)	Ant. surface of mallear head and/or IMJ capsule; medially to AML	Mastoid bone	Ant-med(-inf)	Very thin; Can also originate from the IMJ capsule with partial or full attachment
	Superior anterior	S-AML	1/6 (17 %)	Ant. surface of mallear head; superior to AML	Cavity wall	Ant-sup	In literature also referred to as anterior suspensory mallear ligament (Gulya and Schuknecht, 1995; Mikhael, 2005)
	Lateral	LML	6/6 (100 %)	Neck of the malleus	Cavity wall	Lat-post	Sometimes connects to PML and/or CT at the point of attachment.
	Posterior	PML	6/6 (100 %)	Posterior side of manubrium	Cavity wall	Post	Difficult to distinguish between mucosa and ligament; Passes very closely to CT (laterally), often making contact to it.
	Anterior superior	A-SML	3/6 (50 %)	Sup-ant. surface of mallear head	Cavity wall	Ant-sup	Surrounded by mucosa.
	Posterior superior	P-SML	5/6 (83 %)	Sup-post-med. surface of mallear head and/or sup. IMJ cap	Cavity wall	Sup-post-med	Can also originate from the IMJ capsule with partial or full attachment; Could easily be confused with a IM ligament in some samples.
	Medial	MIML	1/6 (17 %)	Med. side of IMJ cap	Mastoid bone/cav. wall	Med	Splits into 3 branches, 2 running to the mastoid bone and 1 to the cavity wall
	Posterior	PIL	6/6 (100 %)	Med. and lat. side of short process of the incus	Cavity wall	Med OR Lat	Consists of two distinct but connected portions: medial and lateral
	Medial	MIL	3/6 (50 %)	Med. side of the upper part of the long process of the incus	Cavity wall	Med OR Med-ant-sup	Very thin; One instance of a ligament starting on the short process of the incus.
Incus	Lateral	LIL	5/6 (83 %)	Lat. side of the middle part of the long process of the incus	CT	Lat	Very short; One instance with two branches.
	Superior	SSL	1/6 (17 %)	Sup-ant. side of stapes head	Cochlea bone	Sup-ant	Very thin; at the opposite side of the stapedius muscle tendon (attached posteriorly to the stapes head)

Two ligaments were only seen in one sample (not the same sample): the superior anterior malleolar ligament (S-AML) and the superior stapedial ligament (SSL). For an impression of the SSL, see Figure 3-6.

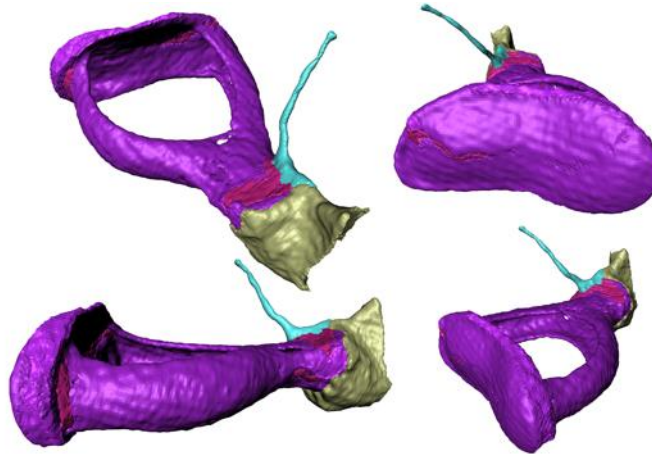


Figure 3-6: Different views of the superior stapedial ligament (thin, light green structure) sample 5.

### 3.3 Topic III: Ossicle Parameters and Dimensions

Table 3-3 presents all results for the mechanical parameters of the ossicles using the inhomogeneous density case (case 2 as defined in section 2.3.3), while Table 3-4 presents the principal moments of inertia (PMI) for the homogeneous density case (case 1). In both tables, statistical differences between cases 1 and 2 for the PMI are indicated by an asterisk (\*). Although the differences between mean PMI are small compared to the standard deviation, the Wilcoxon signed-rank test, taking into account the “matched-pairs” nature of the datasets, reveals significant differences in 5 out of 9 cases. Figure 3-7 provides an impression of the intertrabecular spaces present in the ossicles.

The naming of the principal axes of rotation (PAR) directions in Table 3-3 as ant-post (anterior-posterior), sup-inf (superior-inferior) and lat-med (lateral-medial) is an approximation and is no substitute for the vector notation, but facilitates interpretation of the results.

In Table 3-5, the same information for the incudomalleolar complex is shown (also calculated using density case 2), added by the results of the calculations to assess the influence of the IMC’s center of mass misalignment away from the anatomical rotation axis.

Table 3-3: Mechanical properties of the ossicle bones, using density case 2 (inhomogeneous ossicles). Density values are derived from literature (Sim and Puria, 2008; Zhao et al., 2009); all other values were calculated in this study. The coordinates are relative to the coordinate system described in section 2.3.3. For the principal moments of inertia, statistical differences between density cases 1 (homogeneous) and 2 (inhomogeneous), calculated using the Wilcoxon signed-rank test, are indicated by an asterisk (\*). In the second lower row, approximated directions for the principal axes of rotations are given to facilitate interpretation.

	Malleus			Incus			Stapes		
<b>Density [<math>10^3 \text{ kg/m}^3</math>]</b>									
$\sigma_{\text{bone}}$	2,50			2,25			2,27		
$\sigma_{\text{soft}}$	1,06			1,06			1,06		
<b>Volume [<math>\text{mm}^3</math>]</b>									
$V_{\text{bone}}$	$11,3 \pm 1,4$			$12,28 \pm 0,90$			$1,14 \pm 0,11$		
$V_{\text{soft}}$	$0,57 \pm 0,48$			$0,80 \pm 0,42$			$0,105 \pm 0,050$		
$V_{\text{tot}}$	$11,9 \pm 1,4$			$13,1 \pm 1,1$			$1,24 \pm 0,13$		
$V_{\text{soft}}/V_{\text{tot}}$	$(4,8 \pm 4,1) \%$			$(6,0 \pm 2,9) \%$			$(8,4 \pm 3,6) \%$		
<b>Mass [mg]</b>									
$m_{\text{bone}}$	$26,9 \pm 3,2$			$27,1 \pm 2,1$			$2,62 \pm 0,26$		
$m_{\text{soft}}$	$0,60 \pm 0,51$			$0,85 \pm 0,44$			$0,110 \pm 0,050$		
$m_{\text{tot}}$	$27,5 \pm 3,2$			$28,0 \pm 2,4$			$2,73 \pm 0,28$		
$m_{\text{soft}}/m_{\text{tot}}$	$(2,2 \pm 1,9) \%$			$(3,0 \pm 1,4) \%$			$(4,0 \pm 1,7) \%$		
<b>Center of mass [mm]</b>									
x	$-0,18 \pm 0,19$			$1,95 \pm 0,24$			$1,63 \pm 0,21$		
y	$5,33 \pm 0,23$			$5,89 \pm 0,49$			$1,27 \pm 0,41$		
z	$0,47 \pm 0,42$			$0,87 \pm 0,31$			$3,38 \pm 0,40$		
<b>Principal moments of inertia</b>									
$I_1$ [ $\text{mg}\cdot\text{mm}^2$ ]	$15,0 \pm 3,4$ *			$31,7 \pm 5,4$ *			$1,88 \pm 0,27$ *		
$I_2$ [ $\text{mg}\cdot\text{mm}^2$ ]	$97 \pm 21$			$49,0 \pm 6,3$			$3,98 \pm 0,48$ *		
$I_3$ [ $\text{mg}\cdot\text{mm}^2$ ]	$102 \pm 23$			$72,1 \pm 7,1$			$5,38 \pm 0,70$ *		
$I_1/I_3$ []	$(15,0 \pm 2,3) \%$			$(43,8 \pm 5,1) \%$			$(35,0 \pm 2,0) \%$		
$I_2/I_3$ []	$(95,2 \pm 1,2) \%$			$(68,0 \pm 5,3) \%$			$(74,0 \pm 1,0) \%$		
$I_1/\sigma$ [ $\text{mm}^5$ ]	$6,5 \pm 1,5$			$14,8 \pm 2,5$			$0,86 \pm 0,12$		
$I_2/\sigma$ [ $\text{mm}^5$ ]	$41,8 \pm 9,0$			$22,9 \pm 3,0$			$1,81 \pm 0,22$		
$I_3/\sigma$ [ $\text{mm}^5$ ]	$44,0 \pm 9,9$			$33,7 \pm 3,3$			$2,45 \pm 0,32$		
<b>Principal axes of rotation</b>									
	<b>Ax<sub>1</sub></b>	<b>Ax<sub>2</sub></b>	<b>Ax<sub>3</sub></b>	<b>Ax<sub>1</sub></b>	<b>Ax<sub>2</sub></b>	<b>Ax<sub>3</sub></b>	<b>Ax<sub>1</sub></b>	<b>Ax<sub>2</sub></b>	<b>Ax<sub>3</sub></b>
x [mm]	-0,10	0,14	-0,98	0,11	0,97	0,09	-0,08	0,99	-0,05
y [mm]	0,93	-0,33	-0,14	0,98	-0,11	0,03	-0,17	0,03	0,98
z [mm]	0,34	0,93	0,10	-0,04	-0,09	0,99	0,98	0,09	0,17
Approx. dir.	sup- inf	lat- med	ant- post	sup- inf	ant- post	lat- med	lat- med	ant- post	sup- inf
PMI ratio	15%	95%	100%	44%	68%	100%	35%	74%	100%

Table 3-4: PMI results for the ossicles for density case 1 (homogeneous ossicles). Statistical differences between density cases 1 and 2 (inhomogeneous ossicles), calculated using the Wilcoxon signed-rank test, are indicated by an asterisk (\*).

	<b>Malleus</b>	<b>Incus</b>	<b>Stapes</b>
<b>I<sub>1</sub> [mg.mm<sup>2</sup>]</b>	14,9 ± 3,4 *	31,1 ± 5,1 *	1,82 ± 0,26 *
<b>I<sub>2</sub> [mg.mm<sup>2</sup>]</b>	95 ± 20	50,7 ± 6,9	4,13 ± 0,54 *
<b>I<sub>3</sub> [mg.mm<sup>2</sup>]</b>	100 ± 22	73,3 ± 8,3	5,49 ± 0,72 *

\*:  $p < 0,05$  for comparison between density cases 1 (homogeneous ossicles) and 2 (inhomogeneous ossicles)

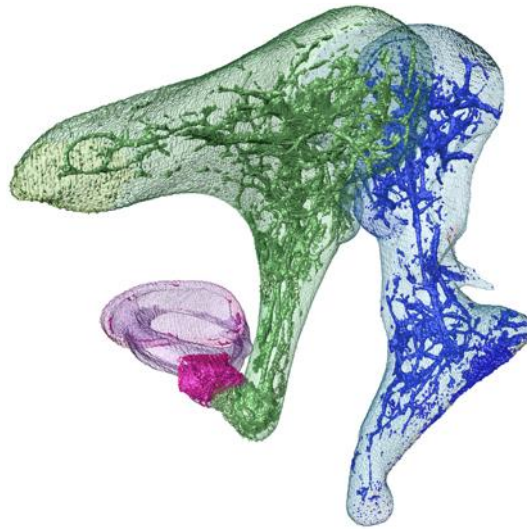


Figure 3-7: Distribution of lower-density intertrabecular spaces inside the ossicles of sample 4. Bone is transparent. Fluid-filled or soft tissue-filled parts are opaque.

Table 3-6 shows the results from the measurements of the ossicular lever arm lengths, as well as the other ossicle dimension measurements as described in section 2.3.3 and results from various other authors. The result for the lever arm ratio defined by the perpendicular distances from the umbo and the IS joint to the anatomical rotation axis induce a SPL increase of  $(2.28 \pm 0.61)$  dB.

### 3.4 Topic IV: Morphology of the Distal Incus

Figure 3-8 shows an example of minimum and maximum width measurements of the pedicle width on sample 6. The results of the width ( $w_{min}$  and  $w_{max}$ ) and thickness ( $d$ ) measurements on the pedicles on all measurements are shown in Table 3-7, as well as a description of their shapes. Both the pedicle's dimensions and shapes feature large inter-individual differences. Besides inconsistent, pedicle shapes are very irregular as well. To give an impression of the irregularity and inconsistency, Figure 3-9 presents superior views of the pedicles in all samples.

Table 3-5: Mechanical properties of the incudomalleal complex, using lower density values for the intertrabecular spaces and the IMJ. Density values are derived from literature (Sim and Puria, 2008; Zhao et al., 2009); all other values are derived from our new data. All coordinates are relative to the coordinate system described in section 2.3.III and depicted in Figure 3-4. In the second lower row, approximated directions for the principal axes of rotations are given to facilitate interpretation.

Density [ $10^3 \text{ kg/m}^3$ ]		Principal moments of inertia			
$\sigma_{\text{malleus}}$	2,50	$I_1$ [ $\text{mg}\cdot\text{mm}^2$ ]	$114 \pm 10$		
$\sigma_{\text{incus}}$	2,25	$I_2$ [ $\text{mg}\cdot\text{mm}^2$ ]	$163 \pm 32$		
	1,06	$I_3$ [ $\text{mg}\cdot\text{mm}^2$ ]	$237 \pm 32$		
Volume [ $\text{mm}^3$ ]		$I_1/I_3$ []	$0,485 \pm 0,039$		
$V_{\text{malleus}}$	$11,3 \pm 1,4$	$I_2/I_3$ []	$0,682 \pm 0,057$		
$V_{\text{incus}}$	$12,28 \pm 0,91$	$I_1/\sigma$ [ $\text{mm}^5$ ]	$53,2 \pm 4,7$		
$V_{\text{joint}}$	$1,68 \pm 0,29$	$I_2/\sigma$ [ $\text{mm}^5$ ]	$76 \pm 15$		
$V_{\text{mall\_can}}$	$0,58 \pm 0,46$	$I_3/\sigma$ [ $\text{mm}^5$ ]	$110 \pm 15$		
$V_{\text{inc\_can}}$	$0,80 \pm 0,40$	Principal axes of rotation			
$V_{\text{tot}}$	$26,7 \pm 2,4$		$Ax_1$	$Ax_2$	$Ax_3$
$V_{\text{soft}}/V_{\text{bone}}$ []	$11,4 \% \pm 3,4 \%$	x [mm]	0,29	0,95	-0,04
Mass [mg]		y [mm]	0,92	-0,28	-0,24
$m_{\text{malleus}}$	$26,9 \pm 3,2$	z [mm]	0,24	-0,03	0,97
$m_{\text{incus}}$	$27,2 \pm 2,1$	Approx. direction	sup-inf	ant-post	lat-med
$m_{\text{joint}}$	$1,78 \pm 0,31$	MOI ratio	49%	68%	100%
$m_{\text{mall\_can}}$	$0,62 \pm 0,49$	COM misalignment effect			
$m_{\text{inc\_can}}$	$0,85 \pm 0,42$	COM-AnAx [mm]	$1,31 \pm 0,19$		
$m_{\text{tot}}$	$57,3 \pm 5,3$	$I_{\text{AnAx\_COM}}$ [ $\text{mg}\cdot\text{mm}^2$ ]	$99 \pm 28$		
$m_{\text{soft}}/m_{\text{tot}}$ []	$5,6 \% \pm 1,7 \%$	$I_{\text{tot}}$ [ $\text{mg}\cdot\text{mm}^2$ ]	$265 \pm 48$		
		$r_{\text{eff}} = I_{\text{AnAx\_COM}}/I_{\text{tot}}$	$(37,1 \pm 6,8) \%$		
		$\Delta f_n$	$(-20,8 \pm 4,3) \%$		

There was in every sample, however, at least one uninterrupted bony connection between the long process of the incus and the lenticular process, even if only a few pixels wide or thick. In none of the samples, the bony pedicle was completely interrupted. Based on their observed high X-ray absorption, the pedicles all consist of either bone or dense calcified cartilage.

Table 3-6: Ossicle dimensions from our data and from various published sources. A dash (-) between two values denotes the range of values, rather than an uncertainty interval. Otherwise, a sole dash represents absent data. An asterisk (\*) indicates data that does not overlap our data. References: (Kirikae, 1960; Ars, 1977; Anson and Donaldson, 1981; Hemila et al., 1995; Gan et al., 2002; Sim et al., 2013; Todd and Creighton, 2013; Quam et al., 2014).

Dimension	Fig. 3-3 mark	De Greef	Kirikae 60	Hemila 95	Ars 78	Anson 81	Unur 02	Gan 02	Todd 13	Sim 13	Quam 14
$d_{1,ax}$ [mm]	A - AnAx	4,47 ± 0,30	-	-	-	-	-	-	-	-	-
$d_{2,ax}$ [mm]	B - AnAx	3,45 ± 0,15	-	-	-	-	-	-	-	-	-
$d_{1,ax}/d_{2,ax}$ []	/	1,30 ± 0,11	-	-	-	-	-	-	-	-	-
$d_{1,IMJ}$ [mm]	A' - C'	6,28 ± 0,36	-	6,24	-	-	-	-	-	-	-
$d_{2,IMJ}$ [mm]	B' - C'	4,83 ± 0,14	-	4,46*	-	-	-	-	-	-	-
$d_{1,IMJ}/d_{2,IMJ}$ []	/	1,30 ± 0,10	-	1,40	-	-	-	-	-	-	-
Malleus head + neck [mm]	K1	4,74 ± 0,29	5,0 ± 0,1	-	-	-	4,85 ± 0,29	-	4,9 ± 0,3	-	-
Malleus manubrium [mm]	K2	4,98 ± 0,39	4,51 ± 0,08*	-	-	4,33 - 5,67	4,70 ± 0,45	4,20*	4,8 ± 0,4	-	4,94 ± 0,31
Incus short proc length [mm]	K3	5,35 ± 0,21	4,81 ± 0,07*	-	-	-	4,88 ± 0,47	4,49*	5,0 ± 0,3	-	5,07 ± 0,37
Incus short to long proc [mm]	K4	5,73 ± 0,16	5,99 ± 0,08*	-	-	-	6,12 ± 0,43	-	5,9 ± 0,4	-	-
Stapes height [mm]	K5	3,37 ± 0,14	3,29 ± 0,15	-	-	-	3,22 ± 0,31	2,87*	-	3,28 ± 0,210	3,44 ± 0,20
SFP long diameter [mm]	K6	2,73 ± 0,10	2,96 ± 0,15	2,99*	-	2,64 - 3,36	2,57 ± 0,33	2,5*	-	2,81 ± 0,158	2,94 ± 0,14
SFP short diameter [mm]	K7	1,306 ± 0,086	1,33 ± 0,11	1,27	-	1,08 - 1,66	1,29 ± 0,22	1,38	-	1,27 ± 0,109	1,39 ± 0,10
Ars XY [mm]	X - Y	4,68 ± 0,34	4,65 ± 0,09	-	4,5 ± 0,5	-	-	-	-	-	-
Ars YZ [mm]	Y - Z	3,19 ± 0,21	-	-	3,1 ± 0,5	-	-	-	-	-	-
Ars XZ [mm]	A - Z	2,81 ± 0,48	-	-	2,5 ± 0,5	-	-	-	-	-	-

\* Ranges not overlapping our data

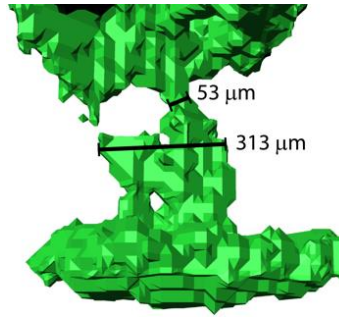


Figure 3-8: Example of a measurement of the minimal and maximal width of the bony pedicle at the lenticular process of the incus in sample 6. The measurement unit is  $\mu\text{m}$ . The precision of the measurement is obviously not  $0.01 \mu\text{m}$  but  $20 \mu\text{m}$ .

Table 3-7: Properties of the bony pedicle of incudal the lenticular process in all samples. We measured the minimal ( $w_{\min}$ ) and maximal width ( $w_{\max}$ ) (both in anterior-posterior direction), and the thickness ( $d$ ) (in superior-inferior direction). Furthermore, a qualitative description of the appearance of the bony connection is provided.

Sample	$w_{\min} \pm 20 (\mu\text{m})$	$w_{\max} \pm 20 (\mu\text{m})$	$d \pm 20 (\mu\text{m})$	Description of appearance
1	246	338	53	Single connection; multiple holes
2	81	387	55	Single connection; irregular, twisted shape
3	260	319	62	Single connection; 1 large hole
4	351	395	50	Single connection; 1 small hole
5	461	559	48	Three equivalent parts
6	53	313	55	1 true connection; 1 very thin/interrupted
<b>Mean</b>	<b>242</b>	<b>385</b>	<b>53,8</b>	
<b>St. Dev.</b>	<b>156</b>	<b>92</b>	<b>4,8</b>	

### 3.5 Topic V: TM and stapes footplate Areas

The results of all operations described in section 2.3.5 are listed in Table 3-8. The uncertainty values for the surface areas and ratio obtained using the ellipse approximation originate from the individual error on the length measurements, which is chosen equal to the voxel size, and are calculated through error propagation. These values are slightly different for each sample but equal after rounding.

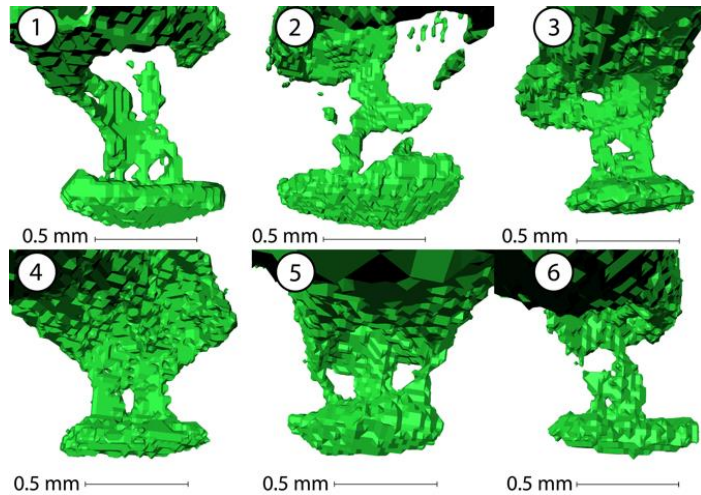


Figure 3-9: Superior views of the incudal lenticular processes of all samples. All scale bars represent 0.5 mm. The views are in perspective but the scale bars are always in the plane of the pedicle of the lenticular process.

Table 3-8: Surface areas of both the pars tensa of the TM and the SFP, using three different approaches, as well as the derived hydraulic area ratio for all samples and methods.

Sample	TM surface area (mm <sup>2</sup> )			SFP surface area (mm <sup>2</sup> )			Hydraulic Ratio			
	Ellipse*	2D Proj	3D Surf	Ellipse**	2D Proj	3D Surf	Ellipse***	2D Proj	3D Surf	
1	64,12	66,0	71,4	2,87	3,15	3,37	22,3	21,0	21,2	
2	64,45	65,9	69,8	2,84	3,08	3,21	22,7	21,4	21,7	
3	55,64	58,1	63,0	2,69	2,85	3,06	20,7	20,3	20,6	
4	57,94	60,0	64,8	3,14	3,29	3,55	18,4	18,2	18,3	
5	45,22	47,3	56,0	2,59	3,04	3,31	17,5	15,6	16,9	
6	58,20	59,4	68,5	2,67	2,84	3,06	21,8	20,9	22,4	
<S>	57,6	59,4	65,6	2,80	3,04	3,26	<R>	20,6	19,6	20,2
$\sigma_s$	7,0	6,9	5,6	0,20	0,17	0,19	$\sigma_R$	2,1	2,3	2,1

\*  $\pm 0,06 \text{ mm}^2$

\*\*  $\pm 0,02 \text{ mm}^2$

\*\*\*  $\pm 0,4$

The results for the hydraulic ratio induce a SPL increase of  $(26.26 \pm 0.91) \text{ dB}$ ,  $(25.83 \pm 1.00) \text{ dB}$  and  $(26.10 \pm 0.71) \text{ dB}$ , for the ellipse, 2D projection and 3D surface methods respectively.

When compared one-to-one, all mutual differences between the three different surface area estimation methods are statistically significant ( $p < 0.05$ ; tested using the Wilcoxon signed-rank test) for the TM surface area, stapes footplate (SFP) surface area and hydraulic ratio. The sole exception is the difference between the hydraulic ratio calculated through either the Ellipse method (for both TM and SFP) or the 3D surface method ( $p = 0.2188$ ).

Conversion factors to convert the surface area, obtained by means of the ellipse ( $S_{\text{ell}}$ ) or 3D surface ( $S_{3\text{D}}$ ) method, to the 2D projected surface area ( $S_{2\text{D}}$ ) were calculated:

- TM
  - $S_{2\text{D}}/S_{\text{ell}} = (103.3 \pm 1.0)\%$
  - $S_{2\text{D}}/S_{3\text{D}} = (90.4 \pm 4.0)\%$
- SFP
  - $S_{2\text{D}}/S_{\text{ell}} = (108.8 \pm 4.6)\%$
  - $S_{2\text{D}}/S_{3\text{D}} = (93.3 \pm 1.4)\%$

These numbers allow authors with different surface data to easily compare or convert their numbers to projected surface areas.

### 3.6 Topic VI: Thicknesses of Different Structures

Application of the ‘shortest distance’ algorithm on the current TM datasets resulted in six thickness maps, one of which is shown in Figure 3-10. The mean thickness  $\langle d \rangle$  over the entire pars tensa, excluding the tympanic annulus and the part of the TM that is connected to the manubrium (similar to Van der Jeught et al. (2013)) was calculated for every sample and was on average  $(81 \pm 18) \mu\text{m}$ , ranging from  $(59 \pm 35) \mu\text{m}$  to  $(106 \pm 35) \mu\text{m}$ . The thickness distribution of the different samples did not suggest a consistent local thickening of the membrane in certain quadrants, and the correlation between the mean TM thickness  $\langle d \rangle$  and the inferior-superior length  $l_{\text{inf-sup}}$  of the TM was insignificant at  $R^2 = 0.0037$ , both in contrast to Van der Jeught et al. (2013). Table 3-9 presents the individual values of these parameters.

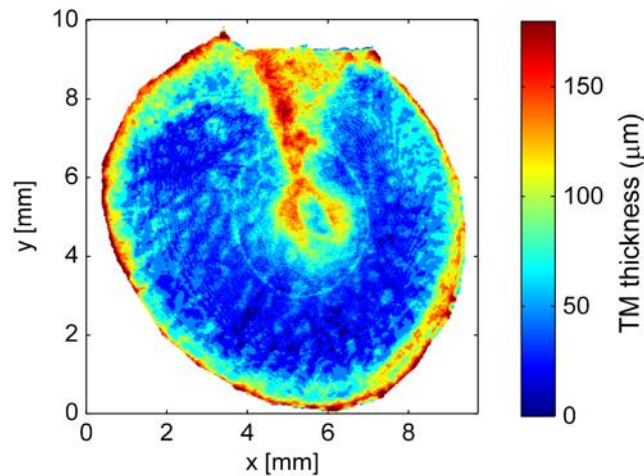


Figure 3-10: Thickness distribution of the TM of sample 2. Thickness values were calculated using the ‘Shortest distance’ algorithm from Van der Jeught et al. (2013).

Table 3-9: Average thickness ( $d$ ) and inferior-superior length of the pars tensa of the TM in all samples. The standard deviation for each individual sample represents the variation of thickness over the entire pars tensa surface.

Sample	$\langle d \rangle$ ( $\mu\text{m}$ )	$\sigma_d$ ( $\mu\text{m}$ )	$l_{\text{inf-sup}}$ (mm) *
1	59	35	9,09
2	93	32	9,34
3	91	31	8,15
4	106	35	8,42
5	66	29	8,00
6	73	39	8,75
<b>Mean</b>	81		8,62
<b>StDev</b>	18		0,53

\*  $\pm 0,02$  mm

To study the thickness of the IMJ, a distinction was made between the consistent excessively thick bulge at the medio-superior part of the joint and the remaining part of the IMJ. For this remaining part, minimum and maximum thicknesses were located and measured. For the ISJ, minimum and maximum thicknesses were recorded as well. The same approach was used for the stapedial annular ligament (SAL) and the round window of the cochlea (RW). All results are given in Table 3-10 (IMJ and ISJ) and Table 3-11 (SAL and RW). In sample 6, the RW was ruptured; hence no data are available for said sample. An impression of the thickness datasets of these four structures is presented in Figure 3-11.

Table 3-10: Minimal and maximal local thicknesses  $d$  of the IMJ and ISJ, as well as the locations of the minimal and maximal thicknesses for all samples. Furthermore, the thickness of the excessive bulge of the IMJ, that is located medio-superiorly, is presented.

Sample	Incudomalleal joint						Incudostapedial joint			
	Mimumum		Maximum		Bulge		Mimumum		Maximum	
	$d$ ( $\mu\text{m}$ ) *	Loc	$d$ ( $\mu\text{m}$ ) *	Loc	$d$ ( $\mu\text{m}$ ) *	Loc	$d$ ( $\mu\text{m}$ ) *	Loc	$d$ ( $\mu\text{m}$ ) *	Loc
1	30	lat	230	inf	1000	med-sup	75	multi	145	post
2	30	lat-sup	240	multi	1150	med-sup	90	sup	190	post
3	30	lat	240	multi	900	med-sup	80	ant	120	post-inf
4	30	lat-sup	250	sup	950	med-sup	75	multi	130	sup
5	40	multi	230	mid	950	med-sup	80	ant-inf	240	post-sup
6	50	lat	220	mid	950	med-sup	70	multi	150	post-sup
<b>Mean</b>	35,0		235		983		78,3		163	
<b>StDev</b>	8,4		10		88		6,8		45	

\*  $\pm 20$   $\mu\text{m}$

Table 3-11: Minimal and maximal local thicknesses  $d$  of the SAL and RW, as well as the locations of the minimal and maximal thicknesses for all samples.

Sample	Stapedial annular ligament				Round window of the cochlea			
	Miminum		Maximum		Miminum		Maximum	
	$d$ ( $\mu\text{m}$ ) *	Loc	$d$ ( $\mu\text{m}$ ) *	Loc	$d$ ( $\mu\text{m}$ ) *	Loc	$d$ ( $\mu\text{m}$ ) *	Loc
1	0	multi	340	ant	45	sup-lat	250	med
2	13	multi	280	ant-inf	35	lat	235	lat-sup
3	0	multi	210	ant-inf	75	mid	260	mid
4	22	multi	330	ant	60	ant-inf	170	ant-inf
5	0	multi	230	ant-inf	60	multi	190	med
6	0	multi	350	ant	N/A	N/A	N/A	N/A
Mean	5,8		290		55		221	
StDev	9,5		60		15		39	

\*  $\pm 20 \mu\text{m}$

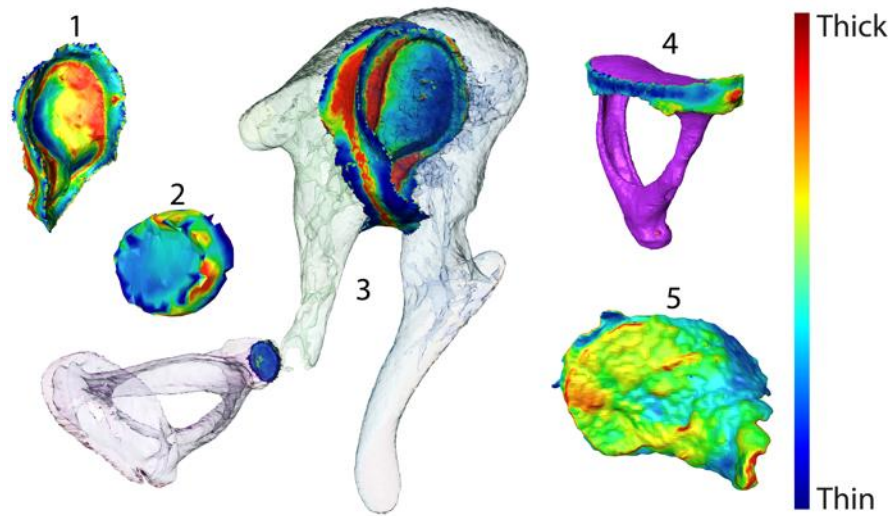


Figure 3-11: Examples of thickness distributions of 1. IMJ; 2. ISJ; 4. SAL attached to the stapes; and 5. RW of the cochlea. Subfigure 3 presents IMJ and ISJ data inserted in the entire ossicular chain with transparent ossicles. The different structures are not in their correct relative spatial positions. The color map limits are different for different structures; all extreme values are listed in Table 3-10 and Table 3-11. Data for 1,2 and 4 are from sample 4. Data for 3 from sample 1. Data for 5 are from sample 3.

## 4. Discussion

### 4.1 Method considerations

Middle ear anatomy is described in many different standard textbooks, in more or less detail. Data are mainly based either on direct visual observation under the microscope or on histologic sections. 3D representations are mainly hand-made drawings to explain the principles of the structure, but such drawings do not contain numerical detail. As an example we refer to the standard work by Anson and Donaldson (1981), where fig. III-35 gives a detailed drawing of the ossicular chain, indicating the place of attachment or position of multiple ME ligaments and muscles.

#### *4.1.1 Contrast-enhanced micro-CT as morphological imaging technique*

Below, the advantages and disadvantages of micro-CT compared to other options for studying ME morphology (surgery, histology, magnetic resonance imaging (MRI), light sheet fluorescence microscopy (LSFM) (Buytaert et al., 2010) and optical coherence tomography (OCT) (Van der Jeught et al., 2013)) are listed. The reason for choosing stained micro-CT for this study is the combination of the mentioned benefits and the fact that our research lab has plenty of experience using the technique.

Advantages:

- Non-contact (in contrast to surgery);
- Non-destructive (i.c.t. histology);
- Easy alignment of different sections (i.c.t. histology);
- No need for bone decalcification (i.c.t. histology);
- Isotropic voxel dimensions (i.c.t. MRI and histology);
- Higher imaging resolution than MRI;
- Imaging of visually unavailable structures with great penetration depth (i.c.t. OCT);
- Bone imaging without intensive and aggressive refractive index manipulation (i.c.t. LSFM);

Disadvantages:

- No in-vivo measurements (i.c.t. surgery and clinical CT);
- No tangible feedback during examination (i.c.t. surgery and ex-vivo dissection);
- Worse specificity for soft-tissue than histology, optical microscopy, MRI and LSFM;
- Staining required (i.c.t. surgery, optical microscope, MRI, OCT);
- Less imaging options than MRI (cfr. different sequences);
- Lower spatial resolution than histology, OCT and LSFM ;

- Longer scan time (increasing the risk of tissue deformation during measurement) than LSFM, which can be performed in real-time;
- Harmful radiation (for the operator), thus extensive safety measures required.

#### 4.1.2 Segmentation operator bias

It has been argued during many review processes in the past that manual segmentation provides results that could be significantly dependent on the operator's subjective input. The influence of the operator on segmentation results has been quantified in Buytaert et al. (2014). The study concluded that the results of a manual segmentation process are only marginally dependent on the operator and that inter-operator repeatability is more than satisfactory, provided that good a-priori guidelines were agreed upon by the different operators.

## 4.2 Interpretation of Results and Comparison to Literature

### 4.2.1 Topic I: Influence of PTA on Ossicle Configuration

Potential tissue alteration caused by staining agents is a topic that should not be neglected in studies that rely on or provide new morphometric data. In Buytaert et al. (2014), the influence of different staining agents, including phosphotungstic acid (PTA), on the volume of different tissue types was investigated. The study concluded that PTA results in the least amount of shrinkage of the studied staining agents: bone exhibits even a negative volume shrinkage of  $(-1.3 \pm 3.9) \%$  (i.e. volume increase) after applying PTA staining, indicating a marginal effect; muscle tissue exhibits significant average volume shrinkage of  $(10.4 \pm 2.6) \%$  (i.e. linear shrinkage of 3.6%) after applying PTA staining.

From the results of the current study (see Table 3-1), it is clear that the influence of the applied staining procedure on the ossicle configuration is very small and that the small alterations do not appear in a systematic manner. Indeed, the measured joint angle changes appear in different directions for different samples. Therefore, we can assume that other results of this study that use the spatial locations of the ossicles are not systematically altered in the same manner by the application of a staining agent, despite the fact that non-negligible soft-tissue shrinkage might have occurred, as investigated and shown in Buytaert et al. (2014).

### 4.2.2 Topic II: Middle Ear Ligaments

For the interpretation of the many abbreviations in this section, we refer the reader to Table 3-2. Our findings confirm that there are various possible sources of confusion and misinterpretation in identifying ME ligaments:

- Many mucosal strands could be easily interpreted as ligaments, and vice versa; this could be the case for the M-AML, the MIL (medial incudal ligament) and the SSL;
- Some ligaments (P-SML and M-AML) had remarkable variation in attachment point to the ossicular chain.

We hope to clear some of the confusion by a close comparison of similar ligaments in all of our samples and a subsequent application of a consistent nomenclature (see Table 3-2).

In the context of middle ear morphology, the anterior malleolar ligament (AML) is often treated as a single structure, attaching to the anterior process of the malleus and disappearing in the petrotympanic fissure. In literature on temporomandibular morphology, however, there is mention of two ligaments that originate from the temporomandibular joint region, travel through the petrotympanic fissure and finally attach to the anterior side of the malleus: the discomalleolar ligament (DML) and a separated branch of the sphenomandibular ligament (SpML) (Kim et al., 2004; Sencimen et al., 2008). The DML connects the malleus to the articular disc of the temporomandibular joint (Cheynet et al., 2003; Kim et al., 2004; Rowicki and Zakrzewska, 2006; Sencimen et al., 2008). The tympanic branch of the SpML, after passing through the petrotympanic fissure, is continuous with the sphenomandibular ligament (Sencimen et al., 2008). In 60-80% of the cases, these two ligaments are merged at the point of attachment to the malleus (Kim et al., 2004; Sencimen et al., 2008), which explains why they are often treated as one ligament in middle ear morphology and mechanics. Both ligaments pass through the petrotympanic fissure and are partially attached to it, limiting their influence on ossicular motion significantly. Only the tympanic branch of the SpML has been observed to induce observable motion in the ossicular chain after overstretching, which is denied for the DML in multiple studies (Kim et al., 2004; Sencimen et al., 2008).

In our micro-CT datasets, the distinction between the DML and the temporal branch of the SpML is not visible at their attachment to the malleus, although the attachment base surface of the combined structure is significantly larger than that of other ligaments, which is consistent with its compound nature. Anterior to the malleus, the combined structure enters the petrotympanic fissure, in which a thin bony wall is observed, that divides the petrotympanic fissure into two unequal compartments and through which the two ligaments separately run. In Figure 3-5, the combined shape of the DML and the tympanic branch of the SpML is captured by a single structure labeled AML.

The other most prominent ligament is the PIL. Together with the AML, the PIL defines the classic anatomical axis of ossicular rotation. Given their thickness and consistency in comparison to the other ME ligaments, we can only confirm their morphologic importance. However, we do not make any claims regarding ossicular motion, as this topic is indeed a debated subject (Cai et al., 2010; Puria and Steele, 2010), certainly at higher frequencies, and addressing of this topic should be reserved for dedicated papers.

It is debatable how important all the other ME ligaments are in terms of ossicular mechanics, given their limited thickness, inconsistent presence and attachment points, and the difficulty to distinguish them from the surrounding mucosal folds and strands. These mucosal folds, however, are sufficiently apparent, numerous and generally large (see Figure 3-5), to suggest that they could have a significant suspensory role in addition to their assumed contribution to

ME gas exchange (Marcusohn et al., 2010) and blood supply to the ossicles (Sim and Puria, 2008).

The identification of the PML as mucosal folds attaching partially to the chorda tympani agrees with Gulya and Schuknecht (1995) in that they call it the posterior malleal fold, which envelopes the chorda tympani.

We plead for a consistent nomenclature of all observed ME ligaments. This could be debatable for the M-AML and the P-SML, as they attach partially or even fully to the capsule of the IMJ in some samples. We propose to name them ‘malleal ligament’ despite this variation in location of attachment so that a clear communication of these structures is facilitated in future literature. Two incudomalleal joint (IMJ) ligaments have been mentioned before (Gulya and Schuknecht, 1995; Lemmerling et al., 1997), namely a medial and a lateral IMJ ligament. These names, however, referred to the medial and lateral portions of the capsule of the IMJ. These joint structures are not included in this topic, but were observed in all samples. However, in one of the samples (sample 1), a ligament was observed that is continuous with the medial portion of the capsule of the IMJ and attaches to the cavity wall and the mastoid bone. This ligament has been named the medial incudomalleal ligament (MIML) in Table 3-2. In order to know whether this is a reoccurring structure in the human ME or rather an anomaly in said single sample, more data is needed.

To the authors’ knowledge, no stapedial ligament, aside from the stapedial annular ligament (SAL), has ever been mentioned in literature. However, there was a clear thin ligamentous connection between the superior side of the stapes head and the cavity wall near the cochlea bone in one of the samples. The authors named it superior stapedial ligament (SSL) and regret to add yet another ligament to the already confusing list. The SAL is not covered in this topic, as it has a clearly different anatomic appearance and morphologic role than the other ME ligaments.

We did not identify a superior incudal ligament (SIL) in any of our samples, although this structure has been mentioned in literature (Federative Committee on Anatomical Terminology (FCAT), 1998; Mikhael, 2005). In Anson and Donaldson (1981) the PIL is described as “a fold of mucous membrane that descends from the tympanic roof to the body of the incus”. Such folds are indeed observed (see Figure 3-5), but were never identified as ligaments, and certainly not posterior but rather superior.

#### *4.2.3 Topic III: Ossicle Parameters and Dimensions*

In many current FE models of the ME, the ossicles are regarded as homogeneous structures with a single mass density value (Fay et al., 2006; Böhnke et al., 2013; De Greef et al., 2014b, i.e. Chapter 5 of this thesis). Sometimes different values are used for different parts of the ossicles, such as the arm, neck and head of the malleus (Kelly et al., 2003; Gan et al., 2006, 2009; Wang et al., 2007; Hoffstetter et al., 2010; Gentil et al., 2011, 2014a). However, the ossicles are not

completely solid, but contain internal blood vessels (Kirikae, 1960) and cavities containing connective tissue, for example at the distal end of the long process of the incus (Karmody et al., 2009). In this study, all non-bone tissue, as said earlier, was combined under the term ‘intertrabecular spaces’ and includes mostly blood vessels, but also collagen and cartilage, particularly at the distal end of the incus and at the head of the stapes (Chien et al., 2009; Karmody et al., 2009). Literature mentions the following mass density values for these materials:

- Blood: 1.06 g/ ml (Cutnell and Johnson, 1999)
- Cartilage: 1.05 g/ml (Joseph et al., 1999); 1.06–1.18 g/ml (Alexander, 2003)
- Collagen: 1.16 g/ml at 95% humidity (Harley et al., 1977)

As the exact contribution ratios of these tissue types in the ossicles were unknown, we have chosen to use 1.06 g/ml as mass density for all intertrabecular spaces in the calculations. This way, the density difference with bone and therefore the influence of the lower density regions was certainly not underestimated.

Our results indicate statistically significant differences for some of the principal moments of inertia (PMI) of the ossicles between density cases 1 (homogeneous ossicles) and 2 (inhomogeneous). However, this does not necessarily imply a relevant impact on ME mechanics, which is a question that needs to be addressed using other tools than the ones in the current study.

For multiple reasons, the incudomalleal complex is often treated as one mechanical unit. Fleischer (1978) points out that the alteration of the mass distribution of the incudomalleal complex (IMC) is an effective way to tune the natural frequency  $f_n$  of the system, because of the following relation:

$$f_n = \frac{1}{2\pi} \sqrt{\frac{K}{I_0 + m_{\text{IMC}} \cdot d_{\text{AnAx-COM}}^2}}, \quad \text{Eq. 3-4}$$

where  $K$  denotes the stiffness of the rotational axis and  $I_{\text{tot}}$  the total moment of inertia of the IMC for rotation around the anatomical axis. According to the parallel axis theorem,  $I_{\text{tot}}$  is the sum of:

- $I_0$ : the moment of inertia of the IMC around an axis parallel to the anatomical axis but through its COM; and
- $I_{\text{AnAx-COM}} = m_{\text{IMC}} \cdot d_{\text{AnAx-COM}}^2$ : as devined in section 2.3.3.

Therefore, by altering  $d_{\text{AnAx-COM}}^2$ , the natural frequency of the IMC can be effectively tuned to the species’ evolutionary needs (Fleischer, 1978). The relative change in natural frequency is given by:

$$\begin{aligned}\Delta f_n &= \frac{f_{\text{misaligned}} - f_{\text{aligned}}}{f_{\text{aligned}}} \\ &= \sqrt{\frac{I_0}{I_{\text{tot}}}} - 1\end{aligned}\tag{Eq. 3-5}$$

where  $f_{\text{aligned}}$  and  $f_{\text{misaligned}}$  denote the natural frequencies calculated using Eq. 3-4 for respectively  $d_{\text{AnAx-COM}} = 0$  and the average  $\langle d_{\text{AnAx-COM}} \rangle$ . The ratio  $r_{\text{eff}} = I_{\text{AnAx-COM}}/I_{\text{tot}}$  is a measure for the degree of efficiency loss due to the misalignment of the COM of the IMC with the anatomical rotation axis. A higher  $r_{\text{eff}}$  indicates a poorer efficiency for the rotation around the anatomical axis.

The results indicate that rotation around the anatomical rotation axis is not as efficient as it could be. If the IMC's COM would coincide with the anatomical axis, the moment of inertia would be  $(37 \pm 7)$  % smaller. This result supports the suggestion that at higher frequencies the 'hinge-like' motion of the IMC becomes very inefficient (Cai et al., 2010; Puria and Steele, 2010). At these frequencies, the IMC does not move as a rigid body, but rather as a system with a flexible joint whose motion is better described by a 'bevel gear' motion (Cai et al., 2010; Puria and Steele, 2010). Furthermore, the current data suggests that the natural frequency of the IMC gets a relative downward shift of  $(21 \pm 4)$  % due to the COM misalignment.

In Sim et al. (2007) the PMIs and principal axes of rotation (PAR) of the malleus, incus and IMC were determined through a similar method using micro-CT measurements. Their results for the PMIs are consistently slightly higher but the error bars of both studies overlap for all values. Notice that they used the standard error of the mean, which is by definition smaller than the corrected standard deviation, used in the current paper. Their determination of the PAR directions aligns with ours. They assumed the intertrabecular spaces to have the same mass density as water (i.e.  $1000 \text{ kg/m}^3$ ), and determined the density of bone by physically weighing the ossicles.

In Puria and Steele (2010), micro-CT was employed as well to obtain shape and inertia data of the three separate ossicles. For comparative reasons, PMI results were normalized to the average density of the bones. No uncertainty data were reported. After normalizing our data to the densities as well, results agree very well with the current data, apart from the middle ( $I_2$ ) and largest ( $I_3$ ) PMI of the malleus, which are significantly higher in our data. The PAR directions of the ossicles were categorized in the same manner as in the current study, and the result of this was equal to our conclusions.

The shapes of the IMC and the stapes were calculated in Weistenhöfer and Hudde (1999) by recording their silhouettes under multiple angles. Subsequently, the PMIs and PARs were derived. No uncertainty intervals are mentioned, and their results were outside of our uncertainty intervals for 3 out of 6 parameters:  $I_2$  and  $I_3$  of the stapes (both higher than ours)

and  $I_1$  of the IMC (lower than ours). Their determination of the PAR directions is consistent with ours.

Finally, in Sim et al. (2013) inertia data for the stapes were published which were very different from our results. PMI values are normalized to the stapes mass, and their results of 0.47 mm<sup>2</sup> for the malleus, 1.00 mm<sup>2</sup> for the incus and 1.35 mm<sup>2</sup> for the stapes are very different from our results of respectively 0.688 mm<sup>2</sup>, 1.457 mm<sup>2</sup> and 1.97 mm<sup>2</sup>, even when taking into account the uncertainty of approximately 10% for both data. Furthermore, the x-axis (ant-post) was identified as the axis with the largest PMI, followed by the y-axis (sup-inf), which is contradictory to our findings, as well as those of Weistenhöfer and Hudde (1999) and Puria and Steele (2010).

For most measured ossicle dimensions we found values which overlap values reported in literature (Table 3-6), although the match with Gan et al. (2002) is rather poor.

An interesting notion is that our ossicular lever arm length ratio of  $(1.3 \pm 0.1)$  with respect to the anatomical axis produces a result which is very similar to the approximated approach from Hemila et al. (1995). Furthermore, our data are consistent with the ossicular morphometric data from Ars (1977).

#### *4.2.4 Topic IV: Morphology of the Distal Incus*

The nature and properties of the lenticular process has been the topic of study and controversy in multiple papers. Asheron (1978) provides a historical overview of the many claims that have been made regarding the existence of a fourth ossicle, named os orbiculare (Asherson, 1978) or os lenticularis (Hoffstetter et al., 2011), that would consist of the bony disk, forming the lateral articulating surface of the incudostapedial joint (ISJ). Pal'chun and Magomedov (1997) reported an extensive study involving 40 incus samples from which was concluded that the lenticular process is a separate bone that is merely connected to the incus by a dense partially developed connective tissue. Chien et al. (2009) performed an even more extensive study, involving histology on 108 specimens, and disagreed fundamentally with Pal'chun and Magomedov (1997). Chien et al. (2009) attribute the different conclusions to discrepancies in tissue dissection, tissue embedding, orientation of the sections and tissue identification. The images of the freely available histologic image library at <http://otopathologynetwork.org/educational-resources/atlas/>, provided by the Massachusetts Eye and Ear Infirmary, suggest that the pedicle of the lenticular process mainly consists of cartilage and underdeveloped bone, based on the absence of osteons in the incudal tissue. This is however based on a single individual, so general insights and inter-individual variability cannot be deduced from these data.

It is suggested in Graboyes et al. (2011) that one of the main sources of confusion may be the lack of widely accepted nomenclature regarding the distal end of the incus: the 'fourth ossicle' itself has been known under different names and the definition of the term lenticular process has been subject to inconsistency as well.

Another possible source of inconsistency is the fact that the delicate anatomical features of the distal incus are very difficult to incorporate in simulations of ME mechanics and are therefore often neglected. Nevertheless, as stressed by Decraemer and Khanna (2004), Funnell et al. (2005) and more recently Chien et al. (2009), the curious anatomy could very well have considerable implications for the mechanics of the ISJ. They argue that the thin pedicle may bend during ossicular motion, “*thereby adding flexibility to the ISJ and reducing the transmission of particular motion components from the incus to the stapes.*” (Chien et al., 2009) [*for a correction of this statement, see section 4.6 of Chapter 6 of this thesis.*]

The technique used in the current study does not allow identification of the soft tissue type, but as elaborated above, this has been studied in other papers (Chien et al., 2009; Karmody et al., 2009) through histology, which is a more suitable technique for this purpose. It is, however, possible to assess the properties of the bony core of the distal incus (Table 3-7). In our datasets, the pedicle of the lenticular process is nowhere interrupted, undermining the existence of a separate ‘fourth ossicle’. This is consistent with the most recent studies on this topic (Chien et al., 2009; Karmody et al., 2009). The quantitative width data are rather inconsistent with the findings of Chien et al. (2009), who reported that the diameter of the pedicle is  $(260 \pm 104) \mu\text{m}$ , while our result is  $(385 \pm 92) \mu\text{m}$ . Both studies however confirm a very large inter-individual variety in structural anatomy.

The micro-CT data cannot distinguish between bone and strongly calcified cartilage. According to Mente and Lewis (1994), the difference in elastic modulus between these tissue types is one order of magnitude. Therefore this distinction is very important: if the pedicle consists mostly of cartilage, the “bending” theory of Decraemer and Khanna (2004) and Funnell et al. (2005) gathers more credibility, while a stiff bony connection would undermine it [*for a correction of this statement, see section 4.6 of Chapter 6 of this thesis.*]. It is clear that more knowledge and consensus on the mechanical parameters of this feature are still needed.

#### 4.2.5 Topic V: TM and stapes footplate Areas

In the literature, many data can be found on either TM and SFP surface areas, both 2D projected areas and real 3D areas, or measurements of ellipse short and long axis lengths. Table 3-12 and Figure 3-12 provide overviews of different literature values. When only axis lengths were reported, we have calculated the approximated ellipse surface area to compare with our results. All literature values lie within or very close to the uncertainty range of the current study (i.e. average  $\pm$  standard deviation).

Table 3-12: Comparison of our results for the TM and SFP surface areas and the hydraulic area ratio to published data. If mentioned, the method used in the cited study is included. Some values are derived by the authors from other values in the referred source. A dash (-) between two values denotes the range of values, rather than an uncertainty interval. Otherwise, a sole dash represents absent data. Figure 12 provides a visual representation of this comparison. References: (Wever and Lawrence, 1954; Kirikae, 1960; Ars, 1977; Molvaer et al., 1978; Rosowski, 1994; Hemila et al., 1995; Nummela, 1995; Stenfelt et al., 2004; Gan et al., 2006; Schraven et al., 2011; Salih et al., 2012; Sim et al., 2013).

Source	Method	TM Area (mm <sup>2</sup> )	SFP Area (mm <sup>2</sup> )	Ratio
De Greef 2015	Ellipse	57,6 ± 7,0	2,80 ± 0,20	20,6 ± 2,1
	2D Proj	59,4 ± 6,9	3,04 ± 0,17	19,6 ± 2,3
	3D Surf	65,6 ± 5,6	3,26 ± 0,19	20,2 ± 2,1
Kirikae 1960	Ellipse	-	3,09 <sup>1</sup>	-
	2D Proj	55,4 ± 4,5	-	17,9 <sup>1</sup>
	3D Surf	57 - 64 <sup>2</sup>	-	-
Ars 1977	Ellipse	59	-	-
Nummela 1995	Ellipse	68,3	-	-
Hemila 1995	Ellipse	68,3	2,98	22,9 <sup>1</sup>
Rosowski 1994	Literature <sup>3</sup>	60	3,2	18,8 <sup>1</sup>
	Theoretical fit	-	-	20
Stenfelt 2004	2D Proj	-	3,85 (3 - 5,3) <sup>2</sup>	-
Gan 2006	3D Surf	72 <sup>1</sup>	-	-
Schraven 2011	Unmentioned	-	3,2	-
Salih 2012	Unmentioned	-	3,16 - 4,09 <sup>2</sup>	-
Sim 2013	2D Proj	-	2,86 ± 0,32	-
	3D Surf	-	3,03 ± 0,33	-

<sup>1</sup> Value derived by authors

<sup>2</sup> Range of values

<sup>3</sup> Wever and Lawrence 1954; Molvaer 1978

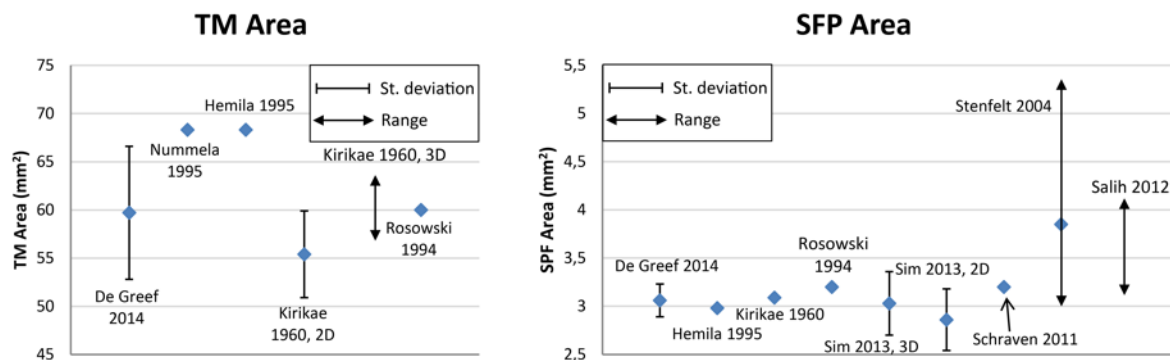


Figure 3-12: Literature comparison of published values for the TM and SFP surface areas.

The question whether the 2D projection method or the 3D projected area method provides the most relevant measure for sound collection is a difficult topic in which the complicated interplay between acoustics and biomechanics needs to be considered. Therefore, we leave these further considerations for dedicated studies.

#### 4.2.6 Topic VI: Thickness of Different Structures

The thickness of the TM has been the subject of study in multiple papers, yet even the most recent ones (Kuypers et al., 2006; Van der Jeught et al., 2013) conclude that more statistical data are needed to make final conclusions. The current data (Table 3-9) are a useful contribution, but should be interpreted with awareness about the possible effect of the applied staining with regard to tissue shrinkage. Nevertheless, the distribution of thickness and the correlation of its statistical properties to other ME dimensions, as suggested by other authors, can be a valuable addition to existing data.

Our findings for the average TM thickness ( $(81 \pm 18) \mu\text{m}$ , range 59.1 – 105.7) are consistent with literature values of  $77.93 - 91.76 \mu\text{m}$  (Van der Jeught et al., 2013),  $40 - 120 \mu\text{m}$  (Kuypers et al., 2006),  $64 - 95 \mu\text{m}$  (Schmidt and Hellström, 1991),  $30-90 \mu\text{m}$  (Lim, 1970) and  $20 - 430 \mu\text{m}$  (Ruah et al., 1991), although the ranges of uncertainty differ significantly between different authors. No correlation between the average TM thickness and the inferior-superior length of the TM was observed, in contradiction to (Van der Jeught et al., 2013).

The IMJ features an excessive bulge at a medio-superior location (see Table 3-10). Presumably, this bigger space between the ossicles allows for a larger attachment surface of the IMJ capsule, consisting mainly of elastic fibers (Willi, 2003). Apart from the area of the bulge, the location of maximal thickness is not consistent, while the thinnest region of the IMJ is consistently located at a lateral or latero-superior position. The mean minimal thickness is consistent with the findings of Sim and Puria (2008), reporting  $(0.04 \pm 0.005) \text{ mm}$  for the mean minimal thickness. Their result for the mean maximal IMJ thickness of  $(0.32 \pm 0.029) \text{ mm}$  is significantly different from ours. The mentioned study used another thickness calculation algorithm and did not exclude the medio-superior bulge from the assessment of maximal thickness.

The ISJ is more regular and flat than the IMJ space (see Table 3-10). The location of minimal thickness is inconsistent between samples, but the maximal thickness is located posteriorly in 5 out of 6 samples.

In 4 out of 6 samples, the stapedial annular ligament (SAL) is unresolvable at multiple places, resulting in an observed thickness of  $0 \mu\text{m}$  (see Table 3-11). This is probably caused by volume averaging artifacts in the micro-CT reconstruction, given the relatively large voxel sizes (voxel pitches of  $22.8 \mu\text{m}$  (samples 1, 3-6) and  $18.5 \mu\text{m}$  (sample 2)) compared to the thickness of the SAL. The maximal thickness of the SAL is consistently located anteriorly or antero-inferiorly. Sim et al. (2013) performed high-resolution micro-CT measurements on separated stapes

samples, enabling a smaller voxel size than in the current study. In that study, no places were reported where the SAL thickness decreased to 0.

Finally, the round window (RW) of the cochlea did not feature consistent locations for either the maximal nor the minimal thickness (see Table 3-11).

As discussed earlier, we should acknowledge that these thickness results could be slightly inaccurate due to PTA-induced tissue shrinkage, although this effect can be expected to be minor, as a linear shrinkage of only 3.6 % is reported in Buytaert et al. (2014) for muscle tissue.

### 4.3 Relevance of Morphological Data for ME modeling

An important application of high-resolution 3D morphological data of the ME is finite element (FE) modeling. The quality and complexity of FE models continue to improve with the availability of increasingly more computational resources. Some small soft tissue structures with complicated mechanical properties are challenging to incorporate in these models, and different approaches have been taken in published models. For instance, in Gan et al. (2009), all ligaments that were found in the sample that was used for shape data were incorporated using the experimentally acquired shape data. In other recent models, however, the ligaments are represented by either simple geometric shapes (Gentil et al., 2014a) or by mechanical elements such as Voight elements (Böhnke et al., 2013). It is however possible that some experimental features of ME functionality, such as the relative flatness of the ME's frequency response function over a broad frequency range, cannot be predicted using these hybrid models. The distributed nature of the ME density, stiffness and other parameters, could be the underlying reason for some of these features. Therefore, it is valuable to continue to make efforts to minimize all possible sources of differences between modeling and experimental outcomes, including low-resolution image data or lumped-parameter elements. The new morphological data presented in this paper could be valuable in the advancements of this effort.

## 5. Conclusions

In this study, multiple topics of ME morphology have been studied by means of segmentation and interpretation of six micro-CT datasets of PTA-stained human temporal bones. Segmentation was done using a combination of automatic and manual segmentation tools. Statistical results have been extracted for all topics. The influence of the PTA staining on the spatial configuration of the ossicles has been demonstrated to be negligible. The following conclusions have been drawn:

- Ligaments (see Table 3-2): The AML, LML, PML and PIL were present in all samples, although the PML was not identified as a ligament. The M-AML, S-AML, A-SML, P-SML, MIML, MIL, LIL and ASL were observed in at least one but not in all samples.

- The COMs, PMIs and PARs of all ossicles and the IMC were calculated and compared against literature data. We revealed a statistically significant influence of the incorporation of ossicle inhomogeneities on some ossicle inertia parameters. Some linear ossicle dimensions were measured and evaluated as well, including the distances that define the ossicular lever arm ratio. This ratio was found to be  $(1.30 \pm 0.11)$ .
- The distal portion of the incus featured an inconsistently shaped bony connection between the long process of the incus and the lenticular process. This pedicle had a mean maximal width of  $(385 \pm 92) \mu\text{m}$  and its mean thickness was  $(54 \pm 20) \mu\text{m}$  and was surrounded by a large amount of soft tissue, yet was nowhere interrupted.
- The surface areas of both TM and SFP have been measured in three different manners (ellipse approximation, 2D projection and 3D surface). For the 2D projection method, the mean TM area was found to be  $(59.4 \pm 6.9) \text{mm}^2$ , for the SFP this was  $(3.04 \pm 0.17) \text{mm}^2$ . The mean TM/SFP area ratio was  $(19.6 \pm 2.3)$ .
- The mean TM thickness was  $(80 \pm 18) \mu\text{m}$ , ranging from  $59 \mu\text{m}$  to  $106 \mu\text{m}$ . The TM thickness distribution of our samples did not suggest consistent local thickening of the membrane in certain quadrants and no correlation between the mean TM thickness and the inferior-superior TM length has been found. The IMJ consistently featured an excessively thick bulge at its medio-superior portion with a thickness of  $(983 \pm 88) \mu\text{m}$  and apart from this a mean thickness minimum of  $(35 \pm 20) \mu\text{m}$  and a mean maximum thickness of  $(235 \pm 20) \mu\text{m}$ , with the thinnest point consistently located laterally. For the ISJ this was  $(78 \pm 20) \mu\text{m}$  and  $(163 \pm 45) \mu\text{m}$  (consistently posterior), for the SAL  $(6 \pm 20) \mu\text{m}$  and  $(290 \pm 60) \mu\text{m}$  (consistently anterior), and for the RW  $(55 \pm 20) \mu\text{m}$  and  $(221 \pm 39) \mu\text{m}$  (no consistent locations).



# Chapter 4. On the Connection between the Tympanic Membrane and the Malleus

---

## Abstract

**Background:** The tympano-malleal connection (TMC) is the soft-tissue connection between the tympanic membrane (TM) and the manubrium of the malleus. Some studies suggest that its mechanical properties may have a substantial influence on the mechanics and transfer function of the middle ear. However, relatively little is known about the dimensions of the TMC and its variability among individuals.

**Method:** Thirteen samples were collected from human temporal bones, consisting of only the malleus and the TM. They were imaged using  $\mu$ CT without contrast enhancing agent. From the  $\mu$ CT images, the TMC dimensions were measured in both anterior-posterior direction (TMC width) and medial-lateral direction (TMC thickness). Three selected samples were examined using histological microscopy.

**Results:** Both TMC width and thickness featured a large variability among individuals. The minimal TMC width along the manubrium for different individuals covered a range between 83 and 840  $\mu$ m. The minimal thickness ranged from 48 to 249  $\mu$ m and the maximal thickness from 236 to 691  $\mu$ m. Histological sections showed that the TMC consists of a narrow core of dense regular connective tissue, surrounded by loose connective tissue. In some samples, either of these two components was absent in the TMC at some manubrium locations. The configuration of these components varied among the samples as well.

**Conclusion:** Our data confirm that a large inter-individual variability exists in the properties of the TM-malleus connection in humans in terms of its dimensions, tissue composition and configuration. Average data and their variability margins will be useful input for testing the importance of the TMC in finite element models.

*Major contributions to the design of the study, the preparation of the  $\mu$ CT scans, image segmentation, data analysis and the writing of the paper.*

*This chapter was published in: De Greef, D., Goyens, J., Pintelon, I., Bogers, J.-P., Van Rompaey, V., Hamans, E., Van de Heyning, P., Dirckx, J.J.J., 2016. On the connection between the tympanic membrane and the malleus. *Hear. Res.* 340, 50–59. doi:10.1016/j.heares.2015.12.002*

## 1. Introduction

The tympanic membrane (TM) and the manubrium (or handle) of the malleus are connected by a soft tissue structure, the tympano-malleolar connection (TMC). In the literature, the TMC has been assigned different names, including manubrial fold (De Greef et al., 2014b, i.e. Chapter 5 of this thesis; Ferrazzini, 2003), stria malleolaris (Hoffstetter et al., 2010), plica malleolaris (Gea and Decraemer, 2010; Gulya and Schuknecht, 1995) or simply TM-malleus attachment (Koike et al., 2002). Multiple studies have attempted to investigate the functional role of the TMC through finite element modeling, yet their conclusions are not aligned. For instance, Koike et al. (2002) concluded that “*the modification of the properties and dimensions [of the TMC] did not greatly influence the vibration mode and displacement of the TM*”, whereas some more recent studies do predict an important role for the TMC in middle ear mechanics (De Greef et al., 2014b, i.e. Chapter 5 of this thesis; Hoffstetter et al., 2010).

Literature data on the morphology of the TMC is limited and inconsistent as well. Most published studies are based on light microscopy of histological sections (Ferrazzini, 2003; Graham et al., 1978; Gulya and Schuknecht, 1995; Politzer, 1892), and to date, one study was published based on micro-computed tomography ( $\mu$ CT) (Gea and Decraemer, 2010). All studies agree that the connection between TM and malleus is tight at the levels of the umbo (inferior tip of the manubrium) and the lateral process of the malleus (superior end of the manubrium) (LPM). Both anatomical locations are indicated in Figure 4-2. However, they disagree substantially on the TMC morphology in the middle part of the manubrium. At this level, the histology-based studies describe the TMC as “a mere ‘stalk’ with a fibrous core and covered by mucosa” (Graham et al., 1978) or “only a narrow bridge” (Politzer, 1892, p. 224), that is clearly much narrower than the manubrium of the malleus. In contrast, Gea and Decraemer (2010) observed on  $\mu$ CT images that the TMC was almost as wide the manubrium at mid-manubrium level. Gea and Decraemer (2010) suggested that “*this discrepancy in width could be caused by (1)*

*shrinking effects during the histological preparation or (2) moisture that had collected in the constriction and showed up on the CT images with a contrast similar to that of the tissue of the PM (plica mallearis = TMC)*". In other words, they assumed that the difference was to be attributed to systematic errors of the sample preparations and imaging techniques, rather than to real variability between individuals. Given the possible importance of this structure, these speculations need to be validated.

The main aim of this study is to extend the knowledge base for the morphology of the TM-malleus connection. For this purpose, we visualized the TMC with both  $\mu$ CT and histology. This way, we can also investigate whether the reported discrepancy in MF dimensions based on  $\mu$ CT imaging (Gea and Decraemer, 2010) and light microscopy of histological sections (Ferrazzini, 2003; Graham et al., 1978; Gulya and Schuknecht, 1995; Politzer, 1892) is a side-effect of either of the two imaging techniques, or whether it represents real inter-individual variability.

## 2. Materials and Methods

### 2.1 Sample preparation

Thirteen human temporal bones were acquired from the University of Antwerp. Microscopic examination of the tympanic membrane was performed by an accredited Otorhinolaryngologist (VVR) before and after fixation. No otoscopic abnormalities were observed, i.e. we did not observe myringosclerosis, (healed) perforation of the tympanic membrane, attical retraction, atelectasis, attical or pars tensa cholesteatoma. A circumferential incision in the ear canal skin enabled the elevation of the tympanic membrane (TM) by means of endoscopy (Caremans et al., 2015; Van Rompaey et al., 2013). All suspensions of the malleus (anterior malleal ligament, tensor tympani tendon, incudo-malleal joint and chorda tympani) were disconnected surgically. Hence, samples consisting only of the malleus, the TM, the tympanic annular ligament and some ear canal skin were obtained. Figure 4-1 shows one of the samples mounted on a stage for  $\mu$ CT. Immediately upon dissection, the samples were submerged into a 4% paraformaldehyde solution (0.1M Phosphate buffer, pH 7.4). Samples were kept in paraformaldehyde for 1 to 9 days before  $\mu$ CT. No contrast-enhancing staining was applied to the samples to avoid shrinkage effects (see section 4.4.2).

### 2.2 Micro-CT scans

To prepare for  $\mu$ CT scanning, the samples were placed in a small custom-made closed container made of PMMA (Plexiglas). The sample laid on a small plateau in the middle of the container, surrounded (but not in contact with) water. This design prevented dehydration of the sample during the long recordings of 1-3h at a temperature of approximately 30°C. Figure 4-1 shows the holder without its wall and cover lid.

The samples were positioned obliquely so that the TM and manubrium were oriented at an angle of approximately  $45^\circ$  with the X-ray direction. This orientation provided an adequate trade-off between sample stability and image quality. To realize this positioning, the superior part of tympanic annular ligament rested on a synthetic foam platform at the edge of the centered PMMA-platform, as shown in Figure 4-1. This material was chosen because of its suitable balance between low X-ray absorption (Gea et al., 2005) and mechanical stability.

$\mu$ CT-scans were performed using a Skyscan 1172 micro CT scanner (Bruker, Kontich, Belgium). Scanner settings were optimized for good contrast between the soft tissue of the TMC and the surrounding air, without image saturation. The most important scanning and reconstruction parameters are listed in Table 4-1. Sample TMC<sub>1</sub> was scanned using different settings than the rest because it was the pilot sample of the experiment and the optimal protocol was not yet established at the time of recording this sample.

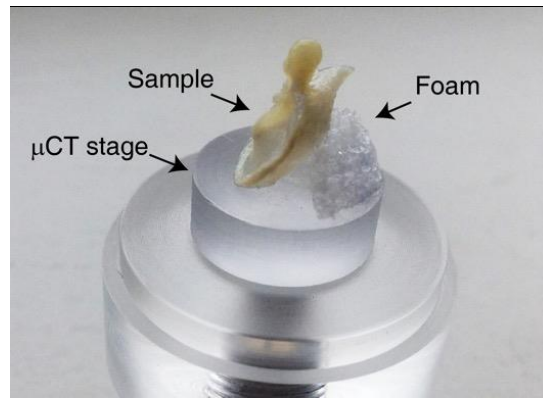


Figure 4-1: Sample on its measurement stage for  $\mu$ CT recording in an oblique position. During scanning, this stage was closed off by a fitted Plexiglas cylinder and a cover lid that are removed for this picture.

Table 4-1:  $\mu$ CT scanning and reconstruction parameters

Parameter	Value for TMCs 2-13	Value for TMC 1
Source voltage	65 kV	52 kV
Source current	153 $\mu$ A	188 $\mu$ A
X-ray sensor size	2664x4000	2664x4000
Exposure time	1.77 s	1.77 s
Rotation step	$0.25^\circ - 0.4^\circ$	$0.2^\circ$
Total scan duration	74-119 min (depending on field of view)	179 min
Physical filter (beam hardening)	0.5 mm Aluminum	0.5 mm Aluminum
Frame averaging	3	4
Reconstruction voxel size	4.98 $\mu$ m	3.36 $\mu$ m

## 2.3 Histologic preparation

Three samples of our dataset were selected after examining the  $\mu$ CT reconstructions: one representing an ‘average’ TMC (sample 1), one with a very narrow TMC (sample 9) and one with a very wide TMC (sample 5). These samples were prepared for histological examination after the  $\mu$ CT scans. The samples were decalcified in a 10% ethylenediaminetetracetic acid (EDTA) solution for 8 to 15 days to enable slicing through the malleus. After embedding the samples in paraffin, 5  $\mu$ m sections were cut on a microtome (Leica Microsystems, Diegem, Belgium). Transverse sections (i.e. perpendicular to the direction of the manubrium, see Figure 4-2) were made. Every 50  $\mu$ m a section was stained using Heidenhain's AZAN trichrome stain. Finally, the sections were digitized by a CCD camera (Olympus DP70, Center Valley, PA, USA) connected to an optical microscope (Zeiss Axiophot, Zeiss, Zaventem, Belgium).

## 2.4 Morphometrics

### 2.4.1 Metric definitions

To facilitate interpretation of the following paragraphs, Figure 4-2 indicates some anatomical and mathematical directions.

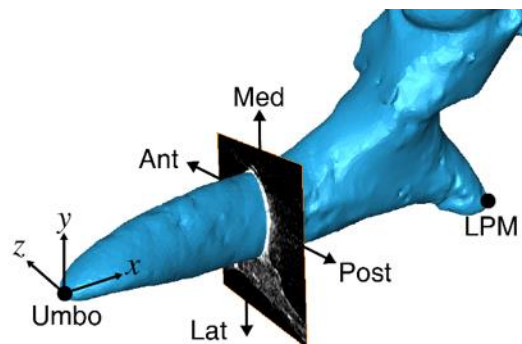


*Figure 4-2: Indication of anatomical and mathematical directions around a manubrium (blue). The depicted slice is a transverse slice, similar to all slices shown in this paper (from both  $\mu$ CT and histology).*

Two quantitative metrics were defined to characterize the morphology of the TMC: TMC width and TMC thickness. Both are indicated in Figure 4-3A. TMC width quantifies the anterior-posterior dimension, TMC thickness quantifies the lateral-medial dimension. The frame of reference for this context is defined by the direction of the manubrium towards the LPM (x-axis), the direction perpendicular to the manubrium towards the middle ear (y-axis) and the direction perpendicular to x- and y-axes, towards the anterior side of the malleus (z-axis) (Figure 4-2).

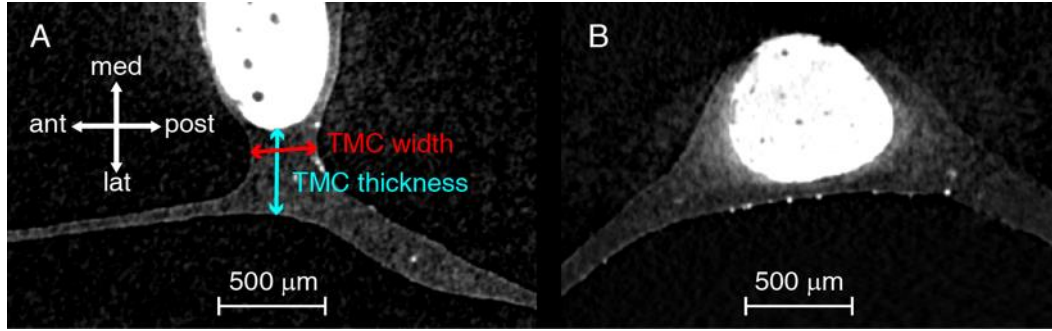


Figure 4-3: A. Visual indication of both TMC width and thickness on a transverse  $\mu$ CT slice of sample 6. Note that the actual calculations took the 3D shape of the boundaries into account; B. A transverse slice of sample 10 showing a ‘tight coupling’ between the TM and manubrium. Here, the determination of TMC width is ambiguous, as explained in section 2.4.4.

We define the TMC width as:

$$w_{ant-post}(x) = \min_y \{ \min(d = \|\overrightarrow{p_{ant}}(x, y) - \overrightarrow{p_{post}}(x', y')\| | \overrightarrow{p_{post}}(x', y') \in S_{post}) \}, \quad Eq. 4-1$$

where,  $\overrightarrow{p_{ant}}(x, y)$  is the 3D vector representation of the points that describe the anterior surface of the TMC,  $\overrightarrow{p_{post}}(x', y')$  is the equivalent for the posterior TMC surface and  $S_{post}$  is the posterior surface itself. In other words, this metric quantifies the shortest distance in three dimensions from any point on the anterior surface to the opposite, posterior surface for every position  $x$  along the manubrium. This distance is not necessarily measured parallel to any of the anatomical directions, but in the direction of shortest distance.

TMC thickness is defined similarly to the width, for the medial and lateral boundary surfaces of the TMC. The medial surface is defined by the interface between the manubrium bone and the TMC soft tissue and the lateral surface by the lateral surface of the TM. Mathematically, we define the TMC thickness by:

$$t_{med-lat}(x) = \min_z \{ \min(d = \|\overrightarrow{p_{med}}(x, z) - \overrightarrow{p_{lat}}(x', z')\| | \overrightarrow{p_{lat}}(x', z') \in S_{lat}) \}, \quad Eq. 4-2$$

#### 2.4.2 Image segmentation

To obtain the geometry of the boundary surfaces of the TMC (anterior, posterior, lateral and medial), the  $\mu$ CT images were imported into Amira® 5.3 (FEI Visualization Sciences Group, Hillsboro, Oregon, USA) for segmentation. In a first step, the images were virtually resliced so that the slices were perpendicular to the manubrium. Next, segmentation (by DDG) was performed by a combination of automatic and manual tools. In most cases, automatic segmentation tools, including threshold-based region growing, edge detecting region growing and slice interpolation, produced satisfactory results. On a minority of the virtual slices, where

a lower contrast or worse SNR did not enable satisfactory segmentation using automatic tools, a minimum of manual intervention was applied using drawing and eraser tools.

### 2.4.3 Algorithm

The segmented volumes were exported from Amira to MATLAB (Release 2012b, The MathWorks, Inc., Natick, Massachusetts, USA). The following algorithm returned the TMC width as a function of manubrium position (for TMC thickness, the algorithm was equivalent):

- Find the anterior and posterior boundaries of the TMC from the segmented volumes. These are now represented as two 2D matrices with rows in the dimension along the manubrium ( $x$ -direction) and columns perpendicular to them in the lateral-medial direction ( $y$ -direction).
- For every individual point on the anterior surface, calculate the three-dimensional distance to all points on the posterior surface in an area of  $100 \times 100$  pixels (corresponding to  $500 \times 500 \mu\text{m}$ ) around the anterior surface point. These values represent  $d$  from Eq. 4-1.
- Find and store the minimum of these distances in a matrix. The result of this step for a single sample is shown in Figure 4-4.
- For each column of the matrix, i.e. each  $x$ -position, find and store the minimum along this column in a new 1D array. In Figure 4-4, the white line indicates the location of these minima for every column of the matrix. This minimum represents the TMC width  $w_{ant-post}(x)$  at the corresponding location along the manubrium.

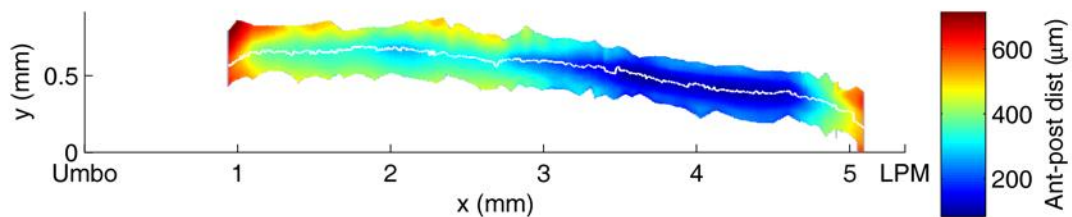


Figure 4-4: Distance between the anterior and posterior surfaces of the TMC as a function of position on the manubrium. The white line indicates the ‘valley’ of minimal width for every position. The color value along this valley is the TMC width as defined in Eq. 4-1. Data is only available at  $(x, y)$ -positions where the anterior surface was segmented.

### 2.4.4 Tight coupling

The above algorithm was applicable at all locations where a clear minimum can be identified, as in Figure 4-3A. However, a subset of CT-slices showed a shape for which the above rationale does not yield an objective value, as in Figure 4-3B. Therefore, at these locations, the TMC width was not quantified but categorized as ‘tight coupling’. The width value in these areas was chosen to be equal to the width at the nearest location that was not tightly coupled. For some samples,

there was a tight coupling along the entire manubrium. The TMC width was then measured manually at the base of the TMC using a native measuring tool in Amira on multiple slices until a minimum was found. The width along the entire manubrium was set to this measured value.

#### 2.4.5 Uncertainty on 3D distance

The measurement uncertainty on all three coordinates  $x$ ,  $y$  and  $z$  of the segmented surfaces was estimated to be equal to the voxel size, i.e.  $4.97 \mu\text{m} \approx 5 \mu\text{m}$  for samples 2-13 and  $3.36 \mu\text{m}$  for sample 1. By performing statistical error propagation, it follows that the uncertainty (UC) on the 3D distance between two of these surface points is equal to  $\sqrt{2} \times 4.97 \mu\text{m} \approx 7 \mu\text{m}$  for samples 2-13 and  $\approx 5 \mu\text{m}$  for sample 1.

## 3. Results

### 3.1 $\mu\text{CT}$ scans

Figure 4-5 shows for every sample the virtual transverse  $\mu\text{CT}$  slice (i.e. perpendicular to the manubrium) with the smallest TMC width. This visual comparison indicates a large variation in minimal TMC width.

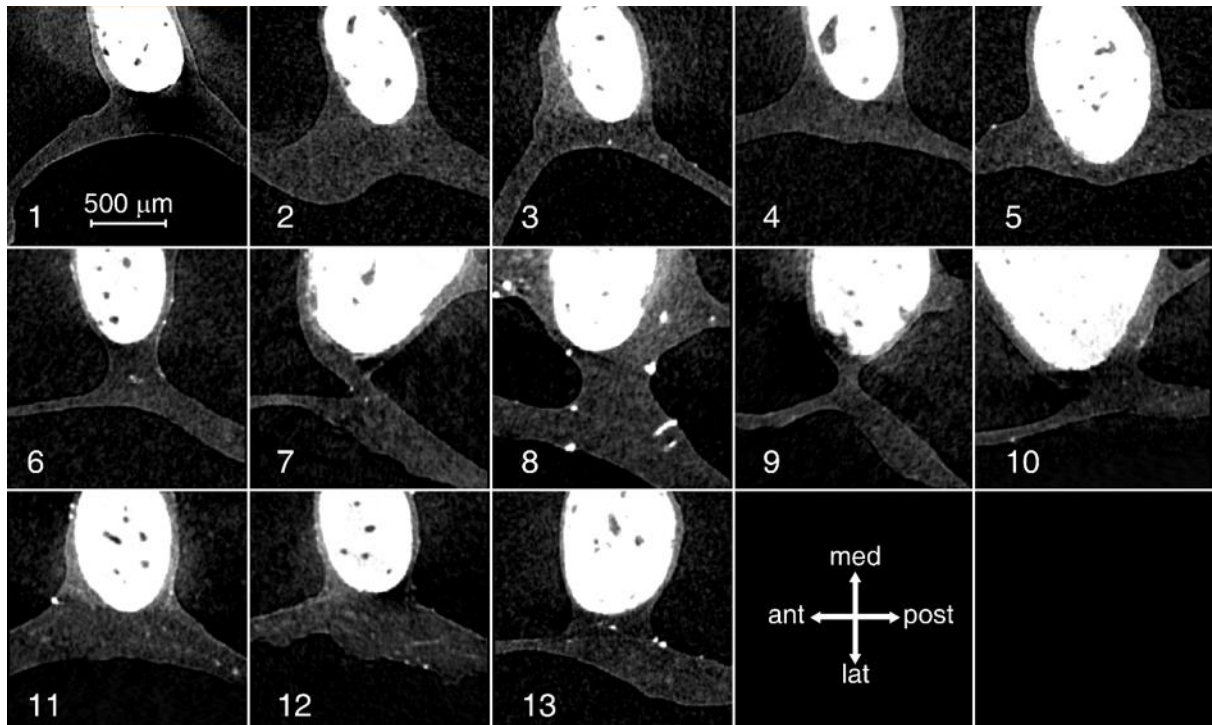


Figure 4-5: Virtual transverse  $\mu\text{CT}$  slices at the position where the TMC is the narrowest. All images have the same scale. In these images, the gray values were optimized for soft tissue contrast. The gray value range of the original images was larger than in these images.

### 3.2 Morphometric results

#### 3.2.1 Tympano-malleal connection width

Figure 4-6 presents the TMC width as a function of the manubrium position for all samples. Again, a large inter-individual variability is clearly apparent. Table 4-2 presents statistical parameters of the data. In most samples the width featured a local minimum in the middle of the manubrium and higher values at the edges. Some samples exhibited a second local maximum in the middle. Because of the mixture of values representing normal TMC width and tight coupling width, calculating an average and standard deviation on these data was not meaningful and therefore avoided.

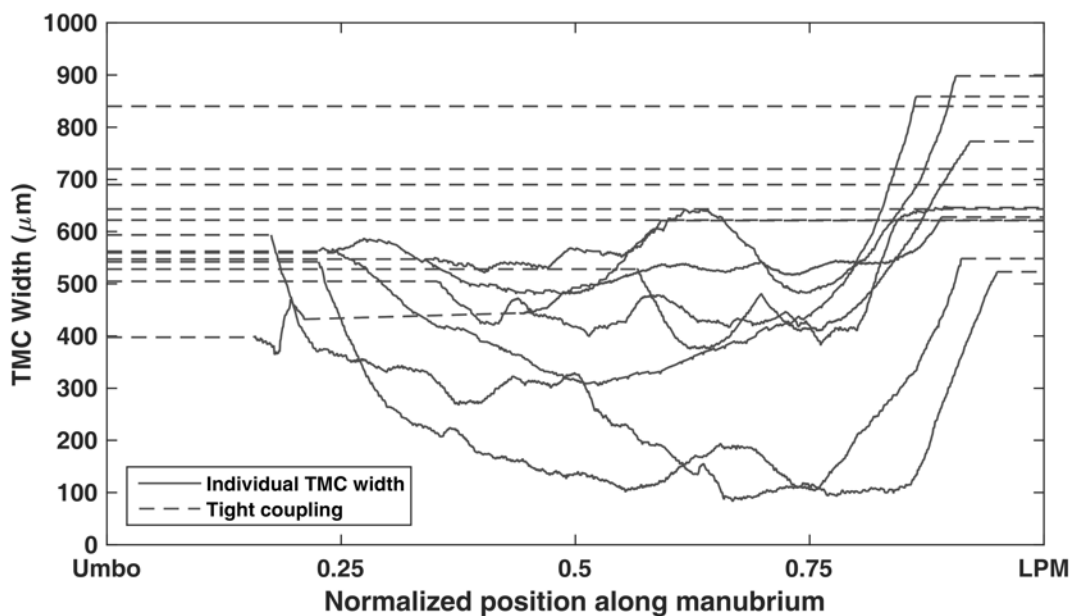


Figure 4-6: Tympano-malleal connection width (anterior-posterior) as a function of manubrium position for different individuals. Solid lines indicate the quantified TMC widths of the different samples. Dotted lines indicate areas of ‘tight coupling’ between the manubrium and TM.

Table 4-2: Statistical parameters of TMC width and thickness. For the width, the maximal value along the manubrium could not be determined unambiguously because it always corresponded to a location of ‘tight coupling’ (see section 2.4.4). UC: uncertainty; SD: standard deviation

Unit: µm	Minimum among samples	Maximum among samples	Average
Minimal TMC width along manubrium	83 ± 7 UC	840 ± 7 UC	470 ± 220 SD
Minimal TMC thickness along manubrium	48 ± 7 UC	249 ± 7 UC	128 ± 71 SD
Maximal TMC thickness along manubrium	236 ± 7 UC	691 ± 7 UC	470 ± 130 SD

### 3.2.2 Tympano-malleal connection thickness

In Figure 4-7, the TMC thickness is shown as a function of manubrium position for all samples except one. The  $\mu$ CT scans of the absent sample (nr.2) exhibited slight motion artifacts that prevented unambiguous segmentation of the medial and lateral TMC surfaces, so this sample was omitted from the thickness results.

The TMC thickness, like the TMC width, exhibits a rather large inter-individual variability. The steep descent at the umbo and steep ascent at the lateral process of the malleus (LPM) are caused by the rounding of the bone at its edges. These steep edges were disregarded for the calculation of the minimal and maximal thicknesses by excluding the first 5% and last 10% of the data. The values of these extrema are included in Table 4-2.

The locations of both the minimal and maximal thickness are clustered for all samples (except one sample's minimum): between 5% and 20% for the minimum (i.e. close to the umbo) and between 70% and 90% for the maximum (i.e. close to the LPM). In between the minimum and maximum thickness, a more or less linear increase can be observed in most samples and in the average curve. Between the maximum and the LPM, the thickness decreases and finally increases again towards the edge of the bone.

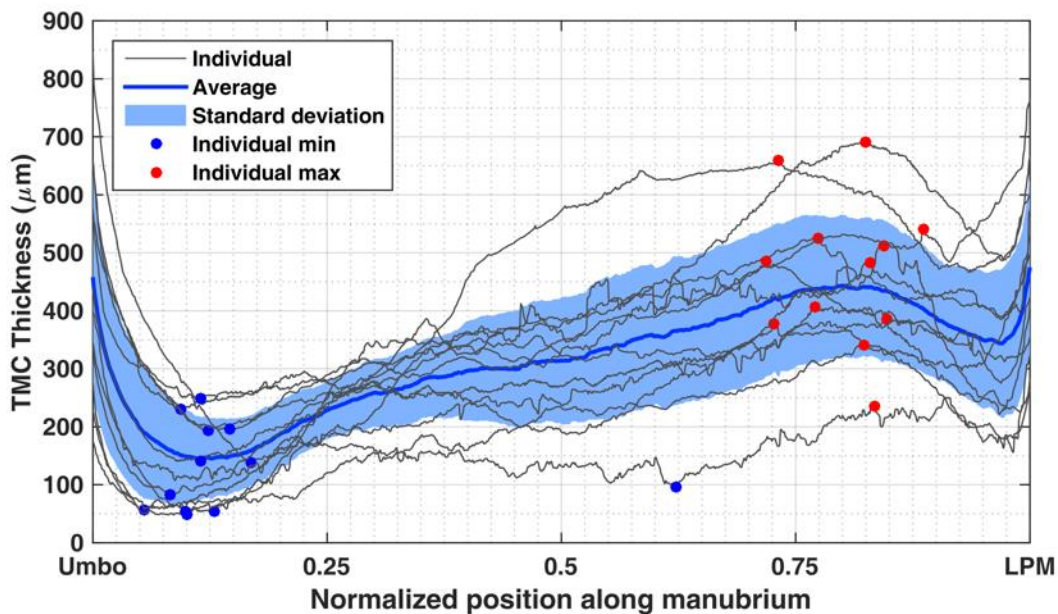


Figure 4-7: Tympano-malleal connection thickness (medial-lateral) as a function of manubrium position for different individuals. Gray lines indicate the quantified TMC thicknesses of the different samples. The thick blue line indicates the average and the light blue area the region between the average plus and minus one standard deviation. The blue and red dots indicate the locations of the minima and maxima of individual samples.

### 3.2.3 Correlation between width and thickness

Figure 4-8 presents TMC width and thickness curves for every individual sample, except for sample nr. 2 (for reason see section 3.2.2). In most samples where the TMC is tightly coupled along the entire manubrium (full length straight red line, samples 3, 4 and 5), the overall TMC thickness is smaller (blue). Sample 11 is an exception on this. Furthermore, where the TMC clearly becomes locally thicker, it tends to become narrower as well, as can be seen in samples 6, 7, 8, 9, 10 and 13. In samples 1 and 12, both width and thickness are approximately constant along the manubrium relative to the overall variation among samples.

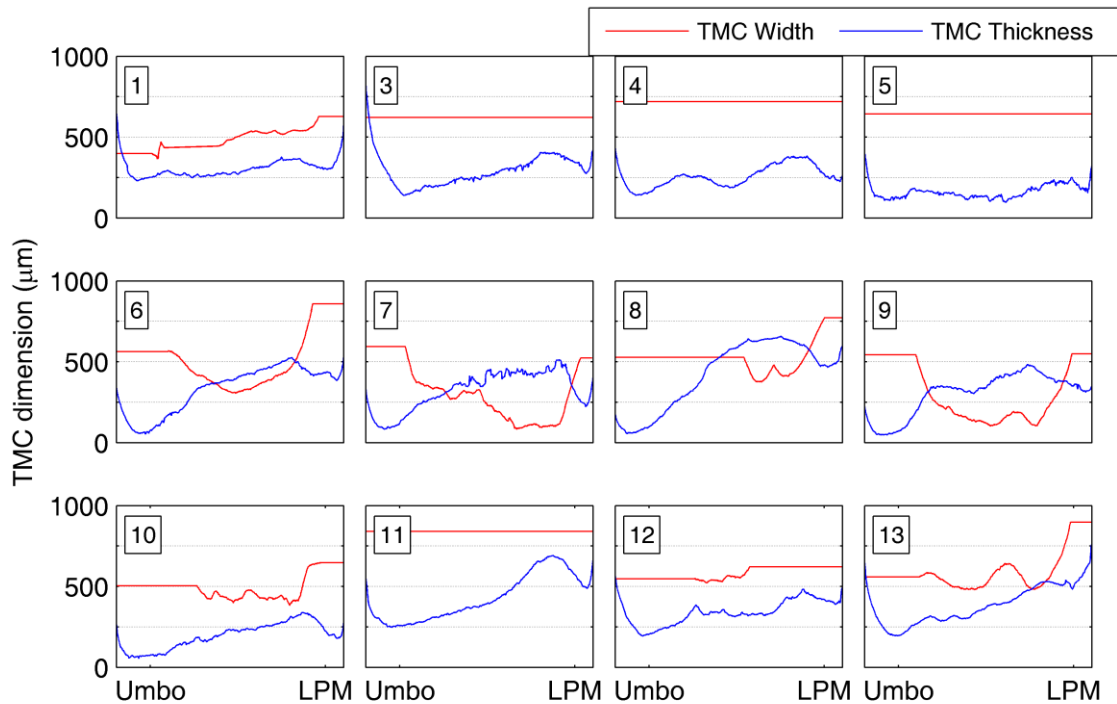


Figure 4-8: TMC width and thickness for every sample (except one).

## 3.3 Interpretation of histologic sections

### 3.3.1 Histologic examination of an 'average' tympano-malleolar connection

Figure 4-9 and Figure 4-10 show transverse histological sections of sample 1 (average TMC). Figure 4-10 A1-B1 (top row) are higher magnifications of Figure 4-9C-D. Figure 4-10A2-B2 (bottom row) present schematic views of the most important tissues identified in the top row.

In sample 1, the connection between the TM and manubrium appears to be most tight at the umbo (Figure 4-9A), gradually becoming looser and more distant (Figure 4-9B-E), before becoming tighter again towards the LPM (Figure 4-9F), consistent with the morphometric observations in this and most other samples. In Figure 4-9F, the cartilaginous cap of the LPM of the malleus is visible.

Figure 4-10A2 indicates that the TMC consists of a core of dense regular connective tissue (DRCT), containing tightly packed collagen fibers, surrounded on both sides by loose connective tissue (LCT). Both the TMC and the malleus perichondrium and periosteum are lined by simple squamous epithelium that is continuous with the most medial TM layer. The DRCT layer runs obliquely from lateral-posterior to medial-anterior. It is continuous with collagenous fibers in the lamina propria layer of the TM at its lateral-posterior end and merges with the perichondrium of the malleus at its medial-anterior end. The DRCT core is present Figure 4-9A and B as well, albeit with different widths.

In Figure 4-10B1-2 (corresponding to Figure 4-9D), the dense core is no longer present. Here, the TMC solely consists of LCT that is continuous with the internal tissue of the TM. This is the case in Figure 4-9E as well.

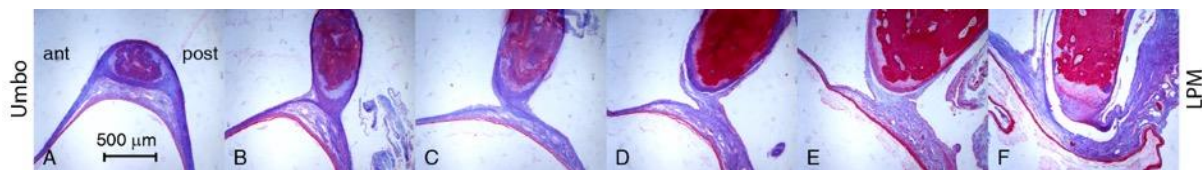


Figure 4-9: Transverse histological sections of sample 1 at different positions along the manubrium. C and D are magnified in Figure 4-10.

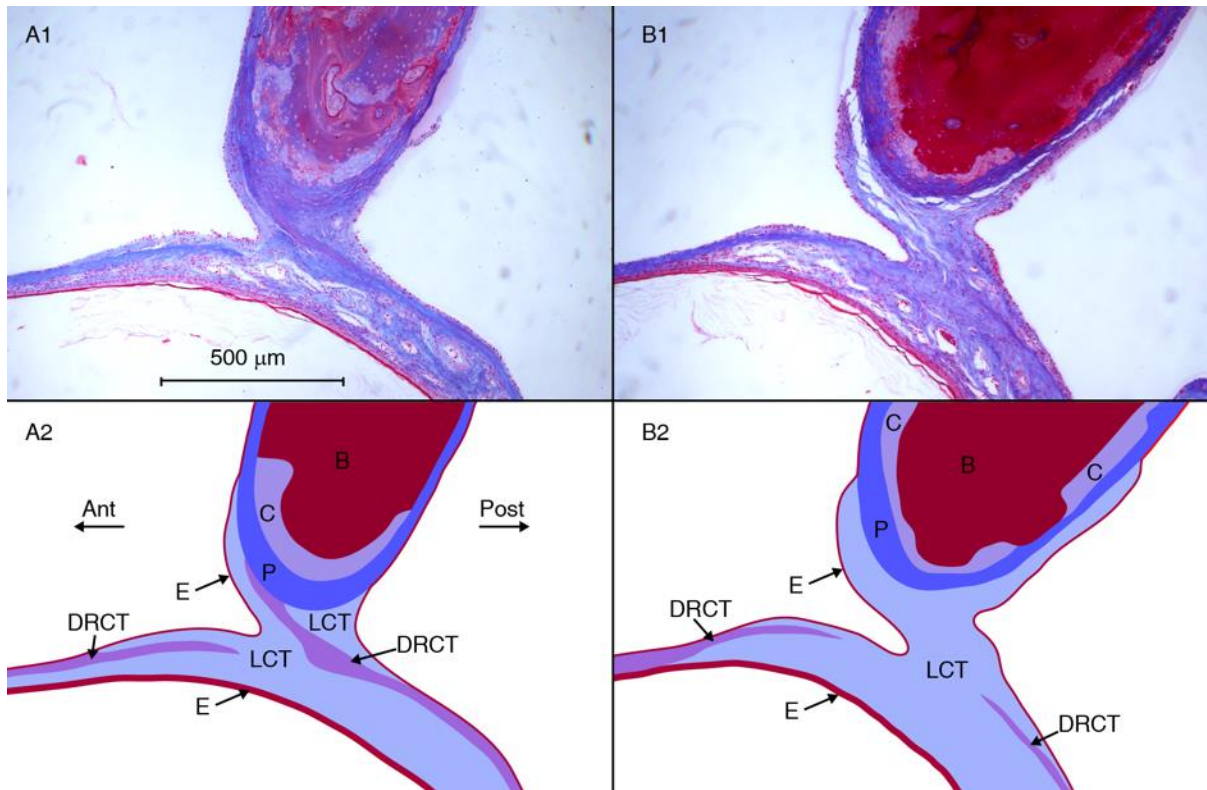


Figure 4-10: Top row: Sections 4 (A1) and 5 (B1) of Figure 4-9 in close-up. A2&B2: schematic representation of A1 and B1; Legend: B: bone; C: Cartilage; P: Perichondrium/periosteum; LCT: Loose connective tissue; DRCT: dense regular connective tissue; E: squamous epithelium.

### 3.3.2 Histologic examination of two 'extreme' tympano-malleal connections

Figure 4-11 displays sections at the middle of the manubrium of samples 5 (A) and 9 (B), which were the samples with the largest and second smallest TMC width of our population, respectively. In both samples, the same tissues can be identified as in the average sample (see Figure 4-9 and Figure 4-10). However, the configuration is different, especially for the widest TMC (sample 5, Figure 4-11A). There, the DRCT in the lamina propria layer of the TM splits up both anteriorly and posteriorly of the manubrium and merges at different locations with the perichondrium/periosteum of the manubrium. A portion of the DRCT fibers passes lateral to the manubrium. The space between the DRCT layers and the manubrium is larger on the anterior side than on the posterior side and is filled with LCT. Further towards the umbo (not shown), the anterior space filled with LCT becomes smaller and filled with DRCT instead, while the posterior part of the connection remains largely similar. At the umbo, the images are similar to the average sample (sample 1). Further towards the LPM, the collagen fiber layer of the TM and its connection to the manubrium become thinner, on both anterior and posterior sides of the manubrium. At the LPM, the tissue configuration is again similar to sample 1.

Figure 4-11B (sample 9) shows that the very narrow TMC consists at mid-manubrium level of a dense collagenous core similar to the average sample (sample 1), connecting the TM to the perichondrium/periosteum of the manubrium. Only on the anterior side of the TMC, a small area of LCT can be identified. In this sample as well, the observations at the umbo and LPM are similar to samples 1 and 5.

## 4. Discussion

### 4.1 Morphometric results

At both the umbo and the LPM, we observed a tight coupling between the manubrium and the TM in all samples. This is consistent with published literature describing the TMC. At locations between the umbo and the LPM, however, large differences between individuals were observed. In this zone, both TMC width and TMC thickness range over (almost) an order of magnitude among samples. The samples exhibiting a narrow, stretched fold in the middle of the manubrium are consistent with histological studies (Ferrazzini, 2003; Graham et al., 1978; Gulya and Schuknecht, 1995; Politzer, 1892), while the samples with a wide, tightly connected TMC are to some extent consistent with Gea and Decraemer (2010), a study based on  $\mu$ CT imaging. This observation indicates that the discrepancy in the literature on TMC morphology could represent real inter-individual variability, rather than being caused by imaging artifacts.

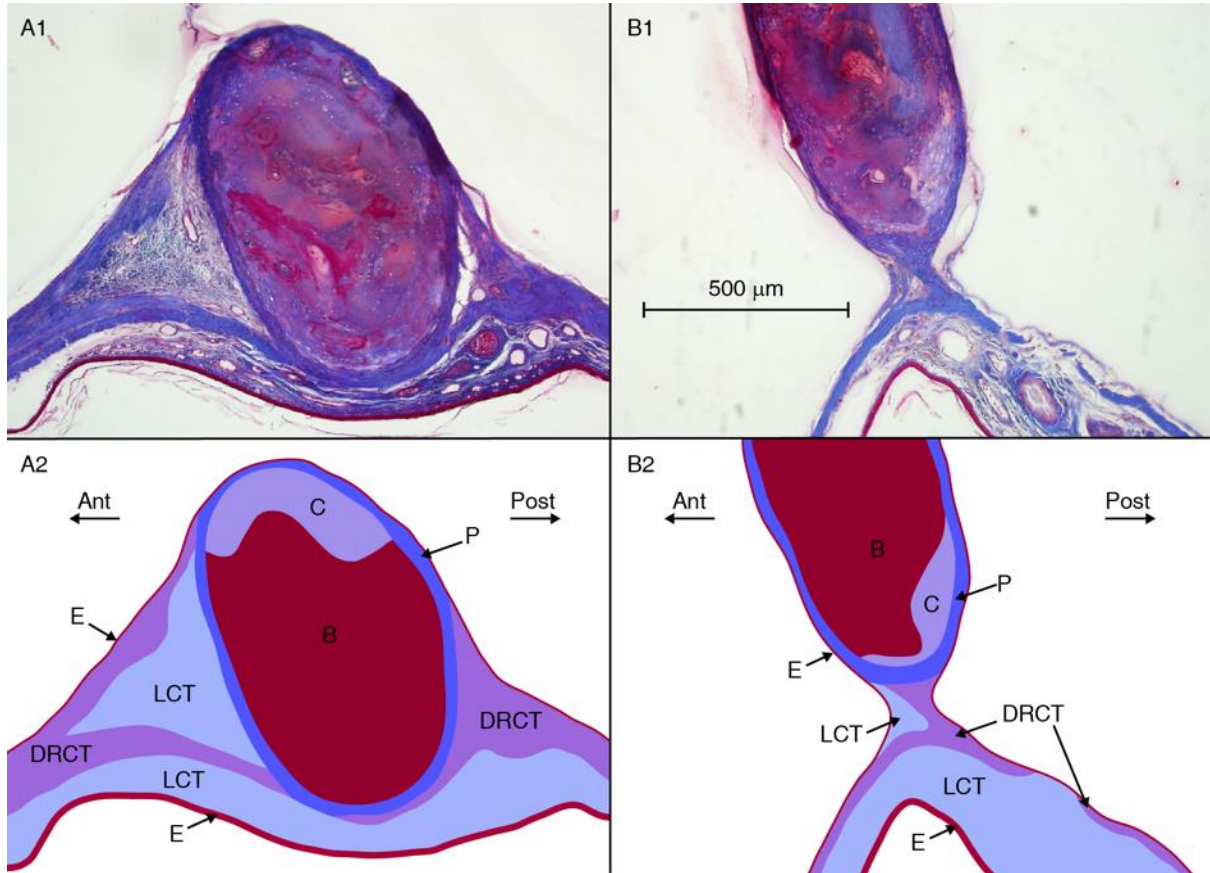


Figure 4-11: Top row: Histology sections at the middle of the manubrium of samples 5 (A) and 9 (B), the samples with the largest and smallest TMC width respectively. A2&B2: schematic representation of A1 and B1; Legend: B: bone; C: Cartilage; P: Perichondrium/periosteum; LCT: Loose connective tissue; DRCT: dense regular connective tissue; E: squamous epithelium.

Gea and Decraemer (2010) reported measurements of TMC dimensions based on  $\mu$ CT-scans of one temporal bone. In the reported case, the TMC thickness (in medial-lateral direction), going from umbo to LPM was reported at 7 evenly spaced locations: 150 - 270 - 330 - 680 - 815 - 440  $\mu$ m. The trend in these values is similar to our data, although none of our samples reaches a thickness of 815  $\mu$ m. The TMC width was reported at two locations near the middle of the manubrium: 540  $\mu$ m and 680  $\mu$ m. Both values are well inside our range of values.

In surgical myringectomy interventions, the TM is surgically detached from the manubrium. This detachment is experienced as being more difficult at the umbo and the LPM than in the middle of the manubrium in many patients (Marquet, 1987). This is in agreement with the findings of the narrow TMC's of this study, but not with the most tightly coupled TMC's.

The locations of both minimal and maximal TMC thickness along the manubrium are rather consistent among samples. This is an interesting starting point for further investigation of the implications of the detailed TMC anatomy. It could be used to construct a statistical 'average' TMC model, along with models of the thin and thick extrema.

The fact that the tightly coupled TMC's represent the samples in the lower range of TMC thicknesses is not surprising. If there is only a small distance between the TM's lateral surface and the malleus's lateral surface (small TMC thickness), there is no space for the TMC to become very narrow between the TM and malleus.

## 4.2 Interpretation of the histologic sections

The histological examination of three of our samples demonstrated that the variability among samples is not merely a question of dimensions, but also of configuration and composition. Consistent with our morphometric results, the histological properties of the TMC are the same for all samples at the umbo and the LPM. At the umbo, the TMC can be described as a splitting collagenous layer of DRCT of the TM (i.e. its lamina propria) that merges with the perichondrium or periosteum of the malleus. At the LPM, the cartilaginous cap of the malleus attaches to the DRCT layer of the TM. In between, the properties are very divergent. In both the narrowest and average TMC's, at mid-manubrium level the TMC has a core of DRCT. The difference between both is a much smaller amount of LCT surrounding the dense core in the narrow sample.

In the widest TMC, however, a qualitatively different connection is observed. Instead of one, there are four locations at which the DRCT layer of the TM attaches to the manubrium, because it splits anterior and posterior to the malleus. The connection was asymmetrical because on the anterior side, large volumes of LCT fill up the space between the manubrium and the DRCT layers.

The observations in the narrowest TMC samples are consistent with the literature based on light microscopy of histological sections (Ferrazzini, 2003; Graham et al., 1978; Gulya and Schuknecht, 1995; Politzer, 1892). However, the majority of TMC's in this study are wider than reported in these sources. The current study therefore clearly shows that the generally accepted narrow TMC shape represents only a portion of the population.

The variation of histological configurations and composition between samples and manubrium positions could have mechanical implications, as DRCT and LCT have significantly different mechanical properties. In DRCT, collagen bundles are aligned in order to provide maximum tensile strength, whereas in LCT, the collagen fibers are loosely packed and separated by abundant matrix, resulting in a more deformable tissue that mainly serves to occupy space and support other structures (Kerr, 2009).

## 4.3 Implications in the clinical context and for middle ear modeling

In a clinical context, the findings of this study will be valuable in understanding middle ear injuries such as malleus fractures and their effect on middle ear mechanics and conductive hearing loss. Our results suggest that treatment in scenarios such as malleus fracture,

malleovestibular prosthesis placement or tympanoplasty could be improved by following a patient-specific approach, based on the type of TMC.

In the context of middle ear modeling, it was emphasized by Funnell et al. (2013, p.7 of chapter) that a priori knowledge of material parameters is always better than “simply adjust[ing] parameters to fit particular experimental results”. It is reasonable to assume that the same is true for anatomical details that could have a significant influence on the system’s mechanics and transfer function (e.g. De Greef et al. (2015), i.e. Chapter 3 of this thesis).

Some recent finite element models of the middle include a simplified geometry for the TMC (Aernouts et al., 2012b; De Greef et al., 2014b, i.e. Chapter 5 of this thesis; Hoffstetter et al., 2010; Koike et al., 2002; Vollandri et al., 2012; Yao et al., 2013). Others either do not include the TMC as a separate structure or are unclear about whether or not they do (Cai et al., 2010; Gentil et al., 2014b; Higashimachi et al., 2013; Kelly et al., 2003; Koike et al., 2002; Liu et al., 2014; Zhao et al., 2009). Vollandri et al. (2012) stated that “a more realistic representation of the complex connection between the TM and the malleus certainly could improve the present model in finding more meaningful parameters”. Our measurements now deliver data of average TMC geometry and its upper and lower dimensional boundaries.

## 4.4 Method considerations

### 4.4.1 Comparison between micro-CT and histology

The results show that  $\mu$ CT and histology are a powerful and complementary combination to fully understand the morphology of a delicate biological component such as the TMC. From unstained  $\mu$ CT images, morphometric parameters can be extracted, because the imaging results in isotropic voxels and misalignment between slices is ruled out completely. However, it is impossible to identify all different tissue types that are present from  $\mu$ CT. This can be seen by comparing the histological sections in Figure 4-9, Figure 4-10 and Figure 4-11 to the corresponding  $\mu$ CT images in Figure 4-5. On the other hand, histology can provide detailed insight into the tissue composition and configuration, but is not as suitable as  $\mu$ CT images for morphometry because of the more aggressive (biochemical) tissue preparation, the anisotropic voxels and the difficult section alignment. Moreover, histology requires irreversible physical sectioning of the sample and is more laborious and expensive.

### 4.4.2 Omission of biochemical X-ray contrast enhancement

Acquiring good contrast on mixed-tissue type samples (both hard and soft tissue) traditionally requires heavy-element staining to enhance the X-ray absorption of the soft tissue. However, Buytaert et al. (2014) demonstrated that many conventional types of staining induce a significant shrinkage of all soft tissue types that were included in the study. Because soft tissue morphometry was the main property of interest of this study, we avoided staining of our samples. Therefore it was necessary that we fully optimized the contrast in other ways. One of

these ways was sample orientation, the other is the removal of excessive bone tissue from the sample.

#### 4.4.3 Paraformaldehyde preservation

The removal of excessive temporal bone enabled us to optimize the X-ray scanner settings for optimal contrast in the samples at hand and hence to omit sample staining. The disadvantage of the dissection is the removal of the in-situ mechanical suspension of the eardrum. Preliminary CT-scans taught us that the membrane is prone to motion artifacts during the long scan durations if no chemical fixation was applied. This is the reason for our choice to preserve the samples in paraformaldehyde. The literature suggests that the influence of tissue shrinkage due to formaldehyde preservation is non-existent or marginal (Kerns et al., 2008; Miller and Dark, 2014).

#### 4.4.4 Segmentation operator bias

As described in section 2.4.2, some degree of manual intervention during the segmentation was indispensable in order to get correct segmentation results. In Buytaert et al. (2014), the influence of the operator on segmentation results on  $\mu$ CT images was quantified. The authors concluded that morphometric results following from a manual segmentation process are only marginally dependent on the operator. Although operator bias depends on the image quality and inherent image contrast of the study at hand, the cited conclusion provides an indication that subjectivity has a small to negligible effect on results of morphometric analysis of  $\mu$ CT images through image segmentation.

## 5. Conclusions

The tympano-malleolar connection exhibits a very large variability between individuals, regardless of the imaging technique used ( $\mu$ CT or histological microscopy).

Morphometrically, we assessed the TMC in two dimensions: the TMC width (in anterior-posterior directions) and the TMC thickness (in medial-lateral direction). In general, at the umbo and LPM, the TMC width was larger and the TMC thickness was smaller than in the region between these two points.

We found that minimal TMC width along the manubrium for different individuals covered a range between  $(83 \pm 7) \mu\text{m}$ , and  $(840 \pm 7) \mu\text{m}$ . In some samples, the TMC is a thin, stretched fold at the middle of the manubrium (e.g. samples 7 and 9 in Figure 4-5), whereas in others, the TMC is entirely different in shape and the malleus is tightly embedded into the TM along the entire manubrium (e.g. samples 5 and 11 in Figure 4-5). The minimal TMC thickness ranged from  $(48 \pm 7) \mu\text{m}$  to  $(249 \pm 7) \mu\text{m}$  and the maximal thickness from  $(236 \pm 7) \mu\text{m}$  to  $(691 \pm 7) \mu\text{m}$ . The locations of both minimum and maximum thicknesses are well clustered near the umbo and the LPM, respectively. The TMC width and thickness seem to be roughly correlated in the

sense that wide TMC's are thinner (these are the tightly coupled cases) and narrow TMC's are thicker (these are the stretched fold cases).

Histologically, we observed that the TMC consists of loose connective tissue (LCT), dense regular connective tissue (DRCT) or both, and is covered by simple squamous epithelium. An average TMC consisted of a core of dense tissue surrounded by loose connective tissue on both sides and the dense core disappears when moving towards the LPM. In the narrow TMC, much smaller amounts of surrounding loose connective tissue were observed, while in the sample with the wide TMC, the tissue configuration was different with dense fibers attaching to the manubrium's anterior and posterior surface while still passing by laterally.

The large variability in morphometry and histology of the TMC suggests that treatment in various clinical scenarios could be improved by following a patient-specific approach, based on the type of TMC. It also suggest a variability in basic mechanics and ME functioning. Therefore, in future work, results of this study will be incorporated in an existing finite element model of the TM-malleus complex (De Greef et al., 2014b, i.e. Chapter 5 of this thesis) to study the functional effect of differences in TMC geometry.

# **PART III - MIDDLE EAR MECHANICS AND MODELING**



# Introduction: Solid Mechanics, Middle Ear Modeling and the Finite Element Method

---

An introduction to the middle ear and all its aspects is provided in the introduction to Part II of this thesis. Complementary to that introduction, the current introductory chapter will present fundamental knowledge that is relevant for the last four chapters of this dissertation. All introductions are kept as condense as possible and contain references to sources for deeper discussions of the subjects. The first section introduces the basics of solid mechanics, or more specifically, of elasticity, viscoelasticity, and vibration theory. The second section briefly discusses different methods that have been used to model the human middle ear. The third section goes deeper into one of these methods, finite element (FE) analysis, since it was used in chapters 5, 6, and 7 of the dissertation.

## 1. Solid mechanics

Under the influence of an external loading, a finite, a physical solid body will deform. Elasticity theory is the theory that describes these deformations and the corresponding internal material stresses by approximating the object as a continuous medium. This theory is applicable for all solid materials as long as static loads are assumed and only the equilibrium state needs to be calculated. However, many materials exhibit internal energy losses, i.e. viscous behavior, when it undergoes deformation. Therefore, when time is a relevant parameter, this behavior should be incorporated in the mathematical description, which is done in viscoelasticity theory. Viscoelastic material models are therefore often needed to describe an object's response to a time dependent or harmonic stimulus. The theory dealing with the latter is called vibration

theory. For more elaborate introductions these subjects, the reader can consult the following recommended sources: Sadd (2005), Banks (2010), and Findley (1989).

## 1.1 Elasticity theory: static

### 1.1.1 Stresses and strains

Any deformation of a body is completely described by the displacement of all material points in the body. An illustration of a deformation is found in Figure III - 1.

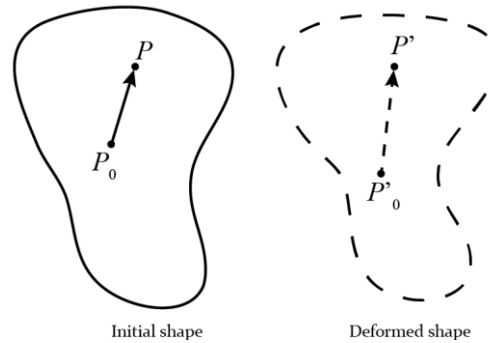


Figure III - 1: General deformation between two neighboring points in a solid.

Point  $P$  and  $P_0$  are displaced along the *displacement vectors*  $\mathbf{u}$  and  $\mathbf{u}^0$  respectively. The theory that is introduced here is referred to as the *small deformation theory*. In this theory, we assume that the components of the displacement vectors are small enough to allow the first-order approximation in the Taylor expansion of their components:

$$u_i = u_i^0 + \frac{\partial u_i}{\partial x_j} r_j, \quad \text{Eq. III - 1}$$

where  $x_i = \{x, y, z\}$  and the Einstein notation for summation was used<sup>10</sup>. The factors  $\frac{\partial u_i}{\partial x_j}$  can be regarded as elements of a tensor that is called the *displacement gradient tensor*. It can be decomposed into symmetric and antisymmetric parts as follows:

---

<sup>10</sup> In Einstein notation, when an index appears twice in a single term, it is implied that the term is summed over all the possible values of that index. E.g.  $\frac{\partial u_i}{\partial x_j} r_j = \sum_{j=1}^3 \frac{\partial u_i}{\partial x_j} r_j = \frac{\partial u_i}{\partial x_1} r_1 + \frac{\partial u_i}{\partial x_2} r_2 + \frac{\partial u_i}{\partial x_3} r_3$  (the index  $j$  appears twice in the first expression).

$$\begin{aligned} \frac{\partial u_i}{\partial x_j} &= \varepsilon_{ij} + w_{ij} \\ &= \frac{1}{2} \left( \frac{\partial u_i}{\partial x_j} + \frac{\partial u_j}{\partial x_i} \right) + \frac{1}{2} \left( \frac{\partial u_i}{\partial x_j} - \frac{\partial u_j}{\partial x_i} \right) \end{aligned} \quad \text{Eq. III - 2}$$

The tensor  $w_{ij}$  is called the the *rotation* tensor and does not contain information about internal changes of the body. This information is all contained within the *small strain tensor*  $\varepsilon_{ij}$  (often simply called *strain tensor*), that describes the deformation of an infinitesimal part in the solid. Since it is symmetric by definition, it contains only six independent components: three *normal strains*  $\varepsilon_{ii} = \varepsilon_i = \frac{\partial u_i}{\partial x_i}$  and three *shear strains*  $\varepsilon_{ij} = 1/2 \left( \frac{\partial u_i}{\partial x_j} + \frac{\partial u_j}{\partial x_i} \right)$ , with  $i \neq j$ .

When a body is subjected to external forces, internal forces are introduced in the body's interior. Within the elasticity theory, it is assumed that these forces are distributed continuously within the solid. The mathematical concept that is used to describe the internal forces in the solid is the *stress tensor*.

Consider a general body subjected to a general external loading as shown in Figure III - 2A. To investigate the internal forces, a virtual section is made through the body as shown in the figure. On this section, consider a small area  $\Delta A$  with normal vector  $\mathbf{n}$ . The resultant surface force acting on  $\Delta A$  is defined by  $\Delta \mathbf{F}$ . The *stress vector* or *traction vector* on this surface is defined as

$$\mathbf{T}(\mathbf{n}) = \lim_{\Delta A \rightarrow 0} \frac{\Delta \mathbf{F}}{\Delta A}. \quad \text{Eq. III - 3}$$

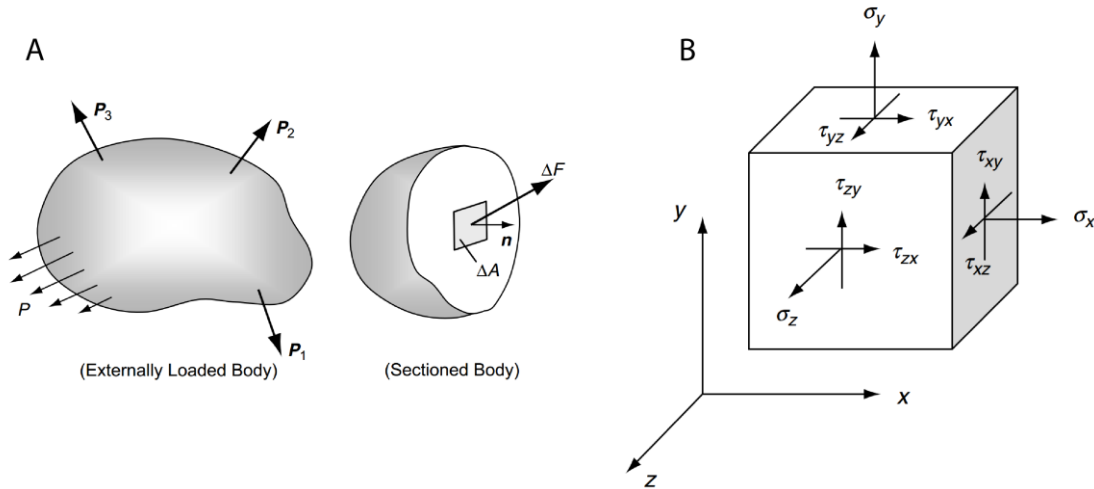


Figure III - 2: A: Sectioned solid body under external loading - B: Components of stress. Both figures from Sadd (2005).

This vector depends on the normal vector of the surface under study. Consider now the special cases in which  $\Delta A$  coincides with each of the three coordinate planes with normal vectors

pointing along the positive axes, as shown in Figure III - 2B. For this case, the traction vectors on each face can be written as:

$$\mathbf{T}(\mathbf{n} = \mathbf{e}_i) = \sigma_{ij}\mathbf{e}_j, \quad \text{Eq. III - 4}$$

where  $\mathbf{e}_i = \{\mathbf{e}_1, \mathbf{e}_2, \mathbf{e}_3\}$  are the unit vectors. The nine quantities  $\sigma_{ij}$  that are the components of the traction vector can be represented by a  $3 \times 3$  tensor, the *Cauchy stress tensor* or, in short, the *stress tensor*. Just as the strain tensor, the stress tensor is symmetric, as can be proven by considering both translational and rotational equilibrium (see Sadd (2005)) in a pyramidal body element. This implies that the stress tensor has just six independent components: three *normal stresses*  $\sigma_{ii} = \sigma_i$  and three *shear stresses*  $\sigma_{ij}$ , with  $i \neq j$ . The shear stresses, i.e. the off-axis components of the stress tensor, are often denoted as  $\tau_{ij}$  instead of  $\sigma_{ij}$  to differentiate them more clearly from the on-axis normal stresses  $\sigma_i$ .

### 1.1.2 Linear, isotropic materials

Mathematical equations that describe the response of a material to certain external stimuli are called '*constitutive equations*'. An example of a constitutive relation is the relation between the stress and strain tensors. In general, the stress in a material is a function of the strains, the rate of strain, the strain history, the temperature and the material properties. In the context of this dissertation, temperature effects are disregarded, because temperature variations in the middle ear are small and slow with respect to the acoustic processes we are interested in. The other four arguments however, will be discussed below. In this subsection, we limit ourselves to non-viscous elasticity theory, in which the strain rate and strain history are not considered. In section 1.2, the theory of viscoelasticity will include them into the framework.

In linear elasticity theory, the 2<sup>nd</sup> order strain and stress tensors are related linearly through the 4<sup>th</sup> order *elasticity tensor*  $\zeta$ :

$$\sigma_{ij} = \zeta_{ijkl}\varepsilon_{kl}. \quad \text{Eq. III - 5}$$

In general, the elasticity tensor has 81 components, but this number is reduced to 36 independent components because of the inherent symmetrical nature of both the strain and stress tensors. The fourth order elasticity tensor is sometimes condensed into the second order *reduced elasticity tensor*  $C$ , containing the linear coefficients that express each unique stress tensor component as a linear combination of all unique strain tensor components:

$$\begin{bmatrix} \sigma_x \\ \sigma_y \\ \sigma_z \\ \tau_{yz} \\ \tau_{zx} \\ \tau_{xy} \end{bmatrix} = \begin{bmatrix} C_{11} & C_{12} & \dots & C_{16} \\ C_{21} & C_{22} & \dots & \\ \vdots & \vdots & \ddots & \\ C_{61} & & & C_{66} \end{bmatrix} \begin{bmatrix} \varepsilon_x \\ \varepsilon_y \\ \varepsilon_z \\ 2\varepsilon_{yz} \\ 2\varepsilon_{zx} \\ 2\varepsilon_{xy} \end{bmatrix}, \quad \text{Eq. III - 6}$$

or, in compact form:  $\sigma_i = C_{ij}\varepsilon_j$ . Reversing this relation reveals the *reduced compliance tensor*  $S$ :  $\varepsilon_i = S_{ij}\sigma_j$ . Using the concept of strain energy, it can be shown that these tensors are symmetric as well, reducing the total number of independent material constants for a linear elastic material to 21 (for proof, see Sadd (2005)).

If a material is isotropic in addition to linear, the elasticity tensor is invariant under all rotations. This implies that the constitutive equation simplifies further so that only two independent parameters are needed to describe the entire behavior of the material under stress:

$$\sigma_{ij} = \lambda \varepsilon_{kk} \delta_{ij} + 2\mu \varepsilon_{ij}, \quad \text{Eq. III - 7}$$

in which the constant  $\lambda$  is *Lamé's constant* and  $\mu$  is the *shear modulus*. Together, these coefficients are called *Lamé's coefficients*. This equation is known as the *generalized Hooke's law* for linear isotropic elastic solids. A more familiar form of Eq. III - 7 describes the strain components as a function of the stress components:

$$\varepsilon_{ij} = \frac{1 + \nu}{E} \sigma_{ij} - \frac{\nu}{E} \sigma_{kk} \delta_{ij}, \quad \text{Eq. III - 8}$$

where  $E$  is the *Young's modulus* and  $\nu$  the *Poisson's ratio* of the material. These are intuitively grasped by imagining an uniaxial stress test, as displayed in Figure III - 3. In the figure, alongside an illustration of the test, the stress and strain tensors are given as well.

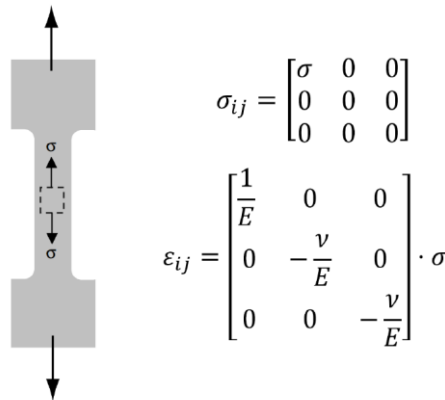


Figure III - 3: Uniaxial stress test and the corresponding stress and strain tensors. Figure adapted from Sadd (2005).

Figure III - 3 illustrates that the Young's modulus is a measure of resistance of strain to stress in the direction of the external force. For the transverse directions, this measure is multiplied by  $-\nu$ , i.e. the Poisson's ratio is the ratio of transverse strain to the axial strain.

### 1.1.3 Linear, orthotropic materials

For some materials, the isotropic material model is remarkably accurate. Off course, many materials require more sophisticated models to be described accurately. Non-isotropic materials are called anisotropic and one subset of anisotropic materials is called *orthotropic*. Orthotropic materials have three mutually perpendicular planes of symmetry. Examples of orthotropic materials are wood, which has a different mechanical strength in the direction of its grains than perpendicular to it, and fiber-reinforced composites. Another example of a material that is approximately orthotropic is the tympanic membrane of mammals, of which the middle layer consists of radially and circumferentially oriented collagen fibers that are mutually perpendicular.

Without loss of generality, we can assume that the mutually perpendicular planes of symmetry coincide with the coordinate planes. In this case, the reduced compliance tensor  $S$  takes the following shape:

$$S_{ij} = \begin{bmatrix} \frac{1}{E_1} & -\frac{\nu_{21}}{E_2} & -\frac{\nu_{31}}{E_3} & 0 & 0 & 0 \\ -\frac{\nu_{12}}{E_1} & \frac{1}{E_2} & -\frac{\nu_{32}}{E_3} & 0 & 0 & 0 \\ -\frac{\nu_{13}}{E_1} & -\frac{\nu_{23}}{E_2} & \frac{1}{E_3} & 0 & 0 & 0 \\ 0 & 0 & 0 & \frac{1}{\mu_{23}} & 0 & 0 \\ 0 & 0 & 0 & 0 & \frac{1}{\mu_{31}} & 0 \\ 0 & 0 & 0 & 0 & 0 & \frac{1}{\mu_{12}} \end{bmatrix}, \quad \text{Eq. III - 9}$$

where  $E_i$  are the Young's moduli in the three material symmetry directions,  $\nu_{ij}$  are the Poisson's ratios defined by  $-\varepsilon_j/\varepsilon_i$  for a stress in the  $i$  direction, and  $\mu_{ij}$  are the shear moduli in the  $i, j$ -planes.

As can be seen in the expression for the reduced compliance tensor in Eq. III - 9, an orthotropic material is described by 12 independent parameters:  $E_1, E_2, E_3, \nu_{12}, \nu_{23}, \nu_{31}, \nu_{21}, \nu_{32}, \nu_{13}, \mu_{23}, \mu_{31}, \mu_{12}$ . In order to keep the elasticity tensor symmetric, however, the Poisson's ratios have to satisfy:

$$\frac{\nu_{ij}}{E_i} = \frac{\nu_{ji}}{E_j}, \quad \text{Eq. III - 10}$$

for all  $i \neq j$ . Therefore, only 9 of the 12 elasticity parameters are independent.

For isotropic materials the Poisson's ratio is limited to  $-1 < \nu < \frac{1}{2}$ , as a higher value leads to a strain energy function that is not positive-definite, which violates conservation of energy, see Sadd (2005). For orthotropic materials however, similar restrictions exist but they have a less compact shape (Lempriere, 1968):

$$|\nu_{ij}| < \sqrt{\frac{E_i}{E_j}}, \quad \text{Eq. III - 11}$$

$$\nu_{12}\nu_{23}\nu_{31} < \left[ 1 - \nu_{12}^2 \left( \frac{E_2}{E_1} \right) - \nu_{23}^2 \left( \frac{E_3}{E_2} \right) - \nu_{31}^2 \left( \frac{E_1}{E_3} \right) \right] / 2 < 1/2 \quad \text{Eq. III - 12}$$

As a consequence, one or even two of the individual Poisson's ratios  $\nu_{ij}$  can have higher values than 0.5, as long as the third ensures that their product does not exceed 0.5. If one is negative, no restriction is placed on the other two.

Li and Barbic (2014) suggested the following simplifications that guarantee the positive-definiteness of the strain energy function, while further reducing the number of tunable parameters from nine to four:

$$\nu_{ij} = \nu \sqrt{\frac{E_i}{E_j}}, \quad \text{Eq. III - 13}$$

$$\mu_{ij} = \frac{\sqrt{E_i E_j}}{2(1 + \nu)}, \quad \text{Eq. III - 14}$$

with  $-1 < \nu < \frac{1}{2}$ . These relations reduce the number of independent elasticity parameters for orthotropic materials to four:  $E_1, E_2, E_3, \nu$ , while still satisfying the inequalities in Eq. III - 11 and Eq. III - 12. These relations are used in the finite element models of the middle ear presented in Chapter 6 and Chapter 7 of this thesis for the orthotropic elasticity parameters of the tympanic membrane.

In the case of the tympanic membrane, the description needs to allow for different material parameters in the circular, radial, and transverse direction. Note that this is still orthotropic as it satisfies the condition of perpendicularity of the planes of symmetry, although the directions of these planes are different for different points in the material. In this case, the elasticity and compliance tensors will have the same appearance, but the parameters are defined relative to the base vectors of the cylindrical coordinate system, i.e. the vectors  $\mathbf{e}_i$ , with  $i = \{r, \theta, z\}$ . The strain components  $\varepsilon_i$  are then defined by:

$$\begin{aligned}\varepsilon_r &= \frac{\partial u_r}{\partial r}, \varepsilon_\theta = \frac{1}{r} \left( u_r + \frac{\partial u_\theta}{\partial \theta} \right), \varepsilon_z = \frac{\partial u_z}{\partial z}, \\ \varepsilon_{r\theta} &= \frac{1}{2} \left( \frac{1}{r} \frac{\partial u_r}{\partial \theta} + \frac{\partial u_\theta}{\partial r} - \frac{\partial u_\theta}{r} \right), \\ \varepsilon_{\theta z} &= \frac{1}{2} \left( \frac{\partial u_\theta}{\partial z} + \frac{1}{r} \frac{\partial u_z}{\partial \theta} \right), \\ \varepsilon_{zr} &= \frac{1}{2} \left( \frac{\partial u_r}{\partial z} + \frac{\partial u_z}{\partial r} \right),\end{aligned}$$

Eq. III - 15

in which  $u_i$  are the components of the displacement vector  $u$  in cylindrical coordinates.

## 1.2 Viscoelasticity: time dependency in the time domain

Viscoelasticity is the property of materials that exhibit both viscous and elastic characteristic when undergoing deformation. The basic mechanical models for these characteristics are the dashpot (for viscosity) and spring (for elasticity). Synthetic polymers, wood, metals at high temperatures, and biological soft tissue all display significant viscoelastic effects. For these materials, the stress is not only dependent on the strain and material properties, but also on the strain rate and strain history. This means that time becomes a parameter in the constitutive equations of these materials.

The deformation response of a purely elastic material to a static load is instantaneous, without any time dependency, and the recovery after release of the load is complete and instantaneous as well. The mechanical response of soft biological tissues like the tympanic membrane, however, is time dependent. The time dependency arises from viscous interactions in the material. Time dependency also becomes apparent when the loading conditions in the system under consideration yield accelerations so that inertial effects are no longer negligible.

Linear viscoelastic behavior is often modeled by a mechanical combination of springs and dashpots in various configurations. For large strains, non-linear viscoelastic models should be employed, but as they are not relevant for this dissertation, they are not covered here.

If a force  $F$  acts on a spring, it will extend by  $x = \frac{F}{R}$ , where  $R$  is the spring constant (note the similarity to the constitutive equation  $e_{ii} = \frac{\sigma}{E}$  relating the normal strain to the stress in isotropic elastic materials, see Figure III - 3). The force  $F$  and extension  $x$  of the spring are equivalent to stress  $\sigma$  and strain  $\varepsilon$  in a solid, so these symbols will be used from now on. Therefore, the spring equation becomes  $\varepsilon = \frac{\sigma}{R}$ . If a force  $\sigma$  acts on a linear viscous dashpot, the time derivative of the displacement  $\dot{\varepsilon} = \frac{d\varepsilon}{dt}$  is proportional to the force:  $\sigma = \eta \dot{\varepsilon}$ .

The most simple viscoelastic material models are the Maxwell and Kelvin-Voigt models. They are combinations of one spring element and one dashpot element in series and parallel configuration, respectively, and are illustrated in Figure III - 4.

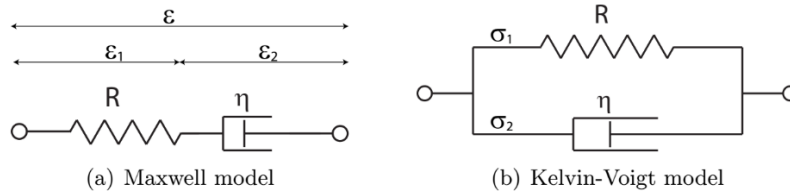


Figure III - 4: Two simple models for viscoelastic materials. (a) Maxwell model, combining a spring and a dashpot in series and (b) Kelvin-Voigt model, combining the same elements in parallel.

For the Maxwell model, the stress-strain relations of the spring and the dashpot are  $\sigma = R\varepsilon_1$  and  $\sigma = \eta\dot{\varepsilon}_2$ . Since both elements are connected in series, they experience the same stress. The total strain is then  $\varepsilon = \varepsilon_1 + \varepsilon_2$ . The constitutive equation of the Maxwell model is therefore:

$$\dot{\varepsilon}(t) = \frac{\dot{\sigma}(t)}{R} + \frac{\sigma(t)}{\eta}. \quad \text{Eq. III - 16}$$

For the Kelvin-Voigt model, the stress-strain relations are  $\sigma_1 = R\varepsilon$  and  $\sigma_2 = \eta\dot{\varepsilon}$ . Since both elements are in parallel, they experience the same strain. The total stress is then  $\sigma = \sigma_1 + \sigma_2$ . The constitutive equation of the Kelvin-Voigt model is therefore:

$$\dot{\varepsilon}(t) + \frac{R}{\eta} \varepsilon(t) = \frac{\sigma(t)}{\eta}. \quad \text{Eq. III - 17}$$

Both of these models are useful in some scenarios but also have their limitations and exhibit unphysical behavior under certain circumstances. The Maxwell model is a poor model for viscoelastic *creep*, a phenomenon where a constant external stress is applied to a material and the material needs time to reach its final strain. The Maxwell model continues to deform indefinitely towards infinity when it is subjected to a constant stress, which is obviously in contradiction with physical viscoelastic materials.

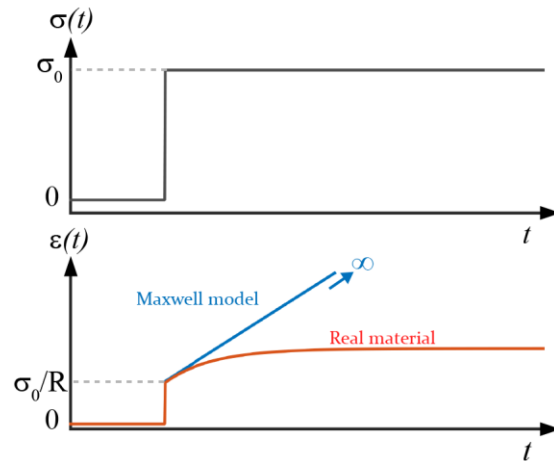


Figure III - 5: Creep in a real viscoelastic material and in the Maxwell model.

The Kelvin-Voigt model on the other hand is a poor model for viscoelastic *stress relaxation*. In this phenomenon, the material is subjected to an instantaneous and constant strain that is maintained for a certain time. In the case of a physical viscoelastic material, the initially high (but finite) stress, right after the onset of the strain, “relaxes” into its final state of a lower stress. However, an instantaneous strain applied to the Kelvin-Voigt model however will induce an infinite stress in the model, which again is an unphysical result.

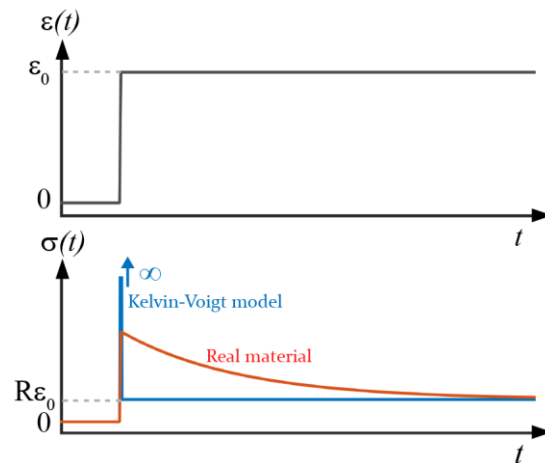


Figure III - 6: Stress relaxation in a real viscoelastic material and in the Kelvin-Voigt model.

In order to model these phenomena realistically, the model needs to include more elements. The standard linear solid model adds a spring in parallel to a Maxwell model. This is the simplest model that simulates both creep and stress relaxation realistically.

An even more general model is the Generalized Maxwell model, in which a spring is in parallel with  $m$  Maxwell models, all of which can possess different parameters for the spring and the dashpot.

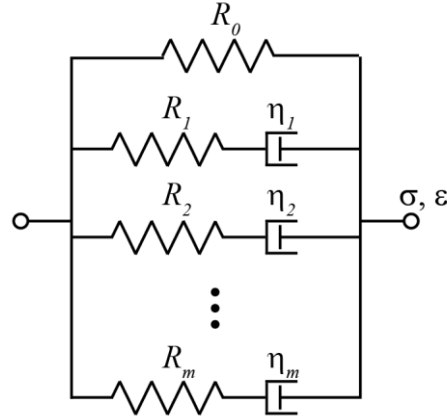


Figure III - 7: Generalized Maxwell model with  $m$  branches.

The total stress of this model is the sum of the stresses in each element. For the first element, the stress due to a strain  $\varepsilon$  is  $\sigma_0 = R\varepsilon$ . For the  $j$ -th Maxwell branch, the strain is represented by:

$$\sigma_j(t) = \frac{D}{D/R_j + 1/\eta_j} \varepsilon(t), \quad \text{Eq. III - 18}$$

Where  $D = d/dt$  denotes differentiation with respect to time. The total stress of the generalized Maxwell model is then:

$$\sigma(t) = \sum_{j=0}^m \sigma_j(t) = \left( R_0 + \sum_{j=1}^m \frac{R_j D}{D + R_j/\eta_j} \right) \varepsilon(t). \quad \text{Eq. III - 19}$$

The larger number of parameters of the generalized Maxwell model compared to the standard linear solid model allows the model to characterize material properties on different time scales, and therefore also for different frequency ranges.

### 1.3 Vibration theory: time dependency in the frequency domain

#### 1.3.1 One dimensional damped harmonic oscillator: free and driven

A one dimensional damped harmonic oscillator can be represented by a mass that is attached to a fixed wall through a parallel combination of a spring and a dashpot. The equation of motion for this system is:

$$m\ddot{x} + c\dot{x} + Rx = 0, \quad \text{Eq. III - 20}$$

with  $m$  the mass of the oscillating particle,  $c$  the damping coefficient,  $R$  the spring constant or stiffness of the spring and  $x$  the displacement of the particle relative to its neutral 'resting' position. In this equation, we introduced the dot-notation for time derivatives:  $\dot{x} = dx/dt$  and  $\ddot{x} = d^2x/dt^2$

In many applications, the object of interest is stimulated harmonically by an external force. This force can be represented by  $F(t) = |F| \sin(i\omega t)$  or by the real part of  $F(t) = \Re(|F|e^{i\omega t})$ . In physics literature, it is conventional to leave out the  $\Re$  symbol and calculate further with the exponentials, as it is mathematically more elegant (this is called the ‘analytical representation’). This is fine as long as we remember to take the real part of the final solution when we compare the theory to physical phenomena. The equation of motion of the sinusoidally driven oscillator is:

$$m\ddot{x} + c\dot{x} + Rx = |F|e^{i\omega t}. \quad \text{Eq. III - 21}$$

This linear differential equation has by definition a solution that oscillates with the same angular frequency  $\omega$  as the force input. We can therefore propose a solution of the form  $x = Ae^{i(\omega t + \phi)}$ , that after substitution in Eq. III - 21 turns out to be:

$$x(t) = \frac{F/m}{\omega_0^2 - \omega^2 + 2i\gamma\omega} e^{i\omega t}, \quad \text{Eq. III - 22}$$

where  $\gamma = c/2m$  and  $\omega_0 = \sqrt{R/m}$  ( $\omega_0$  is called the *resonance* or *natural* frequency of the system). The amplitude and phase of this motion are given by:

$$A = \frac{\frac{F}{m}}{\sqrt{(\omega_0^2 - \omega^2)^2 + 4\gamma^2\omega^2}} \quad \text{Eq. III - 23}$$

$$\phi = \text{atan}\left(-\frac{2\omega\alpha}{\omega_0^2 - \omega^2}\right). \quad \text{Eq. III - 24}$$

Figure III - 8 shows the displacement and velocity amplitude and phase of a system with a certain set of reference parameters and of systems with either increased stiffness, increased mass or decreased damping. From the amplitude plot, it can be seen that the response of a one-dimensional damped oscillator is stiffness-dominated at low frequencies (i.e. frequencies below its resonance frequency), mass-dominated at high frequencies (i.e. frequencies above its resonance) and damping dominated around its resonance frequency. In the phase plot, it can be seen that the force and displacement are in phase at low frequencies, that the phase of the displacement undergoes a gradual phase transition around the resonance and that it lags behind with half a period at high frequencies.

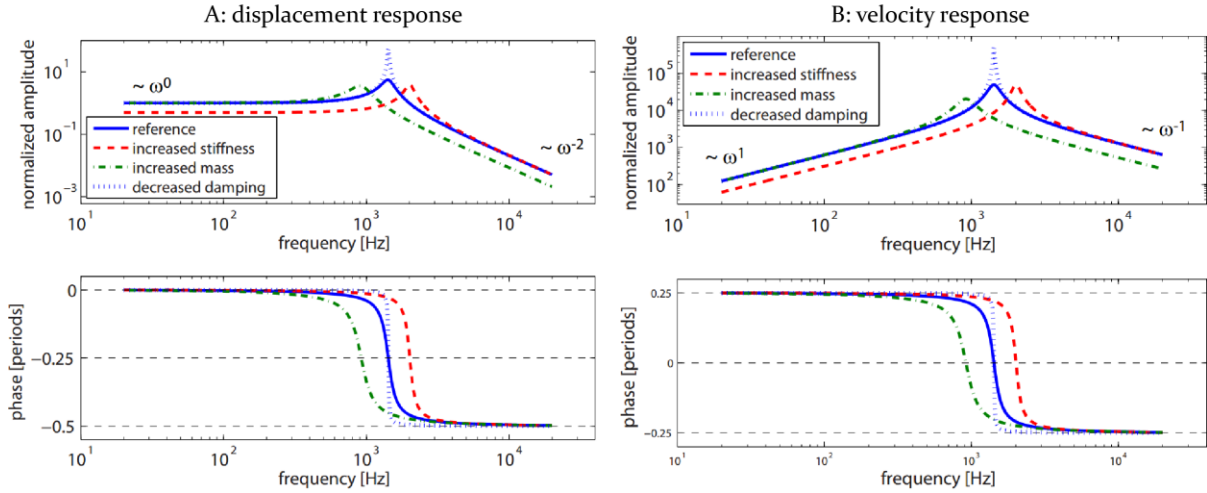


Figure III - 8: A: Displacement response and B: velocity response of a one-dimensional damped harmonic oscillator. The parameters for the reference model are  $F = 1 \cdot 10^{-3}$  N,  $R_1 = 400$  N/m,  $\eta_1 = 8.13 \cdot 10^{-3}$  Ns/m,  $m_1 = 50 \cdot 10^{-7}$  kg; for the dashed red curve, the stiffness is increased to  $R_2 = 800$  N/m; for the dashed-dotted green curve, the mass is increased to  $m_2 = 120 \cdot 10^{-7}$  kg; for the dotted blue curve the damping is decreased to  $\eta_2 = 0.813 \cdot 10^{-3}$  Ns/m. Figure from Aernouts (2012a).

### 1.3.2 Approaches to include damping: Rayleigh damping and loss factor damping

In order to provide a value for the damping coefficient in the equation of motion (Eq. III - 21), there are two different commonly used approaches: Rayleigh damping and loss factor damping.

In Rayleigh damping, the damping coefficient is a linear combination of the mass and the stiffness of the system:  $c = \alpha m + \beta R$ . It requires two parameter values,  $\alpha$  and  $\beta$ , and has been used successfully in many fields of application. These parameters can be selected in order to match the modal damping of two modes.

In loss factor damping, damping is included not by utilizing a damping coefficient but a complex stiffness  $R^*$ . When working in the frequency domain, this is essentially equivalent to an explicit damping coefficient. This can be shown by introducing a complex spring constant in the equation of motion of a harmonically driven oscillator:

$$m \frac{d^2 x}{dt^2} + R^* x = |F| e^{i\omega t}. \quad \text{Eq. III - 25}$$

Here,  $R^* = R' + iR''$ . Since we assume the harmonic solution in the form of  $x = A^* \exp(i\omega t)$ , one has  $\dot{x} = i\omega x$  and hence

$$\Leftrightarrow m\ddot{x} + \frac{R''}{\omega}\dot{x} + R'x = |F|e^{i\omega t}. \quad \text{Eq. III - 26}$$

In this final equation, we can see that the imaginary part of the complex modulus, divided by the angular frequency,  $R''/\omega$ , is equivalent to the damping coefficient  $c$  in the case of an harmonic oscillation.

The real part of the stiffness  $R'$  is called the storage modulus, the imaginary part  $R''$  the loss modulus. The storage modulus is a measure for how much energy is present in the system as potential or kinetic energy, i.e. the elastic portion of the energy. The loss modulus is a measure for the energy that is dissipated every cycle (i.e. it is the area between the curves in a hysteresis plot). The loss factor is defined as  $\eta = \frac{E''}{E'}$ .

For example, we could apply this for the generalized Maxwell model, for which the time-dependent relation between the overall stress and strain is given by Eq. III - 19. If the applied load is an oscillatory strain containing a single angular frequency, the strain can be written as:  $\varepsilon(t) = \varepsilon_0 e^{i\omega t}$ . In the case of a linear, damped system, the stress response is also an oscillation at the same frequency with phase angle  $\delta$ :

$$\sigma(t) = \sigma_0 e^{i(\omega t + \delta)} = \underbrace{\sigma_0 e^{i\delta}}_{\sigma^*} e^{i\omega t} = \sigma^* e^{i\omega t}. \quad \text{Eq. III - 27}$$

The complex modulus is defined as the ratio between the complex values of the strain and the stress (i.e. including information on their phase angles):

$$R^*(\omega) = \frac{\sigma_0 e^{i\delta}}{\varepsilon_0} = \frac{\sigma^*}{\varepsilon_0} = R_0 + \sum_{j=1}^m \frac{i\omega R_j}{i\omega + R_j/\eta_j}. \quad \text{Eq. III - 28}$$

This storage and loss modulus are then given by:

$$R'(\omega) = R_0 + \sum_{j=1}^m \frac{R_j \tau_j^2 \omega^2}{1 + \tau_j^2 \omega^2} \quad \text{Eq. III - 29}$$

$$R''(\omega) = \sum_{j=1}^m \frac{R_j \tau_j \omega}{1 + \tau_j^2 \omega^2} \quad \text{Eq. III - 30}$$

It can be seen from this example that both the stiffness and the loss modulus of the the generalized Maxwell model are frequency dependent. This is true for many other viscoelastic models as well.

### 1.3.3 Relation between loss factor and Rayleigh damping

As demonstrated by Eq. III - 26, the imaginary part of the complex modulus, divided by the angular frequency,  $R''/\omega$ , is equivalent to the damping coefficient  $c$ . Thus  $c = R''/\omega$ .

On the other hand, if Rayleigh damping is employed to model damping, the damping coefficient is given by  $c = \alpha m + \beta R$ . Here,  $R$  is equivalent to the real part of the complex spring constant, i.e.  $R = R'$ . Thus  $c = \alpha m + \beta R'$ .

Equating these two forms of  $c$  provides a relation between the loss factor and the Rayleigh coefficients:

$$\begin{aligned} \frac{R''}{\omega} &= \alpha m + \beta R' \\ \text{(using } \eta &= \frac{R''}{R'}\text{)} &\Leftrightarrow \eta = \frac{m}{R'} \alpha \omega + \beta \omega \\ \text{(using } \omega_0^2 &= \frac{R'}{m}\text{)} &\Leftrightarrow \eta = \alpha \frac{\omega}{\omega_0^2} + \beta \omega \end{aligned} \quad \text{Eq. III - 31}$$

At the natural frequency  $\omega_0$ , the relation is thus  $\eta = \alpha \frac{1}{\omega_0} + \beta \omega_0$ . Extending this relation to other frequencies (which is an assumption) allows a comparison between the loss factor and Rayleigh damping at all frequencies:

$$\eta = \alpha \frac{1}{\omega} + \beta \omega. \quad \text{Eq. III - 32}$$

### 1.3.4 Damping in solid mechanics

Sections 1.3.1 and 1.3.2 described one dimensional damped systems and introduced the concept of a complex spring constant. The analogue concept for this in solid mechanics is a complex elasticity modulus, e.g. a complex Young's modulus:

$$E^* = E' + iE'' = E'(1 + i\eta), \quad \text{Eq. III - 33}$$

where the loss factor  $\eta = E''/E'$  was introduced.

In general, the entire elasticity matrix is multiplied by the factor  $(1 + i\eta)$ . For an isotropic, linearly elastic material, this is equivalent to multiplying the Young's modulus with this same factor, such as in Eq. III - 33. If the material is orthotropic, all orthotropic moduli are multiplied by this factor. This is how damping was incorporated in the material definition for the tympanic membrane in the following three chapters of this dissertation.

## 2. Middle ear modeling

The mammalian middle ear, its anatomy and its function, were presented in the introduction of Part II of this thesis. Models of the mechanics of the middle ear system exist in many different

incarnations, from very simple to very sophisticated. This section will provide a condensed overview of the different types of middle ear models that are developed throughout history and their properties. For more elaborate overviews of middle ear modeling or a subcategory of it, the reader is encouraged to consult Funnel et al (2013), Funnel et al. (2012), Aernouts (2012a), Vollandri et al. (2011) and Vollandri et al. (2012), although this list is certainly not extensive.

The middle ear is of course more than just a mechanical system: it has physiological aspects (e.g., muscle contraction, healing) and biochemical aspects (e.g., gas exchange) that directly affect its mechanical behavior. However, even when disregarding these effects, the modeling of middle ear mechanics is a considerable challenge for many reasons. First, the geometry of the system is highly irregular and complicated, as well as strongly different in shape and size, even among individuals of the same species (e.g., De Greef et al. (2015), i.e. Chapter 3 of this thesis). Its overall dimensions are in the range of tens of millimeters but some important structures have dimensions in the micrometer range, such as the eardrum thickness and the width of the bony core in the lenticular process of incus. Relevant displacements of the system in response to everyday acoustical stimulation are in the order of nanometers, while the displacement response to everyday quasi-static pressure variations is in the order of millimeters. This immediately highlights that the range of pressure variations (micropascals to kilopascals) is very large as well and is correlated to the time scales on which they happen. These time scales range from fractions of milliseconds (20 kHz variations) for up to minutes (mHz variations).

The challenge of modeling the middle ear is further increased by the presence of many different tissue types involved: bone; muscles; cartilage, both calcified and uncalcified; synovial fluid; mucosal layers; dense, regular connective tissue; loose connective tissue. Furthermore, the mechanical properties of air and water (in the cochlea) are directly involved as well.

This section will focus on models of the mechanical aspects of the middle ear with special attention for models that are adequate for the acoustic response of the system. Geometry modeling, i.e. the branch of research that deals with constructing a realistic shape representation of the system at hand, is not elaborately described here. It is however a necessary input for spatially distributed modeling approaches such as the finite element method.

## 2.1 Categories of model approaches

### *2.1.1 Analytical vs numerical*

In general, models can be categorized in analytical and numerical models. Analytical models can be solved exactly using algebra and calculus with limited arithmetic. These models typically contain very few parameters and degrees of freedom compared to numerical models, which has both advantages (easier to handle) and disadvantages (less flexible). A simple example would be to represent the entire middle ear system by a single standard linear solid model (see section 1.2 of this introduction). Numerical models involve less analysis and more arithmetic than analytical models. Numerical models can sometimes be solved exactly (in which case they are

actually analytical models solved using numerical techniques, without assumptions and approximations), but often some assumptions are made, such as discretization of the spatial extent of the object. It is clear that there is no strict border between analytical and numerical models, but rather a smooth continuum.

In the context of middle ear modeling, the first analytical models were based on the ‘curved-membrane’ hypothesis of Helmholtz (1873) (see section 2.3.3 of the introduction of Part II of this thesis) and was further developed by Esser (1947) and by Guelke and Keen (1949). Other attempts to model the eardrum analytically were made were formulated by Wada and Kobayashi (1990), but they were forced to make the assumption of a flat rather than a conical eardrum. Approximate analytical models were also developed in the past, such as the asymptotic technique used by Rabbit and Holmes (1988), and they were more successful in replicating the eardrums behavior.

#### *2.1.2 Parametric vs non-parametric*

Another way to categorize middle ear models is parametric vs non-parametric. In parametric models, the model is formulated as a function of tunable parameters so that it can be adapted to fit into multiple scenarios. Non-parametric models represent a system simply by an array of data, such as a look-up table, and is therefore highly inflexible. An example is the input over output ratio of the middle ear, i.e. the stapes velocity over ear canal pressure. Hybrid approaches are possible as well. For example, in the middle ear model presented in chapters 6 and 7 of this thesis, a finite element model of the middle ear system is presented in which most parts are parametric. The presence of the cochlea however, is modeled by a set of discrete values for the cochlear impedance from experimental measurements at separate frequencies and is therefore non-parametric.

#### *2.1.3 Black-box vs white-box (= structured)*

Another distinction could be made on the basis of the degree in which the internal structure of the model represents internal components of the modeled system. On the one hand, black-box models only by its input and output and have no internal structure related to the components and configuration of the system being modeled. On the other hand, structural models (or white-box models) have at least some internal structure established by a consideration of the system being modeled. Of course, models can have considerably different degrees of internal structure. For example, a single ligament in the middle ear could be represented by one branch of electrical or mechanical components in a circuit model, or by thousands of spatially distributed tetrahedral elements in a finite element model representing the actual shape of the model.

#### *2.1.4 Lumped-parameter vs distributed models*

In lumped-parameter models, the spatial extents of the components is neglected. Distributed parameter models do take this into account so that for example morphological details are allowed to play an explicit, significant role.

## 2.2 Electrical circuit models

A first type of model that has been used often in middle ear research is (electromagnetic) circuit models. It is an example of an analytical, parametric, white-box, lumped parameter model. This modelling approach is based on the solid theoretical framework that was originally developed for electrical circuits containing resistors, capacitors and inductors. The two basic laws for these circuits are the Kirchoff laws:

- Current law: The sum of the currents at each node is zero (i.e. charge is conserved at all times in a closed circuit).
- Voltage law: The sum of the voltages around each loop is zero (i.e. energy is conserved at all times in a closed circuit).

Figure III - 9 shows an example of a circuit model.

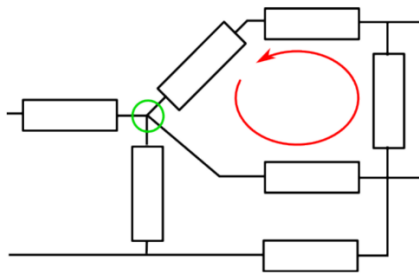


Figure III - 9: Example of an electrical circuit model. The green circle indicates a node in which the net sum of all currents is zero (i.e. all current flowing into the node leaves the node). The red arrow indicates a closed loop around which the sum of voltages is zero. Figure from Funnel et al. (2012).

Electrical circuits can be useful representations of mechanical and acoustical systems because the differential equations describing them have the same shape as the equations describing springs, masses and dashpots. The analogy also applies for the equations of acoustical elements. Table III - 1 illustrates the analogies of physical quantities and equations between electrical circuits, mechanical systems and acoustical systems.

Many circuit models for the middle ear were proposed in the past, starting in 1949 (Onchi 1949). Zwislocki (1957) was the first to also estimate values for the elements of the circuit.

A more flexible approach to model the complex middle ear system was developed by Hudde and Weistenhofer (1997, 2000, 2006). They introduced the notion of 3D generalized circuit models in which each velocity is replaced by six velocities (three translational and three rotational) and each force is similarly replaced by six forces. It is however still less general and explicit than continuum methods such as the finite element method, which is introduced in the next section. Furthermore, although circuit models have proven to be able to reproduce realistic predictions for middle ear mechanics, they are rather abstract and difficult to interpret in an intuitive manner.

Table III - 1: Analogies between quantities and physical relations in electrical, mechanical and acoustical theories.

<b>Electrical</b>	<b>Mechanical</b>	<b>Acoustical</b>
Voltage $V$	Force $F$	Pressure $P$
Current $I$	Velocity $v$	Volume velocity $U$
Resistance $R$	Viscosity $\eta$ (dashpot)	Resistance $R$
Inductance $L$	Mass $m$	Mass $M$
Capacitance $C$	Compliance $1/k$ (spring)	Compliance $C$ (volume)
$V(t) = R \cdot I(t)$	$F(t) = \eta \cdot v(t)$	$P(t) = R \cdot U(t)$
$V(t) = L \frac{dI(t)}{dt}$	$F(t) = m \frac{dv(t)}{dt}$	$P(t) = M \frac{dU(t)}{dt}$
$V(t) = \frac{1}{C} \int_{-\infty}^t I(t) \cdot dt$	$F(t) = k \int_{-\infty}^t v(t) \cdot dt$	$P(t) = \frac{1}{C} \int_{-\infty}^t U(t) \cdot dt$

### 3. The finite element method

The finite element (FE) method is a numerical modelling technique that is generally used for systems of irregular shape and containing multiple distributed parameters, cases in which analytical solutions of the describing differential equations are unattainable. In FE modeling, the arbitrary shape of the object is divided into a mesh of elements of finite size with geometries that are simple enough to permit analytically solving the differential equations within individual elements. In the case of mechanical modeling, the mechanical response of each element is expressed as a function of the displacements of its edges. These expressions can be derived from the material properties and the constitutive stress-strain relations of the material. By coupling the physical quantities of the element nodes of neighboring elements, the entire system can be solved.

The approach may be summarized as follows (Bonet and Wood, 1997): "It is a procedure whereby the solid behavior described at an infinity of points is approximated in terms of a finite number of points, called nodes, located at specific points in the solid. These nodes are used to define regions, called finite elements, over which both the geometry and the primary variables in the governing equations are approximated. For example, in the stress analysis of a solid the finite element could be a tetrahedron defined by four nodes and the primary variables the three displacements in the Cartesian directions. The governing equations describing the nonlinear behavior of the solid are usually recast in a so-called weak integral form using, in the case of mechanics, the principle of virtual work. The finite element approximations are then introduced into these integral equations, and a standard textbook manipulation yields a finite

set of non-linear algebraic equations in the primary variable. These equations are then usually solved using the Newton-Raphson iterative technique.”

FE analysis has been developed so extensively over the last 50 years that it is impossible to give a full overview in just one introductory section. Therefore, what follows is only a very brief introduction to this subject and the reader is referred to more general textbooks such as De Arantes E Oliviera (1968), Bonet and Wood (1997), Zienkiewicz and Taylor (2000) among many others. The sections that follow are roughly based on the introduction on the subject by Funnell et al. (2012).

### 3.1 Basis functions

One of the fundamental principles behind FE analysis is the theorem of minimum potential energy in mechanics. It states that the admissible function<sup>11</sup> that minimizes the functional  $\mathcal{F}(f(x))$  expressing the potential energy of a system is the solution of the system. In practice, it is often very difficult to find the one truly minimizing function for the functional, so the search is limited to a particular subset of admissible functions. The subset that is often chosen is the space of linear combinations of  $n$  admissible basis functions  $g_i(x)$ , i.e. all functions of the form:

$$g(x) = \sum_{i=1}^n c_i g_i(x). \quad \text{Eq. III - 34}$$

Here,  $c_i$  are the coefficients defining the function  $g(x)$ . The basis functions are, by definition, mutually linearly independent. Therefore, the problem is reduced to finding the values for  $c_i$  that minimize the functional. This requires finding the derivative of the functional with respect all  $c_i$  and equating them to zero, resulting in a set of  $n$  equations in  $c_i$ :

$$\frac{\partial}{\partial c_i} \mathcal{F}(g(x)) = \frac{\partial}{\partial c_i} \mathcal{F} \left( \sum_{i=1}^n c_i g_i \right) = 0 \text{ for } i = 1, \dots, n. \quad \text{Eq. III - 35}$$

Thus, the problem is reduced to solving a set of  $n$  linear equations in  $n$  unknowns.

### 3.2 Example: Analysis of a single triangular element

The approach introduced in the previous section can be interpreted more easily if it is applied to a single triangular element using only three basis functions. This could be applied to, for

---

<sup>11</sup> An admissible function is one that satisfies the boundary conditions of the problem as well as certain continuity conditions.

example, a plane membrane, where the functional would be a function of the displacement  $w(x, y)$  in every point. In theory, the ultimate result is independent of the choice of basis functions, as long as they are admissible and linearly independent. A possible choice of basis function is the set  $\{1, x, y\}$ . The displacement at any point within the element is then given by:

$$u(x, y) = c_1 + c_2x + c_3y. \quad \text{Eq. III - 36}$$

Now, the set of equations can be constructed by expressing the potential energy as a function the displacement  $u(x, y)$  and equating its derivative to zero. The set of equation can then be written in a matrix form:

$$Ac = Bp. \quad \text{Eq. III - 37}$$

Both  $A$  and  $B$  are  $3 \times 3$  matrices of which the elements are functions of the coordinates of the nodes of our triangular element and material properties.  $c$  is the vector  $(c_1, c_2, c_3)^T$  and the vector  $p$  contains the nodal values of the pressure field.

To be able to combine this equation with similar equations representing other elements, it must be written in terms of the displacements  $u_i$  at the three nodes. If we write out Eq. III - 36 for the three nodes we obtain:

$$\begin{pmatrix} u_1 \\ u_2 \\ u_3 \end{pmatrix} = \begin{pmatrix} 1 & x_1 & y_1 \\ 1 & x_2 & y_2 \\ 1 & x_3 & y_3 \end{pmatrix} \begin{pmatrix} c_1 \\ c_2 \\ c_3 \end{pmatrix} \quad \text{Eq. III - 38}$$

Or, in matrix notation  $\mathbf{u} = X\mathbf{c}$ . Since the points are not collinear, matrix  $X$  is invertible and the solution of the system is  $\mathbf{c} = X^{-1}\mathbf{u}$ , which can be inserted into Eq. III - 37 so that:

$$\begin{aligned} \underbrace{AX^{-1}}_{K_e} \mathbf{u} &= \underbrace{Bp}_{\mathbf{f}} \\ \Leftrightarrow K_e \mathbf{u} &= \mathbf{f}, \end{aligned} \quad \text{Eq. III - 39}$$

where  $K_e$  is the element stiffness matrix and  $\mathbf{f}$  a vector of nodal forces. The components of  $K_e$  are therefore ratios of forces over displacements.

### 3.3 Coupling the elements and applying boundary conditions

Extending the study to two neighboring triangles illustrates how the elements are coupled in the FE method. Suppose that the triangles share two nodes, as illustrated in Figure III - 10.

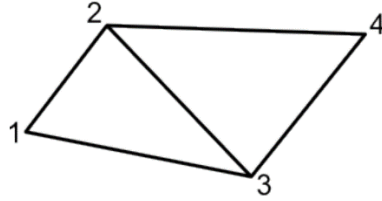


Figure III - 10: Two neighboring triangular elements, sharing two nodes.

For both elements, the nodal displacements and the nodal loads are linked through the element stiffness matrices of the elements:

$$\text{Element 1: } \begin{pmatrix} a_{11} & a_{12} & a_{13} \\ a_{21} & a_{22} & a_{23} \\ a_{31} & a_{32} & a_{33} \end{pmatrix} \begin{pmatrix} u_1 \\ u_2 \\ u_3 \end{pmatrix} = \begin{pmatrix} f_1 \\ f_2 \\ f_3 \end{pmatrix}$$

$$\text{Element 2: } \begin{pmatrix} b_{11} & b_{12} & b_{13} \\ b_{21} & b_{22} & b_{23} \\ b_{31} & b_{32} & b_{33} \end{pmatrix} \begin{pmatrix} u_2 \\ u_3 \\ u_4 \end{pmatrix} = \begin{pmatrix} g_2 \\ g_3 \\ g_4 \end{pmatrix}.$$

Since the elements are connected at nodes 2 and 3, the displacements  $u_2$  and  $u_3$  are the same in both equations. Therefore, the equations can be combined as follows:

$$\begin{pmatrix} a_{11} & a_{12} & a_{13} & 0 \\ a_{21} & a_{22} + b_{11} & a_{23} + b_{12} & b_{13} \\ a_{31} & a_{32} + b_{21} & a_{33} + b_{22} & b_{23} \\ 0 & b_{31} & b_{32} & b_{33} \end{pmatrix} \begin{pmatrix} u_1 \\ u_2 \\ u_3 \\ u_4 \end{pmatrix} = \begin{pmatrix} f_1 \\ f_2 + g_2 \\ f_3 + g_3 \\ g_4 \end{pmatrix}. \quad \text{Eq. III - 40}$$

This approach can be scaled to an arbitrarily large number of elements, so that the matrix equation of the system becomes:

$$K\mathbf{u} = \mathbf{f}, \quad \text{Eq. III - 41}$$

where  $K$  is the system's stiffness matrix of size  $N \times N$  (with  $N$  the total number of nodes/vertices in the entire mesh), and  $\mathbf{u}$  and  $\mathbf{f}$  are both vectors with length  $N$ , containing the nodal displacement of the entire mesh and the nodal forces, respectively.

Finally, the boundary conditions of the full FE problem can be imposed on the matrix equation Eq. III - 41 by prescribing values for some of the displacements or for their derivatives or second derivatives with respect to time.

### 3.4 Solving the formulated problem

When the problem to be solved involves only a stationary study, i.e. time-dependence is disregarded and only the equilibrium state of the system is calculated, the solution to the problem is simply found by solving the matrix equation Eq. III - 41:  $\mathbf{u} = K^{-1}\mathbf{f}$ .

Consider the free response of an undamped vibrating system. The nodal forces are given by  $\mathbf{f} = -M\ddot{\mathbf{u}}$  and the system equation is then

$$K\mathbf{u} + M\ddot{\mathbf{u}} = \mathbf{0}. \quad \text{Eq. III - 42}$$

If we assume a solution of the shape  $\mathbf{u} = \mathbf{U}e^{i\omega t}$ , the vector of accelerations can be written as  $\ddot{\mathbf{u}} = -\omega^2\mathbf{u}$  and the problem becomes an eigenvalue problem:

$$K\mathbf{u} + \omega^2 M\mathbf{u} = \mathbf{0} \Leftrightarrow M^{-1}K\mathbf{u} = \omega^2\mathbf{u}. \quad \text{Eq. III - 43}$$

Solving this problem provides the natural frequencies of the system ( $\omega_i$ ) and the corresponding mode shapes ( $\mathbf{u}_i$ ). In general, systems with irregular shapes and a large number material parameters, such as the mammalian middle ear, need to be models with many degrees of freedom and will have many, densely spaced natural frequencies in a relatively small frequency range. Both for matrix inversion problems and eigenvalue problems, many algorithms have been proposed over time. Often, these algorithms are coded into FE software packages and the most appropriate one is selected automatically. In general, the stiffness equations are non-linear (as  $K$  can depend on the displacements in  $\mathbf{u}$  themselves) and must be solved iteratively, e.g. using the Newton-Raphson algorithm.

If the formulated problem involves a damped vibrational system, the equations become second-order differential equations and introduce the damping matrix  $C$ :

$$K\mathbf{u} + C\dot{\mathbf{u}} + M\ddot{\mathbf{u}} = \mathbf{f}. \quad \text{Eq. III - 44}$$

If the user is only interested in the steady-state response from harmonic loads, a frequency domain study (or harmonic analysis) can be performed. For this type of study, one can model damping using Rayleigh damping or using a complex modulus (see sections 1.3.2 to 1.3.4 of this introduction). If Rayleigh damping is employed, the damping matrix is expressed as a linear combination of the stiffness and mass matrices:  $C = \alpha K + \beta M$ . If a complex modulus is employed, the entire stiffness matrix is multiplied by  $(1 + i\eta)$ . For a frequency domain study, all loads are considered harmonic with the same stimulation frequency  $f = \omega/2\pi$ , and the linear displacement response  $u(t) = |u| \exp(i(\omega t + \phi))$  is calculated.

## 4. Overview of part III of this dissertation

Chapter 5 presents a FE model of the human tympanic membrane (TM) and is a focused study of its viscoelastic properties. Four different damping models for the TM were compared to each other and to experimental data on cadaveric human TM's. Furthermore, the Young's moduli of the TM and the connection between the TM and the malleus were studied.

Chapter 6 presents three FE model of the entire human middle ear, based on three different individual geometries. The models are used to investigate the influences of many different

model parameters on middle ear transmission, tympanic membrane vibration and how model predictions compare to experimental findings.

Chapter 7 uses the three FE models from Chapter 6 to investigate the effect of a fracture in the handle of the first ossicle bone on the transmission of the middle ear for multiple fracture locations.

Chapter 8 describes a study that aimed to determine the buffering capacity and compliance of the tympanic membrane for small, every-day ambient pressure variations of a few 100's of Pascals. This was done through in-vivo pressure measurements inside the middle ear cleft of living patients at the Aalborg University Hospital, Denmark. This project was a collaboration between the Laboratory of Biophysics and Biomedical Physics (University of Antwerp, Belgium) and the Aalborg University, Denmark.

# Chapter 5. Viscoelastic Properties of the Human Tympanic Membrane studied with Stroboscopic Holography and Finite Element Modeling

---

## Abstract

A new anatomically-accurate Finite Element (FE) model of the tympanic membrane (TM) and malleus was combined with measurements of the sound-induced motion of the TM surface and the bony manubrium, in an isolated TM–malleus preparation. Using the results, we were able to address two issues related to how sound is coupled to the ossicular chain: (i) Estimate the viscous damping within the tympanic membrane itself, the presence of which may help smooth the broadband response of a potentially highly resonant TM, and (ii) Investigate the function of a peculiar feature of human middle-ear anatomy, the thin mucosal epithelial fold that couples the mid part of the human manubrium to the TM. Sound induced motions of the surface of ex vivo human eardrums and mallei were measured with stroboscopic holography, which yields maps of the amplitude and phase of the displacement of the entire membrane surface at selected frequencies. The results of these measurements were similar, but not identical to measurements made in intact ears. The holography measurements were complemented by laser-Doppler vibrometer measurements of sound-induced umbo velocity, which were made with fine-frequency resolution. Comparisons of these measurements to predictions from a new anatomically accurate FE model with varied membrane characteristics suggest the TM contains viscous elements, which provide relatively low damping, and that the epithelial fold that connects the central section of the human manubrium to the TM only loosely couples the TM to the manubrium. The laser-Doppler measurements in two preparations also suggested the presence of significant variation in the complex modulus of the TM between specimens. Some animations illustrating the model results are available at our website ([www.uantwerp.be/en/rg/bimef/downloads/tympanic-membrane-motion](http://www.uantwerp.be/en/rg/bimef/downloads/tympanic-membrane-motion)).

*Major contributions to the writing of the paper.*

*This chapter was published in: De Greef, D., Aernouts, J., Aerts, J., Cheng, J.T., Horwitz, R., Rosowski, J.J., Dirckx, J.J.J., 2014. Viscoelastic properties of the human tympanic membrane studied with stroboscopic holography and finite element modeling. *Hear. Res.* 312, 69–80. doi:10.1016/j.heares.2014.03.002*

## 1. Introduction

The natural mechanical properties of the human tympanic membrane (TM) lead to a sensitive response function over a broad frequency range. Despite several studies by different authors, there is still no consensus about which characteristics of the TM are essential for its broadly tuned response function. Proposed influential properties for the general behavior of the TM include the conical shape (Fay, et al., 2006; Koike, et al., 2001), the internal arrangement of collagen fibers (Fay, et al., 2006), internal damping (Zhang & Gan, 2010, 2013), or some combination of these factors. The identification of the essential mechanical properties of the TM would potentially improve the treatment of a wide variety of eardrum pathologies. This paper addresses questions concerning the presence of damping within the TM by a unique combination of stroboscopic holography data of the TM surface motion, laser Doppler measurements of the umbo of the TM, and a finite element (FE) model of the TM structure and motion. We also address a peculiar anatomical feature of the human middle ear, the coupling of much of the length of the manubrium of the human malleus to the TM by a thin mucosal epithelial tissue layer, called the manubrial fold (Graham et al. 1978; Gulya and Schuknecht 1995).

The chosen approach in this paper is to isolate the TM and the first ossicle, the malleus, from the rest of the middle ear and the cochlea. This preparation simplifies the system so we obtain well-defined boundary conditions of both measurement and model, and also remove any contribution of cochlear damping that may complicate estimates of damping within the TM. Experimental data is collected using stroboscopic holography, developed by the middle ear research group at Massachusetts Eye and Ear Infirmary and the Worcester Polytechnical Institute (Cheng, et al., 2010, 2013). Measurements of the sound-induced motion of the complete lateral and medial surfaces of the TM are made at discrete frequencies. The medial surface measurements investigate the role of the not yet fully understood tissue fold interposed

between the TM and the manubrium along much of the manubrial length (Graham et al. 1978). These surface displacement measurements are complemented by single-point vibrometry measurements that finely sample a broader stimulus frequency range, and allow better description of the frequency response of the TM and malleus. These two measurements place different constraints on our estimates of the complex modulus of the TM and the tissue fold that best fit our measurements. The experiments are described in section 2.1. Section 2.2 presents the construction and characterization of the FE model of the TM and the malleus, followed by a description of the approaches we use to investigate each sub goal of the study. Experimental and finite element results are presented in section 3 and are discussed in section 4. Section 5 includes a summary of the conclusions from our work.

## 2. Methods

### 2.1 Experiments

#### *2.1.1 Sample preparation*

Measurements were performed on two fresh human temporal bones without history of otologic disease (TB<sub>1</sub> and TB<sub>2</sub>). During temporal bone sample preparation, the bony external ear canal, cochlea, stapes, incus, stapedia and incudal ligaments and tensor tympani were removed, but the bony tympanic annulus and the anterior malleal ligament were kept intact. A photograph and line drawing of the medial surface of the isolated TM and malleus are shown in Figure 5-1. For holographic experiments, the lateral (external) surface of the TM was painted with a suspension of 60 mg/ml of ZnO (Fisher Scientific Z52-500 Zinc Oxide powder) in saline to increase the amount of light reflected from the surface. The effect of the paint on the vibration pattern of the TM has been shown to be small (Rosowski, et al., 2009). We made three different functional measurements on each prepared bone: holographic measurements were made of the motion of the lateral and medial surfaces of the TM during controlled pure tone stimulation (0.5 – 18 kHz) of the lateral surface (Figure 5-2A&B), and laser Doppler vibrometry was used to measure the broadband (70 Hz – 20 kHz) sound-induced motion of the umbo of the malleus (Figure 5-2C). In between experiments, the samples were stored in refrigerated saline solution to prevent dehydration and the breakdown of the ossicular ligaments and tissues of the TM.

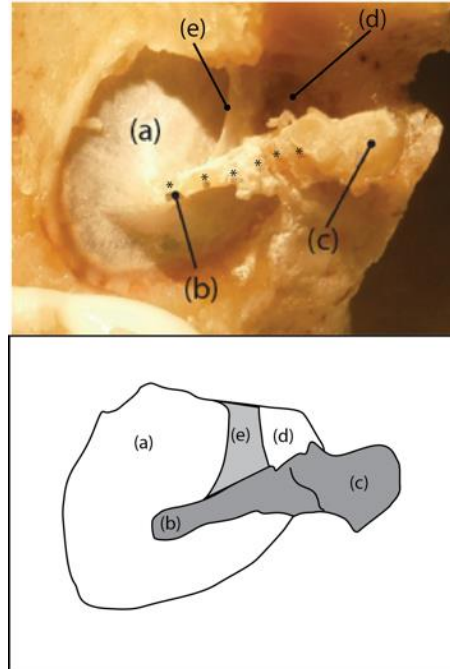


Figure 5-1: A photograph and sketch of the medial surface of a prepared sample (TB1): (a) pars tensa of the TM, (b) umbo of the malleus, (c) malleolar head, (d) pars flaccida of the TM, and (e) the anterior malleolar spine and fold. Six plastic reflective beads (each marked by a \*) are visible along the manubrial arm and neck of the malleus. The six beads were used in measurements reported in Horwitz et al. (2012). In this report we only report measurements made at the umbo.

### 2.1.2 Stroboscopic holography

Schematics of the holography experiments are shown on the left (A) and center (B) of Figure 5-2. The painted and widely exposed TM was placed in a custom made fixture with the annular ring perpendicular to the object beam of the laser. Tonal sound pressures with 10 to 12 different frequencies in the range 0.5-18 kHz and sound pressure amplitudes from 80 dB SPL at low frequencies to 120 dB SPL at high frequencies were applied with a speaker connected to an artificial ear canal, and full-field measurements of the TM displacement component perpendicular to the annular ring were made. Measurements of TM surface motion were made from both the lateral (Figure 5-2A) and medial (Figure 5-2B) sides, while the sound excitation in both cases was presented to the lateral side. Medial measurements were required for the study of the TM-malleus connection, as explained later on in section 2.2.5. The artificial ear canal had a long axis orthogonal to the annular ring of the TM. The actual sound pressure at the TM was measured with a probe-tube microphone (PCB Piezotronics Inc, Model 377C10) located very close to the edge of the TM surface. A series of sound pressure measurements at various probe positions suggested the sound pressure distribution on the TM was uniform in our experiments (Cheng, et al., 2013). This is in contrast to natural circumstances, where the terminal portion of the ear canal is angled relative to the annular ring (Todd, 2009) and the sound field at the TM is not uniform at frequencies above 10 kHz (Stinson 1985). The uniformity of the sound field in our measurements simplified the boundary conditions in both the measurements and the subsequent FE model.

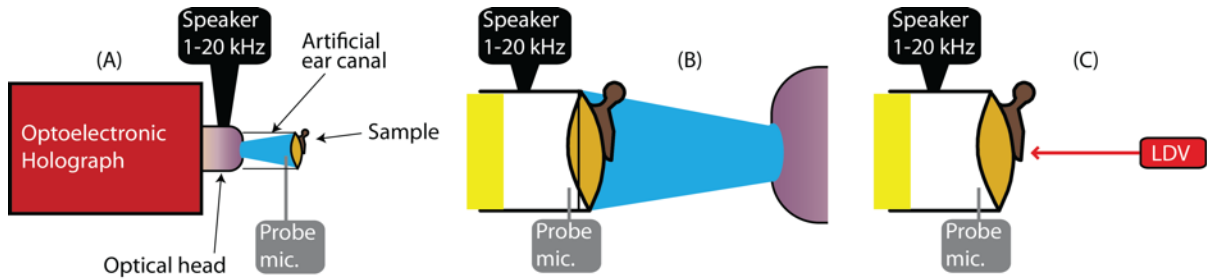


Figure 5-2: Schematics of the measurement setups. In each case a sound source is coupled to the lateral (external) surface of the TM via a clear artificial ear canal, and a probe microphone determines the sound pressure at the bony tympanic ring. (A) Holographic measurement of the lateral TM surface: The blue light is the dispersed laser illumination beam. The red Optoelectronic Holograph box contains the CCD camera and its optics. (B) Holographic measurements of the medial surface while acoustically stimulating the lateral surface. The foam yellow plug sealed the lateral end of the artificial ear canal. (C) Laser-Doppler measurements of the umbo of the malleus during sound stimulation of the TM lateral surface.

In stroboscopic holography mode, the deformation of the TM is computed based on the optical phase difference between reconstructed holograms of the TM surface measured at two different time instants. The instants are defined by the pulsing of the ‘strobe switch’ (an opto-acoustic modulator capable of high-frequency switching) that is phase-locked to the acoustic stimulus. In this study, the sinusoidal motion of the TM driven by a continuous tone was determined from holograms that were gathered during ‘strobed’ laser pulse illumination at each of eight evenly spaced stimulus phases ( $\phi=0, \pi/4, \pi/2 \dots 7\pi/4$ ). The membrane displacement is computed from the change in position between stimulus phase 0 (acting as a temporal reference) and the others. Each laser pulse had a duration of 5 to 10 % of the period of the tonal stimulus. The holographic images of TM surface motions at the eight stroboscopic measurement instances (each image was 800 X 800 pixels) were used to construct full-field displacement maps as a function of time for each pixel on the TM surface. Fourier analysis of the time-dependent displacement waveforms at each measurement point yielded the magnitude and phase angle of the stimulated Fourier component at each point. For a more detailed description, see Hernandez-Montes et al. (2009) and Cheng et al. (2010, 2013).

### 2.1.3 Laser Doppler Vibrometry

A schematic of the laser Doppler vibrometry (LDV) experiment is shown in Figure 5-2C. A reflective bead with a negligible mass was glued on the medial surface of the tip of the malleus (umbo) (Figure 5-1). Tonal sound pressures with frequencies in the range 0.07-20 kHz and sound pressure amplitudes from 80 dB SPL to 100 dB SPL were applied. The velocity of the umbo at the bead position was measured with a laser Doppler vibrometer (Polytec OFV 501 Interferometer and OFV 2600 Laser Controller). The laser beam was focused on the bead and was approximately orthogonal to the TM surface at that point. The umbo transfer function was calculated by dividing the complex velocity, described by amplitude and phase, by the measured sound pressure and has a magnitude with units of  $m/s/Pa$ . The velocity data were also corrected for delays within the LDV velocity processor.

## 2.2 Finite element modeling

### 2.2.1 Morphology

Highly detailed morphologic data were imported from recent micro-CT measurements carried out at the University of Ghent Computer Tomography (UGCT) facility (Masschaele et al., 2007). Soft tissue structures, such as the TM, ligaments and muscles, absorb only a very limited amount of X-ray radiation under natural circumstances, in comparison to bony structures. Therefore, the samples were stained with phosphotungstic acid (PTA) (Metscher, 2009), allowing us to image both soft tissue and bony structures at the same time.

This led to a dataset of  $1764 \times 1775 \times 1506$  cubic voxels with a voxel size of  $18 \mu\text{m}$ . Segmentation of the CT-slices, in which regions that represent the same material are identified, was carried out in Amira<sup>®</sup> 5.3 (FEI Visualization Sciences Group, Hillsboro, Oregon, USA). A first distinction of separate structures was made by threshold-based region growing. However, despite the sample staining, automatic segmentation proved insufficient to detect all boundaries between components, so that significant manual input and expert knowledge of the middle ear anatomy was required in order to distinguish all structures. After segmentation, the different geometrical identities were converted to triangulated surface models and saved as ASCII .stl files (STereoLithography), which were imported in Comsol Multiphysics 4.2 (COMSOL AB, Stockholm, Sweden). The model geometry is based on a different specimen than those used in the motion measurements. Therefore this study cannot provide an exact quantitative comparison of measured and model motions, but does allow qualitative comparison. The geometric models can be downloaded freely at <https://www.uantwerp.be/en/rg/bimef>.

### 2.2.2 Boundary conditions and model description

The FE mesh that was constructed is depicted in Figure 5-3 with color-coded structures. The TM has a curved (tent) shape and has a non-uniform thickness, shown in Figure 5-4. Note that the precision of this thickness determination is limited by the relatively large voxel dimensions ( $18 \mu\text{m}$ ) compared to the TM's thickness. The thickness is calculated based on the segmented voxel data through the 'shortest distance' algorithm, developed and elaborated in Van der Jeught et al. (2013).

In the model, connected structures (e.g. the boundary between the annular ring and the border of the TM) share nodes at their interfaces and are inherently rigidly connected to each other so that they feature equal displacements in these shared nodes. All materials were assumed isotropic. In this study, the pars tensa and pars flaccida were given the same material properties. The bony annulus (red structure on Figure 5-3) is rigidly constrained as a fixed body, is assigned the same material parameters as the malleus and the lateral process and is connected to the outer boundary of the pars tensa. Since it is fully constrained, the annulus is simply a support ring for the TM and does not absorb any computational power. The pars flaccida is not connected to the annulus at its outer rim, but has fixed boundary surfaces at its edges. The end

surface of the anterior ligament was rigidly fixed as well; this ligament, along with the TM, acts to suspend the malleus.

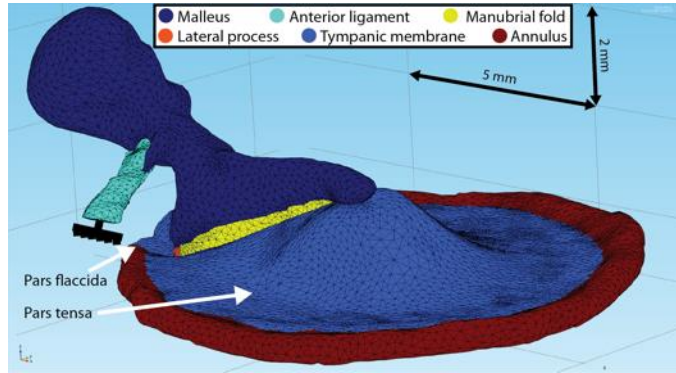


Figure 5-3: Finite element model with imported middle ear structures of a right human ear. The 5 mm and 2 mm scale bars are located in the model's coordinate planes.

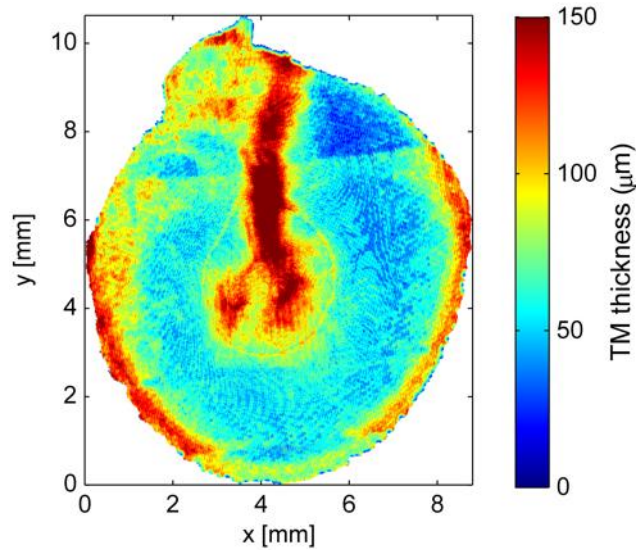


Figure 5-4: The thickness of the TM coded in the finite element model composed from segmentation of CT-images of a right human ear. The segmented TM opposite the manubrium of the malleus is significantly thicker than most other locations.

As described by Graham et al. (1978) and Gulya and Schuknecht (1995), the connection between the TM and the manubrium is tight at the umbo (the tip of the malleus located in the center of the TM) and at the bony lateral process of the malleus (located at the rim of the TM), see the left and right sides of Figure 5-5. Therefore, at these points, the model's bony malleus and lateral process share interface nodes with the TM. In between the umbo and lateral process, the connection between the TM and manubrium is a fine fold of mucosal epithelial membrane called the manubrial fold (middle-panel of Figure 5-5), which is depicted in yellow in Figure 5-3.

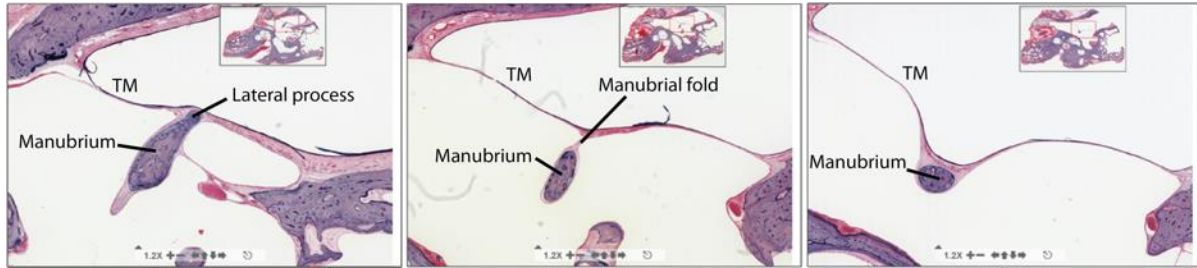


Figure 5-5: Histological sections collected from a single human right ear: at the lateral process (left), at a point midway between the lateral process and the umbo (middle), and at the umbo (right). Images from [www.temporalboneconsortium.org](http://www.temporalboneconsortium.org).

Modeling was done in the frequency domain (harmonic analysis). A uniform single-frequency harmonic pressure was applied as a loading stimulus at the lateral surface of the TM, and the steady-state response of the entire geometry was calculated.

### 2.2.3 Damping

The soft tissues (TM, anterior ligament and manubrial fold) were treated as viscoelastic materials, while the bony structures (malleus, annulus and lateral process) were treated as purely elastic materials (i.e. a loss factor equal to 0). The stiffness and viscoelastic (damping) values of the TM and the TM-manubrium connection (manubrial fold) were investigated in this study. Other values were taken from the literature or based upon previous work that is not discussed here, see Table 5-1.

Table 5-1: Material properties: Young's modulus  $E$ , Poisson's ratio  $\nu$ , loss factor  $\eta$  and density  $\rho$ . Values that are underlined are discussed in this study.

	TM	Manubrial fold	Lateral process	Anterior ligament	Malleus
$E$ [MPa]	<u>10-40</u>	<u>10% of TM</u>	16000	21 <sup>i</sup>	16000 <sup>ii</sup>
$\nu$	0.3 <sup>iii</sup>	<u>0.49</u>	0.3 <sup>iv</sup>	0.3 <sup>iv</sup>	0.3 <sup>iv</sup>
$\eta$	<u>0.01-0.13</u>	<u>same as TM</u>	0	same as TM	0
$\rho$ [kg/m <sup>3</sup> ]	1200 <sup>iv</sup>	1200 <sup>iv</sup>	2200 <sup>v</sup>	1200 <sup>iv</sup>	2200 <sup>v</sup>

<sup>i</sup>: A range of [2.1-21] MPa is used in the literature (Zhao et al., 2009). In our study, 21 MPa gave the best results, although this is not shown in this work.

<sup>ii</sup>: This value is based upon (Soons, et al., 2009).

<sup>iii</sup>: This value is used in most of the current middle ear FE models (Zhao, et al., 2009; Vollandri, et al., 2011), and can be seen as a compromise between an incompressible material ( $\nu = 0.5$ ) and a material composed of parallel fibers with no lateral interaction ( $\nu = 0$ ) (Funnell and Laszlo, 1982). We furthermore compared model outcome for this value with the nearly incompressible case ( $\nu = 0.49$ ), which showed almost no difference.

<sup>iv</sup>: These values are used in most of the current middle ear FE models (Vollandri et al., 2011).

<sup>v</sup>: This value is based upon the reported malleus volume in (Salih, et al., 2012) and the reported malleus mass in (Nummela, 1995).

Viscoelasticity was modeled by using a complex modulus in the frequency domain:

$$E^*(\omega) = E_1(\omega) + i \cdot E_2(\omega) = E_1(\omega) \cdot [1 + i \cdot \eta(\omega)], \quad \text{Eq. 5-1}$$

with  $\omega$  the angular frequency,  $E_1(\omega)$  the storage modulus that accounts for the elastic portion (comparable to the conventional elastic Young's modulus),  $E_2(\omega)$  the loss modulus that accounts for the viscous portion,  $\eta(\omega) = E_2(\omega)/E_1(\omega)$  the loss factor and  $i$  the imaginary unit. A larger  $\eta$  expresses higher internal damping. Comsol uses  $E_1(\omega)$  and  $\eta(\omega)$  as input parameters. Both  $E_1$  and  $E_2$  are expressed in units of stress (Pascal), while  $\eta$  is a dimensionless scalar.

Four sets of possible damping parameters were investigated.

- **Model 1:** To the best of our knowledge, the only work in which the damping or viscoelastic properties of the TM are directly determined at frequencies within the hearing range is (Zhang and Gan, 2010). In that work, tones with frequencies from 0.2 to 8 kHz were used to stimulate cut-out strips of human TM, and the center displacement was measured with a laser Doppler vibrometer. The experiments were then simulated using FE modeling in which the TM was modeled with a generalized Maxwell viscoelastic model (see the appendix). The parameters of the generalized Maxwell model were found through inverse analysis, yielding a loss factor that more or less increased logarithmically over the measured frequency range from 3.5% to 9.5%. We extrapolated these data across our measurement range, yielding a loss factor of 1% at 20 Hz that increases to 13% at 20 kHz. The definitions and values of the parameters of the generalized Maxwell models used by Zhang & Gan and in our extrapolations are provided in the appendix.
- **Models 2 & 3:** In other current middle ear FE models, damping is described in terms of Rayleigh damping instead of using a complex modulus. With Rayleigh damping, the system damping matrix is expressed as  $\alpha M + \beta K$ , where  $M$  and  $K$  are the system mass and stiffness matrices and  $\alpha$  and  $\beta$  the damping parameters. The relation between the loss factor and these Rayleigh parameters is frequency-dependent:  $\eta = \alpha/\omega + \beta\omega$ . The coefficient values of (Vollandri, et al., 2011),  $\alpha = 260$  Hz,  $\beta = 3.7 \cdot 10^{-5}$  s (model 2) and  $\alpha = 0$  Hz,  $\beta = 1 \cdot 10^{-4}$  s (model 3), are used to predict TM function. These values are not based upon experiments but they produced reasonable predictions of the TM function.
- **Model 4:** In a recent study (Aernouts et al., 2012b), the viscoelastic properties of human TM at quasi-static frequencies (0.001 – 3 Hz) were investigated by applying in situ step indentations and measuring force relaxation. The relaxation curves in the time domain were transformed to complex moduli in the frequency domain. The obtained loss factor curves were more or less constant across the measured frequency range with an average value of 7.8%. In the current study, this value was extrapolated over the hearing frequency range.

In summary:

- **Model 1:** Loss factor, 1% at 20 Hz increasing to 13% at 20 kHz (Zhang and Gan, 2010; modified).
- **Model 2:** Rayleigh damping,  $\alpha = 260$  Hz,  $\beta = 3.7 \cdot 10^{-5}$  s (Vollandri, et al., 2011).
- **Model 3:** Rayleigh damping,  $\alpha = 0$  Hz,  $\beta = 1 \cdot 10^{-4}$  s (Vollandri, et al., 2011).
- **Model 4:** Loss factor, 7.8% for all frequencies (Aernouts et al., 2012)b.

The four loss factors are plotted against frequency in Figure 5-6. Note that both the horizontal and vertical axes are logarithmic. The values for the four curves are considerably different, for instance, at 20 kHz the loss factor for the extrapolated measured data of Zhang & Gan (model 1) is 13% while the two Rayleigh damping estimates (models 2 & 3) produces loss factors of 465% and 1257% respectively. There are also large differences between the different damping estimates at low frequencies.

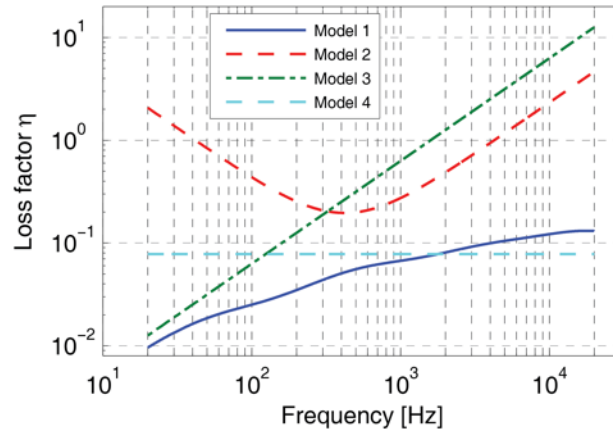


Figure 5-6: Loss factor curves of the four different damping cases, defined in section 2.2.3.

#### 2.2.4 Stiffness

The stiffness of the human TM has been measured in a number of studies. In a recent study, mechanical properties of human TM were investigated using in situ indentation measurements (Aernouts et al., 2012b). For a quasi-static indentation frequency of 0.2 Hz, an average Young's modulus of  $(2.9 \pm 1.3)$  MPa was found. This value is considerably less than most of the values in the literature, which range from 20 MPa to 60 MPa. Aernouts et al., (2012b) also report that the value for the Young's modulus that is needed to fit model predictions to experimental data is very dependent on the thickness used in the model. Since the average TM thickness as well as the thickness distribution varies significantly across different individuals (Van der Jeught, et al., 2013), it is difficult to make a quantitative analysis of TM stiffness if the model is based on a different specimen than the experimental results. The thickness distribution of the model's TM is shown in Figure 5-4 and shows that most of the TM's thickness values in the mid part halfway between the manubrium and the annulus are in the range of 30-100  $\mu\text{m}$ . The thickness values of the TM close to the annulus and in the zone covering the manubrium are significantly higher, up to 240  $\mu\text{m}$ , although it should be noted that neither the manubrial fold nor the annulus itself

were included in this thickness calculation, so the data indicate a true membrane thickening in these parts.

Since the TM should be described as a viscoelastic material, its stiffness is frequency-dependent. In this work, viscoelasticity is incorporated by a complex modulus (Eq. 5-1), which can be characterized by the magnitude  $|E^*(\omega)|$  and loss factor  $\eta(\omega)$  as described in section 2.2.4. We will use the loss factor described by damping model 1 from above to study the stiffness of the TM material. We will compare our measurements with model predictions made while varying the magnitude of the complex modulus: these variations were produced by multiplying the normalized spring constants of the generalized Maxwell model coefficients given in the appendix by a variable constant to fit measurements of the umbo-velocity transfer function in two prepared specimens. The umbo LDV velocity data were used, because their low-frequency values were most affected by variations in membrane stiffness.

### 2.2.5 Manubrial fold

While the human TM and malleus appear tightly coupled at the umbo and lateral process, the coupling between these structures at other locations along the manubrial arm depends on the mechanical properties of the manubrial fold (Graham, et al., 1978; Gulya and Schuknecht, 1995). The manubrial fold is composed of a thin single-cell layer epithelial tissue. In our model the manubrial fold was assumed to be nearly incompressible and given a Poisson's ratio equal to 0.49, which is close to the theoretical upper limit of 0.5. Furthermore, it was assigned a complex modulus to account for viscoelasticity (Eq. 5-1). Since there is no literature on the viscoelastic properties of the manubrial fold, we assumed the loss factor we determined for the TM (i.e. model 1 from section 2.2.3), and model responses were calculated for storage moduli that were 1%, 10% and 100% of the TM storage modulus that was found optimal in the study of TM stiffness (see section 3.2.2).

## 3. Results

In this section, we first present the results of the experimental measurements. Then, the model outcomes for the viscoelastic properties of the TM and the manubrial fold that connects the malleus to the TM are described. For reasons of visual interpretation and to limit the number of figures, experimental and FEM data are often presented in the same figure; however, as noted above, the model predictions are all discussed in a later section of the text.

### 3.1 Experimental results

#### 3.1.1 LDV

Figure 5-7 and Figure 5-8 illustrate experimental LDV data on TB<sub>1</sub> (the dashed blue line in Figure 5-8) and TB<sub>2</sub> (the solid black line in Figure 5-7, and the dashed red line in Figure 5-8). These two figures will be used to assess the real (stiffness) and imaginary (damping) parts of

the complex modulus of the model TM. Both figures show the magnitude and phase of the umbo transfer function (the complex ratio of the magnitude and phase of the umbo velocity and the stimulus sound pressure measured lateral to the TM) as a function of frequency. Each of the measurements feature a damped resonance (near 300 Hz in TB<sub>1</sub> and 600 Hz in TB<sub>2</sub>) where the transfer function magnitude reaches a maximum and the phase angle goes through 0. The resonance in TB<sub>1</sub> is more damped, as illustrated by its less-sharp maximum and gentler phase transition through 0. However, both of these measurements are consistent with other umbo velocities measured in humans after interrupting the ossicular chain (e.g. Rosowski et al. 2008)

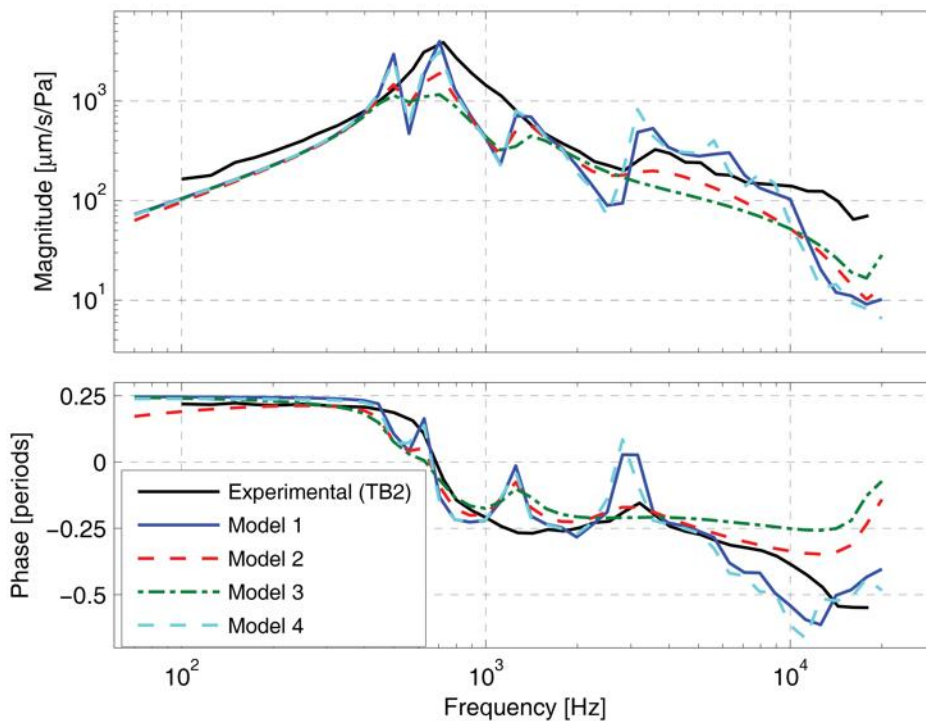


Figure 5-7: Normalized umbo velocity magnitude and angle for the four damping cases (see section 2.2.3 and Figure 5-6) and experimental data from TB<sub>2</sub> (black line).

At frequencies below the frequency of maximal motion magnitude the umbo in TB<sub>1</sub> and TB<sub>2</sub> moves in phase with the pressure wave (the 0.25 period angle difference between the velocity and the stimulus pressure is consistent with an in-phase behavior of pressure and displacement), as is consistent with a stiffness dominated response. Between the frequency of maximal magnitude and 2-3 kHz, the transfer function phase becomes more negative, which is consistent with the effects of damping and an increase in reactance due to inertia. Above 2-3 kHz, the transfer function phase becomes more negative than -0.25 periods and is no longer easily explainable in terms of a simple mechanical element.

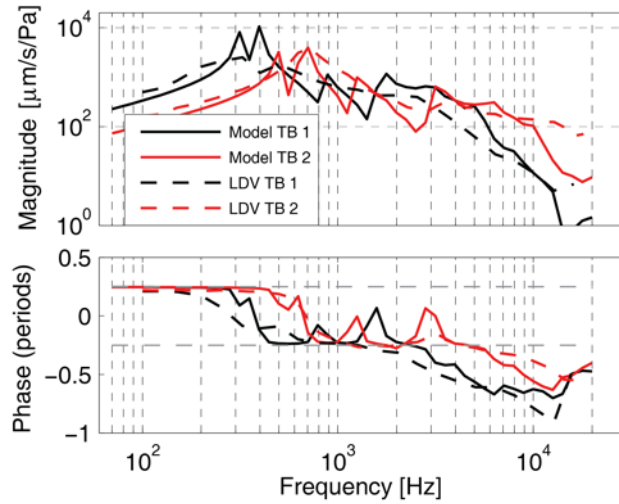


Figure 5-8: Experimental (laser Doppler Vibrometry) and model umbo velocity response for the two samples.

### 3.1.2 Digital holography

The great strength of the developed stroboscopic holographic setup is that full-field information of both amplitude and phase are determined with high spatial resolution. Experimentally derived maps (from TB<sub>1</sub>) are presented in the left-most column of Figure 5-9 for frequencies 1, 7 and 16 kHz. (The illustrated results are exemplary of other measurements made at other frequencies.) The phases in each map are relative to the umbo phase. At 1 kHz, the TM in TB<sub>1</sub> moves with one large and two smaller local areas of maximal displacements, where the two smaller areas are approximately 180° out of phase with the local maximum with the largest area. At higher frequencies, the motion becomes more complex with multiple local displacement maxima that tend to form rings around the manubrium and which show repeating phase variations that are neither continuously varying nor 180° out-of-phase. Similar results were obtained for TB<sub>2</sub>. Overall, these patterns are similar to holographic measurements made in middle ears with intact ossicular chains coupled to inner ears (Cheng et al. 2010, 2013). The location and the number of maxima and the overall magnitudes at the lowest frequencies do differ somewhat from the previous measurements. The higher frequency data show much qualitative similarity to measurements made with an intact incus, stapes and cochlea. Note the presence of graded changes in displacement phase with location, especially between the locations of the spatially small local maxima in displacement magnitude observed at 7 and 16 kHz.

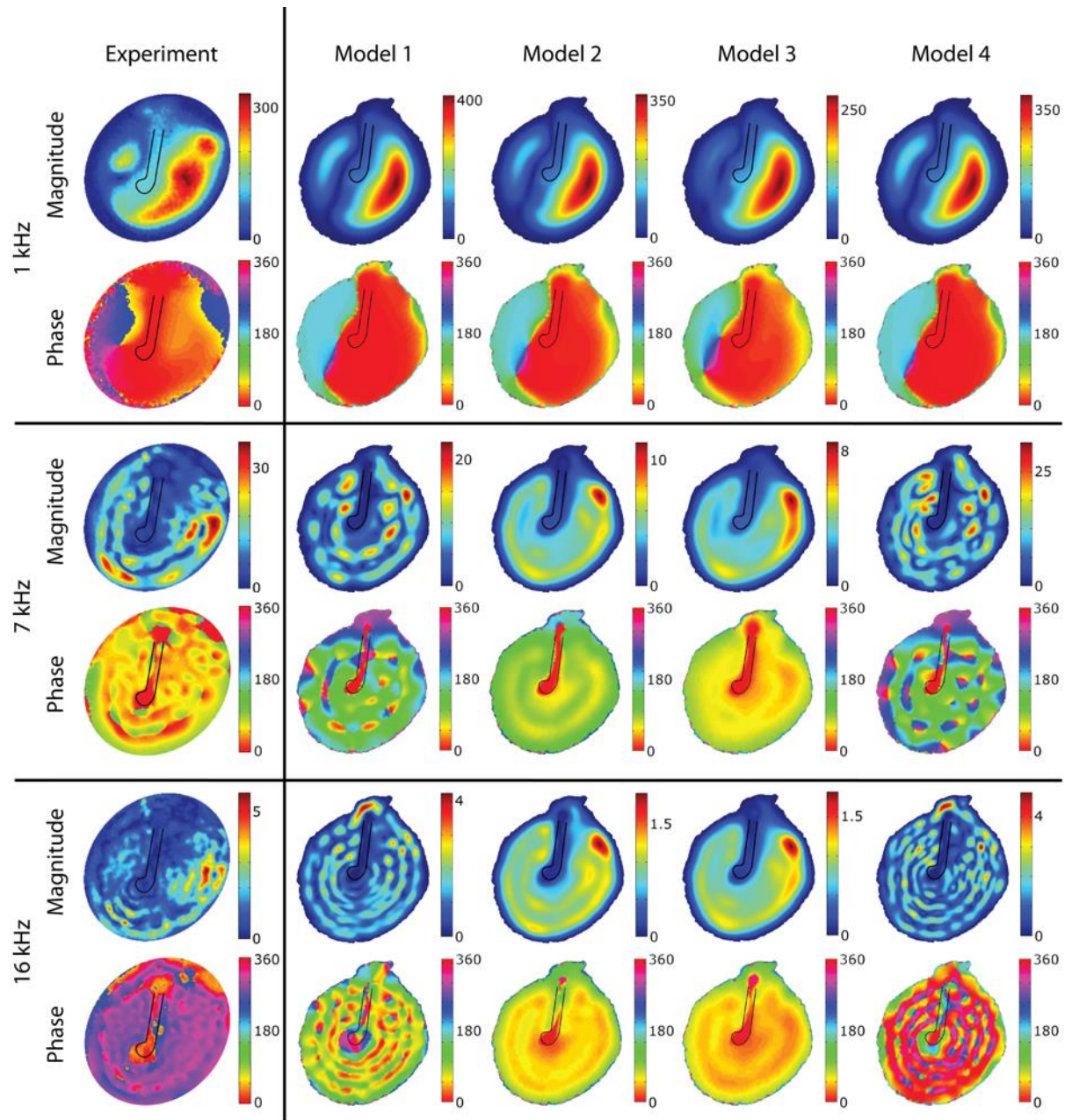


Figure 5-9: Displacement magnitudes [nm/Pa] and phase [deg] of the lateral surface of the TM for selected tonal stimuli of 1, 7 and 16 kHz (the phase is relative to the umbo position). The loss-factors used in the models are defined in section 2.2.3 and illustrated in Figure 5-6.

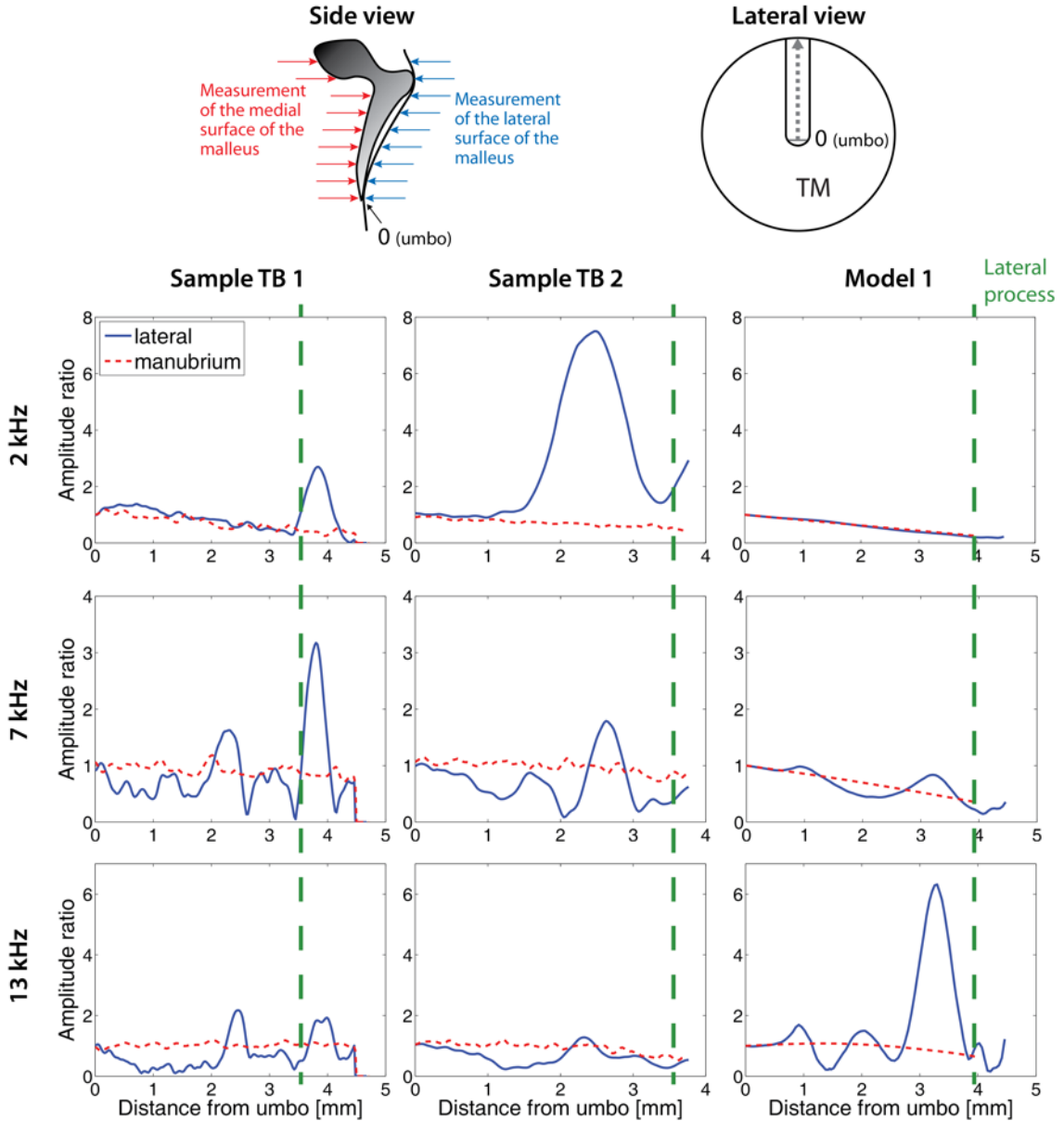


Figure 5-10: Comparison of lateral displacements of the TM along the length of its attachment to the manubrium and medial displacements of the manubrium and malleus neck and head, for frequencies of 2, 7 and 13 kHz. The schematic on the upper right represents the view of the lateral surface of the manubrium from the ear canal. The schematic on the upper left illustrates the motion components that were measured by the holography system when it viewed either the lateral or medial surface of the TM. The data are normalized to the umbo. Left and middle column: Holographically measured displacements from sample TB1 and TB2. Right column: model prediction of the motion of the lateral surface of the TM opposite to the manubrium and the medial surface of the manubrium. The vertical green-dashed lines indicate the location of the lateral process. Locations on the lateral surface of the ear canal superior to the lateral process represent measurements on the surface of the pars flaccida of the TM.

Figure 5-10 contains holographically determined displacements of the TM lateral to the manubrium from the ear canal side in solid lines, and of the manubrium, measured from the medial side (middle ear cavity side) in dashed lines at representative stimulus frequencies of

2 kHz, 7 kHz and 13 kHz. The left column contains data from TB<sub>1</sub>, the middle column from TB<sub>2</sub>. The displayed magnitude and phase are normalized by the displacement at the umbo. The methods are schematized in the inset at the top of Figure 5-10. Note that the entire lateral surface of the TM is visible from the lateral view, including the portion opposite the entire manubrium. In the medial view, however, the lateral process and other parts of the superior manubrium are blocked by the malleus neck and head. Nonetheless, our holography measurements quantify the component of the motion of the head and neck that parallels the illuminating laser beam.

The displacements measured near the umbo in the lateral (blue solid lines) and medial (red dashed lines) views were very similar, consistent with tight coupling of the umbo to the TM. There is also a similarity in the displacement magnitudes measured from the lateral and medial directions near the lateral process (about 3.5 mm from the umbo). In between these two locations, in the middle of the manubrial arm, there are significant differences between the displacement of the TM lateral to the manubrium and the bony medial surface of the manubrium. At certain points along the manubrial arm, the measured displacements along the lateral surface of the TM itself can be up to 5 times larger or smaller (differences of +/-14 dB) than the displacement of the manubrium at that same location. These differences are consistent with the structural observations of weak coupling between the TM and manubrium in between the umbo and the lateral process (Graham et al. 1978).

While there are clear differences between TB<sub>1</sub> and TB<sub>2</sub> in Figure 5-10, the displacement patterns are qualitatively similar. At 2 kHz the motion magnitude of the medial surface of the manubrium decreases regularly with distance from the umbo (consistent with a lever action of the manubrium), and this is matched by a decrease in the motion of the lateral TM surface with distance at locations near the umbo. However, between the umbo and the lateral process there is a significant increase in the motion of the lateral surface in TB<sub>2</sub>, which returns to near the medial displacement levels at the lateral process. At 7 and 13 kHz, the displacements along the medial surface of the manubrium become more constant – consistent with simple translation of the manubrium (Decraemer and Khanna, 2004) – or exhibit variations in the gradient of motion with position – consistent with bending of the manubrium (Decraemer and Khanna, 2004; De La Rochefoucauld and Olson, 2010). On the lateral TM surface there are a number of local maxima and minima in the motion of the TM opposite to the manubrium. These local variations in magnitude are consistent with variations in the magnitude and phase of the motion of the surface of the TM opposite the manubrium that are observed in Figure 5-9, which also suggest a loose coupling of the TM to the manubrium by the fold.

### 3.2 Finite element modeling

In order to constrain the estimates of the damping properties of the TM, we compare our measurements to FE model predictions. The model calculates the umbo transfer function (as defined in 2.1.3) and full field TM surface motions using four different estimates of damping

(Figure 5-7 and Figure 5-9). In performing these model evaluations, the elastic modulus of the TM,  $E_t(\omega)$ , was fixed at a value that produced a low-frequency model response consistent with measurements of the umbo-velocity transfer function (Figure 5-8). After deciding on the best-fit model damping parameters, we use the umbo-velocity transfer function to investigate the effects of variations in the magnitude of the models complex modulus magnitude (Figure 5-11). The predictions of the effects of variations in the storage modulus of the manubrial fold on the motion of the TM and malleus are compared to the results of Figure 5-10.

### 3.2.1 TM damping

Figure 5-7 compares predicted model umbo transfer functions (umbo velocity normalized by the stimulus sound pressure) magnitude (upper panel) and phase (lower panel) using the four different damping cases, defined in section 2.2.3, to a measurement of this transfer function on TB2. While the phase of the measured transfer function changes relatively slowly with frequency, except near 700 Hz where there is an apparent resonance, the model predictions superimpose multiple peaks and valleys accompanied by rapid phase changes on this pattern. Generally the higher the loss factor the smoother the predicted transfer function. While all of the model predictions have some features in common with the measurement, models 1 and 4 match the peak in umbo velocity transfer function (at 0.7 kHz) and the high-frequency response better than the other models. Models 2 & 3 produce a smoother frequency response, but underestimate the measured magnitudes near 0.7 kHz and between 3 and 10 kHz.

As seen in Figure 5-9, the model predictions with the four different damping parameters exhibit very similar spatial vibration patterns at 1 kHz, but the magnitude of motion varies across the four damping cases (pay attention to the color bar limits): The higher the loss factor at 1 kHz, the smaller the motion magnitude. These motion patterns are generally consistent with the displacements measured with the laser. At 7 kHz, the differences between the four predictions are larger. Models 2 and 3 have a higher loss factor at 7 kHz than the others (see Figure 5-6) and produce displacement patterns with fewer local maxima. The same is true at 16 kHz. Models 1 and 4 produce motions of magnitude that are more similar to the measurements and exhibit more of the fine-scale variations in magnitude and phase measured on the surface of the experimental specimen at higher frequencies. Overall, it is clear that models 1 and 4 agree best with the experimental data. Videos 1, 2 and 3 and our website ([www.uantwerp.be/en/rg/bimef/downloads/tympenic-membrane-motion](http://www.uantwerp.be/en/rg/bimef/downloads/tympenic-membrane-motion)) present animated pictures of the response of model 1 at these frequencies. We conclude that a moderate loss factor (< 15%) that is either constant or increases with frequency matches the measured full field TM displacements. Very recently, new data on TM viscoelasticity was published, reporting a loss factor varying from 2% at 1 Hz to 15% at 3800Hz (Zhang and Gan, 2013), which is very similar to our findings. These values were deduced from dynamic mechanical analysis (DMA) measurements in the frequency range of 1-40 Hz and extrapolated using frequency-temperature superposition.

### 3.2.2 TM stiffness

As explained in section 2.2.4, in order to find the TM stiffness, we apply damping model 1 as defined in section 2.2.3 and apply different multiplication factors to the spring constant of the generalized Maxwell model (defined in the appendix) so that it matches optimally with the experimental umbo LDV data of both samples (Figure 5-8). Aside from such differences in the complex modulus magnitude, the models fitting the two experimental results are equal. The resulting magnitudes of the complex moduli are shown in Figure 5-11, together with their common loss factor. For TB1, the complex modulus had a magnitude value of 10 MPa at 70 Hz and grows to 13 MPa at 20 kHz. For TB2, the complex modulus had a magnitude value of 40 MPa at 70 Hz and 52 MPa at 20kHz. Note that both curves differ merely by a multiplication factor of 4.

Figure 5-8 contains comparisons of the experimental magnitude and phase of the umbo velocity transfer functions for the two temporal bones TB1 and TB2 (plotted as dashed lines, blue and red respectively) with model predictions, using the above described best estimates for the TM's complex modulus in 'model TB1' and 'model TB2' respectively (following the same color code). The larger complex modulus needed to fit the TB2 data (Figure 5-11) shifts the resonance frequency upwards and decreases the velocity at lower frequencies (Figure 5-8). This behavior is consistent with the low-frequency behavior of a simple one-dimensional damped oscillator in which the stiffness is increased; however, the multiple peaks and stepped phase changes in the model predictions at higher frequencies are not consistent with such a simple system.

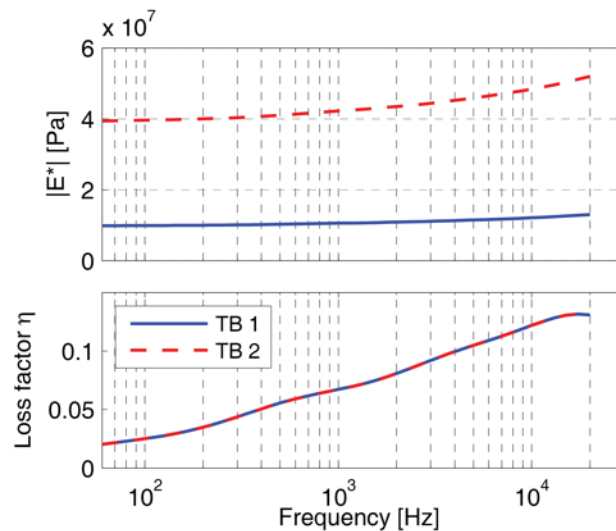


Figure 5-11: Complex modulus magnitude and phase values of the TM used for the two model data sets. Both magnitude curves differ merely by a multiplication factor, while the phase data is equal for both models and represents model 1 defined in section 2.2.3 and depicted in Figure 5-6.

### 3.2.3 Manubrial fold stiffness

Model predictions with varied storage moduli of the manubrial fold were performed to investigate the consequences of this fold on the measurements in Figure 5-10. A storage

modulus of the fold that is 10% of that of the TM storage modulus reproduced some of the measured differences between the motion along the manubrium and the motion along the TM surface just lateral to the manubrium. Although the agreement between model and experiment is far from perfect, there are clear instances of similarity: 1) the deviations of the motion of the lateral surface of the TM from the manubrium are largest between the umbo and the lateral process; 2) the number of areas with large differences in the motion of the lateral TM and medial manubrium surface increase with frequency; 3) the lever-like linear gradient of displacement of the manubrium is observed at 2 kHz and 7 kHz; 4) both the model manubrium and the measurement in TB2 show signs of bending at 13 kHz. A significant difference is that the peak in the magnitude of the displacement of the lateral TM between the umbo and lateral process in TB2 at 2 kHz is not observed in model results. The model also does not predict the increases in motion magnitude of the lateral surface of the TM observed superior to the lateral process (distance > 3.5 mm); these peaks may indicate the presence of the more compliant pars flaccida in the two temporal bones. Differences between pars tensa and flaccida are unexpected in our model because we chose equal membrane parameters for both membrane components.

Reducing the storage modulus of the model's manubrial fold to 1% of the TM storage modulus resulted in a significant increase in the ratio of motion of the lateral TM and the manubrium, characterized by amplitude ratios of up to 35 at 13 kHz. A storage modulus equal to the TM (100%) reduced the motion of the lateral surface of the TM by equalizing the displacements of the manubrial and TM surfaces at frequencies below 12 kHz. The significant inter-individual differences in the spatial variations observed in the two cases together with the less than perfect model fits of the detailed variations is suggestive of significant mutual variations in TM and manubrial fold anatomy between the two experimental specimens and the anatomic specimen used to construct the model. Due to these differences, it is impossible to make a more precise estimation of the properties of the fold.

The manubrial fold seems to be a peculiarity of human middle ear anatomy and is not considered in most middle ear FE models. Exceptions are (Koike, et al., 2002), in which the manubrial fold is modeled with a stiffness that is 1/1000 the stiffness of the TM, and (Sun, et al., 2002) and (Gan, et al., 2004), in which the manubrial fold and the rest of the manubrium is modeled with a stiffness that is one third the stiffness of the ossicles. Although our analysis did not yield a precise quantitative description of the modulus of the fold, our modeling results suggest that the manubrial fold should be included as a separate structure and modeled with a significantly lower stiffness than the TM (10% in our models) to account for the relatively loose coupling between the manubrium and TM motion. This loose coupling allows some independent motion of the manubrium and the lateral TM (Figure 5-10), but does constrain TM motion. This constraint must be responsible for the observation of the low relative motion of the TM lateral to the manubrium compared to the rest of the TM, that is readily visible the experimental data of Figure 5-9 as well as in other published measurements of TM motion in humans (Cheng et al 2010; 2013).

## 4. Discussion

In this section, we discuss the significance of our experimental and modeling results.

### 4.1 The combination of motion measurements and FE modeling

We have combined full-field holographic and single-point laser vibrometer measurements of TM and umbo motion with an anatomically accurate FE model. The measurements were made in two cadaveric human temporal bones with greatly reduced ear canals and with the incus, stapes and inner ear removed. This preparation allowed easy access of the measurement systems to both the lateral and medial sides of the TM. It also simplified the boundary conditions on the FE model.

A limitation on our procedures is that measurements were only made in two temporal bones, and that the anatomical specimen was a third temporal bone. While our measurements and model predictions show many qualitative similarities that allowed estimation of several significant mechanical parameters of the TM, the differences between the two experimental measurements and the small anatomical differences between the anatomical and the experimental specimens prevent better quantitative assessment of these parameters. Nonetheless, our data do demonstrate significant effects of several model parameters and features, and suggest order of magnitude values for these parameters.

### 4.2 Internal damping smooths spatial and frequency-dependent variations in TM motion

Our measurements and model predictions suggest that a low-level of internal damping is required to smooth the frequency dependence of the umbo motion (Figure 5-7), but still allow the observed small regular spatial variations in the magnitude and phase of the motions of the TM surface (Figure 5-9). A too high damping reduces the peak magnitude and the high-frequency response of the umbo-velocity transfer function (Figure 5-7), and also smooths away the small spatial variations in magnitude and phase seen in the model predictions of TM surface motion with lower damping.

While we show no data on this issue, we did look at model predictions when the damping was set to zero. In this case the model also failed to reproduce the multiple local spatially-graded variations in amplitude and phase that are observed in the measurements and model 1 and 4 predictions in Figure 5-9. The consequences of zero damping can be understood in terms of a model of the summed modal motion of a circular plate or membrane that is stimulated harmonically and uniformly (Fletcher, 1992),

$$z(r, \phi; t) = \frac{p}{\rho d} \sum_{m,n} \left[ \frac{\Psi_{mn}(r, \phi) \int_S \Psi_{mn}(r', \phi') dS'}{(\omega_{mn}^2 - \omega^2) + 2i\omega\alpha(\omega)} \right] e^{i\omega t}, \quad \text{Eq. 5-2}$$

with  $z$  describing the time dependent out-of-plane displacement in radial coordinates  $r$  and  $\phi$ ,  $t$  the time,  $p$  the input pressure,  $\rho$  the density,  $d$  a uniform thickness value,  $\Psi_{mn}$  the eigenmodes with radial frequency  $\omega_{mn}$ ,  $S$  the surface area of the membrane,  $\omega$  the driving frequency,  $\alpha(\omega)$  a coefficient accounting for all types of damping (internal and external) and  $i$  the imaginary unit. The eigenmodes have the form:

$$\Psi_{mn}(r, \phi) = [A_{mn}J_m(k_{mn}r) + B_{mn}N_m(k_{mn}r)] \cos m\phi, \quad \text{Eq. 5-3}$$

where  $A_{mn}$  and  $B_{mn}$  are amplitudes of the different Bessel components,  $J_m(x)$  is the  $m^{\text{th}}$  order Bessel function of the first kind,  $N_m(x)$  is the  $m^{\text{th}}$  order Neumann function and  $k_{mn}$  is the wavenumber of the  $mn$  mode. The term in brackets on the right side of Eq. 5-3 describes a series of circular nodes, while the cosine function describes a set of radial nodes. When the damping is set to equal zero in Eq. 5-2, the predicted displacements are all either in phase with each other or completely out of phase. This result suggests, the continuous graded phases of the driven displacements that we observe in our measurements depend on non-zero damping.

The introduction of slow spatial phase gradients into model predictions by the addition of damping within the membrane is of interest. Earlier descriptions of such spatial gradients in the phase of motion on the TM surface have described them as ‘traveling-wave-like’ (Cheng et al. 2010; 2013; Rosowski et al. 2011). The model analysis here suggests that the appearance of traveling-wave-like phase gradients on the TM surface can simply be the result of uniform modal stimulation of a damped membrane.

### 4.3 Eardrum stiffness varies significantly between different specimens

While our estimates of the damping coefficient within the membrane reasonably fit the measurements made in both of our test specimens, it was necessary to vary the magnitude of the storage and loss moduli of the TM by a factor of 4, in order to produce reasonable fits of the low-frequency umbo motion in both preparations (Figure 5-8 and Figure 5-11). Considerable inter-individual variations in the stiffness-bound low-frequency motion of the human TM and middle ear are well documented. Order of magnitude variations have been reported in the low-frequency middle-ear input impedance and umbo velocity of live humans (Margolis and Hunter, 1999; Whittemore et al., 2004) and temporal bones (Rosowski et al., 1990; Rosowski et al., 2007) with intact ossicular chains and cochleae. While it has been noted above that TM stiffness depends on multiple factors, including the storage modulus of the TM material, membrane thickness, membrane shape, etc., we have no precise knowledge of how the two TMs

used in our measurements varied in form or structure. Firmer tests of such relationships must await measurements of both function and precise structure in a series of individual specimens.

#### 4.4 The eardrum and manubrium motions are not well coupled by the more compliant manubrial fold

The holographic measurements we made of the motion of the lateral and medial surface of the same TM with identical sound stimulation (Figure 5-10), clearly demonstrate that the motion of the lateral surface of the TM at locations lateral to the manubrium of the malleus vary in their coupling to the manubrium. Our measurements show similar magnitudes and phase of motion between the TM and the malleus, at the umbo and the lateral process, but also show significant differences between TM motion and manubrial motion at locations between these two points. These observations are consistent with anatomical descriptions of the umbo and lateral processes embedded in the middle fibrous layer of the TM, while other points on the TM are coupled to the manubrium by a loose fold of epithelial tissue (Graham et al. 1978; Gulya & Schuknecht 1995).

The effect of this loose coupling is directly visible in the holographic reconstruction of lateral surface motion in the measurements illustrated in the left-hand column of Figure 5-9. While the motion of the TM surface just lateral to the TM is reduced in those measurements, there are visible phase and displacement variations along the manubrial arm. While the magnitude of these displacement peaks are smaller than those observed at other locations on the lateral TM surface, the density of peaks along the manubrium is similar to the density along the membrane surface. These local variations in magnitude (and phase) are not consistent with the observation of nearly rigid motion of the manubrium described by the measurements of the medial surface (Figure 5-10).

The model analyses we perform varying the properties of the manubrial fold to match the magnitude of the differences between the TM and manubrial motion suggest a small but non-zero storage modulus for this structure. This is consistent with our experimental observations of low but still observable coupling between the manubrium and the TM. On the one hand, a small storage modulus is consistent with our observations of differences in motion of the manubrium and the lateral TM. On the other hand, a non-zero storage modulus is consistent with the repeated observations that the motion of the lateral surface of the human TM is smallest along the arm of the manubrium (Figure 5-9 and other data illustrated in Cheng et al. 2010, 2013).

## 5. Conclusions

In this work, key aspects of human tympanic membrane mechanics were studied using the combination of stroboscopic holography measurements, Laser Doppler vibrometry and finite elements simulations. In the measurements and model analyses, the cochlea, stapes and incus

were removed, as well as their ligaments and tendons. This allowed a more direct study of the TM with a more reliable definition of its boundary conditions.

We found that TM damping needs to be incorporated into the model to accurately model TM displacement patterns at acoustic frequencies. The experimental data was best modeled using a loss factor that increases from 1 % at 20 Hz to 13 % at 20 kHz (model 1) or by using a constant loss factor of 7.8 % (model 4). The typically used Rayleigh damping values (models 2 and 3) are rejected since they yield too much damping, particularly at high frequencies. The best value for the complex modulus, which describes the TM stiffness, was significantly different between the two measured samples, with TB<sub>1</sub> requiring a complex modulus of 10 to 13 MPa and TB<sub>2</sub> 40 to 52 MPa.

Holographic measurements at frequencies above 2 kHz indicate the motions of the lateral surface of the TM and the manubrium become decoupled at points in between the umbo and the lateral process of the malleus in humans. It is believed that the manubrial fold is responsible for this decoupling, and that the manubrial fold should be modeled with a lower stiffness than the TM (10% in our models).

The addition of damping to the TM in the TM-malleus model introduces spatial phase-gradients that mimic those observed in both the isolated TM and intact middle ear measurements. This suggests that a damped modal response of the TM can produce traveling-wave like phase gradients without the introduction of wave travel on the membrane surface.

In summary, we successfully investigated TM stiffness, damping and wave motion as well as its connection to the malleus. All of these aspects are essential to a realistic dynamic computer model of the entire middle ear.

## Appendix

The Maxwell model is composed of a spring in series with a dashpot. The generalized Maxwell model is composed of a spring with linear spring constant  $R_0$  in parallel with  $m$  Maxwell models with spring constants  $R_j$  and dashpot constants  $\eta_j$  ( $j = 1 \dots m$ ); see Figure 5-12. The complex modulus in the frequency domain is written as

$$E^*(\omega) = E_1(\omega) + i E_2(\omega), \quad \text{Eq. 5-4}$$

where  $E_1(\omega)$  is the storage modulus and  $E_2(\omega)$  the loss modulus, in this case given by

$$E_1(\omega) = R_0 + \sum_{j=1}^m \frac{R_j \tau_j^2 \omega^2}{1 + \tau_j^2 \omega^2} \quad \text{Eq. 5-5}$$

$$E_2(\omega) = \sum_{j=1}^m \frac{R_j \tau_j \omega}{1 + \tau_j^2 \omega^2} \quad \text{Eq. 5-6}$$

with  $\tau_j = \eta_j/R_j$ . The loss factor is defined as  $\eta(\omega) = E_2(\omega)/E_1(\omega)$  so that  $E^*(\omega) = E_1(\omega) [1 + i\eta(\omega)]$ .

In (Zhang and Gan, 2010), a third-order Maxwell model was used to fit viscoelastic properties in the frequency range 0.2-8 kHz. The average normalized values that were found are  $R_0 = 0.753$  Pa,  $R_1 = 0.175$  Pa,  $R_2 = 0.0559$  Pa,  $R_3 = 0.0167$  Pa,  $\tau_1 = 2.55 \cdot 10^{-5}$  s,  $\tau_2 = 2.55 \cdot 10^{-4}$  s,  $\tau_3 = 2.5 \cdot 10^{-3}$  s.

Extrapolation of this curve to the frequency range 20 Hz - 20 kHz gives the blue solid loss factor curve in Figure 5-6 (model 1), described by a fourth-order Maxwell model with coefficients:  $R_0 = 0.662$  Pa,  $R_1 = 0.202$  Pa,  $R_2 = 0.0714$  Pa,  $R_3 = 0.0492$  Pa,  $R_4 = 0.0147$  Pa,  $\tau_1 = 6.63 \cdot 10^{-6}$  s,  $\tau_2 = 3.95 \cdot 10^{-5}$  s,  $\tau_3 = 2.55 \cdot 10^{-4}$  s,  $\tau_4 = 2.50 \cdot 10^{-3}$  s. These coefficients are chosen to match the third order model optimally.

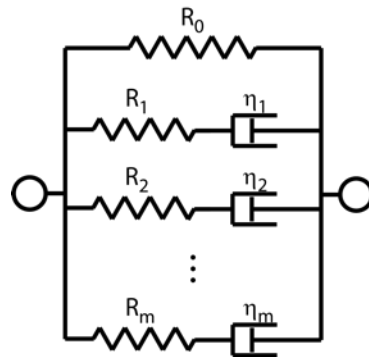


Figure 5-12: Model representation for the generalized Maxwell model.

# Chapter 6. Effects of Model Definitions and Parameter Values in Finite Element Modeling of Human Middle Ear Mechanics

---

## Abstract

**Background:** Despite continuing advances in finite element software, the realistic simulation of middle ear response under acoustic stimulation continues to be challenging. One reason for this is the wide range of possible choices that can be made during the definition of a model. Therefore, an explorative study of the relative influences of some of these choices is potentially very helpful.

**Method:** Three finite element models of the human middle ear were constructed, based on high-resolution micro-computed tomography scans from three different human temporal bones. Interesting variations in modeling definitions and parameter values were selected and their influences on middle ear transmission were evaluated. The models were compared against different experimental validation criteria, both from the literature and from our own measurements. Simulation conditions were restricted to the frequency range 0.1 – 10 kHz.

**Results:** Modeling the three geometries with the same modeling definitions and parameters produces stapes footplate response curves that exhibit similar shapes, but quantitative differences of 4 dB in the lower frequencies and up to 6 dB around the resonance peaks. The model properties with the largest influences on our model outcomes are the tympanic membrane (TM) damping and stiffness and the cochlear load. Model changes with a small to negligible influence include the isotropy or orthotropy of the TM, the geometry of the connection between the TM and the malleus, the microstructure of the incudostapedial joint, and the length of the tensor tympani tendon.

**Conclusion:** The presented results provide insights into the importance of different features in middle ear finite element modeling. The application of three different individual middle ear geometries in a single study reduces the possibility that the conclusions are strongly affected by geometrical abnormalities. Some modeling variations that were hypothesized to be influential turned out to be of minor importance. Furthermore, it could be confirmed that different geometries, simulated using the same parameters and definitions, can produce significantly different responses.

*Major contributions to the development of the FE models from the segmented data, the execution of the simulations, data analysis and writing of the paper.*

*This chapter was published in: De Greef, D., Pires, F., Dirckx, J.J.J., 2017, Effects of Model Definitions and Parameter Values in Finite Element Modeling of Human Middle Ear Mechanics, in press, Hearing Research. doi: 10.1016/j.heares.2016.11.011*

## 1. Introduction

The development of a finite element (FE) model of the human middle ear (ME) is not straightforward. Many choices need to be made by the researcher, from the early stages of temporal bone imaging and the construction of the geometry, to the choice of physics to be included in the model, the applied material parameters, and the boundary conditions. Since the mechanics of the system are complicated, it is often very difficult to accurately and confidently predict the consequences of the possible choices that need to be made. This results in different model definitions for different research groups throughout the research community (De Greef et al., 2014b (Chapter 5 of this thesis)); Fay et al., 2006; Ferrazzini, 2003; Gentil et al., 2014a; Hoffstetter et al., 2010; Homma et al., 2010; Tuck-Lee et al., 2008; Zhang and Gan, 2011a; Zhao et al., 2009).

In this paper, the aim is to determine the importance of some of the choices made throughout the development of a middle ear FE model. This was done by studying the influence of different variations in the model description on the transfer function (TF) of three different FE models, based on the geometries of three different temporal bones. In addition, by applying the same model definitions to different human ME geometries, this study will bring insight into the isolated effect of geometry on the sound transmission of the ME.

## 2. Materials and methods

### 2.1 Study strategy

After evaluating the variations that are described further on, a final model description was constructed that represents a trade-off between agreement with experiments,

structural/morphological observations, effort necessary to implement, and computational cost. For example, if a certain feature did not produce a significant change but improves the resemblance to microstructural observations, it was included in the model only if the required effort to implement it and the additional computational cost were relatively small. An example of this is the incudostapedial joint (ISJ) microstructure (see results and discussion).

Sections 2.22.2 and 2.3 describe how the final models, referred to as the ‘base models’ of this paper, were built and defined and which material parameters were used in them. Since three geometries from three different donors were constructed, there are three base models and most variations were studied for all three geometries.

## 2.2 Geometry

The three temporal bones (TB’s) used in this study were a subset of the six TB’s used for the morphologic study in De Greef et al. (2015, Chapter 3 of this thesis). Therefore, all procedures up to and including the image segmentation are identical to that paper and only a condensed description of the procedures is provided here. Samples 1, 2, and 3 from the current paper are samples 2, 3, and 4 from De Greef et al. (2015, Chapter 3), but we will use numbers 1, 2, and 3 from here on in this paper. Some morphological parameters for the three samples are listed in Table 6-1 to allow the reader to appreciate how the geometries vary. The geometries were selected so that they represent a large (sample 1), small (sample 2), and average (sample 3) ME from our population of six samples.

*Table 6-1: Selection of relevant morphological parameters of the three selected samples. The last column contains statistical parameters from the dataset of 6 samples in De Greef et al. (2015, Chapter 3 of this thesis).*

<b>Parameter</b>	<b>Sample 1</b>	<b>Sample 2</b>	<b>Sample 3</b>	<b>Mean ± St. Dev. (N=6)</b>
<b>TM surface area (mm<sup>2</sup>)</b>	65.9	58.1	60.0	59.4 ± 6.9
<b>IM joint angle (°)</b>	22.5	15.8	12.5	17.5 ± 4.4
<b>IM complex volume (mm<sup>3</sup>)</b>	27.6	23.5	23.8	26.7 ± 2.4
<b>Stapes volume (mm<sup>3</sup>)</b>	1.44	1.18	1.23	1.24 ± 0.13

The three fresh human TB samples were acquired from Cochlear Technology Centre Belgium. Samples 1 (male, 75y) and 2 (male, 73y) are right TB’s; sample 3 (male, 73y) is left. The samples were stained using phosphotungstic acid (PTA) before they were imaged using a micro-computed tomography (μCT) system at the Centre for X-ray Tomography of Ghent University (UGCT) facility (Masschaele et al., 2007). The resulting dataset of the scans had an isotropic voxel pitch of 18.5 μm (sample 1) or 22.8 μm (samples 2 and 3). After 2D-reconstruction of the μCT scans, the image data were segmented using Amira® 6.1 (FEI Visualization Sciences Group, Hillsboro, Oregon, USA). The segmentation procedure was a combination of automatic and manual segmentation tools and is described in more detail in De Greef et al. (2015, Chapter 3 of this thesis). The influence of segmentation operator bias was investigated by Buytaert et al.

(2014) and the authors concluded that the results of a manual segmentation are only marginally dependent on the operator.

After image segmentation, the labeled volumes were meshed into triangulated surface models using a generalized marching cubes algorithm (Hege et al., 1997). Initially very fine (more than 1M triangles), the surfaces were simplified and remeshed using an adaptive remeshing algorithm (Zilske et al., 2008) to approx. 18,000 triangles. Both algorithms are natively implemented in Amira®. The final surfaces were exported to the FE software as ASCII .stl-files (STereoLithography).

The final models contained the following separate structures: pars tensa (PT) of the TM, pars flaccida (PF) of the TM, tympano-malleal connection (TMC), malleus, incus, stapes, incudomalleal joint (IMJ), incudostapedial joint (ISJ) capsule, ISJ interior, anterior malleal ligament, lateral malleal ligament, posterior incudal ligament, stapedial annular ligament (SAL), tensor tympani (TT) tendon, and stapedius muscle (SM) tendon.

A noteworthy feature of our three geometries is the morphology of the lenticular process of the incus. In all samples, only a thin bony core connected the long process of the incus to the lenticular plate. This core was surrounded by soft tissue, which was labeled as ISJ capsule in our models. A close-up image of this is presented in Figure 6-1B.

## 2.3 Finite element analysis

For all FE simulations in this study, Comsol Multiphysics 5.2 (COMSOL AB, Stockholm, Sweden) was used, extended with the Structural Mechanics Module. Once imported into Comsol, the surface models were converted into a tetrahedral volume mesh, to be used in the FE calculation. A mesh refinement study indicated that a surface model of approx. 18,000 triangles, corresponding to a volume mesh containing approx. 120,000 tetrahedral elements, provided an acceptable trade-off between result accuracy and computation time (the difference in the TF between this mesh and a mesh containing almost twice the number of elements (220,000) was at most frequencies less than 1 dB, and at the most 2.2 dB (around the resonance)). The entire model consists of second-order (quadratic) elements. Using this mesh, most of the TM's interior was adequately meshed using a single layer of quadratic elements, except near the TM's edge. A frequency-domain analysis sweeping over 24 frequencies between 0.1 and 10 kHz took approximately 25 minutes to calculate on a PC (CPU: Intel Xeon E5-2630 v3 @ 2.40 GHz, 8 cores (2 processors installed) – RAM: 128 GB – OS: Windows 7). The 24 frequencies were logarithmically evenly spaced at four frequencies per logarithmic decade below 562 Hz and 16 frequencies per logarithmic decade above 562 Hz.

### 2.3.1 Boundary conditions of the base models

The following description applies to the base models of this paper and, if not stated otherwise, to all variation models.

The stimulating load on the model was a uniform sound pressure of 1 Pa on the lateral side of the TM. A contiguous selection of triangular faces at the edge of the TM, as well as the end surfaces of the anterior malleolar ligament, lateral malleolar ligament, posterior incudal ligament, stapedial annular ligament, TT tendon, and stapedius muscle tendon were all fixed. The cochlea was modeled as an acoustic impedance, acting on the medial surface of the stapes footplate (SFP) and the stapedial annular ligament. The value of this impedance was taken from Puria et al. (1997) and is shown Figure 6-6B together with data from other sources. Only the amplitude of the cochlear impedance is shown, although the empirical phase from Puria et al. (1997) was incorporated in the model as well. The complex impedance  $Z_{ac, coch}$  was implemented as a pressure on the SFP through the expression:

$$p_{sfp} = A_{sfp} \cdot Z_{ac, coch} \cdot v_{sfp}, \quad Eq. 6-1$$

where  $A_{sfp} = 3.08 \cdot 10^{-6} m^2$  (De Greef et al., 2015, Chapter 3 of this thesis) is the average footplate area and  $v_{sfp}$  is the instantaneous complex stapes velocity normal to the SFP surface.

### 2.3.2 Material parameters of the base models

All materials except the interior of the ISJ were modelled as solid materials. Most parameter values were adopted from the literature. The Young's moduli of all structures are listed in Table 6-2.

The PT of the TM was modelled as an orthotropic material within a polar coordinate system with its origin at the umbo. Therefore, the indices  $i$  and  $j$  in the equations below represent  $r$  (radial),  $c$  (circumferential), and  $t$  (transverse). The transverse direction is approximated by the  $z$ -direction of the coordinate system, which is perpendicular to the plane of the tympanic annular ring.

The full stress-strain relation of an orthotropic material in a polar coordinate system is given by:

$$\varepsilon_i = S_{ij} \sigma_j, \text{ or} \quad Eq. 6-2$$

$$\begin{bmatrix} \varepsilon_r \\ \varepsilon_c \\ \varepsilon_t \\ 2\varepsilon_{ct} \\ 2\varepsilon_{tr} \\ 2\varepsilon_{rc} \end{bmatrix} = \begin{bmatrix} \frac{1}{E_r} & -\frac{\nu_{cr}}{E_c} & -\frac{\nu_{tr}}{E_t} & 0 & 0 & 0 \\ -\frac{\nu_{rc}}{E_r} & \frac{1}{E_c} & -\frac{\nu_{tc}}{E_t} & 0 & 0 & 0 \\ -\frac{\nu_{rt}}{E_r} & -\frac{\nu_{ct}}{E_c} & \frac{1}{E_t} & 0 & 0 & 0 \\ 0 & 0 & 0 & \frac{1}{\mu_{ct}} & 0 & 0 \\ 0 & 0 & 0 & 0 & \frac{1}{\mu_{tr}} & 0 \\ 0 & 0 & 0 & 0 & 0 & \frac{1}{\mu_{rc}} \end{bmatrix} \cdot \begin{bmatrix} \sigma_r \\ \sigma_c \\ \sigma_t \\ \tau_{ct} \\ \tau_{tr} \\ \tau_{rc} \end{bmatrix}. \quad \text{Eq. 6-3}$$

Because the symmetry of the compliance matrix  $S_{ij}$ , the twelve elasticity parameters (three Young's moduli  $E_i$ , six Poisson's ratios  $\nu_{ij}$ , and three shear moduli  $\mu_{ij}$ ) are reduced to nine independent parameters. In order not to violate the conservation of energy, the strain function energy needs to be positive-definite, placing further restrictions on the Poisson's ratios (Lempriere, 1968).

Li and Barbic (2014) suggested the following simplifications that guarantee the positive-definiteness of the strain energy function, while further reducing the number of tunable parameters from nine to four:

$$\nu_{ij} = \nu \sqrt{\frac{E_i}{E_j}}, \text{ and} \quad \text{Eq. 6-4}$$

$$\mu_{ij} = \frac{\sqrt{E_i E_j}}{2(1 + \nu)}, \quad \text{Eq. 6-5}$$

with  $-1 < \nu < 0.5$ . Thus, four independent parameters remain to be determined:  $E_r$ ,  $E_c$ ,  $E_t$ , and  $\nu$ . The reference value  $\nu$  for Poisson's ratio was chosen at  $\nu = 0.3$ . Note that one or even two of the individual Poisson's ratios  $\nu_{ij}$  can (and in our case, do) have higher values than 0.5 without violating the positive-definiteness of the strain energy function, as long as the third value ensures that their product does not exceed 0.5.

Similar to Tuck-Lee et al. (2008), the radial Young's modulus decreased away from the umbo, emulating the fact that the radially oriented collagen fibers converge at the umbo and manubrium of the malleus, resulting in a higher effective stiffness close to the center. Therefore, the radial Young's modulus was defined by the function

$$E_r(r) = \min\left(40 \text{ MPa} * \frac{2 \cdot 10^{-3} \text{ m}}{r}, 100 \text{ MPa}\right), \quad \text{Eq. 6-6}$$

so that the value of 40 MPa was reached at  $r = 2$  mm from the umbo. In order to avoid divergence when approaching  $r = 0$  mm, the function was limited at 100 MPa. Because the radial Young's modulus is non-uniform, the Poisson's ratios and shear moduli that depend on it are non-uniform as well, so they are not characterized by a single value. Three parameters are homogeneous:  $\nu_{ct} = 0.6$  (circumferential-transverse),  $\nu_{tc} = 0.15$ ,  $\mu_{tc} = 3.85$  MPa.

For the ossicles, no damping was incorporated. For the TM, including pars tensa, pars flaccida, and the tympano-malleal connection, an isotropic loss factor of  $\eta = 0.1$  was used (the motivation for this is provided in section 3.2.1). For other soft tissue solid structures, Rayleigh damping with  $\alpha = 0$  s<sup>-1</sup> and  $\beta = 10^{-4}$  s was used, equal to some published models (Gan et al., 2002; Liu et al., 2009; Sun et al., 2002).

For all soft tissue structures, the mass density was 1200 kg/m<sup>3</sup> (Homma et al., 2009). The densities of the ossicles were 2390 kg/m<sup>3</sup> (malleus), 2150 kg/m<sup>3</sup> (incus), and 2200 kg/m<sup>3</sup> (stapes) (Homma et al., 2009).

The interior of the ISJ in reality encapsulates articular cartilage on both articular surfaces, synovial fluid, and a meniscus, as modelled in detail by Gan and Wang (2014). However, these components are too small to distinguish the different materials on our  $\mu$ CT images, so as an approximation the entire interior was modeled as a fluid, with a bulk modulus of 2.2 GPa (as used in Zhang and Gan (2011b) and Gan and Wang (2014)) and mass density of 1200 kg/m<sup>3</sup>. The physics of the fluid and solid elements were coupled through an acoustic-structure boundary condition in Comsol.

## 2.4 Model variations

### 2.4.1 TM model variations

The effects of quantitative changes to our TM model were examined by changing the TM's Young's modulus and the loss factor (damping). These changes were applied on both PT and PF simultaneously. For the PT, all orthotropic moduli and the maximum value for the radial modulus (i.e. the 100 MPa in equation 6) were scaled by the same factor. The effects of a change in the loss factor of the tympano-malleal connection were calculated as well.

Furthermore, four different material models for the TM were compared. For technical reasons, only the geometries of TB's 1 and 2 were included in this comparison.

- TM model A: isotropic with  $E = 20$  MPa and  $\nu = 0.3$ .
- TM model B: orthotropic with  $E_r = 40$  MPa,  $E_c = 20$  MPa, and  $E_t = 5$  MPa.
- TM model C: non-uniform radial Young's modulus (defined by expression (2)). TM model C is used in the base models from this paper.

*Table 6-2: List of the Young's moduli of all middle ear structures in our models.*

Structure	Young's modulus (MPa)	Source
Tympanic membrane – pars tensa	$E_r(r)$ (eq. 2) (radial)	Current study
	$E_c = 20$ (circumferential)	Current study
	$E_t = 5$ (z-direction)	Current study
Tympanic membrane – pars flaccida	6.7	$E_c/3$ , similar to many sources, see Vollandri et al. (2011)
Tympano-malleal connection	2	$E_c/10$ , (De Greef et al., 2014b, Chapter 3 of this thesis)
Malleus, incus, and stapes	$14.1 \cdot 10^3$	(Cai et al., 2010; Homma et al., 2009)
Incudomalleal joint	7	(Homma et al., 2010)
Incudostapedial joint capsule	6	(Koike et al., 2002)
Anterior malleal ligament	21	(Homma et al., 2009)
Lateral malleal ligament	5	(Gan et al., 2004) (6.7 MPa)
Posterior incudal ligament	4.8	(Homma et al., 2009)
Stapedial annular ligament	0.15	Current study*
Tensor tympani tendon	5	(Homma et al., 2010)
Stapedius muscle tendon	0.38	(Homma et al., 2010)

\* This value provided a good match with experimental ME response curves and sits well inside the range reported in literature: 0.065 MPa (Ferrazzini, 2003) – 5.5 MPa (Gan et al., 2007).

- TM model D: subdivided TM (Figure 6-4B). The TM was subdivided in an attempt to represent the arrangement of the collagen fibers even better, similar to Tuck-Lee et al. (2008). The Young's moduli of all sub-regions are orthotropic, but their coordinate systems were different. The inferior region of the TM was identical to TM model C. The superior region was subdivided into three regions, all orthotropic in a Cartesian system. In the region overlying the manubrium of the malleus (indicated by M in Figure 6-4B), the y axis was defined as lying along the manubrium and the x axis perpendicular to it. In the anterior and posterior regions, the x and y axes were rotated  $30^\circ$  and  $-30^\circ$ , respectively, and the Young's moduli were  $E_x = 40$  MPa and  $E_y = 20$  MPa. In the region overlying the manubrium,  $E_x = 50$  MPa and  $E_y = 10$  MPa, since the radial and circumferential fibers both run more or less along the x axis (perpendicular to the manubrium), so that the stiffness in the x direction is effectively higher. This microstructural description is largely based on the observations in Lim (1970). In all regions,  $E_z = 5$  MPa.

For models B, C, and D, the shear moduli and Poisson's ratios followed the relations in (4) and (5).

#### 2.4.2 Different types of tympano-malleal connection

As reported by De Greef et al. (2016, Chapter 4 of this thesis), the anterior-posterior width of the tympano-malleal connection (TMC) varies over an order of magnitude among individuals: in the narrowest TMC sample the minimal width was  $83 \pm 7 \mu\text{m}$ , while in another sample the

TMC was  $840 \pm 7 \mu\text{m}$  at its narrowest point. Yet all samples exhibited a very similar TMC near the umbo and near the lateral process of the malleus: at both locations, the connection between TM and malleus was wide and tight.

In order to evaluate the influence of the different types of TMC, two models were compared with identical geometry for the entire ME, except for the TMC. To do this, we started from a sample with a narrow TMC by nature (sample 1) and adapted it so that the TM was more tightly connected to the manubrium, similar to the most tight connection reported in De Greef et al. (2016, Chapter 4). To do this, we started from the segmentation masks of sample 1 in Amira<sup>®</sup>, deleted the mask of the TMC and rotated the TM mask towards the manubrium around the anterior-posterior axis through the umbo, so that the distance between TM and malleus decreased. After this, the segmentation of the TM was adapted near the manubrium so that it touches the manubrium along its entire length. In this wide-TMC model, there was no separate material anymore for the TMC, because the microstructural observations in De Greef et al. (2016, Chapter 4) demonstrated that in those cases, the TM is directly connected to the malleus without a distinct connection structure. One cross-section of this segmentation is visible in Figure 6-5B. After this, the masks were triangulated and imported into Comsol in the same way as the other geometries. Then, the same material parameters and boundary conditions were assigned to this geometry and the simulation was run for the same frequencies. The results from this simulation could then be compared to the results from the simulations with the original geometry.

#### 2.4.3 Other ME/IE variations

The effects of quantitative changes in cochlear impedance (by comparing the complex impedances from different literature sources), the Young's moduli of multiple materials, and the Rayleigh damping coefficients of soft tissue (outside the TM) were determined. Finally, the influences of the length of the tensor tympani tendon and of the material model for the incudostapedial joint interior (fluid vs. solid) were studied.

## 3. Results

### 3.1 Base models

Figure 6-1 illustrates our three base FE models, based on three different geometries, together with a close-up of the ISJ of geometry 1.

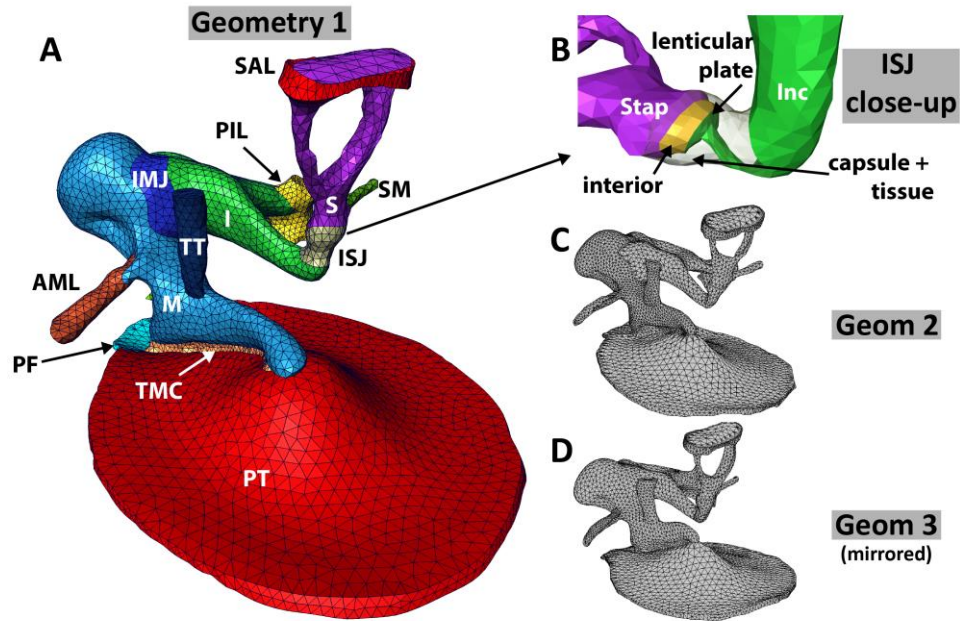


Figure 6-1: A: A detailed screenshot of the surface model of sample 1. B: close-up image of the ISJ (geometry 1). The ISJ interior is modeled as a fluid, the rest of the model as a solid. C & D: geometries 2 and 3.

Figure 6-2A presents the piston component of the SFP velocity amplitude in our three geometries as a function of frequency. The figure also shows a summary of experimental data as presented by Rosowski et al. (2007), consisting of a grand mean of mean curves from multiple independent studies and twice the standard deviation of those means. Between 100 Hz and 750 Hz, the average slope of the model curves is +6.5 dB/octave, similar to the slope of +5.7 dB/octave in the average experimental curve. The first resonance peaks are all near 1 kHz and the average slope between 1.5 and 10 kHz is -8.2 dB/octave in the model and -6.1 dB/octave in the experiments. However, after the peak, the curves of the individual geometries are clearly less smooth than the experimental average and a significant second maximum occurs in all three geometries between 2 and 4 kHz. Therefore, it is valuable to compare the individual model results to individual experimental curves, in contrast to a grand mean of many individuals. Figure 6-2B presents such curves (reported in Aibara et al. (2001)) and indeed shows more intra-specimen variability in the frequency dimension than the average does. The curves were rescaled by a factor of  $1/\sqrt{2}$  compared to the published values to correct for a difference in the normalization. The data in Aibara et al. (2001) were normalized to 1 Pa RMS, whereas our data and those from Rosowski et al (2007) were normalized to 1 Pa peak amplitude (confirmed in personal communication by K.N O'Connor on June 29<sup>th</sup> 2016).

Figure 6-2C shows the average response of our three models, indicating that averaging over more samples indeed smooths the response curve and improves similarity to the experimental average, especially above 2 kHz.

Figure 6-2D presents the phase of the SFP TF and shows approximate agreement with experimental average data from Aibara et al. (2001) (no average TF phase was reported in Rosowski et al. (2007)).

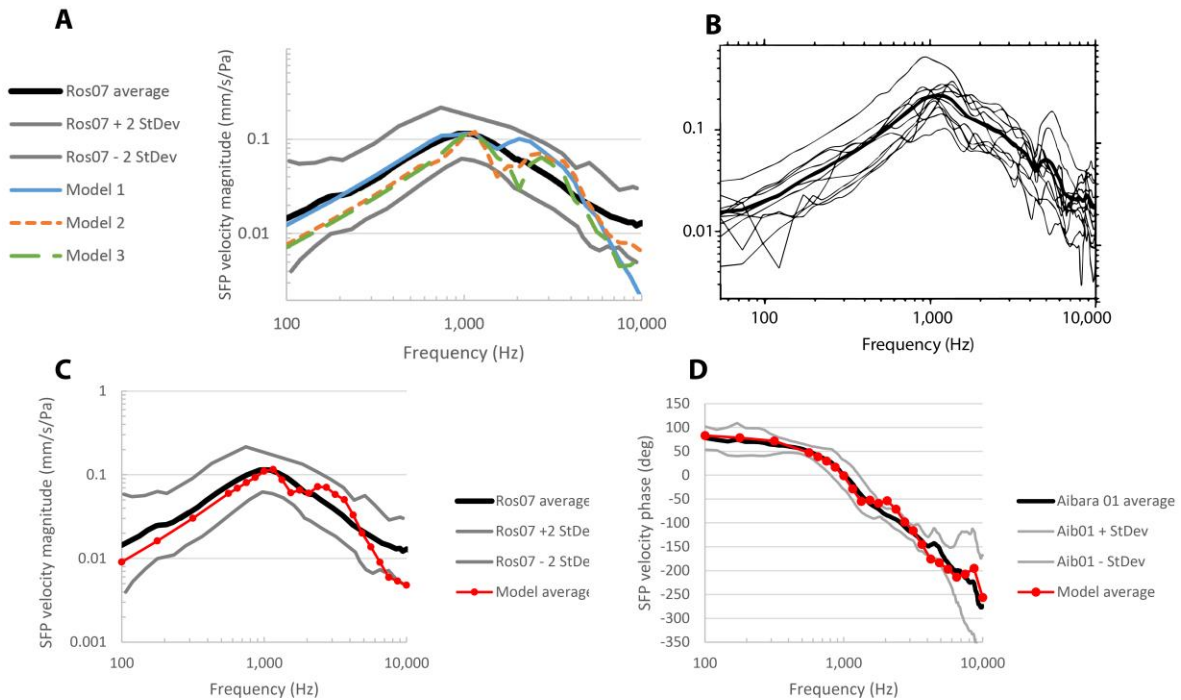


Figure 6-2: A.: Stapes velocity TF of our three geometries, compared to the experimental average from Rosowski et al. (2007) – B: Individual experimental curves of the stapes velocity TF, adapted from Aibara et al. (2001) – C: Average stapes response curve for our three geometries, compared to the average experimental curve from Rosowski et al. (2007) – D: Average phase of the SFP TF relative to the phase of the pressure on the TM for our three models and average experimental data from Aibara et al. (2001).

## 3.2 Tympanic membrane variations

### 3.2.1 TM damping

Figure 6-3A demonstrates the influence of TM damping on the stapes velocity TF. It shows the average TF of the base models and of models with a higher and lower constant loss factor ( $\eta$ ) in the TM. The largest changes occur around 3 kHz, i.e. around the second TF maximum, and at 10 kHz. The maximal differences around 3 kHz are +2.0 dB ( $\eta = 0.02$ ) and -3.4 dB ( $\eta = 0.5$ ), and at 10 kHz +2.3 dB ( $\eta = 0.02$ ) and -3.9 dB ( $\eta = 0.5$ ). Increasing the damping smooths the response curve, making it more similar to the average experimental curve. However, it makes the individual response curves unrealistic, compared to the individual experimental curves from Aibara (2001) (see Figure 6-2B).

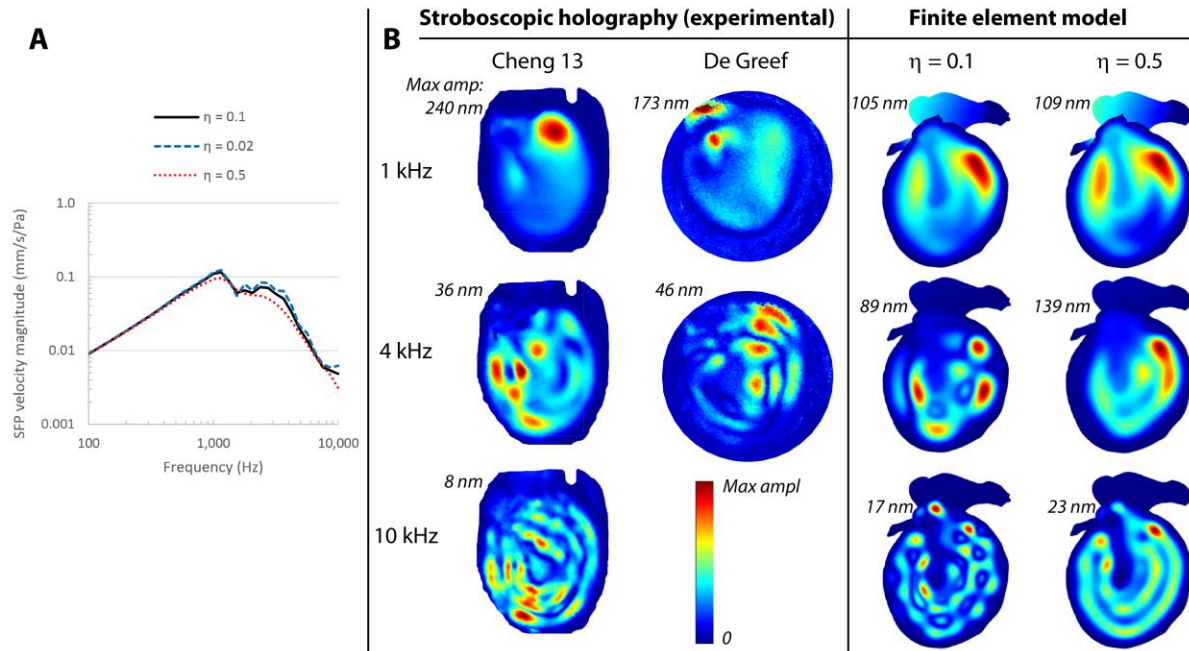


Figure 6-3: A: Influence of TM damping variation on the average SFP TF.  $\eta = 0.1$  represents the base models. The curves represent averages over our three geometries ; B: Vibration magnitude patterns of the TM, determined experimentally (Cheng et al., 2013; De Greef et al., 2014a, Chapter 1 of this thesis) and through our FE model (geometry 1), using two different loss factors. The dataset from De Greef is limited to 6.4 kHz, so no data at 10 kHz is available. The maximum amplitudes for each dataset are mentioned next to the patterns. The displacements are normalized to 1 Pa sound pressure. The color bar is shared by all datasets, but the ranges differ (depending on the maximum amplitude of each dataset).

Furthermore, a comparison of the measured full field vibrational patterns of the tympanic membrane to the calculated patterns in the model (Figure 6-3B) indicates that the match is worse for the model with high damping than for the base model. The higher damping model produces patterns that are too smooth in the spatial domain, compared to the experimental observations. The column titled ‘De Greef’ presents data that has not been published before and that was recorded using the setup for stroboscopic holography at our lab, described in De Greef et al. (2014a, Chapter 1 of this thesis).

### 3.2.2 TM material model: isotropic, orthotropic, non-uniform, and subdivided

Figure 6-4A depicts the difference in SFP velocity for the four different material models of the TM as described in section 2.4. None of the other models deviates more than 3.3 dB from the base model. Figure 6-4B provides an illustration of the coordinate systems in the subdivided TM model (model D). Figure 6-4C presents TM vibration magnitude patterns of the four different TM models at stimulation frequencies of 1 kHz, 4.2 kHz, and 10 kHz. The patterns as well as the maximum vibration amplitude are very similar for the different TM models.

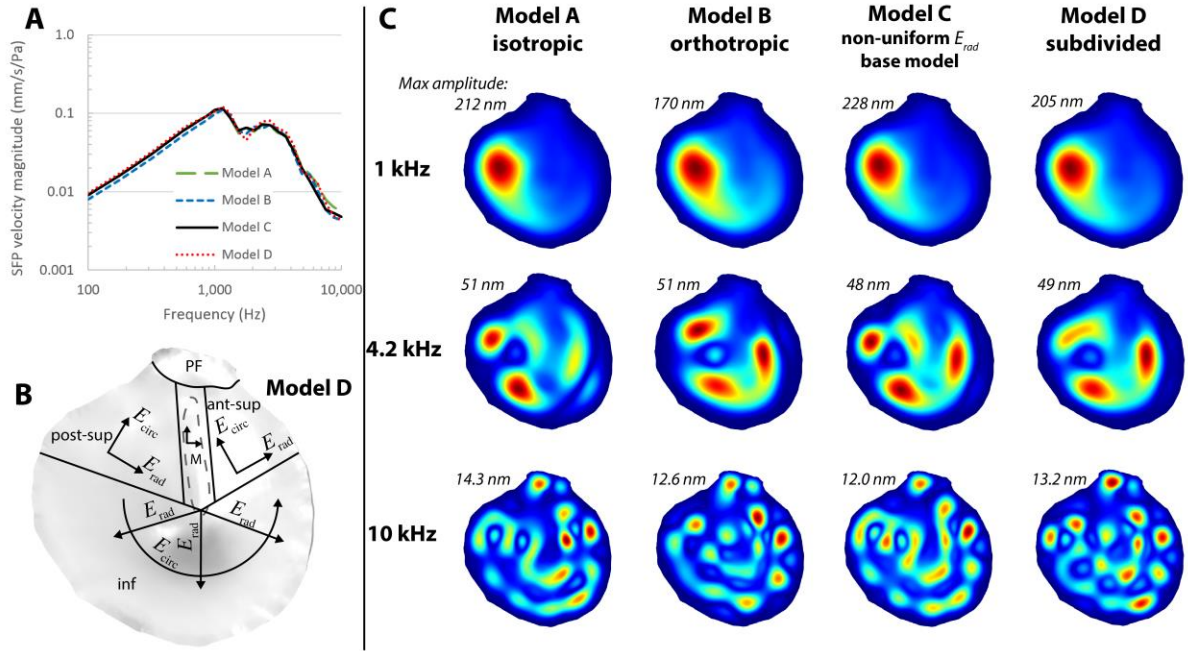


Figure 6-4: A: Influence of TM material models on the average SFP TF from the models based on geometries 1 and 2. Model A: Isotropic - Model B: Orthotropic - Model C: Orthotropic with decreasing  $E_{rad}$  - Model D: Subdivided TM (depicted in subfigure B). B: Subdivided TM model (model D). C: TM vibration magnitude patterns for the four models at three frequencies for the FE model based on geometry 2. The maximum amplitudes for each model and frequency are mentioned next to the patterns.

### 3.2.3 Tympano-malleal connection

The effects of the width and type of tympano-malleal connection (TMC) are illustrated in Figure 6-5A. Figure 6-5B and C illustrate the difference between the wide and narrow TMC geometry halfway along the manubrium. The change in SFP velocity is less than 2.3 dB over the entire frequency range.

### 3.3 Cochlear impedance

Figure 6-6A shows the model responses when using cochlear impedance data from four different previous studies, averaged over our three geometries in each case and keeping all other parameters equal. The model incorporating the impedance from Puria et al. (1997) is our base model and produces a less distinct second peak in the 2-4 kHz range than the other models. Its cochlear impedance has a more positive slope at frequencies above 1 kHz, as shown in Figure 6-6B.

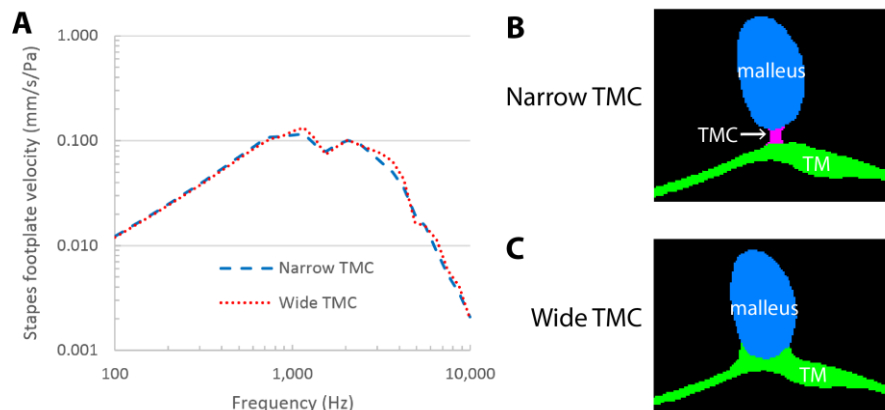


Figure 6-5: A: Impact of the width of the tympano-malleal connection (TMC) on middle ear transmission of the model, based on geometry 1. B & C: Segmented masks representing the malleus, TMC, and TM for the narrow TMC (B) and wide TMC (C) models. In the wide TMC model, the TMC is actually absent and the TM is directly attached to the malleus along the entire manubrium.

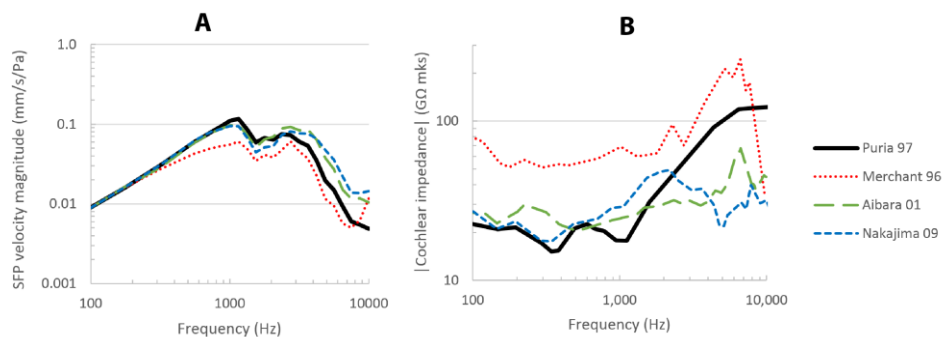


Figure 6-6: A: Effects of the incorporation of cochlear impedance data from different studies on the stapes velocity TF (Aibara et al., 2001; Merchant et al., 1996; Nakajima et al., 2009; Puria et al., 1997). The curves represent averages over our three geometries. B: Comparison of the different literature sources for the magnitude of the acoustic impedance of the cochlea. The legend is the same for both plots. The impedance data from Aibara et al. (2001) was rescaled by a factor of  $\sqrt{2}$  compared to the published values to correct for an error in their calculation of the impedance: there was inconsistency between the velocity and pressure calibrations (the former in peak units and the latter in RMS units) (confirmed in personal communication by K.N O'Connor on August 25<sup>th</sup> 2016).

### 3.4 Other quantitative variations

In Figure 6-7, the effects of other quantitative changes in the model are presented. All variations consist of a multiplication and division by 5 of a single material parameter, keeping all other parameters constant. All plotted curves represent the average response over the three geometries.

Increasing the Young's modulus of the TM shifted the first and second peaks to higher frequencies and decreased the second/first peak ratio from 1.1 ( $E_{TM}/5$ ) to 0.62 (base model) and finally 0.58 ( $E_{TM} \times 5$ ) (Figure 6-7A). The influence (in absolute value) of the Young's moduli of

the TMC and stapedius muscle (Figure 6-7B and G), and the loss factor of the TMC (Figure 6-7H) was nowhere larger than 1.05 dB. Decreasing and increasing the Young's modulus of the ISJ capsule had an effect of 3.8 dB and 1.8 dB at the most, respectively (Figure 6-7D).

The influence of the Young's modulus of the stapedial annular ligament (Figure 6-7C) is largest at frequencies below 1 kHz with changes of at least +4 dB ( $E_{SAL}/5$ ) and -10 dB ( $E_{SAL} \times 5$ ). However, above 2.1 kHz the influence is never larger than +2 dB ( $E_{SAL}/5$ ) and -5 dB ( $E_{SAL} \times 5$ ).

The Young's modulus of the IMJ (Figure 6-7E) has influence over the entire frequency range, with the smaller option ( $E_{IMJ}/5$ ) producing a response change of up to -7.7 dB, while the larger option ( $E_{IMJ} \times 5$ ) results in a change of up to +3.5 dB. While a decrease in TT's stiffness (Figure 6-7F) produces a change of +1.6 dB at most, an increase has an influence of up to -4.8 dB (at 1 kHz). Finally, the  $\beta$ -coefficient of Rayleigh damping (Figure 6-7I), applied to all ME soft tissues except the TM, had an influence around the resonance of up to +6 dB for  $\beta/5$  and -9 dB for  $\beta \times 5$ .

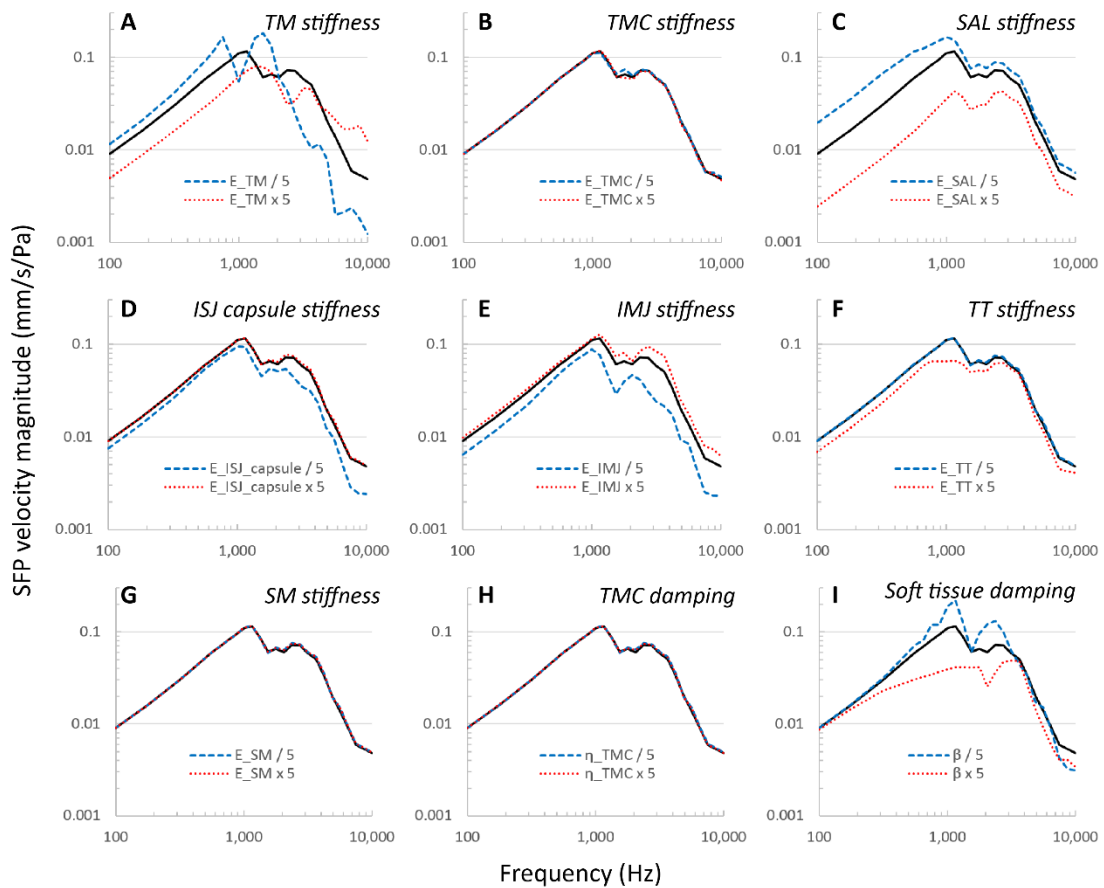


Figure 6-7: Influence of different variations in material parameters. All curves represent average responses over our three geometries.  $E$ : Young's modulus -  $\beta$ : Rayleigh damping parameter of soft tissue structures except TM -  $\eta$ : Loss factor.

### 3.5 Qualitative changes to the ME model

#### 3.5.1 Incudostapedial joint microstructure

In our base model, the ISJ is modelled as a fluid pocket within a solid capsule. This joint model is compared to a fully solid joint model in Figure 6-8A. The motivation for this comparison is discussed in section 4.5.1. In the case of a fully solid joint, three scenarios are compared in which the Young's modulus of both the ISJ interior and the ISJ capsule were changed: 0.6 MPa (as in Prendergast et al. (1999) and Gan et al. (2004)), 6 MPa (as in Cai et al. (2010)), and 60 MPa (for consistency). For the solid model with  $E = 0.6$  MPa, the response change compared to the base fluid model ranges from -0.8 dB to -2.7 dB below 2.5 kHz and -3.0 dB to -6.7 dB above 2.5 kHz, while for the solid model with,  $E = 6$  MPa, it differs by at most 0.9 dB from the fluid model. Increasing the Young's modulus further to 60 MPa increased the differences again, so that they are up to 2.2 dB (at 8.7 kHz), but still smaller than 1 dB below 3 kHz.

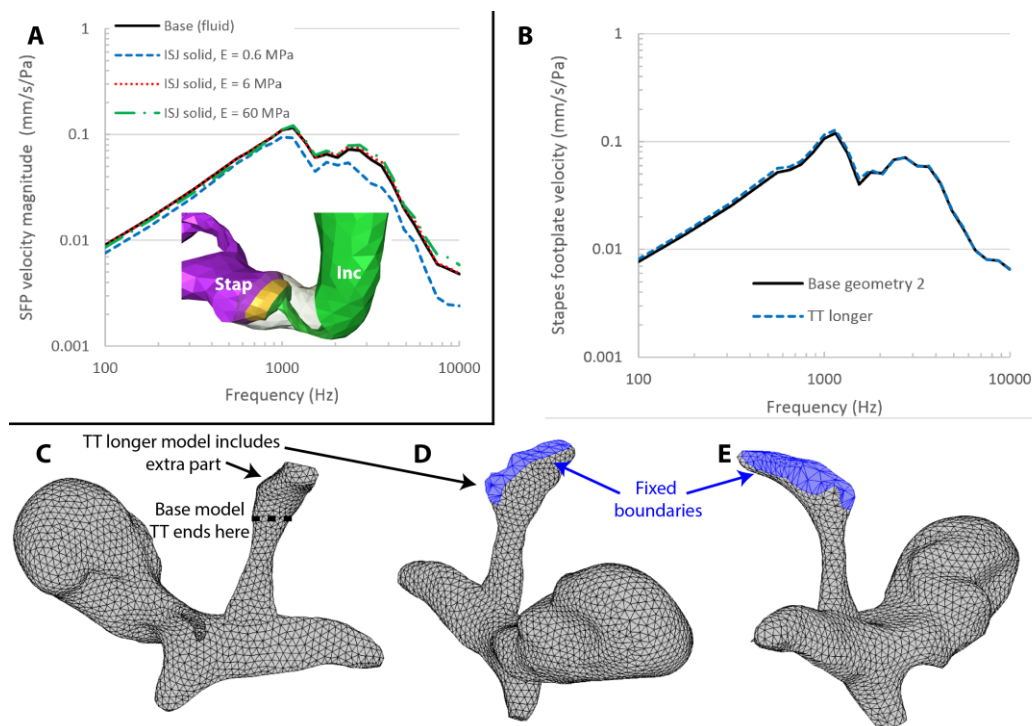


Figure 6-8: A: Influence of modeling the ISJ interior as a fluid or solid, for two different Young's moduli of both ISJ interior and capsule in the case of the solid model. Note that the red dotted line and the black base curve differ only by nature of the ISJ: solid or fluid. All curves represent the average responses for our three geometries. B: Influence of the length of the tensor tympani tendon on ME transmission of the model based on geometry 2. Note that the two curves almost overlap. C: Illustration of the lengths of the TT geometry in the base model and the model with a longer TT. The dashed line indicates where the TT tendon terminates in the base models of all three geometries. D&E: views from the postero-superior (D) and postero-inferior (E) side of the malleus of the model with a longer TT. Blue surfaces indicate fixed boundary conditions (only boundary conditions at the tendon are shown).

### 3.5.2 Tensor tympani tendon length

As can be seen in Figure 6-1, the base models contain only a portion of the tensor tympani tendon. An alternative model was constructed for geometry 2, in which a larger part of the tendon was included (see Figure 6-8C, D, and E). The motivation for this comparison is presented in section 4.5.2. Figure 6-8B (blue curve) shows that the influence of this change is smaller than 1 dB over the entire frequency range, and for this reason, the additional effort of including the longer TT tendon model was not made for the other geometries. For the sake of consistency, the shorter TT tendon version was used in the final model of geometry 2 as well.

## 4. Discussion

### 4.1 Model validations

The agreement between the model results and reported experimental results can be judged from Figure 6-2 and Figure 6-3. The largest discrepancy between our modeling results and reported average experimental ME response curves is the local maximum in our models between 2-4 kHz. The peak is present in all three geometries, but has a larger relative height with respect to the first resonance in geometry 1 than in the other two (see Figure 6-2A).

Since the models represent individual ears, they should each result in the response of an individual measurement, not the average response in which variations in the frequency domain are smoothed due to the averaging (see Figure 6-2). If an attempt is made to match the response of a ME model based on a single geometry to the average experimental response, the risk exists that unrealistic material parameters need to be applied, as discussed in the next section on TM damping. On the other hand, when applying the same set of parameters to different geometries, the average result should approach the average experimental result as the number of tested geometries increases and this would be a fine confirmation of the correctness of the parameters. Since constructing additional models based on different geometries is labor intensive, the number was limited to three in this paper. Nevertheless, the average model response presented in Figure 6-2C suggests that the currently used parameter set is adequate for middle ear modeling within the context of linear simulations in the frequency range 0.1 – 10 kHz, with some reservations between 2 and 4 kHz, where all three models differ from the experimental data.

### 4.2 TM damping

Figure 6-3 shows that one possible parameter change that has enough influence to reduce the discrepancy between model and experiment at 2-4 kHz is an increase in TM damping. Many published ME models employ Rayleigh damping in the TM, with coefficients  $\alpha = 0 \text{ s}^{-1}$ ,  $\beta = 0.75 \cdot 10^{-4} \text{ s}$  (Gan et al., 2006, 2004), or  $\alpha = 0 \text{ s}^{-1}$ ,  $\beta = 1 \cdot 10^{-4} \text{ s}$  (Liu et al., 2009; Sun et al., 2002). In the case of  $\beta = 0.75 \cdot 10^{-4} \text{ s}$ , converted through  $\eta = \frac{\alpha}{\omega} + \beta\omega$ , this corresponds to  $\eta = 0.047$  at 100 Hz,  $\eta = 0.47$  at 1 kHz, and  $\eta = 4.7$  at 10 kHz, i.e. higher than  $\eta = 0.5$  at most

frequencies above 1 kHz. However, the results presented in Figure 6-3 strongly suggest that a loss factor of  $\eta = 0.5$  (and consequently, higher values as well) results in unrealistic TM vibration patterns that are overdamped and exhibit too few local maxima. Very similar behavior was observed in the model of De Greef et al. (2014b, Chapter 5 of this thesis) that was focused on (and consisted of only) the TM and the malleus. It should be noted that the frequency spacing used in this paper is rather coarse compared to the fine structure of the TF in the high frequency range ( $> 4$  kHz) (see Figure 6-2B), which limits the reliability of conclusions about damping in this range.

### 4.3 Cochlear impedance

The incorporated cochlear impedance obviously has a profound influence on the motion of the stapes footplate. Therefore, the choice of the values used for this impedance has a large influence on the ME TF. The reported sources for cochlear impedances (see Figure 6-6) determined the impedance values through differing methods and show large mutual differences. The discussed 2-4 kHz discrepancy between our models and experimental TF's was smallest when implementing the data from Puria et al. (1997). Nakajima et al. (2009) highlighted the difficulties of experimentally determining the cochlear impedance at frequencies above 1 kHz, since in that range the stapes motion becomes multi-dimensional and the full 3D motion of the stapes should be determined. Therefore, additional experimental data on this will be very useful, and for now the dataset was implemented that produced results with the smallest deviation from experimental ME TF's, i.e. the cochlear impedance from Puria et al. (1997), even though it is not the most recent source.

### 4.4 Other TM model variations

The results in Figure 6-4 demonstrate that the different degrees of sophistication of the TM material model explored in this study lead to differences of less than 3.3 dB over the frequency range 0.1 – 10 kHz. In addition to this, the vibration patterns of the TM also did not change in a fundamental way when applying the different TM models. These conclusions are contradictory to the conclusions posed in Fay et al. (2006) and Tuck-Lee et al. (2008), but these papers studied feline (as opposed to human) middle ear models with different modeling approaches and parameter values. However, our results suggest that for linear modeling of an intact, non-pathological middle ear in the auditory frequency spectrum, a simple isotropic TM model could be as appropriate as a more sophisticated model.

The Young's modulus of the TM has a very strong influence on ME transmission, as observed in Figure 6-7A. This is expected and similar to findings of other studies, e.g Hoffstetter et al. (2010) and Maftoon et al. (2015).

The influence of the type of tympano-malleal connection (narrow or wide) was limited to 2.3 dB (see Figure 6-5). In both models, the connection was tight at the umbo and lateral process

of the malleus and how tight the connection is in between these two ends appears to be almost irrelevant. However, this is currently only confirmed within the limits of this study, i.e. an intact, non-pathological middle ear model in the linear, auditory regime. Furthermore, it should be noted that, in order to construct the wide TMC model, the angle between the TM and the rest of the model needed to be changed. This could have a separate effect on ME transmission that confounds the results. Koike et al. (2002) also performed a comparison of FE models with tight and loose TMC's and concluded that "*the modification of the attachment between the malleus handle and the tympanic membrane did not greatly influence the vibration mode and displacement of the tympanic membrane*".

Finally, the studied variation in TMC loss factor introduced a maximal difference of 0.8 dB (Figure 6-7H), i.e. a negligible influence.

#### 4.5 Qualitative changes to the ME model

The two reported qualitative changes to the ME models were chosen on the basis of the hypothesis that they could reduce the peak between 2-4 kHz in the TF and thereby improve the match with experimental ME TF's, as discussed in the following sections.

##### 4.5.1 Incudostapedial joint microstructure

A previous version of our model included a solid ISJ interior with a Young's modulus of 0.6 MPa. Upon inspecting the different subsystems in our ME models (TM, incudomalleal complex, and stapes), the stapes featured the highest resonance frequency, between 3-5 kHz (results not shown). Therefore, the hypothesis was formulated that if the stapes motion were coupled more strongly to the motion of the much heavier incudomalleal complex (their mass ratio is approximately 20 to 1 (De Greef et al., 2015, Chapter 3 of this thesis)), the free motion of the stapes and therefore also the resonance mode at the 'problematic' frequencies would be suppressed.

As can be seen in Figure 6-8A, increasing the Young's modulus to 6 MPa did change the overall stapes velocity, but replacing the interior with a fluid did not alter the ME response further for our model. The ME model by Gan and Wang (2014) contained more microstructural details in the ISJ, such as articular cartilage and a meniscus, and their results suggested that modeling the synovial nature of the joint improves the match with experimental data and is therefore influential for ME transmission. Other dedicated studies on modeling the ISJ, including Funnell et al. (2005) and (2006) and Zhang et al. (2011b), also included more microstructural details than our model, but were restricted to low frequency stimulations (not further specified). Further focused study is needed to make final conclusions about the role of ISJ microstructure in sound transmission of the human ME.

#### 4.5.2 Tensor tympani tendon length

Since the 2-4 kHz peak is situated at frequencies higher than the system's first resonance (around 1 kHz), another hypothesis was that it is caused by the absence of a mass in our model that is present in real TB's. The rationale behind this was that the mechanical response of a system is dominated by inertia, i.e. by mass, at frequencies above its resonance. One candidate is the tensor tympani tendon, a relatively bulky structure compared to other ME muscles and tendons, that was only partly included in our base model. The results presented in Figure 6-8B show that incorporating a significantly larger portion of the TT tendon only alters the model's response by less than 1 dB in the frequency range 0.1 - 10 kHz. Because of this small influence, because the entire TT was difficult to segment, and because the definition of boundary conditions is ambiguous when the entire tendon and muscle are included, only a portion of the TT tendon was included in our final model.

#### 4.6 Comparison to other studies and limitations of the current study

Already in 1978, researchers were investigating the influence of parameter variation in FE models of the ME (Funnell and Laszlo, 1978). More recently, Hoffstetter et al. (2010) published an extensive study of which the design was very similar to the current paper: after constructing a FE model of the human ME, based on realistic geometry, many different parameters and model features were varied and their influences on the stapes footplate transfer function were evaluated.

For the TM damping, similar results to ours were reported: the influence is modest and only notable between 1-4 kHz, i.e. around and above the resonance frequency. Outside of this range, a change of 25% in material damping had an effect of less than 5% (Hoffstetter et al., 2010).

For the TMC, contradictory results were reported – they found a large influence (> 25% change) when excluding or including the TMC (named stria mallearis there), although their approach to modeling and varying the TMC was different from ours and the results are therefore difficult to compare.

Hoffstetter et al. (2010) varied only the mass of the cochlear fluid, not other components of the acoustical impedance, and found that changing it by 50% had a negligible (<5%) effect on ME transmission for all simulated frequencies. They found that varying the TM's stiffness had a very large influence above 500 Hz, but almost none below it. This latter observation is contradictory to our results. Another significant difference between the conclusions is that they reported a negligible influence (5%) of the stapedia annular ligament, compared to a very large influence observed through our models. They found that the IS and IM joints had comparable, large influences, in contrast to our results that suggest that only the IM joint's parameters are very influential. Their observation regarding the effect of the stiffness of both middle ear muscles was on the other hand similar to ours.

It should be mentioned that one limitation of the current study is the variation of just a single parameter at a time. In complex mechanical systems such as the ME, parameter influences can be coupled, i.e. the effect of changing parameter A could be different for different values of parameter B. These coupled effects are not detected using the current method. In the interpretation of the results it is important to keep this methodological limitation in mind.

At this point we also need to rectify two errors in a previous paper by the same first author (De Greef et al., 2015, Chapter 3 of this thesis). In that paper, the bending theory of the pedicle of the lenticular process of the incus was mentioned (Funnell et al., 2005). Funnell et al. proposed the possibility that the thin pedicle may bend during ossicular motion in certain vibration modes (especially at higher frequencies), “thereby adding flexibility to the [incudostapedial joint] and reducing the transmission of particular motion components from the incus to the stapes”. In the paper by De Greef et al., it was stated that if the pedicle consists of bone instead of strongly calcified cartilage (which are not distinguishable from each other on micro-CT images but have a different Young’s modulus by approximately a factor of 10), the ‘bending theory’ would be undermined. However, Funnell et al. did indeed propose bending in a full bony pedicle, not only a cartilaginous one. Furthermore, the paper by Decraemer and Khanna (2004) was cited to mention bending in the pedicle of the lenticular process as well, but the concept is not covered by Decraemer and Khanna.

## 5. Conclusion

This study aimed to examine the influence of various quantitative and qualitative variations in parameter values and model definitions on sound transmission in human ME FE models. The most important quantitative parameters were found to be the Young’s moduli of the tympanic membrane (TM), the stapedial annular ligament, the incudomalleolar joint, and the tensor tympani, the loss factor of the TM, the  $\beta$  Rayleigh damping coefficients for the soft tissues outside the TM, and the choice of cochlear impedance. Less influential parameters were the Young’s moduli of the tympano-malleolar connection, incudomalleolar joint capsule, and stapedius muscle, and the loss factor of the tympano-malleolar connection.

The inclusion of multiple individual geometries in a single FE study allowed the calculation of an average stapes velocity response function, and confirmed that this matches experimental average response curves better than individual models. The largest discrepancy appeared in the 2-4 kHz range, where the model response was higher than the average experimental result. Due to the wide variation in experimental response curves of individuals, the average outcome of the models falls within the standard deviation observed for individual temporal bones at most frequencies.



# Chapter 7. The Effect of Malleus Handle Fracture on Middle Ear Transmission, predicted using Finite Element Analysis

---

## Abstract

**Hypothesis:** Finite element modeling predicts that a malleus handle fracture decreases the acoustic transfer of the human middle ear.

**Background:** Cases of isolated malleus handle fractures are rare and easily missed, making clinical studies difficult. Recently, an in-vitro study on malleus handle fracture was reported. Now, numerical modeling is used to expand our understanding of this injury.

**Methods:** Three finite element models were developed from three different human temporal bones. In each model, fractures were introduced in the manubrium at four different positions separately. After validation calculations, multiple clinical scenarios were simulated.

**Results:** For most frequencies, the models predicted similar results as seen in the experiments. Both with and without a cochlear impedance, increasing the umbo-to-fracture distance resulted in an overall larger loss of stapes footplate velocity. Removing the distal malleus fragment had an effect of less than 1 dB on average for all fracture positions except for the one superior to the tensor tympani tendon. An intimate, wide tympanomalleal connection resulted, after malleus fracture, in a footplate velocity loss that was on average 2.9-5.1 dB less than for a loose, narrow connection.

**Conclusions:** This study investigates the effect of a fracture in the malleus handle through finite element analysis. The models predicted observed in-vitro hearing loss adequately, so they constitute a reliable base for predicting other clinical conditions.

*Major contributions to the development of the FE models, the execution of the simulations, data analysis and writing of the paper.*

*This chapter is submitted for publication in the Journal of the Association for Research in Otolaryngology.*

## 1. Introduction

In otology literature, cases of isolated malleus handle (or manubrium) fractures are uncommon: only about 40 cases were reported in the latest 30 years (Niklasson et al., 2010) and less than 80 since 1855 (Blanchard et al., 2011). However, it is very probable that many cases of isolated manubrium fractures are missed and that the condition is less rare than was believed in the past. The reason for this is that they are difficult to find if not specifically looked for because the symptoms are rather diffuse (Niklasson et al., 2016). The difficult diagnosis combined with the low prevalence makes it very difficult to gather enough clinical material for randomized clinical studies of treatment methods. As a result of this there is not yet a consensus on the optimal approach for restoring the patient's hearing after a malleus handle fracture trauma. Nevertheless, the need for adequate treatment is pertinent, since the conductive hearing loss can be as high as 45 dB (Chien et al., 2008) and spontaneous healing is difficult for ossicular bones (Chien et al., 2008).

The typical clinical presentation of isolate malleus fracture is a sudden unilateral hearing loss after retracting one's finger out of the wet ear canal, during or shortly after a shower. Right after the retraction, the patient often experiences a "pop", usually associated with very loud sound and strange noises after the trauma, and a short painful sensation. The wet finger acts as an airtight seal, so that a sudden underpressure is created upon retraction from the ear canal. This underpressure causes the tympanic membrane to be displaced laterally, which induces an inwardly directed reflex contraction of the tensor tympani. This results in high internal stress conditions in the manubrium of the malleus, and in some cases, manubrium rupture and a permanent mild hearing loss or dullness in the ear. If otomicroscopy is performed, a fracture line is sometimes seen, and with pneumatic otoscopy a hypermobile malleus shaft/umbo is often evident. Gentle palpation on the malleus shaft can also be useful in revealing this hypermobility. Watchful waiting, a hearing aid or an ossiculoplasty are options available for

these patients. A recent in-vitro study indicated that significant differences exist in terms of stapes footplate (SFP) velocity restoration between different treatment methods for manubrium fractures that were proposed in the past (Niklasson and Tano, 2010). The authors needed to remove the cochlear fluid in order to be able to measure the SFP vibration without having to create an additional opening in the tympanic cavity. A model-oriented approach will be helpful in comparing the proposed treatment methods in the presence of a cochlear impedance.

Our research group has recently built three finite element (FE) models of the intact human middle ear, based on three different individual temporal bones (De Greef et al., 2016, submitted in Hearing Research, Chapter 6 of this thesis). The current study will build further on these models by simulating both in-vitro (with removed cochlea) and clinical conditions (with intact cochlea) related to malleus handle fractures. The in-vitro simulations allow us to validate the model by comparing the model results to the experimental results, and the clinical simulations allow us to investigate conditions that are difficult to examine experimentally.

## 2. Materials and methods

### 2.1 Middle ear models

Three different FE models were constructed based on three different temporal bones. The full description of the construction and definition of the ‘intact’ middle ear models can be found in De Greef et al. (2016, submitted, Chapter 6) and a condensed description is provided here.

Three temporal bones (1: male 75y, right – 2: male 73y, right – 3: male 73y, left) were imaged using micro-computed tomography ( $\mu$ CT) after they were stained with phosphotungstic acid (PTA). The isotropic voxel size of the datasets was 18.5  $\mu$ m (sample 1) or 22.8  $\mu$ m (samples 2 and 3). The reconstructed images were segmented into different materials and converted into surface models in Amira<sup>®</sup> 6.1 (FEI Visualization Sciences Group, Hillsboro, Oregon, USA). The surface models were then imported into Comsol Multiphysics<sup>®</sup> 5.2 (COMSOL AB, Stockholm, Sweden), where they were converted into volume meshes of approx. 120,000 tetrahedral elements.

The stimulating load on the model was a direct, uniform, harmonic pressure of 1 Pa peak amplitude on the lateral side of the TM to simulate incident acoustic waves. A contiguous selection of triangles at the edge of the TM, as well as the end surfaces of the anterior malleal ligament (AML), lateral malleal ligament (LML), posterior incudal ligament (PIL), stapedial annular ligament (SAL), tensor tympani (TT) tendon and stapedius muscle (SM) tendon were all fixed. The influence of the cochlea was modeled as an acoustic complex impedance, acting on the medial surface of the SFP and the SAL. The value of this impedance was frequency-dependent taken from Puria et al. (1997).

All materials except for the interior of the incudostapedial (IS) joint were modeled as solid materials. The Young's moduli of all structures are listed Table 6-2. The TM was modeled as an orthotropic material within a polar coordinate system with its origin in the umbo. Similar to Tuck-Lee et al. (2008), the radial Young's modulus decreased away from the umbo:

$$E_{rad}(r) = \min\left(40 \text{ MPa} * \frac{2 \cdot 10^{-3} \text{ m}}{r}, 100 \text{ MPa}\right). \quad \text{Eq. 7-1}$$

Other material parameters, including damping and mass densities, can be found in De Greef et al. (2016, submitted, Chapter 6).

## 2.2 Malleus handle fracture models

In the three models, malleus fractures were simulated by removing a small volume of material from both the malleus and tympanomalleal connection (TMC) between two planes that were perpendicular to the manubrium and mutually 10  $\mu\text{m}$  apart. A convergence test with decreasing gap width ensured that this gap width was small enough not to influence the model results in a significant way, while it was still wide enough to avoid contact between the two fractured fragments during vibration. The fracture was positioned at four locations (Figure 7-1): a first one at 1 mm from the umbo, a second one at 2 mm, a third one just inferior to the location of attachment of the TT tendon (infTT), and a fourth one just superior to the TT tendon (supTT). The distance from the infTT fracture to the umbo differed between the three models: 3.00 mm (model 1), 2.20 mm (model 2) and 2.45 mm (model 3). The same was true for the supTT fracture: 3.60 mm (model 1), 3.30 mm (model 2) and 3.35 mm (model 3). In any model, either no or one fracture was introduced, never more than one.

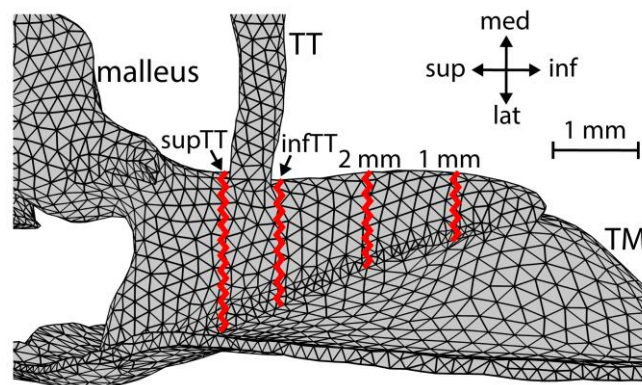


Figure 7-1: Illustration of the position of the malleus handle fractures (in red) in model 1. TT: Tensor tympani. TM: Tympanic membrane. The fractures are positioned (from right to left): 1 mm from the umbo, 2 mm from the umbo, just inferior to the TT tendon (infTT) and just superior to the TT tendon (supTT). For the sake of clarity, not all structures that were included in the models are shown here.

The SFP velocity ratio of the fractured model to the intact model was compared to experimental results from Niklasson et al. (2016). In that study, laser Doppler vibrometry was used to

determine the effect of malleus handle fracture and different reconstructive interventions on the SFP velocity. In these experiments the cochlear fluid was drained from the inner ear for practical reasons, so that the cochlear impedance was essentially eliminated. Therefore, the model was evaluated without a cochlear impedance so that a meaningful comparison with the experiments can be made and the fracture model can be validated.

After this, a cochlear impedance was added to the model in order to investigate clinically relevant scenarios. First, the SFP velocity in the case of a fractured manubrium in the presence of a cochlea was determined. Next, the distal fragment of the fractured manubrium (i.e. the fragment to the right of the fracture in Figure 7-1) was removed from the geometry in order to simulate the surgical removal of this fragment.

Finally, the effect of different types of tympanomalleal connection (TMC) was studied. As reported by De Greef et al. (2016), the minimal anterior-posterior width of the TMC varies over an order of magnitude among individuals, ranging from  $83 \pm 7 \mu\text{m}$  to  $840 \pm 7 \mu\text{m}$  in their study population of 13 individuals. However, near the umbo and the lateral process of the malleus the TMC was wide and tight in all samples of the cited study (2016).

For one geometry of this study (model 1) with a narrow TMC by nature, an alternative model in which the TM was more tightly connected to the manubrium was constructed, similar to the most wide connection reported in De Greef et al. (2016). This was realized by rotating the TM towards the manubrium around the antero-posterior axis through the umbo, so that the distance between TM and malleus decreased. In the wide TMC model, there was no separate material anymore for the TMC: based on microstructural observations, De Greef et al. (2016) demonstrated that in those cases, the TM is directly connected to the malleus without a distinct connective structure. The result of this segmentation is visible in Figure 7-6A, alongside the original histologic sections of the two extreme TMC samples from De Greef et al. (2016).

In all scenarios, a frequency-domain analysis was carried out sweeping over 24 frequencies between 0.1 and 10 kHz. The 24 frequencies were evenly spaced on a logarithmic scale at four frequencies per logarithmic decade below 562 Hz and 16 frequencies per logarithmic decade above 562 Hz.

## 3. Results

### 3.1 Comparison to experiments

#### 3.1.1 Different fracture positions: one TB

For one TB, Niklasson et al. (2016) reported SFP velocity ratios for three different fracture positions: 1 mm from the umbo, 2 mm from the umbo and just inferior to the TT (infTT). Therefore, we calculated the SFP velocity for our three models for these three fracture positions.

For these simulations, no cochlear impedance was included in the model, similar to the experimental conditions. The results of these simulations are presented in Figure 7-2.

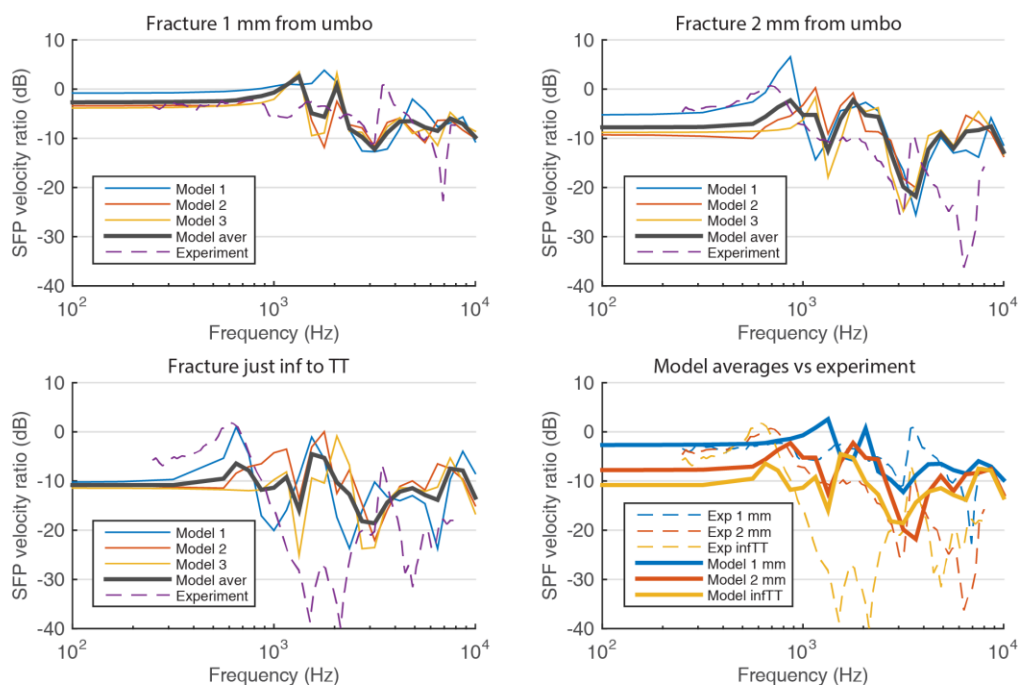


Figure 7-2: The stapes footplate (SFP) velocity ratio of the middle ear (ME) with fractured malleus handle to the intact ME for one temporal bone (experimentally) and our three models, for three different fracture locations. Bottom-right depicts the experimental SFP results and the average model result for all three fracture positions (average calculated on dB-scale).

The experimental data are available from 0.2 to 8 kHz, the model results were evaluated from 0.1 to 10 kHz. For all curves, at most frequencies a velocity loss is observed after fracturing the malleus.

At frequencies below 750 Hz, both in experimental (from Niklasson et al. (2016)) and model curves, the velocity ratio is almost constant and is the most negative for the infTT fracture and the least negative for the 1 mm fracture. After this, all curves increase to their first maximum (sometimes above 0 dB) at different frequencies, ranging from 600 Hz to 1800 Hz. Beyond the first maximum, a decline is observed, followed by a second, local, maximum. At higher frequencies the curves become more complicated. However, the same order between the three fracture positions (1 mm - 2mm - infTT) is maintained at most frequencies (Figure 7-2, bottom right).

The differences in SFP velocity ratio between different fracture locations at low frequencies are smaller in the experiments than in the models. In addition, the peaks in the model curves appear sharper. Furthermore, the experimental curves drop to lower minima than the model curves, especially the infTT fracture curve. However, as will be seen in Figure 7-3, the TB used for

measuring the fracture effect at different fracture locations exhibited the most extreme velocity loss of all TB's. A last difference between experiment and model results is that the experimental curves appear to be generally decreasing with increasing frequency, a tendency that is not equally clear in most model curves.

### 3.1.2 Fracture just inferior to the tensor tympani tendon: eight TB's

The SFP velocity loss due to a infTT manubrium fracture was measured for eight different TB's in Niklasson et al. (2016). Above 4 kHz, data for only five of the eight TB's were obtained. In Figure 7-3, these data are compared to the model results for the infTT fracture in our three FE models. At frequencies 0.2 – 0.3 kHz, the velocity loss in our models is larger than for the TB's. Between 0.7 and 8 kHz, most of the uncertainty ranges overlap, except for a small band between 1.4 and 2 kHz. Above 8 kHz and below 0.2 kHz, no experimental data are available so no comparison can be made.

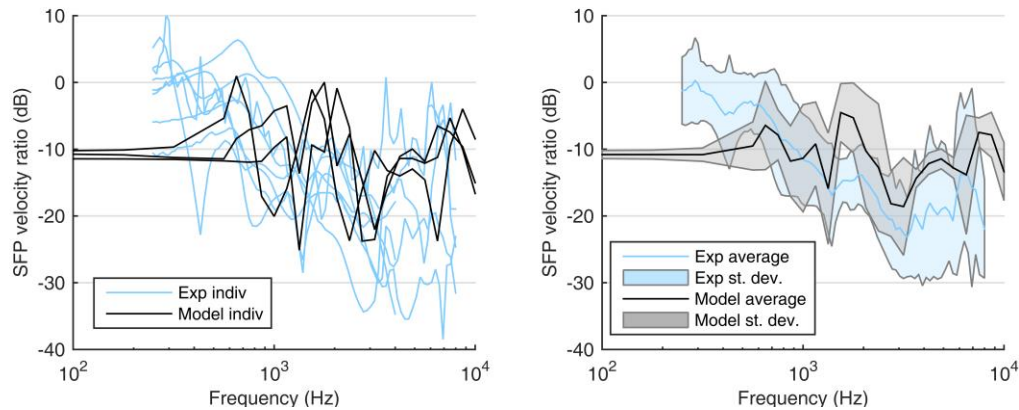


Figure 7-3: Left: Individual curves of experimental (blue) and simulated (black) stapes footplate (SFP) velocity ratios in case of a malleus handle fracture just inferior to the tensor tympani tendon. Right: Average curves of the individual experimental (blue) and simulated (black) SFP velocity ratios. The shaded areas illustrate the average plus and minus one standard deviation of the respective populations. The experimental data originates from Niklasson et al. (2016).

## 3.2 Model predictions for clinical scenarios

### 3.2.1 Fractures with intact cochlea

Figure 7-4 illustrates the SFP velocity loss due to a malleus handle fracture in the presence of an intact cochlea as predicted by our three models. The average velocity ratios for all models over the frequency range 0.1 – 10 kHz are -4.2 dB (1 mm), -8.5 dB (2 mm), -11.1 dB (infTT) and -14.7 dB (supTT). These averages were calculated on a dB-scale and were compensated for the sparser frequency points evaluated at frequencies below 562 Hz by interpolation.

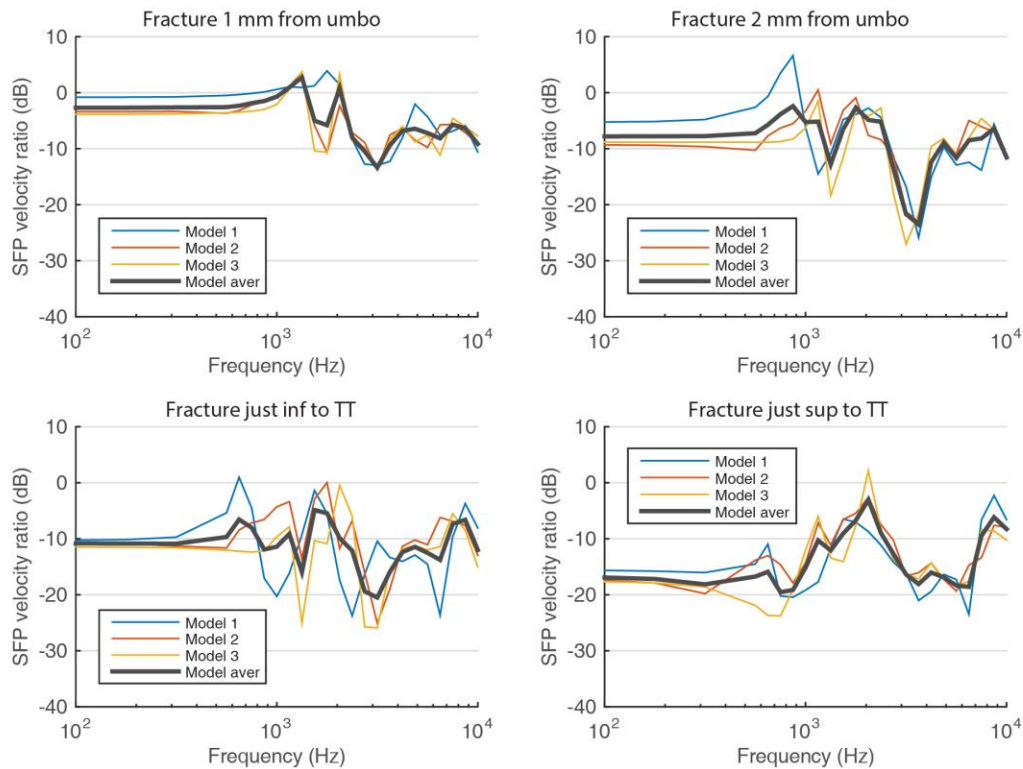


Figure 7-4: Stapes footplate velocity ratio for different fracture positions and models with intact cochlea, grouped per fracture position. The average curves on each graph are calculated on a dB-scale.

Similar to the condition without cochlear impedance, at low frequencies the curves are relatively flat. The first peak frequency decreases with increasing umbo-to-fracture distance for the 1 mm, 2 mm and infTT fracture. The supTT fracture exhibits rather different curve shapes from the other fracture positions with all models reaching a distinct local maximum around 1.5-2 kHz. At low frequencies, the velocity loss is clearly related to the fracture position (1 mm < 2 mm < infTT < supTT).

When running the models with (as opposed to without) a cochlear impedance, the absolute values of the SFP velocity changed substantially for certain frequencies (up to 15 dB), but the velocity loss after manubrium fracture changed on average less than 0.1 dB for all fracture positions and at the most 1.4 dB for the infTT fracture at 10 kHz (no figure shown).

### 3.2.2 Removal of the distal malleus fragments

Figure 7-5 displays the effect of the removal of the distal malleus fragment on the SFP velocity loss. The reported ratios are ratios of the model with the distal part removed and the model with manubrium fracture but with the distal part still in place. On average, the ratios are 0.04 dB (1 mm), 0.10 dB (2 mm), -0.09 dB (infTT) and 1.69 dB (supTT).

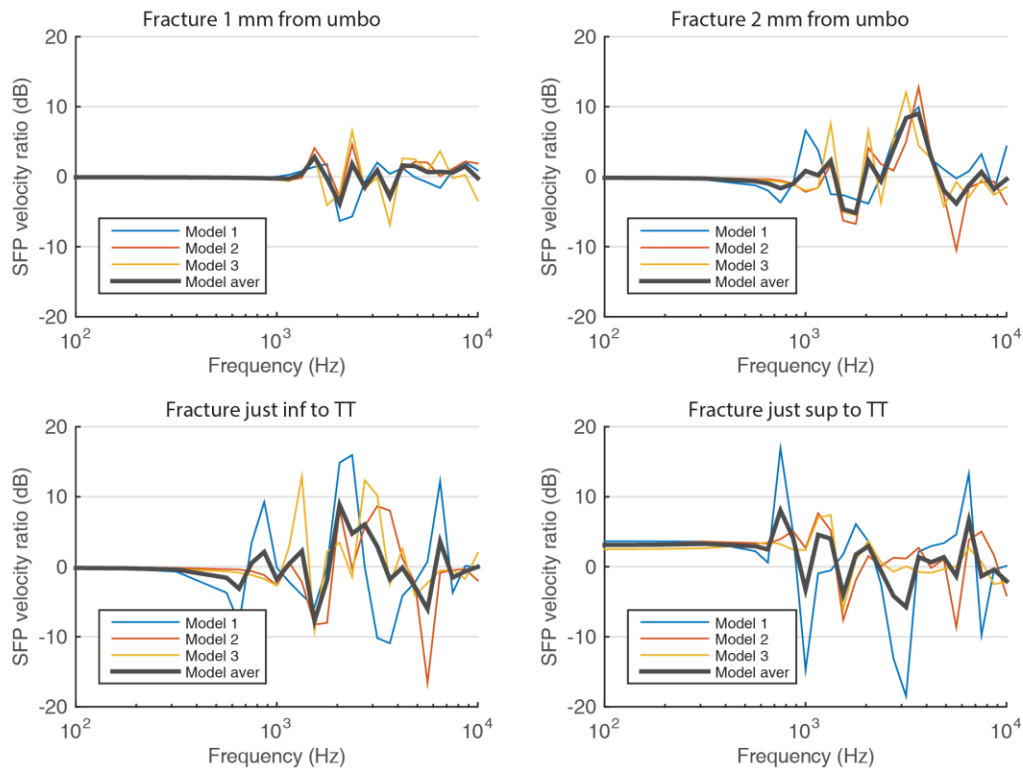


Figure 7-5: Stapes footplate velocity ratios of the models with removed malleus fragment, relative to the original fractured models.

At low frequencies, there is almost no effect in all cases except for the supTT fracture. At higher frequencies, the curves do deviate farther from 0 dB, although not consistently towards positive or negative values.

### 3.2.3 Influence of tympanomalleal connection

Figure 7-6A illustrates the difference between the wide and narrow tympanomalleal connection (TMC) geometry halfway along the manubrium. In the wide TMC model, the TMC actually is absent and the TM is directly attached to the malleus along the entire manubrium. The difference in SFP velocity ratio between these two ME models is shown in Figure 7-6B. The average velocity ratio over the frequency range 0.1 – 10 kHz is mentioned in the legends, as well as the differences of these averages. For all fracture positions, the wide TMC model exhibits on average less SFP velocity loss than the narrow TMC model.

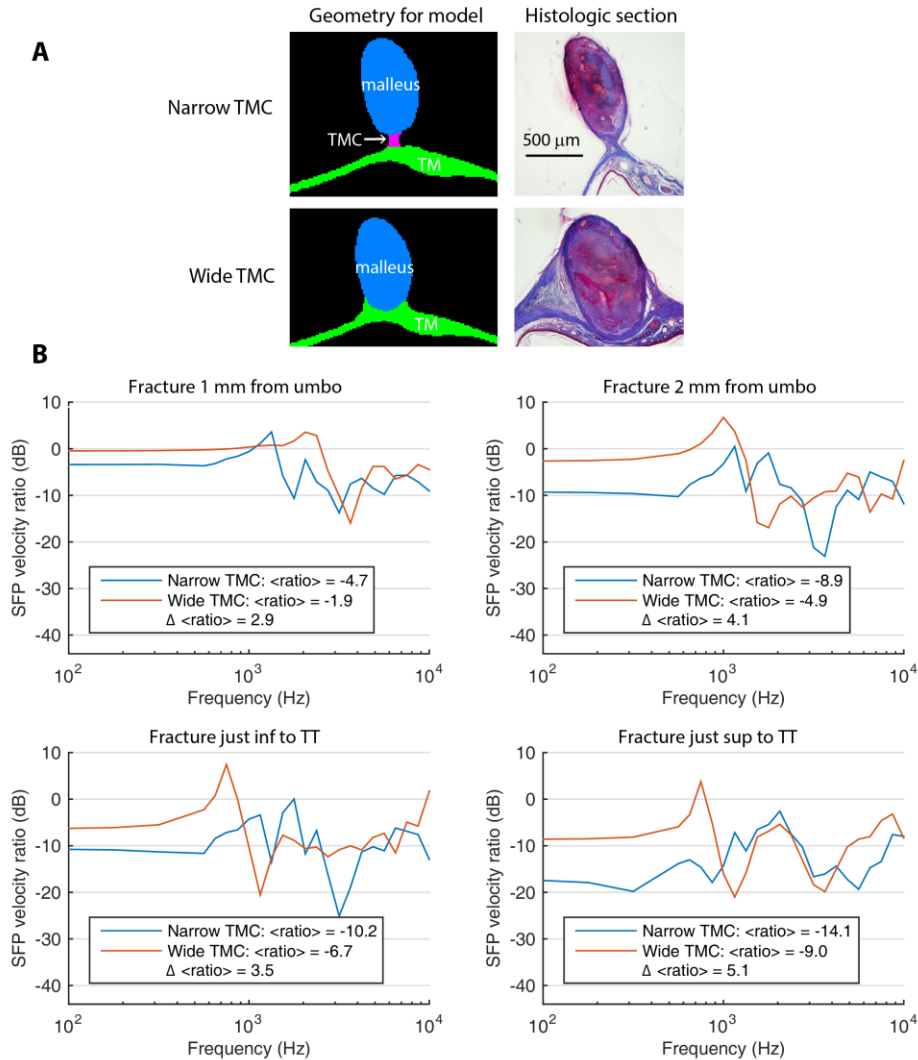


Figure 7-6: A, left: Segmented masks representing the malleus, tympanomalleolar connection (TMC) and tympanic membrane (TM) for the narrow TMC and wide TMC models. In the wide TMC model, the TMC actually is absent and the TM is directly attached to the malleus along the entire manubrium. A, right: histologic sections from De Greef et al. (2015), illustrating the microstructure of the TMC in two extreme cases on which our new two geometries are based qualitatively. B: Stapes footplate velocity ratios of model 1, with either a narrow or a wide tympanomalleolar connection (TMC).

## 4. Discussion

### 4.1 Comparison to experiments

In De Greef et al. (2016, submitted, Chapter 6), the intact ME FE model was validated and compared to experimental data from TB measurements. It was concluded that the model represented the measured vibration response adequately at most frequencies, with the largest discrepancy between 2 and 4 kHz. In the current study, the match with available experimental

data in the case of malleus handle fracture just inferior to the tensor tympani tendon (Niklasson et al., 2016) is found to be less than optimal for frequencies below 0.4 kHz and between 1.5 and 2 kHz, where the uncertainty ranges do not overlap (Figure 7-3, right). Furthermore, in the range 3.5-6 kHz, the models predict less velocity loss than the experimental observations report, in which the velocity loss appears to increase with increasing frequency, although the uncertainty ranges still overlap for all frequencies. If overlap of uncertainty ranges is the criterion, we can conclude that the model accurately predicts the experimental results for malleus handle fracture from 0.4 to 1.5 kHz and from 2 kHz to 8 kHz. Above 8 kHz and below 0.2 kHz, no conclusions can be drawn due to the lack of quantitative experimental observations, although both the slope of the experimental curves at 0.2 kHz and the predictions by the models below 0.2 kHz suggest that below 0.2 kHz, the loss does not differ much from the value at 0.2 kHz.

Typical audiometry results in clinical cases of isolated malleus handle fracture indicate an air-bone gap across all frequencies, inferring conductive hearing loss that is larger at the higher frequencies (above on average 1 kHz) (Chien et al., 2008). It was hypothesized by Chien et al. (2008) that there might be “still sufficient contact between the fractured ends of the manubrium to permit sound transmission at low frequencies, with progressively greater dissipation (shunting) of sound energy away from the ossicular chain at the fracture site at higher frequencies”. The observation that the hearing loss is larger at higher frequencies was not clearly predicted by our models. The main reason for this is probably that the hearing loss at low frequencies is too large in our models. This could be linked to the hypothesis of Chien et al. (2008): in our models there is no contact at all between the malleus fragments. Incorporating contact modeling in the future might reduce the difference between model and experiment at low frequencies.

Given the wide range of reported severities of conductive hearing loss in cases of isolated manubrium fractures (from 6.5 dB (Harris and Butler, 1985) to 45 dB (Chien et al., 2008)) and the wide range of other mechanical observations in the middle ear that are reported in literature, it is difficult to claim complete confidence in middle ear models. By validating the model for different scenarios and checking whether the model predicts results that are correct in terms of order-of-magnitude and general trends, confidence in the reliability of the model increases. The presented simulations in section 3.1 in this paper constitute such additional validations.

Blanchard et al. (2011) report that in most cases of isolated malleus fracture they encountered,  $\mu$ CT revealed that the fractured fragments of the malleus were displaced with respect to their original anatomical position. In those cases, the inferior fragment was consistently lateralized, while the superior segment was medialized. This complication was not taken into account in the current study so the presented results are not necessarily relevant for those cases in which displacement of the fragments has happened.

## 4.2 Model predictions for clinical scenarios

Because of the difficulties in gathering clinical data of cases with isolated malleus handle fractures, other study approaches can bring new insights. The recent in-vitro study on surgically manipulated temporal bones (Niklasson et al., 2016) was therefore very valuable, and the current model-oriented paper will further improve the understanding of this condition. Using our models it was shown that the calculated velocity loss differed on average less than 0.1 dB when the simulations were carried out with versus without a cochlear impedance. This suggests that the removal of the cochlea for in-vitro experiments, such as by Niklasson et al. (2016), influences the velocity loss results very little.

In section 3.2.2, the effect of removing the distal fractured fragment of the malleus was examined. It is observed that this intervention alone has a very small average influence on the stapes velocity. Only in the case of a supTT fracture, the improvement was on average more than 1 dB over the frequency range 0.1-10 kHz and at least 2.5 dB for frequencies below 850 Hz. Therefore, further intervention is needed in order to restore the patient's hearing noticeably, such as the placement of a malleus prosthesis made of cortical bone (Niklasson et al., 2016) or the placement of a Partial Ossicular Replacement Prosthesis (PORP) (Blanchard et al., 2011; Chien et al., 2008) or Total Ossicular Replacement Prosthesis (TORP) (Abo-Khatwa et al., 2005). A proposed surgical approach that does not involve the removal of the distal fractured fragment is fixation of the broken shaft with bone cement (Delrue et al., 2015; Hato et al., 2007).

The simulations involving different types of tympanomalleolar connection (TMC) revealed that this geometric feature has a significant effect on hearing loss in case of a malleus handle fracture (Figure 7-6). The difference in velocity loss was between 2.9 dB (for the 1mm fracture) and 5.1 dB (for the supTT fracture), depending on the fracture position. In De Greef et al. (2016, submitted, Chapter 6) it was observed that the type of TMC had only a small influence of at most 2.2 dB between 0.1 and 10 kHz on the SFP velocity transfer function in an intact ME model. In that study, the same two geometries, material parameters and model definitions were used as in the current study. It appears that the TMC type matters little as long as the malleus handle is intact, but that a ME with a wide TMC suffers less velocity loss than one with a narrow TMC when it sustains a malleus fracture injury. These observations suggest that a tight connection allows more energy transfer from the TM to the ossicular chain than a narrow TMC when only a part of the manubrium is directly connected to the rest of the ossicular chain.

## 4.3 Conclusions

In this study, three existing FE models of the human ME were utilized to study the effect of a malleus handle fracture on the SFP velocity. Validation of the model using simulations without a cochlear impedance (the condition in which the experimental data were obtained) revealed that the model mimicked experimental results adequately for the frequencies 0.4 - 1.5 kHz and 2 - 8 kHz.

After the validation, the model was used to predict multiple clinical scenarios, i.e. in the presence of a cochlear impedance. This flexibility highlights the value of the model-based approach. A malleus handle fracture in the presence of a cochlea infers a SFP velocity loss ranging from on average -4.8 dB (for a fracture 1 mm from the umbo) to -13.7 dB (for a fracture just superior to the tensor tympani tendon). Furthermore, the model predicted that removing the distal fractured fragment of the malleus does not improve SFP velocity in a clinically significant way unless the fracture is superior to the TT tendon, in which case the velocity is restored by 1.2 dB on average and at least 2.5 dB for frequencies below 850 Hz. Finally, the models predicted that the type of tympanomalleolar connection (TMC) has a notable effect on the SFP velocity change due to a malleus handle fracture. The average velocity loss was 2.9 to 5.1 dB smaller in the case of a wide, tight TMC, compared to a narrow TMC. The studied TMC shapes were population extremes as reported by De Greef et al. (2016).



# Chapter 8. Pressure Buffering by the Tympanic Membrane. In Vivo Measurements of Middle Ear Pressure Fluctuations during Elevator motions

---

## Abstract

**Objectives:** The tympanic membrane (TM) represents a pressure buffer, which contributes to the overall pressure regulation of the middle ear (ME). This buffer capacity is based on its viscoelastic properties combined with those of the attached ossicular chain, muscles and ligaments. The current work presents a set of in vivo recordings of the ME pressure variations normally occurring in common life: elevator motion. This is defined as a situation of smooth ambient pressure increase or decrease on a limited range and at a low rate of pressure change. Based on these recordings, the purpose was a quantitative analysis of the TM buffer capacity including the TM compliance.

**Methods:** The pressure changes in seven normal adult MEs with intact TM's were continuously recorded directly inside the ME cavity during four different elevator trips using a high precision instrument. The TM buffer capacity was determined by the ratio between the changes in ME and the ambient pressure. Further, the ME volumes were calculated by Boyle's Law from pressure recordings during inflation-deflation tests; subsequently the TM compliance could be also calculated. Finally, the correlation between the ME volume and buffer function was determined.

**Results:** Twenty-one elevator trips were used for the analysis. The overall mean TM pressure buffering capacity was 23.3 % (SEM = 3.4), whereas the mean overall compliance was  $28.9 \times 10^{-3}$   $\mu\text{L}/\text{Pa}$  (SEM = 4.8). A strong negative linear correlation was found between the TM buffer capacity and the ME volumes ( $R^2 = 0.92$ ).

**Conclusions:** These results were in fair agreement with the literature obtained in clinical as well as temporal bone experiments, and they provide an in vivo reference for the normal ME function as well as for ME modeling. The TM buffer capacity was found more efficient in smaller mastoids. Possible clinical implications are discussed.

*Major contributions to the data analysis and writing the appendices, minor contribution to the writing of the paper.*

*This chapter was published: Padurariu, S., De Greef, D., Jacobsen, H., Nlandu Kamavuako, E., Dirckx, J.J.J., Gaihede, M., 2016. Pressure buffering by the tympanic membrane. In vivo measurements of middle ear pressure fluctuations during elevator motion. *Hear. Res.* 340, 113–120. doi:10.1016/j.heares.2015.12.004*

## 1. Introduction

The overall pressure regulation of the middle ear (ME) is influenced by several factors, where gas exchange and the function of the Eustachian tube (ET) are the most prominent in current research. However, the tympanic membrane (TM) also plays an important role in counterbalancing pressure changes; it represents a viscoelastic barrier between the ambient air in the external ear canal (EEC) and the gas volume entrapped in the closed rigid cavity of the ME. Thus, the TM is subject to both environmental and inner physiological changes in pressure resulting in varying pressure gradients. Actions like diving in water, travelling by airplane or simply taking an elevator for several floors may create such environmental pressure changes, whereas underpressures are well known in diseased ears with an impaired physiological pressure regulation. The environmental pressure changes are usually transient in nature, whereas the underpressures generated by impaired physiological changes, for instance towards more intense gas absorption, often combined with an ET dysfunction, can be sustained for longer periods. Regardless the case, the TM responds as a pressure buffer and may become a pressure victim (Ars et al., 2012).

The formation of sustained underpressures is a common clinical condition in otology, which may result in development of retraction pockets, atelectasis of the ME and cholesteatoma including erosion of the ossicles and severe conductive hearing loss (Ars et al., 1989; Sadé and Ar, 1997). The mechanism has been attributed to degeneration of the fibrous lamina propria of the TM due to the pressure load, and subsequently resulting in a decreased mechanical stiffness and increased susceptibility towards further pressure load (Ars et al., 1989; Sadé and Ar, 1997; Knutsson et al., 2011). Thus, the buffering function of the TM as well as the magnitude and periods of underpressures are important factors in the development of a range of pathological conditions.

Direct measurements of the ME pressure with long-term monitoring is an important method to study pressure variations and the overall regulation of ME pressure. Tideholm et al. (1996) has reported pressure monitoring over 24-hours by an EEC mould with a built-in transducer and measuring via a TM perforation. Whereas this method may illustrate a range of daily pressure variations, it does not include the physiological buffering of the TM. Another approach has been reported with a catheter inserted into the mastoid tip and connected to a pressure transducer and a logger device for 24- or 48-hours pressure sampling (Dirckx et al., 2008). However, both these methods are limited by great variations in pressures and very large amounts of data, so that the detailed interpretation is complex; one approach has been to calculate a “gliding” mean pressure, which may decrease the pressure variations, but it may also conceal important observations (Tideholm et al., 1996). Consequently, another approach has been to focus on smaller well defined experiments, where the conditions are controlled and allow for an exact interpretation of the events and data; thus, the ME counter-regulation of smaller experimental pressure changes as well as temporal analysis of ET openings have been reported (Gaihede et al., 2010; Gaihede et al., 2013).

The current study reports on the buffer function of the TM based on the same investigations with direct measurements via a catheter inserted into the mastoid tip. During a set of these experiments the participants were subject to various elevator rides with vertical movements up to 43 m; this resulted in corresponding changes in ambient pressure of elevator cabin. These were reflected by changes in the ME pressure and mainly buffered by the TM system. Thus, the elevator rides illustrated daily activity ME pressure variations, but also allowed the TM buffer capacity to be determined. In addition, the ME volume was determined and the correlation between the buffering capacity and the volume was investigated. The combined knowledge of the ME volume and TM buffering capacity also enabled us to calculate the compliance of the TM.

## 2. Materials and Methods

### 2.1 Participants

Seven adult subjects with no sign or history of previous ME diseases were included in the study based on normal results at otomicroscopy, audiometry and tympanometry. Their mean age was 50 years (SD = 11) and included three male and four female participants. These participants underwent parotidectomy under standard intravenous anesthesia (propofol og ultiva) due to a tumor in their parotid gland, and this procedure exposed the antero-lateral tip of the mastoid. Thus, a hole of 3 mm diameter and 5-10 mm depth was drilled through the compact bone into the mastoid air cells, and a sterile plasticized PVC catheter of 3,5/2 mm (outer/inner) diameter and 15 cm in length was inserted; the wound was subsequently closed routinely with a double layer of sutures to ensure tightness. The day after surgery, after a 22-24 continuous recording the catheter was removed similarly to a normal wound drainage catheter. Informed written

consent was obtained from all subjects before their participation, and the study was approved by the regional ethical committee (VEK Nordjylland 2005/50).

## 2.2 Instrumentation

The measuring system as well as the validation of the procedure has been presented elsewhere (Dirckx et al., 2008; Gaihede et al., 2010; Gaihede et al., 2013). In short, the catheter was connected to a pressure transducer and a pocket-size logger for saving the pressure data. The transducer had a measurement accuracy of 1 Pa, and a recording sample frequency of 10 counts per second. In order to keep close to physiological levels of pressure, the measurement range was set to the interval -4 to 4 kPa. The system allowed monitoring of recordings by connection to a portable PC at any time.

## 2.3 Experiments

### *2.3.1 Procedure for measurements during elevator trips*

After approximately 2 hours from the end of surgical intervention and catheter insertion, the subjects followed their first elevator trip on the way from recovery unit to the bed unit; the last three trips by elevator occurred the next morning, on their way to the outpatients' clinic. The trips included:

1. From the basement up to the 7<sup>th</sup> floor (trip UP<sub>1</sub> = 30.9 m, 24 s)
2. From the 7<sup>th</sup> to 10<sup>th</sup> floor (trip UP<sub>2</sub> = 12 m, 13 s)
3. From the 10<sup>th</sup> floor to the basement (trip DOWN = 42.9 m, 10 s)
4. From the basement to the 1<sup>st</sup> floor (trip UP<sub>3</sub> = 6.2 m, 30 s)

During the elevator trips the ME pressure was continuously monitored; precautions were taken to avoid interruption of the motion, though this was not always possible; such cases were excluded from the analysis. Further, in other cases pressure equilibrations by ET openings influenced the course of the pressure curve; such cases were also excluded from analysis. An individual example of a pressure recording has been depicted in Figure 8-1, which illustrates a trip from the 10<sup>th</sup> floor to the basement; initially, the smooth ME pressure decrease is interrupted by two separate ET openings before reaching the basement.

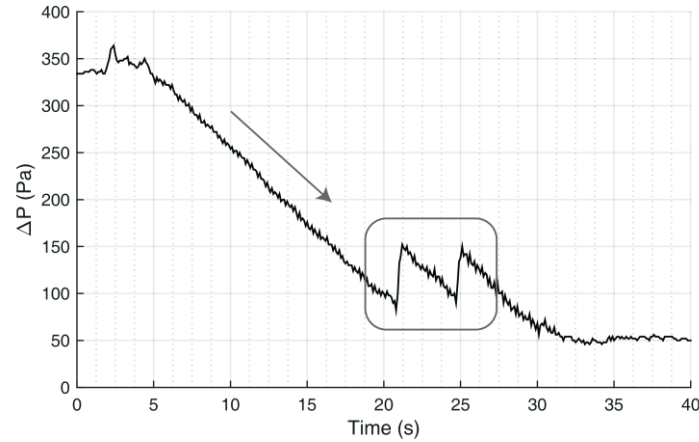


Figure 8-1: Excluded trip. Trip DOWN from the 10th floor to the basement (43 m) in an individual recording, where the pressure decrease inside the ME is plotted against time. This dataset was excluded, because two ET openings were identified on the pressure curve towards the end of the ride (marked; subject 4).

### 2.3.2 Procedure for ambient measurements during the elevator trips

A separate set of reference measurements was subsequently made in order to measure the ambient pressure variations along the same trips and using the same measuring equipment. The system was closed with a 10 mL syringe (BD Plastipak) containing ambient air connected to the pressure transducer instead of the ME cavity. The measuring system was placed on a towel in a tray and it was allowed to get into thermodynamic equilibrium with ambient for 10 minutes before measurement. This was achieved by an open ventilation valve interposed between the syringe and pressure logger, which subsequently was closed during measurements.

### 2.3.3 Procedure for experimental gas volume deviations

For calculating the individual compliance values of the TM, it was necessary to determine the ME gas volume of each participant. A precise determination was not possible, but estimation could be achieved by applying Boyle's gas law to a set of ME pressure gradients obtained by injecting and extracting known volumes of air into and from the ME of the same participants in a separate set of experiments. The method is an adaptation of the method described by Flisberg et al. (1963).

Measurements were made subsequent to the elevator trips, using the same instrumentation, and following the method described earlier (Gaihede et al., 2010). In short, air volumes of  $\pm 50$ ,  $\pm 100$ ,  $\pm 200$  and  $\pm 300$   $\mu\text{L}$  were in turn injected or respectively extracted by the catheter inserted into the mastoid using a 500  $\mu\text{L}$  gas syringe mounted on the ventilation valve. The pressure changes were recorded during all these manipulations. All the measurements where the curve presented irregularities suggesting pressure equilibration during the inflation or deflation, leakage, interruptions during injection/extraction of air or out-of-range pressure were excluded from analysis.

## 2.4 Data acquisition and analysis

Data for elevator trips as well as data for ME gas volume deviation were acquired using a Matlab 32-bit interface. Data recorded during the elevator trips were aligned and normalized.

## 2.5 Assumptions

A set of assumptions allowed the calculation of ME gas volume variation with elevator movement: a) the ambient temperature variations were considered negligible during all elevator trips; b) the amount of gas enclosed in the intact ME can be regarded as constant for second-wise frames and it obeys Boyle's ideal gas law (Mover-Lev et al., 1998); c) the ambient pressure changed linearly with the height change, and within a low range of values for meter-wise vertical distances from ground level (Dirckx et al., 2013). Extrapolating the ME to the situation of a rigid cavity, and comparing the ME pressure changes during each elevator trip to the respective ambient pressure changes, the pressure buffer capacity by the TM displacement at the changing heights could be calculated both during ascent and descent.

## 2.6 Calculations

### 2.6.1 The pressure buffer capacity of the TM.

When a pressure change  $\Delta P_{\text{amb}}$  occurs in ambient, it implicitly occurs to the air in the external ear canal (EEC), thus a pressure gradient  $P_{\text{ME-amb}}$  develops over the TM. If the TM was perfectly rigid, this pressure gradient would be equal to the EEC pressure change, provided that the ME temperature and the amount of gas remain constant. If the TM was perfectly flaccid, the pressure gradient would be zero.

We define the pressure buffer capacity of the TM ( $\text{Buffer}_{\text{TM}}$ ) as the ratio of the pressure change measured inside the ME ( $\Delta P_{\text{ME}}$ ) to the ambient pressure change reflected in the EEC during an elevator ride. Mathematically, TM pressure buffer capacity can be noted as follows:

$$\text{Buffer}_{\text{TM}} = \frac{\Delta P_{\text{ME}}}{\Delta P_{\text{amb}}}, \quad \begin{array}{l} E \\ q \\ \cdot \\ 8 \\ - \\ 1 \end{array}$$

where 'Δ' denotes a change over time.

The measurements provided us with the pressure gradients over the TM's,  $P_{\text{ME-amb}}$ , at different values of ambient pressure (caused by changing heights). The values of the change in TM pressure gradient,  $\Delta P_{\text{ME-amb}}$ , were obtained by calculating the difference between the end and start TM pressure gradient for each trip averaged over the initial and the last four seconds.

As a reference for ambient pressure change, we used the measurements of the pressure difference between the gas enclosed in the rigid cavity of a 10 mL syringe and the ambient air,  $P_{\text{syr-amb}}$ , under the same circumstances of changing ambient pressure. Using these measured quantities, Eq. 8-1 can be rewritten as follows:

$$\text{Buffer}_{\text{TM}} = 1 - \frac{\Delta P_{\text{ME-amb}}}{\Delta P_{\text{syr-amb}}}, \quad \text{Eq. 8-2}$$

where  $\Delta P_{\text{ME-amb}}$  denotes the change in pressure gradient between MEs and ambient, and  $\Delta P_{\text{syr-amb}}$  denotes the change in pressure gradient between the syringe and ambient. *[A more extensive elaboration of this can be found in Appendix I.]*

### 2.6.2 The ME volume calculation.

To estimate the individual ME gas volume  $V_{\text{ME}}$  of the subjects from the experimental gas volume deviations, the ME pressure was experimentally altered in each subject up to values where the TM was tensed to the point of becoming ‘a rigid wall’ to a good approximation (Gaihede et al., 2010). We assumed that the volume displacement of the TM (and therefore the volume change of the ME) caused by addition of small amounts of gas is no longer significant at gradients of 1,500 Pa or higher for (Dirckx and Decraemer, 1992). The ME volume  $V_{\text{ME}}$  could be then calculated using the following formula (deduced from the Boyle’s gas law):

$$V_{\text{ME}} = \frac{P_{\text{amb}} T_{\text{ME}}}{\Delta P_{\text{ME}} T_{\text{amb}}} V_{\text{add}} \quad \text{Eq. 8-3}$$

where the atmospheric pressure  $P_{\text{amb}} = 101,325$  Pa,  $\Delta P_{\text{ME}}$  denotes the measured ME pressure change caused by the gas volume addition  $V_{\text{add}}$ ,  $T_{\text{amb}} = 295\text{K}$  (room temperature),  $T_{\text{ME}} = 310\text{K}$  (human body temperature).

In some subjects, the gas additions systematically failed to produce a smooth pressure increase, for instance by ET opening during the air injection, leakage, or other artifacts reflected on the recordings. For these subjects, the ME volume was estimated by extrapolating the value of ME volume calculated for gas additions at a lower initial pressure, using an extrapolation factor. This factor was calculated using data from subjects in which gas additions at both low and high initial pressures were performed. *[A more extensive elaboration of this can be found in Appendix II.]*

### 2.6.3 TM compliance.

The compliance of the TM is defined as the ratio of the volume displacement of the TM ( $\Delta V_{\text{TM}}$ ) to the change over time of the pressure gradient over the TM, or mathematically:

$$C_{\text{TM}} = \frac{\Delta V_{\text{TM}}}{\Delta P_{\text{ME-amb}}}. \quad \text{Eq. 8-4}$$

The denominator is the change of the difference between ME and ambient during the elevator experiments. The numerator was calculated by applying the Boyle's gas law to the gas enclosed in the ME at the start and at the end of the elevator trips, assuming that the ME volume change is equal to the TM volume displacement for very short time-frames:

$$\Delta V_{TM} = \Delta V_{ME} = V_{ME} \left( \frac{P_{ME}(t_1)}{P_{ME}(t_1) + \Delta P_{ME}} - 1 \right), \quad \text{Eq. 8-5}$$

where

$$\Delta P_{ME} = \Delta P_{ME-amb} - \Delta P_{syr-amb} \quad \text{Eq. 8-6}$$

and  $P_{ME}(t_1)$  is the ME pressure at the start of the elevator trip, which we take equal to atmospheric pressure  $P_{ME}(t_1) = 101,325$  Pa. [A more extensive elaboration of this can be found in Appendix III.]

As an additional measure of the TM's displacement, the average linear displacement of the TM perpendicular to its circumference,  $\Delta d_{TM}$ , was also calculated, by dividing  $\Delta V_{TM}$  by the average TM surface recently reported of  $59.43$  mm<sup>2</sup> (De Greef et al., 2015, i.e. Chapter 3 of this thesis).

#### 2.6.4 Statistical analysis

Average results over all subjects are reported together with the standard error of the mean (SEM). Individual results (e.g. ME volumes or TM compliances) are reported together with their individual error (Err), calculated using standard error propagation rules. Furthermore, the statistical correlation between ME volume and TM buffer capacity was calculated using Kendall's tau rank correlation test (Kendall, 1938).

## 3. Results

### 3.1 Elevator measurements

In total, the seven subjects were participating in 28 elevator trips; from these we could validate 21 trips for analysis. Thus, 7 experiments were excluded due to interruption of the elevator ride before the target floor, ET openings or technical factors, which altogether influenced the expected course of the pressure change (subject 1: UP3; subject 2: UP3; subject 4: DOWN; subject 6: UP1, UP2, DOWN; subject 7: UP1). Moreover, one trip was treated separately due to deviation from the trip protocol, as the subject took the elevator from basement back to the 7<sup>th</sup> floor instead of getting to the next building at the 1<sup>st</sup> floor (trip 4 in subject 5). This trip coincided with Trip UP 1; therefore it was included in the respective dataset and was named as 'subject 5b'.

### 3.2 TM buffer capacity

The changes in ambient pressure during elevator motion described smooth slopes ranging in the interval  $-470$  to  $+370$  Pa respectively by descent from 43 m height and ascent to 31 m (Reference lines on Figure 8-2 a & b). Correspondingly, the pressure changes in the MEs were lower, ranging up to respectively 350 Pa during ascent and  $-420$  Pa during descent, and the ambient pressure changed at an average rate of 20 Pa/s (Figure 8-2).

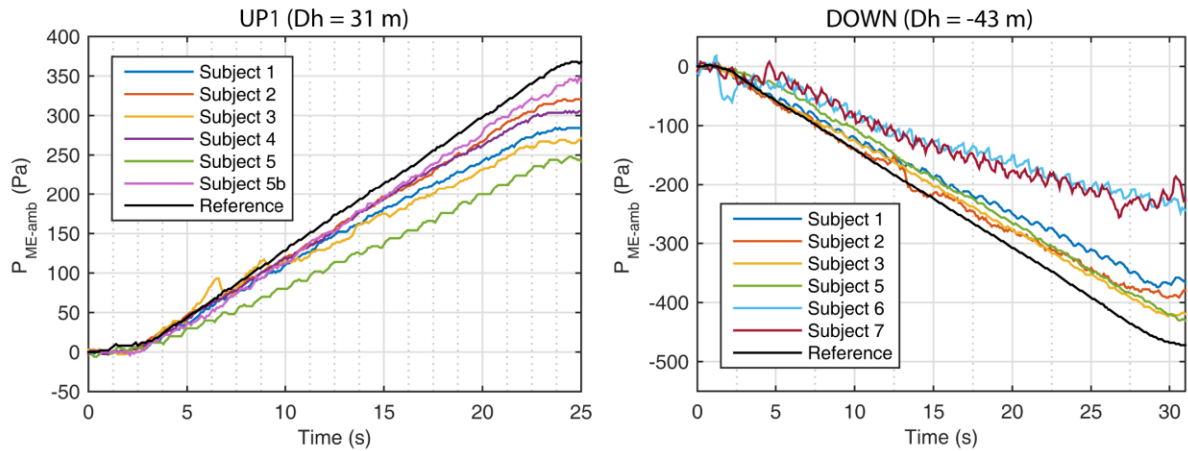


Figure 8-2: The ME pressure change during an ascent and descent by elevator. The left panel illustrates a trip up from the basement to the 7th floor (UP<sub>1</sub>), whereas the right panel illustrates a trip down from the 10th floor to the basement (DOWN). Both panel represent all valid recordings and the reference.

Figure 8-2 illustrates the changes in ME pressure for the individual measurements for two sets of trips (UP<sub>1</sub> and DOWN) as well as the changes in ambient pressure (Reference). The mean TM buffering capacities determined for each set of trips was 20.1 (SEM 4.2), 23.3 (SEM 6.5), 22.9 (SEM 16.3), and 23.7 (SEM 6.2) % for trips UP<sub>1</sub>, UP<sub>2</sub>, UP<sub>3</sub>, DOWN, respectively; the overall mean was 23.3 % (SEM 3.4). The values for the individual buffer capacity are presented in Table 8-1 to Table 8-4, whereas their distribution corresponding to the trips is represented in Figure 8-3.

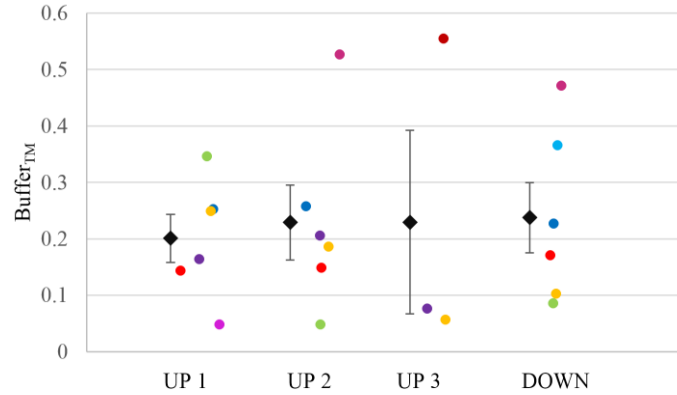


Figure 8-3: The distribution of the buffer capacity according to the elevator trips. The color legend is identical to Figure 8-2. The black marks represent the means and the lines represent the standard errors of the means.

### 3.3 ME volume estimations

Thirty-one volume-addition measurements out of 56 were successful and could be used for ME volume estimations. In subjects 2 and 5 only peak pressures up to 1.5 kPa were available. In two subjects (no. 4 and 6) none of the gas volume deviations could be used, due to interruptions in all trials. Four of the calculated ME volumes were larger, ranging from 9.4 to 11.7 mL, and one was as small as 5.5 mL (Table 8-1 to Table 8-4). The mean ME volume was 9.7 mL (SEM = 1.1), and the individual ME volumes have been outlined in Table 8-1 to Table 8-4. In these tables, a summary of TM buffering parameters during elevator trips is presented, including the pressure change recorded within middle ears ( $\Delta P_{ME-amb}$ ), the buffer capacity ( $Buffer_{TM}$ ), the middle ear volume ( $V_{ME}$ ), the volume displacement ( $\Delta V_{ME}$ ) and the linear displacement ( $\Delta d_{TM}$ ) by tympanic membrane buffering; and the compliance ( $C_{TM}$ ). The height ( $\Delta h$ ) and reference measurement ( $\Delta P_{syr-amb}$ ) is also indicated for each elevator trip.

Table 8-1: Trip UP1 ( $\Delta h = 31$  m;  $\Delta P_{syr-amb} = 370$  Pa)

Subject	$\Delta P_{ME-amb}$ (Pa)	$Buffer_{TM}$ (%)	$V_{ME}^*$ (mL)	$\Delta V_{ME}$ ( $\mu$ L)	$C_{TM}^*$ ( $10^{-3}$ $\mu$ L/Pa)	$\Delta d_{TM}$ (mm)
1	276.6	25	9.4 (0.5)	9.1	32.9 (2.3)	0.153
2	316.8	14	11.7 (0.7)	6.4	20.2 (1.3)	0.107
3	277.9	25	10.4 (0.6)	9.8	35.4 (2.3)	0.166
4	309.2	16	-	-	-	-
5	241.8	35	11.6 (0.4)	15.4	63.5 (3.6)	0.258
5b	352.0	5	11.6 (0.4)	2.2	6.1 (0.6)	0.036
Mean(SEM)	295.7	20.1 (4.2)	-	8.6 (2.2)	31.6 (9.5)	0.144 (0.036)

\*Mean (Err)

Table 8-2: Trip UP2 ( $\Delta h = 12$  m;  $\Delta P_{syr-amb} = 148$  Pa)

Subject	$\Delta P_{ME-amb}$ (Pa)	Buffer <sub>TM</sub> (%)	$V_{ME}^*$ (mL)	$\Delta V_{ME}$ ( $\mu$ L)	$C_{TM}^*$ ( $10^{-3}$ $\mu$ L/Pa)	$\Delta d_{TM}$ (mm)
1	109.8	26	9.4 (0.5)	3.7	33.9 (2.7)	0.063
2	122.0	18	11.7 (0.7)	3.1	25.5 (2.1)	0.052
3	120.4	19	10.4 (0.7)	2.9	24.5 (2.1)	0.050
4	117.6	21	-	-	-	-
5	140.9	5	11.6 (0.4)	0.8	6.0 (1.3)	0.014
7	70.2	53	5.5 (0.7)	4.6	64.9 (7.6)	0.077
Mean (SEM)	113.5	23.3 (6.5)	-	3.0 (0.6)	31.0 (9.6)	0.051 (0.010)

\*Mean (Err)

Table 8-3: Trip UP<sub>3</sub> ( $\Delta h = 6.3$  m;  $\Delta P_{syr-amb} = 70$  Pa)

Subject	$\Delta P_{ME-amb}$ (Pa)	Buffer <sub>TM</sub> (%)	$V_{ME}^*$ (mL)	$\Delta V_{ME}$ ( $\mu$ L)	$C_{TM}^*$ ( $10^{-3}$ $\mu$ L/Pa)	$\Delta d_{TM}$ (mm)
3	66.0	6	10.4 (0.7)	0.4	6.5 (2.4)	0.007
4	64.7	8	-	-	-	-
7	31.2	55	5.5 (0.7)	2.3	72.9 (9.4)	0.038
Mean (SEM)	54.0	22.9 (16.3)	-	1.3 (0.9)	39.7 (33.2)	0.023 (0.016)

\*Mean (Err)

Table 8-4: Trip DOWN ( $\Delta h = -43$  m;  $\Delta P_{syr-amb} = 470$  Pa)

Subject	$\Delta P_{ME-amb}$ (Pa)	Buffer <sub>TM</sub> (%)	$V_{ME}^*$ (mL)	$\Delta V_{ME}$ ( $\mu$ L)	$C_{TM}^*$ ( $10^{-3}$ $\mu$ L/Pa)	$\Delta d_{TM}$ (mm)
1	363.2	23	9.4 (0.5)	10.4	27.3 (2.0)	0.175
2	389.8	17	11.7 (0.7)	9.6	23.7 (1.4)	0.162
3	421.5	10	10.4 (0.7)	5.2	11.8 (0.8)	0.087
5	429.6	9	11.6 (0.4)	4.8	10.8 (0.7)	0.081
6	298.0	37	-	-	-	-
7	248.5	47	5.5 (0.7)	12.9	48.1 (5.9)	0.218
Mean(SEM)	358.4	23.7 (6.2)	-	7.2 (1.9)	25.8 (7.4)	0.145(0.026)

\*Mean (Err)

### 3.4 TM compliance

The ME volumes served for calculation of the TM compliance for different subjects and trips. For all upward trips the mean compliance was  $32.7 \times 10^{-3}$   $\mu$ L/Pa (SEM = 6.7), whereas for the downward trip the mean was  $25.8 \times 10^{-3}$   $\mu$ L/Pa (SEM = 7.4); thus, the TM compliance exhibited an asymmetry between movement directions (Figure 8-4). The individual compliance values have been included in Table 8-1 to Table 8-4.

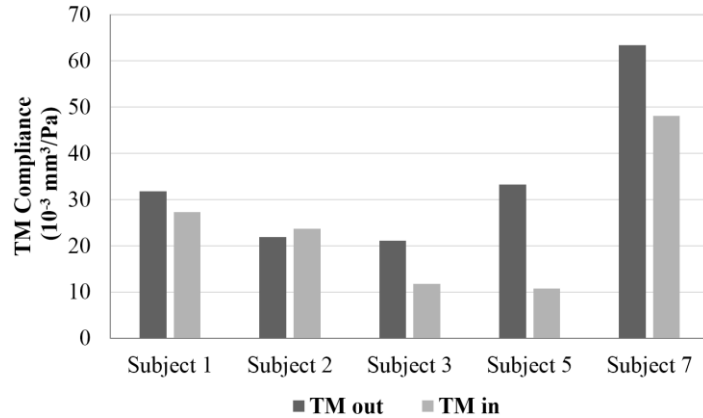


Figure 8-4: The asymmetry of the TM compliance between UP and DOWN trips. The inward (TM in) and outward (TM out) displacement of the TM corresponding respectively to averaged UP-trips and DOWN-trip are represented in each subject, where the ME volume calculation was possible.

In addition, the individual TM volume displacement ( $\Delta V_{ME}$ ) and the TM linear displacement ( $\Delta d_{TM}$ ) values are included in Table 8-1 to Table 8-4.

### 3.5 Buffer capacity vs. ME volume correlation

The TM buffer capacity averaged by subject presented a significant negative linear correlation with the corresponding ME volume ( $R^2 = 0.92$ ) (Figure 8-4). The statistical correlation between the individual buffer values ( $n = 21$ ) and the ME volumes is significant (Kendall rank correlation test:  $n = 21$ ;  $p = 0.005$ ).

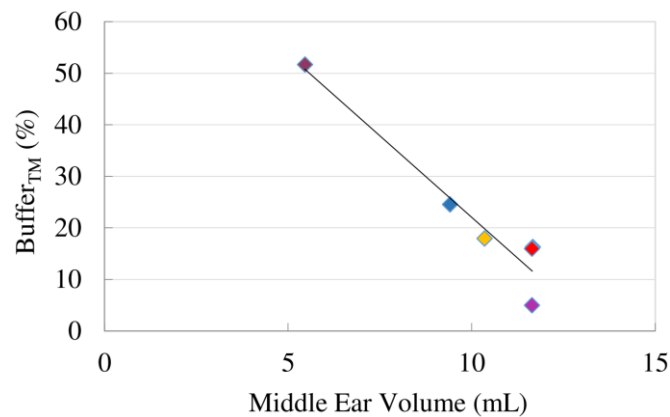


Figure 8-5: Linear correlation between the individual mean buffer capacity and the ME volume. The color legend is identical to Figure 8-2; correlation analysis:  $y = -6.3269x + 85.361$ ;  $R^2 = 0.927$ .

## 4. Discussion

### 4.1 Study design and outcomes

The current study demonstrated the ME pressure variations in intact normal ME's during vertical motion by elevator with up to 43 m changes in height; these pressure variations reflected the buffer capacity of the TM and other ME structures.

During the elevator trips, the ME pressure changed smoothly in the same direction with the ambient pressure, presenting a gradually increasing difference from the ambient pressure changes (Figure 8-2). The ME pressure changes resulted in a simultaneous proportional volume displacement of the TM, which reflected the viscoelastic properties of the entire ME system, i.e. the TM and the attached ossicular chain, muscles and ligaments (Hüttenbrink, 1988; Zhang and Gan, 2011b). However, given the low pressure range of the current measurements, their short time frames and the fact that the TM constitutes the most elastic part of TM system, we may assume that the TM had the major contribution to the buffering of the ambient pressure changes during elevator movements.

To our knowledge, no similar studies on in vivo ME pressure monitoring during elevator trips have been so far reported, though they can be compared to experiments in temporal bones or artificial models.

*Ex-vivo* pressure measurements following intratympanic gas additions and extractions on a fresh temporal bone concluded that the TM can compensate up to 25 % (Decraemer and Dirckx, 1998), which is in good agreement with the average of the current results. In an artificial model of the ME with a flexible TM Cinamon and Sadé (2003) obtained for intratympanic gas additions and extractions a maximal buffer capacity of 33 % in a 10 mL and 41% in a 5 mL ME model. This is also in fair agreement with our results, which ranged up to 35 % in 10 mL-order MEs and 55 % in the 5 mL ME.

The calculation of individual ME volumes was necessary in the analysis and interpretation of the pressure variations. The ME volume could be estimated from the Boyle's gas law, assuming that the TM became nearly "rigid" at pressure loads beyond 1600 Pa (Dirckx and Decraemer, 1991). Our results including a summed volume of the tympanic cavity and the mastoid fitted well within the range of recent investigations using 3D reconstruction of CT scanning images, reporting the normal ME volume between 5 to 15 mL (Alper et al., 2011; Csakanyi et al., 2011).

The pressure change rate of ca. 20 Pa/sec could be compared to the magnitude of pressure change rate for sound waves of 87.9 dB SPL (0.5 Pa RMS) at 5 Hz. For this frequency, Von Békésy found a TM compliance of  $21.5 \times 10^{-3} \mu\text{L}/\text{Pa}$  at a sound pressure of 100 Pa RMS (Békésy (1936) in Dirckx and Decraemer, 1992). Other measurements in temporal bones found a TM compliance of  $19.5 \times 10^{-3} \mu\text{L}/\text{Pa}$  for 140 Pa pressure in quasi-static conditions (Dirckx and Decraemer, 1992),

whereas an interpolation of the values earlier obtained by Elner et al. at -500 and 500 Pa in 101 healthy ears gave an estimate of  $18.3 \times 10^{-3} \mu\text{L}/\text{Pa}$  (Elner et al., 1971; Dirckx and Decraemer, 1992). In clinical experiments with similar slow pressure changes a median compliance of  $25 \times 10^{-3} \mu\text{L}/\text{Pa}$  has been reported (Gaihede, 1999). The slow rate of pressure change places the current measurements into a quasi-static regime, where the buffering of the TM can be considered almost insensitive to the change rate (Fung, 1993).

The asymmetry of TM compliance reflected by the overall averages for ME over- and underpressure of respectively  $32.7 \times 10^{-3} \mu\text{L}/\text{Pa}$  and  $25.8 \times 10^{-3} \mu\text{L}/\text{Pa}$  is also in agreement with previous reports of ex-vivo measurements, where the volume displacement by TM motion in overpressure was found to be higher than in underpressure (Dirckx and Decraemer, 1992). This is basically explained by the asymmetric and conical shape of the TM, as well as the presence of other structures in contact with the inner side of TM, which facilitates the TM's outward rather than inward movement (Dirckx et al., 2013).

It is noticeable that in subject 7 having much smaller ME volume, the compliance values in both directions are much larger compared to the 4 subjects having an almost double ME volume. However, the compliance is an intrinsic property of the TM, which might accidentally be higher in this healthy ME.

The TM volume displacements ranged between 0.4 and 15.4  $\mu\text{L}$ , being also in agreement with the interval up to 20  $\mu\text{L}$  reported by Dirckx and Decraemer (1992), as well as with the interval of -10 to 10  $\mu\text{L}$  for ear canal pressures between -500 Pa and 500 Pa obtained by Gaihede and Kabel (2000).

Following on Figure 8-3 and Table 8-1 to Table 8-4 it can be noticed that the values for TM-buffer capacity for the largest ME volume (subject 5) tend to be the lowest in all elevator trips, and the smaller the ME volume is, the higher the TM buffer capacity is. Thus in subject 7, representing the smallest ME, the TM buffer capacity was found highest averaging 53.8 %.

The plot between the TM buffer capacity and the ME volume showed a strong negative correlation ( $R^2 = 0.92$ , Figure 8-4); this may well be influenced by subject 7 with the smallest ME volume representing an outlier in the material. However, the ME volume of this subject is still within range of normal ME volumes, and if we exclude this data set, the analysis still produced a negative correlation although not as strong ( $R^2 = 0.56$ ).

## 4.2 Limitations of the study

Despite the small group of subjects, which was due to the difficult accessibility to direct ME pressure recordings, the measurements had a high pressure and time resolution; however, this meant also that the results were susceptible to errors like interruptions of the elevator trip and ET openings.

In the first two hours after the catheter insertion, the patient rested in the recovery unit nearby the surgical unit. This interval corresponded to the 2-hour “coupling period” of regaining a steady state and overcoming eventual disturbances in ME gas composition and pressure (Brattmo et al., 2003).

A local bleeding and inflammatory reaction at the site of the catheter insertion cannot be excluded. However, any possible bleeding during measurements could be seen at any time through the transparent catheter and constituted a reason for exclusion.

Furthermore, the current study was based on several assumptions. The first of them was that for changes within very low pressure ranges, the ME pressure buffer was effectuated predominantly by the TM displacement. Indeed, the ME is described as an almost rigid bony cavity, where three factors can contribute to pressure counter-regulation: the ET, the gas exchange, and the compliance of the TM as well as of the extensive mucosa covering the bony surface. The ET equilibrates large and fast pressure changes by 0.4-second openings, which are reflected by a well-defined steep pressure change on direct continuous recordings (Gaihede et al., 2013). The presence of these patterns was a criterion for exclusion in the current study, so that ET openings did not influence our results.

Moreover, the gas exchange across the mucosa can be considered negligible, since this is very slow. In a previous study on gas exchange, the gas gain is 41.0  $\mu\text{L}/\text{hour}$  and the gas loss 34.8  $\mu\text{L}/\text{hour}$  (Mover-Lev et al., 1998); this means less than 1  $\mu\text{L}/\text{min}$  gas volume change in either direction, whereas any of the elevator trips took up to 30 s. The ME mucosa has been suggested to play a role in pressure regulation by changes in its congestion and volume, which will ultimately affect the pressure of the ME; a change in mucosa thickness of 0.006 mm may change the ME pressure 1000 Pa (Magnuson et al., 2003). However, these changes depend on vascular changes over time, and they are probably reflected by the slow gradual counter-regulation in ME pressure described earlier, where the numerical mean rate of pressure change is 68 Pa/min (Gaihede et al., 2010). Thus, mucosal-dependent pressure changes are only around 1 Pa/s compared with our elevator or height dependent pressure changes, which are around 20 Pa/s.

The inner volume size of catheter of approximately 0.47 mL (inner diameter 2 mm, length 150 mm) constituted a source of bias. Nevertheless, the ME volume estimations were corrected for this bias. Rearranging Boyle’s gas law enabled correction of the TM buffer capacity as well. This resulted in small changes towards higher TM buffer capacity values. The relative change was 3-4 % for most samples (e.g. from 25.24 % to 26.15 %, representing a relative change of 3.6 %). However, the uncorrected values have been reported here, as these changes were negligible. Moreover, the correction required the knowledge of the ME volume, which was not available for all subjects, and this would have reduced the already limited data set. *[An elaboration of the correction calculations can be found in Appendix IV]*

A possible bias due to eventual expansion of the catheter and syringe materials can be excluded. The Young’s modulus of plasticized PVC catheter is in the order of 0.6 – 1.6 GPa, whereas the

one of the polycarbonate syringe is around 2.6 GPa (Pita et al., 2002; [www.engineeringtoolbox.com](http://www.engineeringtoolbox.com), last accessed 13-10-2015). Both values are much higher than that of the TM in the order of 2 – 10 MPa (Aernouts et al., 2012b; Gaihede et al., 2007). Thus their expansion under the very small pressure changes will be negligible as compared to the volume changes in the ME.

The assumption of insignificant volume change by small volume gas injection or extraction resulting in an initial peak pressure over 1.6 kPa is based on data reported by Dirckx and Decraemer (1992). According to Figure 8-5 in their report, the volume change approximated  $5 \times 10^{-3}$   $\mu\text{L}/\text{Pa}$  between 1.2 kPa and 1.6 kPa of ME overpressure, a small change compared to the volume of the ME (order of magnitude 10 mL). Thus, in subjects 2 and 5, where the peak pressures only reached up to 1.5 kPa, the ME volume calculations may overestimate the real values if the TM still expanded where it was approximated to a “rigid wall”.

Furthermore, during the elevator movements the gas expansion is semi-adiabatic, which means that small temperature variations can occur, with some influence on the values. We assume that this influence is marginal, as the measurements were made in the closed cabin of an elevator.

### 4.3 Clinical relevance of the study

The TM represents a vulnerable structure of the ME, where the integrity of its lamina propria determines its properties in response to both acoustic and static pressures; its sensitivity to sound pressures is important for hearing, while its buffer capacity and compliance in the static pressure regime is important to resist ambient and physiological as well as pathophysiological pressure changes (Knutsson et al., 2011). However, degeneration and thinning of its lamina propria may result from long-standing ME underpressures and more rarely from scar-tissue formation at the insertion site of ventilation tubes. Clinically this situation is recognized as areas of atrophy in the TM, and once established such areas are further susceptible to underpressures resulting in a vicious circle ultimately leading to retraction pockets, atelectasis and cholesteatoma formation (Ars et al., 1989). More recent studies on the thickness distribution of the TM have described larger variations in thickness both inter-individually as well as local differences with thinner parts, which correlate with the sites of frequent formation of retraction-pockets (Van der Jeught et al., 2013).

The current study provided a reference for an overall in vivo buffer capacity of the TM system for lower pressure changes in the range of 100's Pa, where the TM may play the main role. This buffer capacity displayed a negative correlation between the ME volume, so that the buffer capacity was found higher in ME's with a smaller volume. This observation may have important clinical implications, since it may contribute to the explanation of the relative success of mastoid obliteration in cholesteatoma ears. In this type of surgery, the recurrence of a new retraction pocket and ultimately a new cholesteatoma is a major problem, but obliteration has

become increasingly popular, because the recurrence rates are smaller (Takahashi et al., 2007; Vercruyse et al., 2008; Csakanyi et al., 2014). The obliteration of the mastoid results in a decreased ME volume more or less corresponding to only the tympanic cavity itself. An interpretation of the increased buffer capacity resulted in a smaller ME volume might be that less gas volume in the closed cavity will correspond to less buffering volume displacement of the TM compared with a larger ME volume at the same pressure deviation. Consequently, the stretching of the TM will be relatively smaller, when the buffer capacity is higher, and thus, the displacements of the lamina propria fibers is smaller, so that degeneration and possible disintegration of fibers is less likely to develop. Ultimately, this may contribute to maintaining the mechanical stability of the TM and prevent formation of susceptible thin areas with atrophy, which may result in unstable conditions and formation of new retraction pockets (Ars et al., 1989).

## 5. Conclusions

The normal pressure buffering capacity of the human TM system has been determined in vivo for pressure changes between 350 and -420 Pa together with the TM compliance and displacement parameters, based on physiological ME pressure variations under daily circumstances. These data may serve for an additional understanding of the mechanical properties of the ME and as reference for modeling of the normal TM. The TM buffer capacity was found higher in cases with a smaller ME volume, which meant that the volume displacement of the TM in such MEs was more efficient; this may result in less stretching of the lamina propria fibers so that degeneration and disintegration of the fibers may be prevented. This may contribute to the decreased recurrence rate of cholesteatoma in MEs with mastoid obliteration, because obliteration markedly reduces the ME volume, and thus, increases the TM buffer capacity, so that more stable conditions are obtained.

## Appendices

These appendices were not included in the published article. They are included only in this thesis with the intention to go a little deeper into the physics and mathematics behind the calculations of this study.

### Appendix I: calculation of the TM buffer capacity

The TM buffer capacity or buffer function ( $b_{TM}$ ) is the percentage of the pressure difference over the TM, caused by an ambient pressure change, that is compensated by the displacement of the TM itself. This effect is a result of the non-zero compliance of the TM. Mathematically, the buffer capacity is represented by:

$$b_{\text{TM}} := \frac{\Delta P_{\text{ME}}}{\Delta P_{\text{amb}}} = \frac{P_{\text{ME}}(t_2) - P_{\text{ME}}(t_1)}{P_{\text{amb}}(t_2) - P_{\text{amb}}(t_1)}, \quad \text{Eq. 8-7}$$

where  $\Delta$  denotes a difference over time,  $P_{\text{ME}}$  the absolute pressure inside the ME cleft and  $P_{\text{amb}}$  the absolute ambient pressure.

The in-vivo pressure logger measures the difference between the ME cavity pressure and the ambient pressure. The parameter that is relevant for the TM buffer function is the difference of this value between the end and the start of the elevator trips. This value can be described as the time difference of the pressure difference between ME cleft and ambient gas and denoted by

$$\begin{aligned} \Delta P_{\text{ME-amb}} &= P_{\text{ME-amb}}(t_2) - P_{\text{ME-amb}}(t_1) \\ &= (P_{\text{ME}}(t_2) - P_{\text{amb}}(t_2)) - (P_{\text{ME}}(t_1) - P_{\text{amb}}(t_1)) \\ &= \Delta P_{\text{ME}} - \Delta P_{\text{amb}}. \end{aligned} \quad \text{Eq. 8-8}$$

The reference measurement, using a syringe with a fixed volume instead of a ME cleft, yields a similar mathematical expression:

$$\begin{aligned} \Delta P_{\text{syr-amb}} &= P_{\text{syr-amb}}(t_2) - P_{\text{syr-amb}}(t_1) \\ &= (P_{\text{syr}}(t_2) - P_{\text{amb}}(t_2)) - (P_{\text{syr}}(t_1) - P_{\text{amb}}(t_1)) \\ &= P_{\text{amb}}(t_1) - P_{\text{amb}}(t_2) \\ &= -\Delta P_{\text{amb}}. \end{aligned} \quad \text{Eq. 8-9}$$

By taking the ratio of equations (2) and (3), we arrive at

$$\begin{aligned} \frac{\Delta P_{\text{ME-amb}}}{\Delta P_{\text{syr-amb}}} &= \frac{\Delta P_{\text{ME}} - \Delta P_{\text{amb}}}{-\Delta P_{\text{amb}}} \\ &= 1 - \frac{\Delta P_{\text{ME}}}{\Delta P_{\text{amb}}}. \end{aligned} \quad \text{Eq. 8-10}$$

Therefore:

$$b_{\text{TM}} = 1 - \frac{\Delta P_{\text{ME-amb}}}{\Delta P_{\text{syr-amb}}}. \quad \text{Eq. 8-11}$$

This is an expression of the desired buffer capacity as a function of the measured quantities  $\Delta P_{\text{ME-amb}}$  and  $\Delta P_{\text{syr-amb}}$ .

## Appendix II: calculation of the ME volume

The individual ME volume of the subjects can be estimated from the stepwise gas addition experiments. We will assume that the volume displacement of the TM (and therefore the volume change of the ME) is not significant for small gas additions if the initial pressure difference over the TM is 1.5 kPa or higher. Although certainly not perfect, this assumption is reasonable, since the response of the TM is non-linear and the curve becomes rather flat at higher pressure differences (see Figure 8-6).

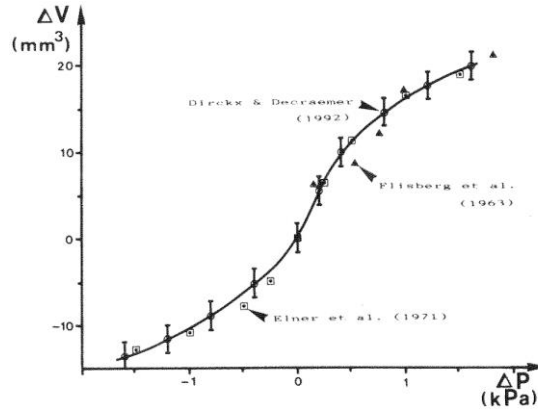


Figure 8-6: Volume displacement of the TM as a function of applied pressure. The data points are from different sources. Figure from Dirckx and Decraemer (1992).

To extract an expression for the ME volume, we start from the universal gas law, written explicitly for the states of the ME gas before and after the addition of an external volume of gas:

$$\text{Before:} \quad P_{ME}(t_1)V_{ME}(t_1) = n_{ME}(t_1)RT_{ME}, \quad \text{Eq. 8-12}$$

$$\text{After:} \quad P_{ME}(t_2)V_{ME}(t_2) = n_{ME}(t_2)RT_{ME}, \quad \text{Eq. 8-13}$$

where  $P$  is pressure,  $V$  volume,  $n$  the amount of substance,  $R = 8.314 \frac{\text{J}}{\text{mol K}}$  the universal gas constant and  $T$  the temperature. As stated above, we assume that  $V_{ME}(t_1) = V_{ME}(t_2) = V_{ME}$  if the initial TM pressure is 1.5 kPa or higher. Subtracting the above equations gives:

$$\begin{aligned} (P_{ME}(t_2) - P_{ME}(t_1))V_{ME} &= (n_{ME}(t_2) - n_{ME}(t_1))RT_{ME} \\ \Leftrightarrow V_{ME} &= \frac{\Delta n_{ME}}{\Delta P_{ME}} RT_{ME}, \end{aligned} \quad \text{Eq. 8-14}$$

where  $T_{ME}$  was chosen at  $310\text{K} = 36.85^\circ\text{C}$ .

The added amount of gas  $\Delta n_{ME}$  can be calculated through the ideal gas law as well:

$$\Delta n_{ME} = \frac{P_{amb} V_{add}}{RT_{amb}}, \quad \text{Eq. 8-15}$$

where  $P_{amb}$  is the ambient gas pressure,  $V_{add}$  the volume of the added gas and  $T_{amb}$  the ambient gas temperature. Substituting Eq. 8-14 in Eq. 8-15 gives an expression for the ME volume in which all values are known after performing the experiment of adding a known volume and measuring the resulting pressure change:

$$V_{ME} = \frac{P_{amb} T_{ME}}{\Delta P_{ME} T_{amb}} V_{add}, \quad \text{Eq. 8-16}$$

The ambient gas pressure is chosen at  $p_{amb} = 1 \text{ atm} = 1.01325 \times 10^5 \text{ Pa}$  and the ambient gas temperature at  $T_{amb} = 295 \text{ K} = 21.85^\circ \text{C}$ .

Because of the experiment protocol, the measured ME pressures were no round numbers, resulting from the addition of fixed volumes of gas to the ME. In order to facilitate the interpretation of the results, we categorized the pressures by rounding them to the nearest multiple of 1 kPa. In this way, we could apply systematic approaches in different subjects. Obviously, the actual measured values, not the rounded values, were used for the calculations. In terms of multiples of 1 kPa, we considered the pressure jumps from 2 → 3 kPa or from −2 → −3 kPa to be cases in which the above stated assumption of a rigid TM was acceptable.

Not in all of the subjects, pressure increases from 2 → 3 kPa or from −2 → −3 kPa were applied (due to practical considerations). In two subjects, however, both cases −2 → −3 kPa and −1 → −2 kPa were available, and in one subject, both cases 2 → 3 kPa and 1 → 2 kPa were available. These data were used to calculate conversion factors from the ( $\pm 1 \rightarrow \pm 2$  kPa) transitions to the ( $\pm 2 \rightarrow \pm 3$  kPa) transitions:

$$\kappa_+ = \frac{V_{ME}(2 \rightarrow 3 \text{ kPa})}{V_{ME}(1 \rightarrow 2 \text{ kPa})} \quad \text{Eq. 8-17}$$

$$\kappa_- = \frac{V_{ME}(-2 \rightarrow -3 \text{ kPa})}{V_{ME}(-1 \rightarrow -2 \text{ kPa})} \quad \text{Eq. 8-18}$$

These conversion factors were subsequently used to extrapolate the ME volume values for subjects in which only ( $\pm 1 \rightarrow \pm 2$  kPa) transitions were measured to values that correspond to hypothetical ( $\pm 2 \rightarrow \pm 3$  kPa) transitions. The uncertainty analysis performed to determine the uncertainty on the final ME volume for all patients took the above calculations into account.

## Appendix III: Expression for TM compliance

The compliance of the TM is defined as the ratio of the volume displacement of the TM ( $\Delta V_{TM}$ ) to the change over time of the pressure difference over the TM, or mathematically:

$$C_{TM} = \frac{\Delta V_{TM}}{\Delta P_{ME-amb}}, \quad \text{Eq. 8-19}$$

The denominator in Eq. 8-19 could be directly extracted from the elevator experiments. The nominator could be extracted from the elevator experiments and the ME volume estimations, as explained below.

The ME volume change over time can be deducted from applying Boyle's law to the ME gas for the situations before and after the elevator trips:

$$P_{ME}(t_1)V_{ME}(t_1) = P_{ME}(t_2)V_{ME}(t_2), \quad \text{Eq. 8-20}$$

We can express the end pressure and volume as follows:

$$P_{ME}(t_2) = P_{ME}(t_1) + \Delta_t P_{ME}, \quad \text{Eq. 8-21}$$

$$P_{ME}(t_2) = P_{ME}(t_1) + \Delta_t P_{ME}, \quad \text{Eq. 8-22}$$

Allowing us to rewrite Eq. 8-20:

$$\Delta V_{ME} = V_{ME}(t_1) \left( \frac{P_{ME}(t_1)}{P_{ME}(t_1) + \Delta P_{ME}} - 1 \right), \quad \text{Eq. 8-23}$$

In Eq. 8-23, we can use the estimated ME cleft volumes for  $V_{ME}(t_1)$  and the atmospheric pressure,  $P_{ME}(t_1) = P_{atm} = 1.01325 \times 10^5 \text{ Pa}$ .

An expression for  $\Delta P_{ME}$  as a function of the measured quantities  $\Delta P_{ME-amb}$  and  $\Delta P_{syr-amb}$  can be obtained by combining Eq. 8-8 and Eq. 8-9:

$$\Delta P_{ME} = \Delta P_{ME-amb} - \Delta P_{syr-amb}, \quad \text{Eq. 8-24}$$

Finally, we finally assume that the ME volume change is equal to the TM volume displacement:

$$\Delta V_{TM} = \Delta V_{ME}. \quad \text{Eq. 8-25}$$

With this, all parts necessary to calculate the compliance of the TM are present:

$$C_{TM} = \frac{1}{\Delta P_{ME-amb}} V_{ME}(t_1) \left( \frac{P_{atm}}{P_{atm} + \Delta P_{ME-amb} - \Delta P_{syr-amb}} - 1 \right) \quad \text{Eq. 8-26}$$

#### Appendix IV: correction for the catheter tube volume

The catheter tube used in all measurements had an internal volume of 0.47 mL (radius = 1 mm; length = 15 cm). Compared to the obtained mastoid volumes of 5-12 mL, this is not negligible. Therefore, obtained results should be compensated for this additional artificial volume that is not present under natural circumstances. This section explains how different obtained quantities in the paper should be corrected.

##### *TM Compliance*

The TM compliance value should not be corrected: it is an intrinsic property of the TM, regardless of the volume that is attached to it. As long as the volume that is used in the elevator experiments is the same as the volume that is used in the calculation of the compliance from these experiments, the result will be independent of this volume.

##### *ME volume*

The ME volume estimates, derived directly from the experimental gas deviations, should be subtracted by 0.47 mL. The extrapolation factor for going from a volume estimation at low absolute pressure to a more reliable estimation at higher pressure needs to be recalculated and the final results should be recalculated using this new factor. This has been done in the values that are reported in the paper.

##### *TM pressure buffer capacity*

The problem to solve is: calculate the buffer capacity  $b_{corr}$ , given the following values which are all known:  $V_{ME}$ ,  $C_{TM}$  (compliance),  $\Delta P_{amb}$ ,  $P_{ME}(t_1) = P_{atm} = 1013hPa$ .

We repeat the definition of the TM buffer capacity:

$$b_{TM} = \frac{\Delta P_{ME}}{\Delta P_{amb}}. \quad \text{Eq. 8-27}$$

In Eq. 8-27,  $\Delta P_{amb}$  is given, so the problem shifts to finding  $\Delta P_{ME}$  under the given circumstances.

To find  $\Delta P_{ME}$ , we can find two independent relations between  $\Delta P_{ME}$  and  $\Delta V_{ME}$ , which are both unknown at the moment.

1. From the definition of the compliance follows the following

$$\begin{aligned} C_{TM} &= \frac{\Delta V_{ME}}{\Delta P_{TM}} \\ &= \frac{\Delta V_{ME}}{\Delta P_{ME-amb}} \\ &= \frac{\Delta V_{ME}}{\Delta P_{ME} - \Delta P_{amb}} \end{aligned}$$

$$\Leftrightarrow \Delta P_{ME} = \frac{\Delta V_{ME}}{C_{TM}} + \Delta P_{amb}. \quad \text{Eq. 8-28}$$

2. From Boyle's law we can derive (with  $t_1$  at the start of the elevator trip and  $t_2$  at the end of the trip), assuming that the temperature in the ME remains constant throughout the elevator trip:

$$P_{ME}(t_1)V_{ME}(t_1) = P_{ME}(t_2)V_{ME}(t_2)$$

$$\Leftrightarrow P_{ME}(t_1)V_{ME}(t_1) = (P_{ME}(t_1) + \Delta P_{ME})(V_{ME}(t_1) + \Delta V_{ME})$$

$$\Leftrightarrow \Delta V_{ME} = V_{ME}(t_1) \cdot \left( \frac{P_{ME}(t_1)}{P_{ME}(t_1) + \Delta P_{ME}} - 1 \right). \quad \text{Eq. 8-29}$$

Eq. 8-28 and Eq. 8-29 are two equations with two unknowns:  $\Delta P_{ME}$  and  $\Delta V_{ME}$ . The other values are all known. If we solve this system for  $\Delta P_{ME}$  by substituting Eq. 8-29 into Eq. 8-28, we get a quadratic equation in  $\Delta P_{ME}$ :

$$C_{TM}\Delta P_{ME}^2 + (C_{TM}(P_{ME}(t_1) - \Delta P_{amb}) + V_{ME}(t_1)) \cdot \Delta P_{ME} - C_{TM}P_{ME}(t_1)\Delta P_{amb} = 0 \quad \text{Eq. 8-30}$$

This second order equation has two analytical solutions:

$$\Delta P_{ME1,2} = \frac{-b \pm \sqrt{b^2 - 4ac}}{2a}, \quad \text{Eq. 8-31}$$

With  $a$ ,  $b$  and  $c$  the coefficients of the quadratic equation Eq. 8-30 of  $\Delta P_{ME}^2$ ,  $\Delta P_{ME}$  and the linear term, respectively. These coefficients can be calculated using the known values of  $V_{ME}$ ,  $C_{TM}$  compliance,  $\Delta P_{amb}$ ,  $P_{ME}(t_1) = P_{atm} = 1013 \text{ hPa}$ .

As shown below, one of the two (with the minus-sign) produces a negative result (in the order of -100,000%), so we should continue with only the results generated by the plus sign.

As a check for this calculation, we could fill in  $V_{ME} = V_{ME+cat}$ . Then we should get the buffer capacity values that were directly calculated from the experimental data. The results of this test calculation can be found in Table 8-5. ( $b_{TM_1}$  and  $b_{TM_2}$  are the two solutions based on the two different solutions of the quadratic equation in  $\Delta P_{ME}$ ,  $b_{TM_{direct}}$  is the uncorrected value, calculated directly from the experimental results):

*Table 8-5: Check for the calculation to correct the TM buffer capacity values for the finite volume of the connected catheter tube in the experiments. The columns ' $b_{TM_1}$ ' and ' $b_{TM_2}$ ' represent the two solutions of the quadratic equation for the corrected TM buffer capacity in Eq. 8-30. If one of these solutions is equal to ' $b_{TM_{direct}}$ ', the calculation can be assumed to be solid.*

<b>Subject</b>	<b><math>b_{TM_1}</math></b>	<b><math>b_{TM_2}</math></b>	<b><math>b_{TM_{direct}}</math></b>
1	-108568,67%	25,22%	25,24%
2	-190310,47%	14,39%	14,39%
3	-110066,06%	24,88%	24,89%
5	-79121,33%	34,61%	34,64%
5b	-562926,40%	4,86%	4,86%

The minuscule differences between columns 3 and 4 are most probably due to calculating with rounded values.

This result gives the confidence that the above described correction for the buffer capacity is solid. Now we can apply the correction for the catheter volume by filling in the corrected values  $V_{ME} = V_{ME+cat} - V_{cat}$ . The results for this correction can be found in Table 8-6.

As stated in the main text of the paper, the values reported in it are uncorrected. The reason for this is twofold. First, the changes are not large compared to the inter-individual variations. Second, the correction required the knowledge of the ME volume, which was not available for all subjects, and this would have reduced the size of our already limited data set.

*Table 8-6: Original and corrected values for the buffer capacity results of the TM.*

Trip	Subject	$b_{TM_{uncorr}}$	$b_{TM_{corr}}$
Up 1	1	25,24%	26,15%
	2	14,39%	14,90%
	3	24,89%	25,72%
	5	34,64%	35,54%
	5b	4,86%	5,06%
Up 2	1	25,79%	26,73%
	2	17,57%	18,16%
	3	18,63%	19,31%
	5	4,79%	4,98%
	7	52,56%	54,57%
Up 3	3	5,71%	5,96%
	7	55,45%	57,46%
Down	1	22,72%	23,60%
	2	17,06%	17,65%
	3	10,33%	10,75%
	5	49,30%	8,92%
	7	47,13%	49,30%

#### Appendix V: Theoretical relation between TM buffer capacity, TM compliance and ME volume

It is possible to deduce the theoretical relation between the TM buffer capacity, the TM compliance and the ME cleft volume, and this section will illustrate how.

Starting from the definitions for TM buffer capacity and TM compliance,

$$b_{TM} = \frac{\Delta P_{ME}}{\Delta P_{amb}}, \quad \text{Eq. 8-32}$$

and

$$C_{TM} = \frac{\Delta V_{TM}}{\Delta P_{ME-amb}}, \quad \text{Eq. 8-33}$$

we can express the TM buffer capacity as:

$$b_{TM} = \frac{\Delta V_{ME}}{C_{TM} \cdot \Delta P_{amb}} + 1. \quad \text{Eq. 8-34}$$

The ME volume change can be expressed as a function of the ME volume, the buffer capacity, the external pressure and the external pressure change (derived from Eq. 8-29):

$$\Delta V_{ME} = V_{ME} \cdot \frac{-b \cdot \Delta P_{amb}}{P_{amb} + b \cdot \Delta P_{amb}}, \quad \text{Eq. 8-35}$$

so that Eq. 8-34 can be rewritten as a quadratic equation in  $x = b_{TM}$ :

$$c \cdot \Delta P_{amb} \cdot x^2 + (C_{TM} \cdot P_{amb} - C_{TM} \cdot \Delta P_{amb} + V_{ME})x - C_{TM} \cdot P_{amb} = 0 \quad \text{Eq. 8-36}$$

This equation has two solutions, one of which produces negative, unphysical values for the buffer capacity. The other solution, however, gives the relation between the TM buffer capacity, the ME volume, the TM compliance, the external pressure and the external pressure change:

$$b_{TM} = \frac{-(C_{TM} \cdot P_{amb} - C_{TM} \cdot \Delta P_{amb} + V_{ME}) + \sqrt{D}}{2 \cdot C_{TM} \cdot \Delta P_{amb}}, \quad \text{Eq. 8-37}$$

where

$$D = (C_{TM} \cdot P_{amb} - C_{TM} \cdot \Delta P_{amb} + V_{ME})^2 + 4 \cdot C_{TM} \cdot P_{amb} \cdot \Delta P_{amb}. \quad \text{Eq. 8-38}$$

This relation is plotted for a fixed  $\Delta P_{amb} = 1000$  Pa and different values for  $C_{TM}$  in Figure 8-7 and for a fixed  $C_{TM} = 30 \cdot 10^{-3}$   $\mu\text{L}/\text{Pa}$  and different values for  $\Delta P_{amb}$  in Figure 8-8.

These results confirm that there is a negative relation between the ME volume and the TM buffer capacity, as observed in this study and illustrated in Figure 8-5. As intuitively expected, the TM buffer capacity is always 100% if the ME volume is zero, for every value of TM compliance, external pressure and external pressure change and converges to 0% for  $V_{ME} \rightarrow \infty$ .

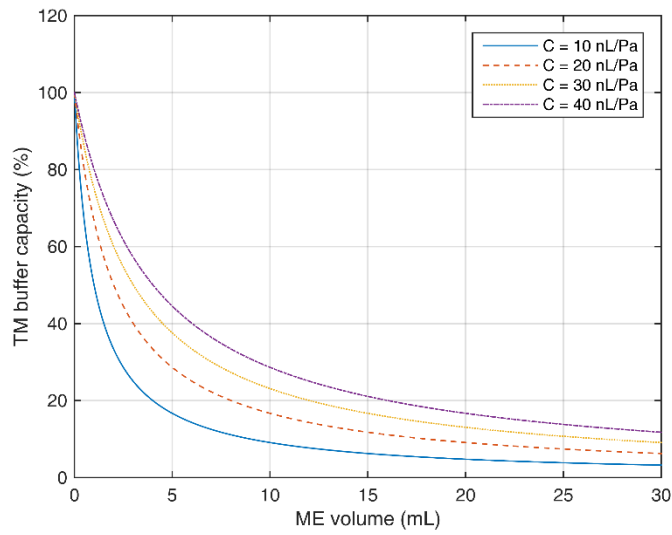


Figure 8-7: Theoretical relation between the TM buffer capacity and ME volume for an external pressure of  $10^5$  Pa and an external pressure change of  $\Delta P_{amb} = 1000$  Pa, for TM compliance values. Higher ME volumes lead to lower TM buffer capacity values, whereas increasing the TM compliance increases the TM buffer capacity.

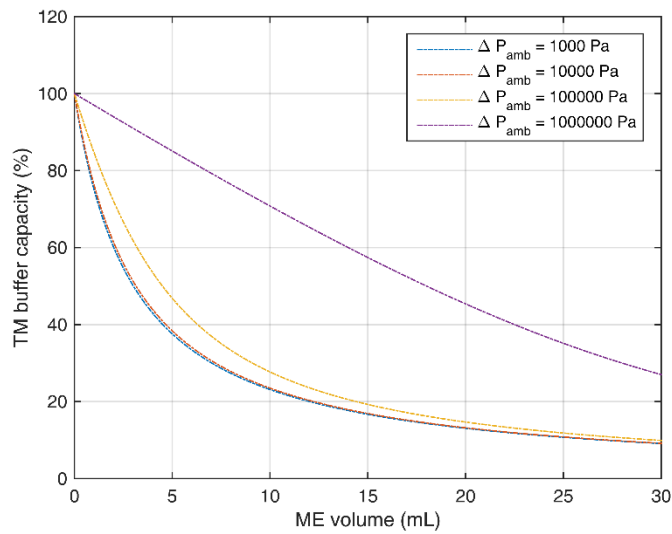


Figure 8-8: Theoretical relation between the TM buffer capacity and the ME volume for an external pressure of  $10^5$  Pa and a TM compliance of  $C_{TM} = 30 \cdot 10^{-3}$   $\mu\text{L}/\text{Pa}$ , for different levels of external pressure change. A larger external pressure change leads to a higher TM buffer capacity.



# GENERAL CONCLUSIONS

## Summary of conclusions

This thesis presents research projects that are centered around the human middle ear (ME) and tools to study it. In this chapter, we summarize the most important conclusions from each chapter, except from Chapter 2, as it is not a research project.

In Chapter 1, a new setup for stroboscopic digital holography, incorporating a high-energy pulsed laser and advanced trigger electronics, was described and presented. The setup was demonstrated using results of measurements on a vibrating rubber membrane for frequencies ranging from 5 Hz to 16.7 kHz. This range is limited by the response of the object and the stimulation device (i.e. in our case an acoustic speaker) rather than the technique itself. The possible range of the technique with the current components extends to 250 kHz. Two tests were performed to make an assessment of the accuracy and repeatability of the technique. The accuracy tests revealed that the measured displacements are in good accordance with the applied indentations, provided that material compression of the measured object was taken into account. The average absolute magnitude and phase difference at a single data point between subsequent measurement of the same phenomenon was 8,7 nm/Pa and 0,017 cycles, respectively, averaged over all measured frequencies.

Chapter 3 covered an extensive study using micro-computed tomography ( $\mu$ CT) on multiple morphological aspects of the human middle ear. The studied topics were: the ME ligaments; morphometric and mechanical parameters of the ossicles; the detailed morphology of the distal incus; the contact surface areas of the tympanic membrane (TM) and of the stapes footplate; and the thickness of multiple ME structures. The findings of these topics were taken into account when constructing the finite element models of the ME in later chapters.

Chapter 40 focused on a particularly interesting feature of ME morphology, tympano-malleal connection (TMC), i.e. the connection between the TM and the first ossicle, the malleus. By combining the strengths of  $\mu$ CT and histologic microscopy, the inter-individual variation of the TMC was studied in 13 samples. The minimal TMC anterior-posterior width along the manubrium was found to range between  $(83 \pm 7) \mu\text{m}$ , and  $(840 \pm 7) \mu\text{m}$ . The minimal TMC thickness ranged from  $(48 \pm 7) \mu\text{m}$  to  $(249 \pm 7) \mu\text{m}$  and the maximal thickness from  $(236 \pm 7) \mu\text{m}$  to  $(691 \pm 7) \mu\text{m}$ . Perhaps more tellingly is the fact that in some samples, the TMC is a thin, stretched fold at the middle of the manubrium made up of only loose connective tissue, whereas in others, the TMC has an entirely different shape and the malleus is tightly embedded into the TM along the entire manubrium.

In Chapter 5, a FE model of the human TM and malleus was constructed based on  $\mu$ CT images. The model was used to study damping and stiffness of the eardrum. The study also presented new measurements on an isolated TM-malleus sample using stroboscopic holography and laser Doppler vibrometry. TM damping needed to be incorporated into the model to accurately model TM displacement patterns at acoustic frequencies. The experimental data was best modeled using a loss factor that increases from 1 % at 20 Hz to 13 % at 20 kHz or by using a constant loss factor of 7.8 %. Typically used Rayleigh damping values were rejected since they yield too much damping, particularly at high frequencies. The best value for the magnitude of the complex modulus, which describes the TM stiffness, was significantly different between the two measured samples, with TB<sub>1</sub> requiring a complex modulus of 10 to 13 MPa and TB<sub>2</sub> 40 to 52 MPa. Holographic measurements at frequencies above 2 kHz indicate the motions of the lateral surface of the TM and the manubrium become decoupled at points in between the umbo and the lateral process of the malleus in humans. It is believed that the manubrial fold is responsible for this decoupling, and that the manubrial fold should be modeled with a lower stiffness than the TM (10% in our models).

Chapter 6 presented FE models of the entire human ME from three different individuals. The aim of the study was to examine the influence of various quantitative and qualitative variations in parameter values and model definitions on ME transmission. The most important quantitative parameters were found to be the Young's moduli of the TM, the stapedial annular ligament, the incudomalleal joint, and the tensor tympani, the loss factor of the TM, the  $\beta$  Rayleigh damping coefficients for the soft tissues outside the TM, and the choice of cochlear impedance. Less influential parameters were the Young's moduli of the tympano-malleal connection, incudomalleal joint capsule, and stapedius muscle and the loss factor of the tympano-malleal connection. The inclusion of multiple individual geometries in a single FE study allowed the calculation of an average stapes velocity response function and confirmed that this matches experimental average response curves better than individual models. The largest discrepancy between model and experiment appeared in the 2-4 kHz range, where the average model response was higher than the average experimental result. However, due to the wide variation in experimental response curves of individuals, the average outcome of the

models still falls within the standard deviation observed for individual temporal bones at most frequencies.

Chapter 7 presented a study in which the same three FE models of the human ME from the previous chapter were utilized to study the effect of a malleus handle fracture on the SFP velocity. Validation of the model using simulations without a cochlear impedance (the condition in which the experimental data were obtained) revealed that the model reproduced experimental results adequately for the frequencies 0.4 - 1.5 kHz and 2 - 8 kHz. After the validation, the model was used to predict the effect of a malleus fracture in clinical conditions, i.e. in the presence of a cochlear impedance. This flexibility highlights the value of the model-based approach. A malleus handle fracture in the presence of a cochlea infers a SFP velocity loss ranging from on average 4.8 dB (for a fracture 1 mm from the umbo) to 13.7 dB (for a fracture just superior to the tensor tympani tendon). Furthermore, the model predicted that removing the distal fractured fragment of the malleus does not improve SFP velocity in a clinically significant way. The biggest improvement was seen when the fracture was superior to the TT tendon, in which case the velocity was restored by 1.2 dB on average and at least 2.5 dB for frequencies below 850 Hz. Finally, the models predicted that the type of tympanomalleal connection has a notable effect on the SFP velocity change due to a malleus handle fracture. The average velocity loss was 2.9 to 5.1 dB smaller in the case of a wide, tight TMC, compared to a narrow TMC, depending on the position of the fracture. The studied TMC dimensions were population extremes based on Chapter 4 of this thesis.

In Chapter 8, the normal pressure buffering capacity of the human TM system was determined *in vivo* for pressure changes between 350 and -420 Pa, as well as estimations for the ME volume and TM compliance of the different patients. The overall mean buffer capacity was  $23.3\% \pm 3.4\%$  (standard error of the mean (SEM)). The mean ME volume was  $9.7 \pm 1.1$  mL (SEM). The TM buffer capacity was found higher in cases with a smaller ME volume, which meant that the volume displacement of the TM in such MEs was more efficient; this may result in less stretching of the lamina propria fibers so that degeneration and disintegration of the fibers may be prevented. This may contribute to the decreased recurrence rate of cholesteatoma in MEs with mastoid obliteration, because obliteration markedly reduces the ME volume. The average TM compliance was  $32.7 \times 10^{-3}$   $\mu\text{L}/\text{Pa}$  (SEM = 6.7) in the case of an ambient pressure decrease, and  $25.8 \times 10^{-3}$   $\mu\text{L}/\text{Pa}$  (SEM = 7.4) for an ambient pressure increase; thus, the TM compliance exhibited an asymmetry between movement directions.

### Links between the chapters of this thesis

In Part 1, Chapters 1 and 2, our experimental setup and the accompanying graphical user interface for stroboscopic holography were described. Measurements from this setup were used in the research for chapters 6 and 7 of Part 3.

In Part 2, Chapters 3 and 4, various morphological aspects of the human ME were studied in detail. The findings from these studies were subsequently incorporated in the studies of ME mechanics in chapters 6 and 7 of Part 3.

Chapter 5 (Part 3) presented a study about tympanic membrane (TM) mechanics, based on finite element modeling and experimental results from laser Doppler vibrometry and stroboscopic holography. The experiments were performed at the ME research group at Massachusetts Eye and Ear Infirmary (MEEI) and the Worcester Polytechnic Institute in Boston, USA during the PhD research of Jef Aernouts. The geometry of the model was based on one of the six middle ear micro-CT datasets from Chapter 3 (Part 2) and was also used as one of the three full middle ear models in Chapters 6 and 7 (Part 3). Chronologically, Chapter 5 (Part 3) was the first chapter of this thesis to be written and published, so it was not possible to include morphological insight from Chapters 3 of 4 (Part 2) in this study.

The geometries of all three models in Chapters 6 and 7 (Part 3) were all present in Chapter 3 (Part 2) as well. Some of the insights from Chapters 3 and 4 (Part 2) were taken into account in the construction of the full middle ear models used in Chapters 6 and 7. These insights include the selection of middle ear ligaments to include, the morphology of the distal incus, and the population limits of the dimensions of the tympano-malleolar connection.

The experimental setup and graphical user interface, presented in Chapters 1 and 2 (Part 1) were developed fully only after the measurements of Chapter 5 (Part 3) had taken place, so they were not used for the experimental data in that chapter. Results of our setup/GUI on a human tympanic membrane were included in Chapter 6 as a validation of the full middle ear model and were also used in the research behind Chapter 7. The data of this was however not included in the final paper, as other graphs were more crucial for the conclusions of the paper.

Chapter 8 presents a study about the quasi-static pressure regulation of the middle ear. It is the result of an international collaboration which did not directly connect to the other chapters. However, the results of this chapter about the present ME pressure variations and the eardrum's response to these, provide insights into ME mechanics in the quasi-static regime. The obtained results are valuable validation data for possible future ME models in the quasi-static pressure regime.

# **BACK MATTER**



## Samenvatting (Nederlands)

---

Ons vermogen om te horen is een fundamenteel onderdeel van het omgaan met anderen en met de maatschappij in het algemeen. Volgens de *World Health Organization* lijden wereldwijd 360 miljoen mensen aan een gehoorverlies van 40 decibel of meer in het beter horende oor<sup>12</sup>. Zelfs met een milder gehoorverlies ondervinden mensen aanzienlijke moeilijkheden in het dagelijkse leven, zoals wanneer ze converseren met anderen in een luide of drukke omgeving. Het vinden van geschikte behandelingen voor alle vormen van gehoorverlies is daarom een van de meeste relevante medische uitdagingen van onze tijd. Deze doctoraatsthesis gaat over onderzoek naar de werking van het menselijke middenoor, het subsysteem van het gehoororgaan tussen de gehoorgang van het buitenoor en het slakkenhuis van het binnenoor. Het middenoor bevat het trommelvlies, de drie kleinste beentjes van het menselijke lichaam (de gehoorbeentjes) en ondersteunende structuren zoals kleine spiertjes, pezen en ligamenten. De belangrijkste functie van het middenoor is het overbrengen van de energie en de informatie van binnenkomend geluid van de gehoorgang naar het binnenoor.

Deze thesis bevat acht hoofdstukken over de onderwerpen stroboscopische holografie en de werking van het menselijke middenoor. Vijf van deze hoofdstukken werden gepubliceerd in *peer-reviewed* tijdschriften en twee andere zijn nog *under review for publication*. De hoofdstukken zijn gegroepeerd in drie delen. Elk deel begint met een inleidend hoofdstuk

---

<sup>12</sup> Bron: [www.who.int](http://www.who.int); geraadpleegd op 18 oktober 2016; pagina voor het laatst aangepast in maart 2015.

waarin de basistheorie en achtergrondinformatie worden gegeven die relevant zijn voor de hoofdstukken die volgen in dat deel.

Deel I (**Part I**) bevat twee hoofdstukken over onze opstelling, controlesoftware en *graphical user interface of GUI* (grafische gebruikersomgeving) voor stroboscopische digitale holografie. Deze optische meettechniek stelt ons in staat om opnames te maken van volveld vibratiemappen van trillende oppervlakken met uitwijkingen gaande van enkele nanometer tot enkele micrometer. In het middenooronderzoek kan deze techniek worden gebruikt om de vibratierespons van het trommelvlies en de voetplaat van de stijgbeugel<sup>13</sup> te meten ten gevolge van geluidsstimulatie.

Hoofdstuk 1 (**Chapter 1**) beschrijft de specifieke eigenschappen van de optische opstelling en de elektronica die gebruikt werd voor het besturen van de opstelling. De techniek werd gedemonstreerd met metingen op een rubberen membraan en geëvalueerd aan de hand van een nauwkeurigheds- en herhaalbaarheidstest. In hoofdstuk 2 (**Chapter 2**) wordt de GUI beschreven die ontwikkeld werd om de stroboscopische holografie opstelling te besturen en de data ervan te verwerken.

In Deel II (**Part II**) wordt de focus verlegd naar het menselijke middenoor. De twee hoofdstukken in dit deel zoomen in op meerdere details van de morfologie<sup>14</sup> van het middenoor. De resultaten werden geïnterpreteerd in het licht van hun mogelijk belang voor de mechanica en modellering van het middenoor.

Hoofdstuk 3 (**Chapter 3**) presenteert een studie van zes verschillende aspecten van de morfologie van het menselijke middenoor die kwalitatief en/of kwantitatief onderzocht werden. De bestudeerde onderwerpen waren onder andere de ligamenten van het middenoor, de morfologie van (het distale deel van) de incus en de dikte van het trommelvlies. Dit gebeurde door het verwerken en interpreteren van micro-CT (*micro X-ray computed tomography*) data op zes menselijke rotsbeenderen (het deel van de schedel waarin het gehoororgaan zich bevindt).

Hoofdstuk 4 (**Chapter 4**) bericht over een studie die volledig gericht was op de verbinding tussen het trommelvlies met de hamer (het eerste gehoorsbeentje), ofwel de '*tympanomalleolar connection*'. Ook hier was de belangrijkste experimentele techniek micro-CT (op dertien specimens), ditmaal aangevuld met histologische microscopie (op drie van die dertien

---

<sup>13</sup> Het trommelvlies kan beschouwd worden als het 'input' oppervlak voor vibratie-energie van het middenoor. Op een gelijkaardige manier kan de voetplaat van de stijgbeugel beschouwd worden als het 'output' oppervlak van het middenoor. De stijgbeugel is het gehoorsbeentje dat het verst van het trommelvlies verwijderd zit.

<sup>14</sup> Morfologie is de tak in de biologie die zich bezig houdt met de studie van de vorm en structuur van organismen.

specimens). De dimensies van de *tympanomalleolar connection* werden gemeten in twee richtingen loodrecht op de steel van de hamer. Beide dimensies vertoonden een opvallend grote variatie tussen individuen.

Deel III (**Part III**) bevat vier onderzoeksartikelen over de mechanica en modellering van het menselijke middenoor. In hoofdstukken 5, 6 en 7 was de belangrijkste onderzoekstechniek *eindige elementen modellering*, een numerieke simulatietechniek die de onderzoeker in staat stelt om het fysisch gedrag van complexe systemen zoals het middenoor te modelleren.

In hoofdstuk 5 (**Chapter 5**) wordt een eerste eindige elementen model voorgesteld, bestaande uit het trommelvlies en het eerste gehoorbeentje, de hamer. De geometrie van het model was gebaseerd op micro-CT beelden van een menselijk rotsbeen. De studie richtte zich op de materiaaleigenschappen van het trommelvlies, meer bepaald zijn stijfheid en interne demping. De resultaten van het model werden aangevuld met experimentele vibratiedata van het trommelvlies, bekomen met behulp van stroboscopische holografie en *laser Doppler vibrometrie*<sup>15</sup>.

In hoofdstuk 6 (**Chapter 6**) wordt het model van hoofdstuk 5 uitgebreid tot een volledig middenoormodel, van trommelvlies tot stijgbeugel. Er werden ook nog twee nieuwe modellen bijgemaakt, zodat in totaal drie middenoormodellen gebruikt konden worden in deze studie. Het hoofddoel van dit project was om de effecten van veranderingen in de definitie van het model op het mechanisch gedrag van het model te evalueren. Deze informatie is relevant, aangezien er tijdens het definiëren van middenoormodellen veel keuzes noodzakelijkerwijs gemaakt moeten worden op basis van onvolledige informatie. Het is dus waardevol om te weten welke van deze keuzes een groter effect hebben op het uiteindelijke model dan andere keuzes.

Hoofdstuk 7 (**Chapter 7**) bestaat uit een studie over het effect van een geïsoleerde fractuur in de hamersteel op de geluidstransmissie in het middenoor. Deze zeldzame maar interessante aandoening werd in de literatuur nog niet vaak bestudeerd en met onze drie eindige elementen modellen van hoofdstuk 6 kon de aandoening nu in detail onderzocht worden zonder klinische studies op te moeten zetten. Breuken werden in het model geïntroduceerd door het verwijderen van kleine (virtuele) botsneden uit de hamersteel. De resultaten van het model werden eerst vergeleken met experimentele data op rotsbeenderen en de overeenkomst was goed voor middelhoge en hoge frequenties. De modellen werden ook gebruikt om het effect te voorspellen van het verwijderen van het afgebroken stukje van de hamersteel.

---

<sup>15</sup> Laser Doppler vibrometrie is een optische meettechniek die de vibratie van oppervlakken kan meten op een enkel punt met een hoge tijdsresolutie. De techniek detecteert de snelheid van het trillend object door gebruik te maken van de Doppler verschuiving, een fysisch fenomeen waarbij de frequentie van een golf wordt verschoven als de golf uitgezonden of gereflecteerd wordt door een bewegend oppervlak.

Tenslotte beschrijft hoofdstuk 8 (**Chapter 8**) een studie in het domein van de drukregulatie in het middenoor op zeven levende patiënten. Het bestudeerde fenomeen is genaamd het buffereffect van het trommelvlies. Als de druk in het middenoor gelijk is aan de omgevingsdruk, dan bevindt het trommelvlies zich in zijn neutrale positie. Een verandering in de omgevingsdruk veroorzaakt een vervorming van het trommelvlies en daardoor ook een drukverandering in het middenoor. De vervorming van het trommelvlies is telkens in die zin die ervoor zorgt dat het drukverschil tussen het middenoor en de omgeving afneemt. Dit effect heet het buffereffect van het trommelvlies. In deze studie werd de middenoordruk in zeven patiënten gemeten tijdens het nemen van een lift. De veranderingen in omgevingsdruk die overeenkwamen met de verschillende liftverplaatsingen werden eveneens gemeten. Dit stelde ons in staat om voor het eerst de capaciteit van het buffereffect van het trommelvlies kwantitatief te bepalen in levende patiënten. Bijkomende metingen gaven ook nieuwe waarden voor het volume van de middenoorcaviteit en de compliantie van het trommelvlies. Deze laatste grootte is relevant voor de mechanica van het middenoor in het regime van quasi-statische drukfluctuaties.

# List of abbreviations

---

$f_n$	Natural frequency
$r_{\text{eff}}$	Efficiency ratio of the incudomalleal complex
$\mu\text{CT}$	Micro-computed tomography
AML	Anterior malleal ligament
AnAx	Anatomical axis (AML - PIL)
ant	Anterior
AR	Annular ring
ASCII	American Standard Code for Information Interchange
ASE	Acoustical stimulation element
A-SML	Anterior superior malleal ligament
CCD	Charge-coupled device
CMOS	Complementary metal-oxide semiconductor
COM	Center of mass
CT	Computed tomography
DC term	Direct current term, i.e. the 0 Hz component.
DMA	Dynamic mechanical analysis
DML	Discomalleal ligament
DRCT	Dense, regular connective tissue
EC	Ear canal
EDTA	Ethylenediaminetetracetic (decalcifying agent)
EEC	External ear canal
ET	Eustachian tube
FE	Finite element
FFT	Fast-fourier transform
GBE	Gallilean beam expander
GUI	Graphical user interface
GUIDE	Graphical User Interface Development Environment
I	Incus
ICC	Intraclass correlation
IM	Incudomalleal
IMC	Incudomalleal complex
IMJ	Incudomalleal joint
inf	Inferior
infTT	Malleus handle fracture just inferior to the tensor tympani tendon
IS	Incudostapedial
ISJ	Incudostapedial joint
lat	Lateral
LCT	Loose connective tissue

LDV	Laser Doppler vibrometry
LIL	Lateral incudal ligament
LML	Lateral malleolar ligament
LPM	Lateral process of the malleus
LSFM	Light sheet fluorescence microscopy
M	Malleus
M-AML	Medial anterior malleolar ligament
ME	Middle ear
med	Medial
MF	Manubrial fold (= tympanomalleolar connection)
MIL	Medial incudal ligament
MIML	Medial incudomalleolar ligament
MRI	Magnetic resonance imaging
Nd:YAG laser	Neodymium-doped yttrium aluminum garnet laser
NPBS	Non-polarizing beamsplitter
OB	Object beam
OCT	Optical coherence tomography
PAR	Principal axis of inertia
PBS	Polarizing beamsplitter
PF	Pars flaccida (of the tympanic membrane)
PIL	Posterior incudal ligament
PM	Plica malleolaris
PMI	Principal moment of inertia
PML	Posterior malleolar ligament
post	Posterior
P-SML	Posterior superior malleolar ligament
PT	Pars tensa (of the tympanic membrane)
PTA	Phosphotungstic acid
RB	Reference beam
RMS	Root mean square
ROI	Region of interest
RW	Round window
S	Stapes
SAL	Stapedial annular ligament
S-AML	Superior anterior malleolar ligament
SD	Standard deviation
SEM	Standard error of the mean
SFP	Stapes footplate
SIL	Superior incudal ligament
SM	Stapedius muscle
SNR	Signal-to-noise ratio

SPL	Sound pressure level
SpML	Sphenomandibular ligament
SSL	Superior stapedial ligament
stl	Stereolithography
sup	Superior
supTT	Malleus handle fracture just superior to the tensor tympani tendon
TB	Temporal bone
TF	Transfer function
TM	Tympanic membrane
TMC	Tympanomalleolar connection (= manubrial fold)
TT	Tensor tympani
TTM	Tensor tympani muscle
UC	Uncertainty
UGCT	Center for X-ray Tomography of the Ghent University



# Bibliography

---

- Abo-Khatwa, M., Addams-Williams, J., Vincent, R., Osborne, J., 2005. Malleus-handle fracture: literature review and a new surgical approach. *Internet J. Otorhinolaryngol.* 4.
- Aernouts, J., 2012a. Mechanical Properties of the Tympanic Membrane : Measurement and Modeling. University of Antwerp.
- Aernouts, J., Aerts, J.R.M., Dirckx, J.J.J., 2012b. Mechanical properties of human tympanic membrane in the quasi-static regime from in situ point indentation measurements. *Hear. Res.* 290, 45–54. doi:10.1016/j.heares.2012.05.001
- Aibara, R., Welsh, J.T., Puria, S., Goode, R.L., 2001. Human middle-ear sound transfer function and cochlear input impedance. *Hear. Res.* 152, 100–109. doi:10.1016/S0378-5955(00)00240-9
- Alexander, R., 2003. Principles of animal locomotion. Princeton, NJ: Princeton University Press.
- Alper, C.M., Kitsko, D.J., Swarts, J.D., Martin, B., Yuksel, S., Cullen Doyle, B.M., Villardo, R.J.M., Doyle, W.J., 2011. Role of the mastoid in middle ear pressure regulation. *Laryngoscope* 121, 404–8. doi:10.1002/lary.21275
- Anson, B.J., Donaldson, J.A., 1981. *Surgical Anatomy of the Temporal Bone*, Third. ed. Raven Press, New York.
- Ars, B., 1977. Bijdrage tot de heerkundige anatomie van het tympano-ossiculair systeem. *Acta Otorhinolaryngol Belg* 31, 50–68.
- Ars, B., Decraemer, W., Ars-Piret, N., 1989. The lamina propria and cholesteatoma. *Clin. Otolaryngol.* 14, 471–475. doi:10.1111/j.1365-2273.1989.tb00406.x
- Ars, B., Dirckx, J., Ars-Piret, N., Buytaert, J., 2012. Insights in the physiology of the human mastoid: Message to the surgeon. *J. Int. Adv. Otol.* 8, 296–310.
- Asherson, N., 1978. The fourth auditory ossicle: fact or fantasy? *J. Laryngol. Otol.* 92, 453–65.
- Banks, H.T., Hu, S., Kenz, Z.R., 2011. A brief review of elasticity and viscoelasticity for solids. *Adv. Appl. Math. Mech.* 3, 1–51. doi:10.4208/aamm.10-m1030
- Blanchard, M., Abergel, A., VÉrillaud, B., Williams, M.T., Ayache, D., 2011. Isolated malleus-handle fracture. *Auris Nasus Larynx* 38, 439–443. doi:10.1016/j.anl.2010.11.011
- Bluestone, C., Doyle, W., 1988. Anatomy and physiology of eustachian tube and middle ear related to otitis media. *J. Allergy Clin. Immunol.* 81, 997–1003. doi:10.1016/0091-6749(88)90168-6
- Böhne, F., Bretan, T., Lehner, S., Strenger, T., 2013. Simulations and Measurements of Human Middle Ear Vibrations Using Multi-Body Systems and Laser-Doppler Vibrometry with the Floating Mass Transducer. *Materials (Basel)*. 6, 4675–4688. doi:10.3390/ma6104675
- Bonet, J., Wood, R.D., 1997. *Nonlinear Continuum Mechanics for Finite Element Analysis*. Cambridge University Press, Cambridge. doi:10.1017/CBO9780511755446
- Brattmo, M., Tideholm, B., Carlborg, B., 2003. Chronic Tympanic Membrane Perforation: Middle Ear Pressure and Tubal Function. *Acta Otolaryngol.* 123, 569–574. doi:10.1080/00016480310001231
- Buytaert, J. a. N., Adriaens, D., Dirckx, J.J.J., 2010. Orthogonal-plane fluorescence optical sectioning: a technique for 3-D imaging of biomedical specimens, in: Méndez-Vilas, A., Díaz, J. (Eds.), *Microscopy : Science, Technology, Applications and Education*, Vol. 2. Formatex Research Center, pp. 1356–1365.

- Buytaert, J., Goyens, J., De Greef, D., Aerts, P., Dirckx, J., 2014. Volume Shrinkage of Bone, Brain and Muscle Tissue in Sample Preparation for Micro-CT and Light Sheet Fluorescence Microscopy (LSFM). *Microsc. Microanal.* 20, 1208–1217. doi:10.1017/S1431927614001329
- Bylander, A., 1986. Pathophysiological aspects on Eustachian tube function and SOM. *Scand. Audiol. Suppl.* 26, 59–63.
- Cai, H., Jackson, R.P., Steele, C.R., Puria, S., 2010. A Biological Gear in the Human Middle Ear, in: *Proceedings of the COMSOL Conference 2010*.
- Caremans, J., Hamans, E., Muylle, L., Van de Heyning, P., Van Rompaey, V., 2015. Endoscopic procurement of allograft tympano-ossicular systems: valuable to replace the Schuknecht bone plug technique? *Cell Tissue Bank.* 16, 91–6. doi:10.1007/s10561-014-9445-x
- Cheng, J.T., Aarnisalo, A.A., Harrington, E., Hernandez-Montes, M. del S., Furlong, C., Merchant, S.N., Rosowski, J.J., 2010. Motion of the surface of the human tympanic membrane measured with stroboscopic holography. *Hear. Res.* 263, 66–77. doi:10.1016/j.heares.2009.12.024
- Cheng, J.T., Hamade, M., Merchant, S.N., Rosowski, J.J., Harrington, E., Furlong, C., 2013. Wave motion on the surface of the human tympanic membrane: holographic measurement and modeling analysis. *J. Acoust. Soc. Am.* 133, 918–37. doi:10.1121/1.4773263
- Cheyne, F., Guyot, L., Richard, O., Layoun, W., Gola, R., 2003. Discomalleolar and malleomandibular ligaments: anatomical study and clinical applications. *Surg. Radiol. Anat.* 25, 152–7. doi:10.1007/s00276-003-0097-y
- Chien, W., McKenna, M.J., Rosowski, J.J., Merchant, S.N., 2008. Isolated fracture of the manubrium of the malleus. *J. Laryngol. Otol.* 122, 898–904. doi:10.1017/S0022215107000990
- Chien, W., Northrop, C., Levine, S., Pilch, B.Z., Peake, W.T., Rosowski, J.J., Merchant, S.N., 2009. Anatomy of the distal incus in humans. *J. Assoc. Res. Otolaryngol.* 10, 485–96. doi:10.1007/s10162-009-0179-6
- Cinamon, U., Sade, J., 2003. Mastoid and Tympanic Membrane as Pressure Buffers : A Quantitative Study in a Middle Ear Cleft Model Experiment. *Otol. Neurotol.* 24, 839–842. doi:10.1097/00129492-200311000-00002
- Csakanyi, Z., Katona, G., Josvai, E., Mohos, F., Sziklai, I., 2011. Volume and Surface of the Mastoid Cell System in Otitis Media With Effusion in Children. *Otol. Neurotol.* 32, 64–70. doi:10.1097/MAO.0b013e3181fcec84
- Csakanyi, Z., Katona, G., Konya, D., Mohos, F., Sziklai, I., 2014. Middle Ear Gas Pressure Regulation: The Relevance of Mastoid Obliteration. *Otol. Neurotol.* 35, 944–953. doi:10.1097/MAO.0000000000000282
- Cutnell, J.D., Johnson, K.W., 2009. *Physics*, 8TH ED. ed. Wiley.
- De Arantes E Oliveira, E.R., 1968. Theoretical foundations of the finite element method. *Int. J. Solids Struct.* 4, 929–952. doi:10.1016/0020-7683(68)90014-0
- De Greef, D., 2011. *Volveld tijdsgeresolveerde digitale holografie : vierdimensionale beeldvorming van vibraties en vervormingen met nanometer resolutie*. University of Antwerp.
- De Greef, D., Dirckx, J.J.J., 2012. Digital holographic vibrometry using stroboscopic illumination for full field , time resolved 4D imaging of nanometer vibrations, in: *Proceedings of ISMA2012-USD2012*. pp. 1435–1444.
- De Greef, D., Soons, J., Dirckx, J.J.J., 2014a. Digital Stroboscopic Holography Setup for Deformation Measurement at Both Quasi-Static and Acoustic Frequencies. *Int. J. Optomechanics* 8, 275–291. doi:10.1080/15599612.2014.942928

- De Greef, D., Aernouts, J., Aerts, J., Cheng, J.T., Horwitz, R., Rosowski, J.J., Dirckx, J.J.J., 2014b. Viscoelastic properties of the human tympanic membrane studied with stroboscopic holography and finite element modeling. *Hear. Res.* 312, 69–80. doi:10.1016/j.heares.2014.03.002
- De Greef, D., Buytaert, J.A.N., Aerts, J.R.M., Van Hoorebeke, L., Dierick, M., Dirckx, J., 2015. Details of human middle ear morphology based on micro-CT imaging of phosphotungstic acid stained samples. *J. Morphol.* 276, 1025–46. doi:10.1002/jmor.20392
- De Greef, D., Goyens, J., Pintelon, I., Bogers, J.-P., Van Rompaey, V., Hamans, E., Van de Heyning, P., Dirckx, J.J.J., 2016. On the connection between the tympanic membrane and the malleus. *Hear. Res.* 340, 50–59. doi:10.1016/j.heares.2015.12.002
- de La Rochefoucauld, O., Kachroo, P., Olson, E.S., 2010. Ossicular motion related to middle ear transmission delay in gerbil. *Hear. Res.* 270, 158–72. doi:10.1016/j.heares.2010.07.010
- Decraemer, W.F., Dirckx, J.J.J., 1998. Pressure regulation due to displacement of the pars flaccida and pars tensa of the tympanic membrane. *Oto-Rhino-Laryngologia Nov.* 8, 277–281. doi:10.1159/000027915
- Decraemer, W.F., Khanna, S., 2004. Measurement, visualization and quantitative analysis of complete three-dimensional kinematical data sets of human and cat middle ear, in: Wada, H. (Ed.), *Proceedings of the 3rd Symposium on Middle Ear Mechanics in Research and Otology*. World Scientific, Singapore, pp. 3–10.
- Delrue, S., De Foer, B., Van Dinther, J., Zarowski, A., Somers, T., Casselman, J., Offeciers, E., 2015. Handling an isolated malleus handle fracture: Current diagnostic work-up and treatment options. *Ann. Otol. Rhinol. Laryngol.* 124, 244–249. doi:10.1177/0003489414550240
- Dirckx, J.J.J., Decraemer, W.F., 1991. Human tympanic membrane deformation under static pressure. *Hear. Res.* 51, 93–105. doi:10.1016/0378-5955(91)90009-X
- Dirckx, J.J.J., Decraemer, W.F.S., 1992. Area change and volume displacement of the human tympanic membrane under static pressure. *Hear. Res.* 62, 99–104. doi:10.1016/0378-5955(92)90206-3
- Dirckx, J.J.J., Gaihede, M., Jacobsen, H., Buytaert, J.A.N., Aernouts, J., 2008. Pressure fluctuations in the normal and intact middle ear and its relation to speed of transmucosal gas exchange, in: Ars, B. (Ed.), *Chronic Otitis Media: Pathogenesis-Oriented Therapeutic Management*. Kugler Publications, pp. 155–170.
- Dirckx, J.J.J., Marcusohn, Y., Gaihede, M.L., 2013. Quasi-static Pressures in the Middle Ear Cleft, in: Puria, S., Fay, R.R., Popper, A.N. (Eds.), *The Middle Ear: Science, Otosurgery, and Technology*. Springer New York, pp. 93–133. doi:10.1007/978-1-4614-6591-1\_5
- Elnér, Å., Ingelstedt, S., Ivarsson, A., 1971. The elastic properties of the tympanic membrane system. *Acta Otolaryngol* 72, 397–403.
- Esser, M.H.M., 1947. The mechanism of the middle ear: Part II. The drum. *Bull. Math. Biophys.* 9, 75–91. doi:10.1007/BF02478294
- Fay, J.P.J.P., Puria, S., Steele, C.R., 2006. The discordant eardrum. *Proc. Natl. Acad. Sci. U. S. A.* 103, 19743–19748. doi:10.1073/pnas.0603898104
- Federative Committee on Anatomical Terminology (FCAT), 1998. *Terminologica Anatomica: International Anatomical Terminology*. Thieme, Stuttgart.
- Ferrazzini, M., 2003. Virtual middle ear A dynamic mathematical model based on the finite element method. Swiss Federal Institute of Technology.
- Findley, W.N., 1989. *Creep and relaxation of nonlinear viscoelastic materials*, 2nd ed. ed, Polymer. Courier Corporation. doi:10.1016/0032-3861(78)90187-8

- Fleischer, G., 1978. Evolutionary principles of the mammalian middle ear. *Adv. Anat. Embryol. Cell Biol.* 55, 3–70. doi:10.1121/1.384051
- Fletcher, N.H., 1992. *Acoustic Systems in Biology*. Oxford University Press, New York.
- Flisberg, K., Ingelstedt, S., Örtengren, U., 1963. On Middle Ear Pressure. *Acta Otolaryngol.* 56, 43–56. doi:10.3109/00016486309139992
- Fung, Y.C., 1993. Bio viscoelastic solids, in: *Biomechanics: Mechanical Properties of Living Tissues*. Springer, New York, pp. 242–295. doi:10.1115/1.2901550
- Funnell, W.R.J., Laszlo, C.A., 1978. Modeling of the cat eardrum as a thin shell using the method. *J. Acoust. Soc. Am* 63, 1461–1467.
- Funnell, W.R., Laszlo, C.A., 1982. A critical review of experimental observations on ear-drum structure and function. *ORL. J. Otorhinolaryngol. Relat. Spec.* 44, 181–205.
- Funnell, W.R.J., 1983. On the undamped natural frequencies and mode shapes of a finite-element. *J. Acoust. Soc. Am* 73, 1657–1661.
- Funnell, W.R.J., Heng Siah, T., McKee, M.D., Daniel, S.J., Decraemer, W.F., 2005. On the coupling between the incus and the stapes in the cat. *J. Assoc. Res. Otolaryngol.* 6, 9–18. doi:10.1007/s10162-004-5016-3
- Funnell, W.R.J., Daniel, S.J., Alsabab, B., Liu, H., 2006. On the coupling between the incus and the stapes, in: Ninth “Mechanics of Hearing” Workshop. Portland, p. 22.
- Funnell, W.R.J., Maftoon, N., Decraemer, W.F., 2012. Mechanics and modelling for the middle ear.
- Funnell, W.R.J., Maftoon, N., Decraemer, W.F., 2013. Modeling of Middle-Ear Mechanics, in: Puria, S., Fay, R.R., Popper, A.N. (Eds.), *The Middle Ear: Science, Otosurgery, and Technology*, Springer Handbook of Auditory Research. Springer New York, New York, NY, pp. 1–35. doi:10.1007/978-1-4614-6591-1
- Furlong, C., Rosowski, J.J., Hulli, N., Ravicz, M.E., 2009. Preliminary Analyses of Tympanic-Membrane Motion from Holographic Measurements. *Strain* 45, 301–309. doi:10.1111/j.1475-1305.2008.00490.x
- Gabor, D., 1971. Nobel Lecture on Holography. *Imp. Coll. Sci. Technol.* 1948–1971.
- Gaihede, M., 1999. Mechanics of the middle ear system: computerized measurements of its pressure–volume relationship. *Auris Nasus Larynx* 26, 383–399. doi:10.1016/S0385-8146(99)00018-8
- Gaihede, M.L., Kabel, J., 2000. The normal pressure-volume relationsil of the middle ear system and its biological variation, in: Rosowski, J.J., Merchant, S.N. (Eds.), *The Function and Mechanics of Normal, Diseased and Reconstructed Middle Ears*. Kugler Publications, The Hague, pp. 59–70.
- Gaihede, M., Liao, D., Gregersen, H., 2007. In vivo areal modulus of elasticity estimation of the human tympanic membrane system: modelling of middle ear mechanical function in normal young and aged ears. *Phys. Med. Biol.* 52, 803–814. doi:10.1088/0031-9155/52/3/019
- Gaihede, M., Dirckx, J.J.J., Jacobsen, H., Aernouts, J., Søvsø, M., Tveterås, K., 2010. Middle ear pressure regulation--complementary active actions of the mastoid and the Eustachian tube. *Otol. Neurotol.* 31, 603–11. doi:10.1097/MAO.0b013e3181dd13e2
- Gaihede, M., Padurariu, S., Jacobsen, H., De Greef, D., Dirckx, J.J.J., 2013. Eustachian tube pressure equilibration. Temporal analysis of pressure changes based on direct physiological recordings with an intact tympanic membrane. *Hear. Res.* doi:10.1016/j.heares.2013.01.003
- Gan, R.Z., Sun, Q., Dyer, R.K., Chang, K.-H., Dormer, K.J., 2002. Three-dimensional Modeling of Middle Ear Biomechanics and Its Applications. *Otol. Neurotol.* 23, 271–280. doi:10.1097/00129492-200205000-00008

- Gan, R.Z., Feng, B., Sun, Q., 2004. Three-dimensional finite element modeling of human ear for sound transmission. *Ann. Biomed. Eng.* 32, 847-59.
- Gan, R.Z., Sun, Q., Feng, B., Wood, M.W., 2006. Acoustic-structural coupled finite element analysis for sound transmission in human ear--pressure distributions. *Med. Eng. Phys.* 28, 395-404. doi:10.1016/j.medengphy.2005.07.018
- Gan, R.Z., Reeves, B.P., Wang, X., 2007. Modeling of sound transmission from ear canal to cochlea. *Ann. Biomed. Eng.* 35, 2180-2195. doi:10.1007/s10439-007-9366-y
- Gan, R.Z., Cheng, T., Dai, C., Yang, F., Wood, M.W., 2009. Finite element modeling of sound transmission with perforations of tympanic membrane. *J. Acoust. Soc. Am.* 126, 243-53. doi:10.1121/1.3129129
- Gan, R.Z., Wang, X., 2014. Modeling Microstructure of Incudostapedial Joint and the Effect on Cochlear Input Finite Element Modeling of ISJ Microstructure, in: *Mechanics of Hearing Proceedings*. Cape Sounio.
- Gea, S.L.R., Decraemer, W.F., Dirckx, J.J.J., 2005. Region of interest micro-CT of the middle ear: A practical approach. *J. XRay Sci. Technol.* 13, 137-148.
- Gea, S.L.R., Decraemer, W.F., 2010. Tympanic Membrane Boundary Deformations Derived from Static Displacements Observed with Computerized Tomography in Human and Gerbil. *Jaro-Journal Assoc. Res. Otolaryngol.* 11, 1-17. doi:10.1007/s10162-009-0192-9
- Gelfand, S.A., 2009. *Essentials of Audiology*. Thieme.
- Gentil, F., Parente, M., Martins, P., Garbe, C., Jorge, R.N., Ferreira, A., Tavares, J.M.R.S., 2011. The influence of the mechanical behaviour of the middle ear ligaments: a finite element analysis. *Proc. Inst. Mech. Eng. P* 225, 68-76.
- Gentil, F., Garbe, C., Parente, M., Martins, P., Ferreira, A., Jorge, R.N., Santos, C., Paço, J., 2014a. Analysis of Eardrum Pathologies Using the Finite Element Method. *J. Mech. Med. Biol.* 14, 1450034. doi:10.1142/S0219519414500341
- Gentil, F., Garbe, C., Parente, M., Martins, P., Santos, C., Almeida, E., Jorge, R.N., 2014b. The biomechanical effects of stapes replacement by prostheses on the tympano-ossicular chain. *Int. j. numer. method. biomed. eng.* 30, 1409-20. doi:10.1002/cnm.2664
- Graboyes, E.M., Hullar, T.E., Chole, R.A., 2011. The lenticular process of the incus. *Otol. Neurotol.* 32, 1600-4. doi:10.1097/MAO.0b013e318232e268
- Graham, M., Reams, C., Perkins, R., 1978. Human tympanic membrane-malleus attachment: preliminary study. *Ann Otol Rhinol Laryngol.*
- Guelke, R., Keen, J.A., 1949. A study of the vibrations of the tympanic membrane under direct vision, with a new explanation of their physical characteristics. *J. Physiol.* 110, 226-236. doi:10.1113/jphysiol.1949.sp004435
- Gulya, A.J., Schuknecht, H.F., 1995. *Anatomy of the temporal bone with surgical implications*. Parthenon Pub. Group.
- Hariharan, P., Oreb, B.F., 1986. Stroboscopic holographic interferometry: Application of digital techniques. *Opt. Commun.* 59, 83-86. doi:10.1016/0030-4018(86)90454-2
- Harley, R., James, D., Miller, A., White, J.W., 1977. Phonons and the elastic moduli of collagen and muscle. *Nature* 267, 285-287. doi:10.1038/267285a0
- Harris, J.P., Butler, D., 1985. Recognition of Malleus Handle Fracture in the Differential Diagnosis of Otologic Trauma. *Laryngoscope* 95, 665--70decim. doi:10.1288/00005537-198506000-00006

- Hartman, W.F., 1971. An Error in Helmholtz's Calculation of the Displacement of the Tympanic Membrane. *J. Acoust. Soc. Am.* 49, 1317. doi:10.1121/1.1912495
- Hato, N., Okada, M., Hakuba, N., Hyodo, M., Gyo, K., 2007. Repair of a malleus-handle fracture using calcium phosphate bone cement. *Laryngoscope* 117, 361–363. doi:10.1097/01.mlg.0000246952.85668.24
- Hege, H., Seebass, M., Stalling, D., Zockler, M., 1997. A Generalized Marching Cubes Algorithm Based On Non-Binary Classifications. *ZIB Prepr.* sc-97-05.
- Helmholtz, H. von, 1873. *The mechanism of the ossicles of the ear and the membrana tympani.* New York William Wood Co.
- Hemila, S., Nummela, S., Reuter, T., 1995. What middle ear parameters tell about impedance matching and high frequency hearing. *Hear. Res.* 85, 31–44.
- Hernandez-Montes, M. del S., Furlong, C., Rosowski, J.J., Hulli, N., Harrington, E., Cheng, J.T., Ravicz, M.E., Santoyo, F.M., 2009. Optoelectronic holographic otoscope for measurement of nano-displacements in tympanic membranes. *J. Biomed. Opt.* 14, 34023. doi:10.1117/1.3153898
- Herráez, M.A., Burton, D.R., Lalor, M.J., Gdeisat, M. a, 2002. Fast two-dimensional phase-unwrapping algorithm based on sorting by reliability following a noncontinuous path. *Appl. Opt.* 41, 7437–44.
- Higashimachi, T., Shiratake, Y., Maeda, T., Sug, K., Toriya, R., 2013. Three-dimensional finite element analysis of the human middle ear and an application for clinics for tympanoplasty, in: *Surface Effects and Contact Mechanics XI - Computational Methods and Experiments.* pp. 61–72. doi:10.2495/SECM130061
- Hoffstetter, M., Lugauer, F., Kundu, S., Wacker, S., Perea-Saveedra, H., Lenarz, T., Hoffstetter, P., Schreyer, A.G., Wintermantel, E., 2011. Middle ear of human and pig: a comparison of structures and mechanics. *Biomed. Tech. (Berl).* 56, 159–65. doi:10.1515/BMT.2011.011
- Hoffstetter, M., Schardt, F., Lenarz, T., Wacker, S., Wintermantel, E., 2010. Parameter study on a finite element model of the middle ear. *Biomed. Eng. (NY).* 55, 19–26. doi:10.1515/BMT.2010.006
- Holmes, M.H., Rabbitt, R.D., Holmes, M.H., 1988. Three-dimensional acoustic waves in the ear canal and their interaction with the tympanic membrane. *J. Acoust. Soc. Am.* 83, 1064. doi:10.1121/1.396051
- Homma, K., Du, Y., Shimizu, Y., Puria, S., 2009. Ossicular resonance modes of the human middle ear for bone and air conduction. *J. Acoust. Soc. Am.* 125, 968–79. doi:10.1121/1.3056564
- Homma, K., Shimizu, Y., Kim, N., Du, Y., Puria, S., 2010. Effects of ear-canal pressurization on middle-ear bone- and air-conduction responses. *Hear. Res.* 263, 204–15. doi:10.1016/j.heares.2009.11.013
- Horwitz, R., Cheng, J.T., Harrington, E., Dobrev, I., Flores-Moreno, J.M., Furlong, C., Rosowski, J.J., 2012. Coupling of the motion of the tympanic membrane to the manubrium in human cadaveric temporal bones, in: *Abstracts of the Thirty-Fifth Meeting of the Association for Research in Otolaryngology.* p. 124.
- Hudde, H., Weistenhofer, C., 1997. A Three-Dimensional Circuit Model of the Middle Ear. *Acta Acust. united with Acust.* 83, 535–549.
- Hudde, H., Weistenhöfer, C., 2000. Circuit models of middle ear function, in: Rosowski, J.J. (Ed.), *The Function and Mechanics of Normal, Diseased and Reconstructed Middle Ears.* Kugler Publications, The Hague, pp. 39–58.
- Hudde, H., Weistenhöfer, C., 2006. Key Features of the Human Middle Ear. *ORL* 68, 324–328. doi:10.1159/000095274
- Hüttenbrink, K.B., 1988. *The Mechanics of the Middle-Ear at Static Air Pressures: The Role of the Ossicular Joints, the Function of the Middle-Ear Muscles and the Behaviour of Stapedial Prostheses.* *Acta Otolaryngol.* 105, 1–35. doi:10.3109/00016488809099007

- Ingelstedt, S., Jonson, B., 1967. Mechanisms of the Gas Exchange in the Normal Human Middle Ear. *Acta Otolaryngol.* 63, 452–461. doi:10.3109/00016486709123624
- Joseph, D., Gu, W., Mao, X., Lai, W., Mow, V., 1999. True density of normal and enzymatically treated bovine articular cartilage. *Trans. Orthop Res Soc* 24, 642.
- Karmody, C.S., Northrop, C.C., Levine, S.R., 2009. The incudostapedial articulation: new concepts. *Otol. Neurotol.* 30, 990–7. doi:10.1097/MAO.0b013e3181b0fff7
- Kelly, D.J., Prendergast, P.J., Blayney, a W., 2003. The effect of prosthesis design on vibration of the reconstructed ossicular chain: a comparative finite element analysis of four prostheses. *Otol. Neurotol.* 24, 11–19. doi:10.1097/00129492-200301000-00004
- Kendall, M.G., 1938. A New Measure of Rank Correlation. *Biometrika* 30, 81. doi:10.2307/2332226
- Kerns, M.J.J., Darst, M. a, Olsen, T.G., Fenster, M., Hall, P., Grevey, S., 2008. Shrinkage of cutaneous specimens: formalin or other factors involved? *J. Cutan. Pathol.* 35, 1093–6. doi:10.1111/j.1600-0560.2007.00943.x
- Kerr, J.B., 2009. *Functional Histology*, 2nd ed. ed. Elsevier.
- Kim, H.J., Jung, H.S., Kwak, H.H., Shim, K.S., Hu, K.S., Park, H.D., Park, H.W., Chung, I.H., 2004. The discomalleolar ligament and the anterior ligament of malleus: an anatomic study in human adults and fetuses. *Surg. Radiol. Anat.* 26, 39–45. doi:10.1007/s00276-003-0170-6
- Kinsler, L.E., 2000. *Fundamentals of Acoustics*, 4th ed. John Wiley & Sons.
- Kirikae, I., 1960. *The structure and Function of the Middle Ear*. University of Tokyo Press.
- Knutsson, J., Bagger-Sjöbäck, D., von Unge, M., 2011. Structural Tympanic Membrane Changes in Secretory Otitis Media and Cholesteatoma. *Otol. Neurotol.* 32, 596–601. doi:10.1097/MAO.0b013e318214ea62
- Koike, T., Wada, H., Kobayashi, T., 2001. Effect of Depth of Conical-Shaped Tympanic Membrane on Middle-Ear Sound Transmission. *JSME Int. J. Ser. C* 44, 1097–1102.
- Koike, T., Wada, H., Kobayashi, T., 2002. Modeling of the human middle ear using the finite-element method. *J. Acoust. Soc. Am.* 111, 1306–1317. doi:10.1121/1.1451073
- Kulkarni, A., Colburn, H.S., 1998. Role of spectral detail in sound-source localization. *Nature* 396, 747–749. doi:10.1038/25526
- Kuypers, L.C., Decraemer, W.F., Dirckx, J.J.J., 2006. Thickness distribution of fresh and preserved human eardrums measured with confocal microscopy. *Otol. Neurotol.* 27, 256–64. doi:10.1097/01.mao.0000187044.73791.92
- Lemmerling, M.M., Stambuk, H.E., Mancuso, a a, Antonelli, P.J., Kubilis, P.S., 1997. CT of the normal suspensory ligaments of the ossicles in the middle ear. *Am. J. Neuroradiol.* 18, 471–7.
- Lempriere, B.M., 1968. Poisson's ratio in orthotropic materials. *AIAA J.* 6, 2226–2227. doi:10.2514/3.4974
- Lewin, A., Mohr, F., Selbach, H., 1990. Heterodyn-Interferometer zur Vibrationsanalyse / Heterodyne interferometers for vibration analysis. *tm - Tech. Mess.* 57, 335–345. doi:10.1524/teme.1990.57.jg.335
- Li, Y., Barbic, J., 2014. Stable Orthotropic Materials, in: *Proceedings of the 2014 ACM SIGGRAPH/Eurographics Symposium on Computer Animation*.
- Lim, D.J., 1970. Human Tympanic Membrane: An Ultrastructural Observation. *Acta Otolaryngol* 70, 176–186.
- Liu, Y., Li, S., Sun, X., 2009. Numerical analysis of ossicular chain lesion of human ear. *Acta Mech. Sin. Xuebao* 25, 241–247. doi:10.1007/s10409-008-0206-6

- Liu, H., Rao, Z., Huang, X., Cheng, G., Tian, J., Ta, N., 2014. An incus-body driving type piezoelectric middle ear implant design and evaluation in 3D computational model and temporal bone. *ScientificWorldJournal*. 2014, 121624. doi:10.1155/2014/121624
- Maftoon, N., Funnell, W.R.J., Daniel, S.J., Decraemer, W.F., 2015. Finite-Element Modelling of the Response of the Gerbil Middle Ear to Sound. *JARO - J. Assoc. Res. Otolaryngol.* 16, 547-567. doi:10.1007/s10162-015-0531-y
- Magnuson, B., 2003. Functions of the mastoid cell system: auto-regulation of temperature and gas pressure. *J. Laryngol. Otol.* 117. doi:10.1258/002221503762624512
- Marcusohn, Y., Ar, A., Dirckx, J.J.J., 2010. Perfusion and diffusion limitations in middle ear gas exchange: the exchange of CO<sub>2</sub> as a test case. *Hear. Res.* 265, 11-4. doi:10.1016/j.heares.2010.03.078
- Margolis, R.H., Hunter, L.L., 1999. Tympanometry: basic principles and clinical applications, in: *Contemporary Perspectives in Hearing Assessment*. Allyn & Bacon, Boston, pp. 89-130.
- Marquet, J., 1987. Allografts and tympanoplasty and other forms of middle ear surgery, in: Ballantyne, J.C., Morrison, A.W. (Eds.), *Operative Surgery*. Butterworths, London, pp. 102-126. doi:10.1002/micr.1920080216
- Masschaele, B.C., Cnudde, V., Dierick, M., Jacobs, P., Van Hoorebeke, L., Vlassenbroeck, J., 2007. UGCT: New X-ray radiography and tomography facility. *Nucl. Instruments Methods Phys. Res. Sect. A Accel. Spectrometers, Detect. Assoc. Equip.* 580, 266-269. doi:10.1016/j.nima.2007.05.099
- McGraw, K.O., Wong, S.P., 1996. Forming inferences about some intraclass correlation coefficients. *Psychol. Methods* 1, 30-46. doi:10.1037//1082-989X.1.1.30
- Mente, P.L., Lewis, J.L., 1994. Elastic modulus of calcified cartilage is an order of magnitude less than that of subchondral bone. *J. Orthop. Res.* 12, 637-47. doi:10.1002/jor.1100120506
- Merchant, S.N., Ravicz, M.E., Rosowski, J.J., 1996. Acoustic input impedance of the stapes and cochlea in human temporal bones. *Hear. Res.* 97, 30-45.
- Metscher, B.D., 2009. MicroCT for comparative morphology: simple staining methods allow high-contrast 3D imaging of diverse non-mineralized animal tissues. *BMC Physiol.* 9, 11. doi:10.1186/1472-6793-9-11
- Mikhael, C., 2005. *Finite-Element Modelling of the Human Middle Ear*. McGill University.
- Miller, J.L., Dark, M.J., 2014. Evaluation of the effect of formalin fixation on skin specimens in dogs and cats. *PeerJ* 2, e307. doi:10.7717/peerj.307
- Moller, A.R., 1974. The acoustic middle ear muscle reflex, in: *Handbook of Sensory Physiology*. Vol. 1. Springer-Verlag, New York, pp. 519-548. doi:10.1007/978-3-642-65829-7\_16
- Molvaer, O.I., Vallersnes, F.M., Kringlebotn, M., 1978. The size of the middle ear and the mastoid air cell. *Acta Otolaryngol.* 85, 24-32.
- Mover-Lev, H., Priner-Barenholtz, R., Ar, A., Sade', J., 1998. Quantitative analysis of gas losses and gains in the middle ear. *Respir. Physiol.* 114, 143-151. doi:10.1016/S0034-5687(98)00059-0
- Muyshondt, P.G.G., De Greef, D., Soons, J., Dirckx, J.J.J., 2014. Optical techniques as validation tools for finite element modeling of biomechanical structures, demonstrated in bird ear research, in: *AIP Conference Proceedings* 1600. Ancona, pp. 330-337. doi:10.1063/1.4879599
- Nakajima, H.H., Dong, W., Olson, E.S., Merchant, S.N., Ravicz, M.E., Rosowski, J.J., 2009. Differential intracochlear sound pressure measurements in normal human temporal bones. *JARO - J. Assoc. Res. Otolaryngol.* 10, 23-36. doi:10.1007/s10162-008-0150-y

- Niklasson, A., Tano, K., 2010. Self-inflicted negative pressure of the external ear canal: a common cause of isolated malleus fractures. *Acta Otolaryngol.* 130, 410–416. doi:10.3109/00016480903177521
- Niklasson, A., Rönnblom, A., Muysshondt, P.G.G., Dirckx, J., von Unge, M., Tano, K., 2016. Ossiculoplasty on Isolated Malleus Fractures. *Otol. Neurotol.* 37, 895–901. doi:10.1097/MAO.0000000000001086
- Nummela, S., 1995. Scaling of the mammalian middle ear. *Hear. Res.* 85, 18–30. doi:10.1016/0378-5955(95)00030-8
- Onchi, Y., 1949. A Study of the Mechanism of the Middle Ear. *J. Acoust. Soc. Am.* 21, 404. doi:10.1121/1.1906527
- Pal'chun, V., Magomedov, M., 1997. Some anatomical features of the long process of the incus. *Vestn Otorinolaringol* 2, 19–20.
- Pang, X.D., Peake, W.T., 1986. How Do Contractions of the Stapedius Muscle Alter the Acoustic Properties of the Ear?, in: *Peripheral Auditory Mechanisms*. Springer Berlin Heidelberg, pp. 36–43. doi:10.1007/978-3-642-50038-1\_5
- Pedrini, G., Osten, W., Gusev, M.E., 2006. High-speed digital holographic interferometry for vibration measurement. *Appl. Opt.* 45, 3456–62.
- Pita, V.J.R.R., Sampaio, E.E.M., Monteiro, E.E.C., 2002. Mechanical properties evaluation of PVC/plasticizers and PVC/thermoplastic polyurethane blends from extrusion processing. *Polym. Test.* 21, 545–550. doi:10.1016/S0142-9418(01)00122-2
- Politzer, A., 1892. *The anatomical and histological dissection of the human ear in the normal and diseased condition*. Baillière, Tindall and Cox, London.
- Poon, T.-C., 2007. *Optical scanning holography with MATLAB, Computer*. Springer.
- Powell, R.L., Stetson, K.A., 1965. Interferometric Vibration Analysis by Wavefront Reconstruction. *J. Opt. Soc. Am.* 55, 1593–1597. doi:10.1364/JOSA.55.001593
- Prades, J.M., Dumollard, J.M., Calloc'h, F., Merzougui, N., Veyret, C., Martin, C., 1998. Descriptive anatomy of the human auditory tube. *Surg. Radiol. Anat.* 20, 335–340. doi:10.1007/s00276-998-0335-4
- Prendergast, P.J., Ferris, P., Rice, H.J., Blayney, A.W., 1999. Vibro-Acoustic Modelling of the Outer and Middle Ear Using the Finite-Element Method. *Audiol. Neuro-Otology* 4, 185–191. doi:10.1159/000013839
- Puria, S., Peake, W.T., Rosowski, J.J., 1997. Sound-pressure measurements in the cochlear vestibule of human-cadaver ears. *J. Acoust. Soc. Am.* 101, 2754–2770. doi:10.1121/1.418563
- Puria, S., Steele, C., 2010. Tympanic-membrane and malleus-incus-complex co-adaptations for high-frequency hearing in mammals. *Hear. Res.* 263, 183–90. doi:10.1016/j.heares.2009.10.013
- Puria, S., Fay, R., Popper, A.N., 2013. *The Middle Ear*, Springer Handbook of Auditory Research. Springer New York, New York, NY. doi:10.1007/978-1-4614-6591-1
- Quam, R.M., Coleman, M.N., Martínez, I., 2014. Evolution of the auditory ossicles in extant hominids: metric variation in African apes and humans. *J. Anat.* 225, 167–96. doi:10.1111/joa.12197
- Rosowski, J.J., Davis, P.J., Merchant, S.N., Donahue, K.M., Coltrera, M.D., 1990. Cadaver middle ears as models for living ears: comparisons of middle ear input immittance. *Ann. Otol. Rhinol. Laryngol.* 99, 403–12.
- Rosowski, J.J., 1994. Outer and middle ears, in: *Comparative Hearing: Mammals*. Springer New York, pp. 172–247. doi:10.1007/978-1-4612-2700-7\_6

- Rosowski, J.J., Chien, W., Ravicz, M.E., Merchant, S.N., 2007. Testing a method for quantifying the output of implantable middle ear hearing devices. *Audiol. Neurootol.* 12, 265–76. doi:10.1159/000101474
- Rosowski, J.J., Nakajima, H.H., Merchant, S.N., 2008. Clinical utility of laser-Doppler vibrometer measurements in live normal and pathologic human ears. *Ear Hear.* 29, 3–19. doi:10.1097/AUD.0b013e31815d63a5
- Rosowski, J.J., Cheng, J.T., Ravicz, M.E., Hulli, N., Hernandez-Montes, M. del S., Harrington, E., 2009. Computer-assisted time-averaged holograms of the motion of the surface of the mammalian tympanic membrane with sound stimuli of 0.4–25 kHz. *Hear. Res.* 253, 83–96.
- Rosowski, J.J., Cheng, J.T., Merchant, S.N., Harrington, E., Furlong, C., 2011. New data on the motion of the normal and reconstructed tympanic membrane. *Otol. Neurotol.* 32, 1559–67. doi:10.1097/MAO.0b013e31822e94f3
- Rowicki, T., Zakrzewska, J., 2006. A study of the discomalleolar ligament in the adult human. *Folia Morphol. (Warsz).* 65, 121–5.
- Ruah, C.B., Schachern, P. a, Zelterman, D., Paparella, M.M., Yoon, T.H., 1991. Age-related morphologic changes in the human tympanic membrane. A light and electron microscopic study. *Arch. Otolaryngol. Head. Neck Surg.* 117, 627–34.
- Sadd, M., 2009. *Elasticity: theory, applications, and numerics.* Elsevier.
- Sade, J., Ar, A., 1997. Middle ear and auditory tube: Middle ear clearance, gas exchange, and pressure regulation. *Otolaryngol. - Head Neck Surg.* 116, 499–524. doi:10.1016/S0194-5998(97)70302-4
- Salih, W.H.M.W., Buytaert, J.A.N.A.N., Aerts, J.R.M., Vanderniepen, P., Dierick, M., Dirckx, J.J.J., 2012. Open access high-resolution 3D morphology models of cat, gerbil, rabbit, rat and human ossicular chains. *Hear. Res.* 284, 1–5. doi:10.1016/j.heares.2011.12.004
- Sanjay, K.K., Muthukumar, R., Balasubramanian, T., 2012. Endoscopic Tympanomastoid Exploration. *Online J. Otolaryngol.* 2, 34–142.
- Schraven, S.P., Hirt, B., Gummer, A.W., Zenner, H.-P., Dalhoff, E., 2011. Controlled round-window stimulation in human temporal bones yielding reproducible and functionally relevant stapedial responses. *Hear. Res.* 282, 272–82. doi:10.1016/j.heares.2011.07.001
- Sencimen, M., Yalçın, B., Doğan, N., Varol, A., Okçu, K.M., Ozan, H., Aydintuğ, Y.S., 2008. Anatomical and functional aspects of ligaments between the malleus and the temporomandibular joint. *Int. J. Oral Maxillofac. Surg.* 37, 943–7. doi:10.1016/j.ijom.2008.07.003
- Shaw, E.A.G., 1974. The External Ear, in: *Auditory System.* Springer Berlin Heidelberg, pp. 455–490. doi:10.1007/978-3-642-65829-7\_14
- Sim, J.H., Puria, S., Steele, C., 2007. Calculation of inertial properties of the malleus-incus complex from micro-CT imaging. *J. Mech. Mater. Struct.* 2, 1515–1524. doi:10.2140/jomms.2007.2.1515
- Sim, J.H., Puria, S., 2008. Soft tissue morphometry of the malleus-incus complex from micro-CT imaging. *J. Assoc. Res. Otolaryngol.* 9, 5–21. doi:10.1007/s10162-007-0103-x
- Sim, J.H., Rösli, C., Chatzimichalis, M., Eiber, A., Huber, A.M., 2013. Characterization of stapes anatomy: investigation of human and Guinea pig. *J. Assoc. Res. Otolaryngol.* 14, 159–73. doi:10.1007/s10162-012-0369-5
- Soons, J.A.M., Aernouts, J., Dirckx, J.J.J., 2010. Elasticity modulus of rabbit middle ear ossicles determined by a novel micro-indentation technique. *Hear. Res.* 263, 33–7. doi:10.1016/j.heares.2009.10.001
- Stenfelt, S., Hato, N., Goode, R.L., 2004. Fluid volume displacement at the oval and round windows with air and bone conduction stimulation. *J. Acoust. Soc. Am.* 115, 797. doi:10.1121/1.1639903

- Stinson, M.R., 1985. The spatial distribution of sound pressure within scaled replicas of the human ear canal. *J. Acoust. Soc. Am.* 78, 1596. doi:10.1121/1.392797
- Sun, Q., Gan, R.Z., Chang, K.-H., Dormer, K.J., 2002. Computer-integrated finite element modeling of human middle ear. *Biomech. Model. Mechanobiol.* 1, 109–22. doi:10.1007/s10237-002-0014-z
- Takahashi, H., Iwanaga, T., Kaieda, S., Fukuda, T., Kumagami, H., Takasaki, K., Hasebe, S., Funabiki, K., 2007. Mastoid obliteration combined with soft-wall reconstruction of posterior ear canal. *Eur. Arch. Oto-Rhino-Laryngology* 264, 867–871. doi:10.1007/s00405-007-0273-5
- Tideholm, B., Jönsson, S., Carlborg, B., Welinder, R., Grenner, J., 1996. Continuous 24-hour Measurement of Middle Ear Pressure. *Acta Otolaryngol.* 116, 581–588. doi:10.3109/00016489609137893
- Todd, N.W., Creighton, F.X., 2013. Malleus and incus: correlates of size. *Ann. Otol. Rhinol. Laryngol.* 122, 60–5.
- Tonndorf, J., Khanna, S.M., 1970. The role of the tympanic membrane in middle ear transmission. *Ann. Otol. Rhinol. Laryngol.* 79, 743–53.
- Tonndorf, J., Khanna, S.M., 1972. Tympanic-membrane vibrations in human cadaver ears studied by time-averaged holography. *J. Acoust. Soc. Am.* 52, 1221–33.
- Trillo, C., Doval, A.F., Mendoza-Santoyo, F., Pérez-López, C., de la Torre-Ibarra, M., Deán, J.L., 2009. Multimode vibration analysis with high-speed TV holography and a spatiotemporal 3D Fourier transform method. *Opt. Express* 17, 18014–25.
- Tuck-Lee, J.P., Pinsky, P.M., Steele, C.R., Puria, S., 2008. Finite element modeling of acousto-mechanical coupling in the cat middle ear. *J. Acoust. Soc. Am.* 124, 348–62. doi:10.1121/1.2912438
- Unur, E., Ulger, H., Ekinçi, N., 2002. Morphometrical and morphological variations of middle ear ossicles in the newborn. *Erciyes Med. J.* 24, 57–63.
- Van der Jeught, S., Dirckx, J.J.J., Aerts, J.R.M., Bradu, A., Podoleanu, A.G.H., Buytaert, J. a N., 2013. Full-field thickness distribution of human tympanic membrane obtained with optical coherence tomography. *J. Assoc. Res. Otolaryngol.* 14, 483–94. doi:10.1007/s10162-013-0394-z
- Van Rompaey, V., Caremans, J., Hamans, E., Muylle, L., Van De Heyning, P., 2013. Endoscopic procurement of tympano-ossicular allografts: Alternative to the transcranial or retroauricular technique. *Cell Tissue Bank.* 14, 511–514. doi:10.1007/s10561-012-9344-y
- Vercruyse, J.-P., De Foer, B., Somers, T., Casselman, J.W., Offeciers, E., 2008. Mastoid and Epitympanic Bony Obliteration in Pediatric Cholesteatoma. *Otol. Neurotol.* 29, 953–960. doi:10.1097/MAO.0b013e318184f4d6
- Volandri, G., Di Puccio, F., Forte, P., Carmignani, C., 2011. Biomechanics of the tympanic membrane. *J. Biomech.* 44, 1219–36. doi:10.1016/j.jbiomech.2010.12.023
- Volandri, G., Di Puccio, F., Forte, P., Manetti, S., 2012. Model-oriented review and multi-body simulation of the ossicular chain of the human middle ear. *Med. Eng. Phys.* 34, 1339–55. doi:10.1016/j.medengphy.2012.02.011
- Wada, H., Kobayashi, T., 1990. Dynamical behavior of middle ear: Theoretical study corresponding to measurement results obtained by a newly developed measuring apparatus. *J. Acoust. Soc. Am.* 87, 237. doi:10.1121/1.399290
- Wada, H., Metoki, T., Kobayashi, T., 1992. Analysis of dynamic behavior of human middle ear using a finite-element method. *J. Acoust. Soc. Am.* 92, 3157–68.
- Wang, X., Cheng, J.T., Gan, R.Z., 2007. Finite-element analysis of middle-ear pressure effects on static and dynamic behavior of human ear. *J. Acoust. Soc. Am.* 122, 906–917. doi:10.1121/1.2749417

- Weistenhöfer, C., Hudde, H., 1999. Determination of the shape and inertia properties of the human auditory ossicles. *Audiol. Neurotol.* 4, 192–6.
- Wever, E.G., Lawrence, M., 1954. *Physiological Acoustics*. Princeton Univ. Press, Princeton, N.J. doi:10.1126/science.119.3095.560
- Whittemore, K.R., Merchant, S.N., Poon, B.B., Rosowski, J.J., 2004. A normative study of tympanic membrane motion in humans using a laser Doppler vibrometer (LDV). *Hear. Res.* 187, 85–104. doi:10.1016/S0378-5955(03)00332-0
- Wightman, F.L., Kistler, D.J., 1992. The dominant role of low-frequency interaural time differences in sound localization. *J. Acoust. Soc. Am.* 91, 1648–1161. doi:10.1121/1.402445
- Willi, U.B., 2003. *Middle ear mechanics: The dynamic behavior of the incudo-malleolar joint and its role during the transmission of sound*. Universität Zürich.
- Yamaguchi, I., Zhang, T., 1997. Phase-shifting digital holography. *Opt. Lett.* 22, 1268–1270. doi:10.1364/OL.22.001268
- Yao, W., Ma, J., Huang, X., 2013. Numerical simulation of the human ear and the dynamic analysis of the middle ear sound transmission. *J. Instrum.* 8, C06009–C06009. doi:10.1088/1748-0221/8/06/C06009
- Zhang, X., Gan, R.Z., 2011a. A comprehensive model of human ear for analysis of implantable hearing devices. *IEEE Trans. Biomed. Eng.* 58, 3024–3027. doi:10.1109/TBME.2011.2159714
- Zhang, X., Gan, R.Z., 2011b. Experimental measurement and modeling analysis on mechanical properties of incudostapedial joint. *Biomech. Model. Mechanobiol.* 10, 713–26. doi:10.1007/s10237-010-0268-9
- Zhang, X., Gan, R.Z., 2010. Dynamic properties of human tympanic membrane – experimental measurement and modelling analysis. *Int. J. Exp. Comput. Biomech.* 1, 252. doi:10.1504/IJECB.2010.035260
- Zhang, X., Gan, R.Z., 2013. Dynamic properties of human tympanic membrane based on frequency-temperature superposition. *Ann. Biomed. Eng.* 41, 205–14. doi:10.1007/s10439-012-0624-2
- Zhao, F., Koike, T., Wang, J., Sienz, H., Meredith, R., 2009. Finite element analysis of the middle ear transfer functions and related pathologies. *Med. Eng. Phys.* 31, 907–16. doi:10.1016/j.medengphy.2009.06.009
- Zienkiewicz, O.C., Taylor, R.L., 200AD. *The Finite Element Method: Solid mechanics*, 5th ed. ed. Butterworth-Heinemann.
- Zilske, M., Lamecker, H., Zachow, S., 2008. Adaptive Remeshing of Non-Manifold Surfaces. *Eurographics 2008 Annex to Conf. Proc.* 27, 211–214.
- Zwislocki, J., 1957. Some Impedance Measurements on Normal and Pathological Ears. *J. Acoust. Soc. Am.* 29, 1312. doi:10.1121/1.1908776
- Zwislocki, J.J., 1965. Analysis of some auditory characteristics, in: *Handbook of Mathematical Psychology* Vol. III. John Wiley & Sons, pp. 1–97.

# List of publications

---

## Journal publications with peer review

- Aerts, J.R.M., De Greef, D., Peacock, J., Dirckx, J.J.J., 2011. Laser vibrometry for measurement of non-linear distortions in the vibration of weakly non-linear slowly time-varying systems, in: Rodríguez-Vera, R., Díaz-Urbe, R. (Eds.), Proceedings of SPIE. p. 80118M–80118M–8. doi:10.1117/12.902073
- Gaihede, M., Padurariu, S., Jacobsen, H., De Greef, D., Dirckx, J.J.J., 2013. Eustachian tube pressure equilibration. Temporal analysis of pressure changes based on direct physiological recordings with an intact tympanic membrane. *Hear. Res.* doi:10.1016/j.heares.2013.01.003
- Buytaert, J., Goyens, J., De Greef, D., Aerts, P., Dirckx, J., 2014. Volume Shrinkage of Bone, Brain and Muscle Tissue in Sample Preparation for Micro-CT and Light Sheet Fluorescence Microscopy (LSFM). *Microsc. Microanal.* 20, 1208–1217. doi:10.1017/S1431927614001329
- De Greef, D., Aernouts, J., Aerts, J., Cheng, J.T., Horwitz, R., Rosowski, J.J., Dirckx, J.J.J., 2014. Viscoelastic properties of the human tympanic membrane studied with stroboscopic holography and finite element modeling. *Hear. Res.* 312, 69–80. doi:10.1016/j.heares.2014.03.002
- De Greef, D., Soons, J., Dirckx, J.J.J., 2014. Digital Stroboscopic Holography Setup for Deformation Measurement at Both Quasi-Static and Acoustic Frequencies. *Int. J. Optomechatronics* 8, 275–291. doi:10.1080/15599612.2014.942928
- De Greef, D., Buytaert, J.A.N., Aerts, J.R.M., Van Hoorebeke, L., Dierick, M., Dirckx, J., 2015. Details of human middle ear morphology based on micro-CT imaging of phosphotungstic acid stained samples. *J. Morphol.* 276, 1025–46. doi:10.1002/jmor.20392
- De Greef, D., Goyens, J., Pintelon, I., Bogers, J.-P., Van Rompaey, V., Hamans, E., Van de Heyning, P., Dirckx, J.J.J., 2016. On the connection between the tympanic membrane and the malleus. *Hear. Res.* 340, 50–59. doi:10.1016/j.heares.2015.12.002
- Muyshondt, P.G.G., Soons, J.A.M., De Greef, D., Pires, F., Aerts, P., Dirckx, J.J.J., 2016. A single-ossicle ear: Acoustic response and mechanical properties measured in duck. *Hear. Res.* 340, 35–42. doi:10.1016/j.heares.2015.12.020
- Padurariu, S., De Greef, D., Jacobsen, H., Nlandu Kamavuako, E., Dirckx, J.J.J., Gaihede, M., 2016. Pressure buffering by the tympanic membrane. In vivo measurements of middle ear pressure fluctuations during elevator motion. *Hear. Res.* 340, 113–120. doi:10.1016/j.heares.2015.12.004

De Greef, D., Pires, F., Dirckx, J.J.J., 2017, Effects of Model Definitions and Parameter Values in Finite Element Modeling of Human Middle Ear Mechanics, in press, Hearing Research. doi: 10.1016/j.heares.2016.11.011

### **Under review/soon to be submitted**

De Greef, D., Muyshondt, P., Dirckx, J.J.J., The Effect of Malleus Handle Fracture on Middle Ear Transmission, predicted using Finite Element Analysis, *submitted for publication in JARO*.

## Conference contributions

<sup>(P)</sup> Presenting author

**OPTIMESS 2012:** De Greef, D. <sup>(P)</sup>, Dirckx, J.J.J., 2013. Fullfield Time-Resolved Digital Holographic Interferometry: Four-Dimensional Imaging of Nanometer Vibrations using Stroboscopic Illumination, in: Dirckx, J.J.J., Buytaert, J.A.N. (Eds.), Optical Measurement Techniques for Systems & Structures III. Shaker Publishing B.V., Antwerp, p. 536.

**AIVELA 2012:** De Greef, D. <sup>(P)</sup>, Dirckx, J. J. J., 2012. Single-shot digital holographic interferometry using a high power pulsed laser for full field measurement of traveling waves, in AIP Conference Proceedings, 2012, vol. 1457, pp. 444-450. doi:10.1063/1.4730587

**ISMA 2012:** De Greef, D. <sup>(P)</sup>, Dirckx, J.J.J., 2012. Digital holographic vibrometry using stroboscopic illumination for full field , time resolved 4D imaging of nanometer vibrations, in: Proceedings of ISMA2012-USD2012. pp. 1435-1444.

**Bruker User Meeting 2013:** De Greef, D. <sup>(P)</sup>, Buytaert, J. A. N., Dirckx, J. J. J., Studying the functional morphology of the middle ear by visualizing bone and soft tissue structures with microCT, in Bruker Micro-CT User Meeting 2013 Abstract Book, 2013, p. 343.

**ICTMS 2013:** Buytaert, J. A. N. <sup>(P)</sup>, Aerts, J. R. M., Salih, W. H. M., De Greef, D., Peacock, J., Dierick, M., Van Hoorebeke, L., Dirckx, J. J. J., 2013. Visualizing middle ear structures with CT - Studying morphology (bone and soft tissue) & dynamics, in ICTMS 2013 Proceedings, pp. 3-6.

**ALSFM Workshop 2013:** Buytaert, J. A. N. <sup>(P)</sup>, Goyens, J., De Greef, D., Aerts, P., Dirckx, J. J. J., 2013. Shrink volume quantification when imaging soft and bony tissue, in: 5th Annual Light-Sheet Fluorescence Microscopy Workshop. New York. vol. 171, no. 4.

**Fringe 2013:** De Greef, D. <sup>(P)</sup>, Dirckx, J. J. J., 2014. A Synchronized Stroboscopic Holography Setup for Traveling Wave Analysis on Biomechanical Structures, in Osten, W. (Ed.), Fringe

2013: 7th International Workshop on Advanced Optical Imaging and Metrology. Springer Berlin Heidelberg, Berlin, Heidelberg, pp. 433–438. doi:10.1007/978-3-642-36359-7\_77

**ARO 2014:** Buytaert, J. A. N. <sup>(P)</sup>, De Greef, D., Aerts, J. R. M., Dirckx, J. J. J., 2014. Visualizing Soft-Tissue in Human Temporal Bones Using MicroCT and PTA Staining, in Abstracts of the 37th Annual Midwinter Meeting of the Assoc. Res. Otolaryngol., San Diego, vol. 37, pp. 480–481.

**Bruker User Meeting 2014:** Goyens, J. <sup>(P)</sup>, Buytaert, J. A. N., De Greef, D., Aerts, P., Dirckx, J. J. J., 2014. Quantifying the tissue shrinkage caused by sample preparation for micro-CT and LSFM, in Bruker Micro-CT User Meeting 2014 Abstrack Book. Oostende.

**WAS-dag 2014:** De Greef, D. <sup>(P)</sup>, Muyshondt, P., Buytaert, J. A. N., Soons, J. A. M., Dirckx, J. J. J., 2014. Holographic interferometry measurements of eardrum vibrations as input for finite element modelling of middle ear mechanics, WAS-dag May 2014

**AIVELA 2014:** De Greef, D. <sup>(P)</sup>, Dirckx, J. J. J., 2014. Measurement of rabbit eardrum vibration through stroboscopic digital holography, in AIP Conference Proceedings, Ancona. vol. 1600, pp. 323–329. doi:10.1063/1.4879598

**AIVELA 2014:** Muyshondt, P., De Greef, D. <sup>(P)</sup>, Soons, J. A. M., Dirckx, J. J. J., 2014. Optical techniques as validation tools for finite element modeling of biomechanical structures, demonstrated in bird ear research, in AIP Conference Proceedings, Ancona, vol. 1600, pp. 330–337. doi:10.1063/1.4879599

**Comsol Conference 2014:** Muyshondt, P. <sup>(P)</sup>, De Greef, D., Soons, J. A. M., Peacock, J., Dirckx, J. J. J., 2014. Determination of the Mechanical Properties in the Avian Middle Ear by Inverse Analysis, in Proceedings of the 2014 COMSOL Conference, Rotterdam.

**ARO 2015:** De Greef, D., Buytaert, J. A. N., Aerts, J. R. M., Soons <sup>(P)</sup>, J. A. M., Dirckx, J. J. J., 2015. Human Middle Ear Morphology: New Data from MicroCT and PTA Staining, in Abstracts of the 38th Annual Midwinter Meeting of the Assoc. Res. Otolaryngol., Baltimore, pp. 461–462.

**OPTIMESS 2015:** De Greef, D. <sup>(P)</sup>, Dirckx, J.J.J., 2016. Stroboscopic digital holography as a quantitative tool for the characterization of the mammal tympanic membrane, in: Dirckx, J.J.J., Buytaert, J.A.N. (Eds.), Optical Measurement Techniques for Systems & Structures 2. Shaker Publishing B.V., Antwerp, p. 384.

**OPTIMESS 2015:** Muyshondt, P. G. G. <sup>(P)</sup>, De Greef, D., Soons, J.A.M., Dirckx, J.J.J., 2016. Optical interferometry and finite element modeling as input techniques for inverse analysis on the mechanical propertis of the avian middle ear, in: Dirckx, J.J.J., Buytaert, J.A.N. (Eds.), Optical Measurement Techniques for Systems & Structures 2. Shaker Publishing B.V., Antwerp, p. 384.

**MEMRO 2015:** De Greef, D. <sup>(P)</sup>, Goyens, J., Pintelon, I., Bogers, J.-P., Van Rompaey, V., Hamans, E., Van de Heyning, P., Dirckx, J. J. J., 2015. On the connection between the eardrum and the malleus: a detailed study through micro-CT and histology, in: MEMRO 2015 - 7th International Symposium on Middle Ear Mechanics in Research and Otology. Aalborg, pp. 29–30.

**MEMRO 2015:** Muyshondt, P. <sup>(P)</sup>, Soons, J. A. M., De Greef, D., Aerts, P., Dirckx, J. J. J., 2015. A single-ossicle ear: acoustic response and mechanical properties measured in duck, in: MEMRO 2015 - 7th International Symposium on Middle Ear Mechanics in Research and Otology. Aalborg, p. 27.

**Measurement by Light (Shell) 2015:** De Greef, D. <sup>(P)</sup>, Dirckx, J. J. J., 2015. Stroboscopic Digital Holography as a Quantitative validation Tool for the Characterization of the Mammal and Avian Eardrum, Measuring by Light 2015, Rijswijk

**AIVELA 2016:** Keersmaekers, L., Keustermans, W. <sup>(P)</sup>, De Greef, D., Dirckx, J.J.J., 2016. Full-field vibration measurements of the violin using digital stroboscopic holographic interferometry and electromagnetic stimulation of the strings, in: AIP Conf. Proc 1740, 040005. doi:10.1063/1.4952664

**AIVELA 2016:** Keustermans, W. <sup>(P)</sup>, Pires, F., De Greef, D., Vanlanduit, S.J.A., Dirckx, J.J.J., 2016. Digital stroboscopic holographic interferometry for power flow measurements in acoustically driven membranes, in: AIP Conf. Proc 1740, 040005. doi:10.1063/1.4952660